# The Rift to Drift Transition and Sequence Stratigraphy At Passive Continental Margins

*Volume I*



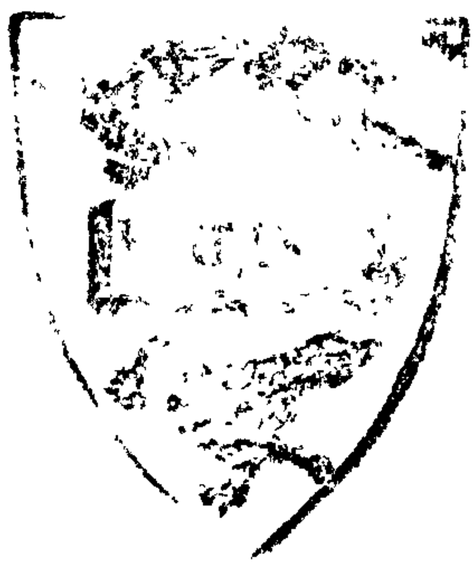

Thesis submitted in accordance with the requirements
of the University of Liverpool
for the degree of Doctor of Philosophy
by Timothy John Couzens

September 1992

# ABSTRACT

Most passive margins display a prominent breakup unconformity coinciding with the rift to drift transition. The unconformity, as defined by Falvey, (1974) is of broad regional extent affecting both basins and highs and is easily recognised on seismic sections. Criteria for the recognition of the breakup unconformity include an inflection in the subsidence curve, fault terminations and volcanic strata (and/or evaporites) at the level of the unconformity. Falvey considered that it was caused by "erosion during the final uplift pulse associated with pre-breakup upwelling in the mantle". It is more likely that the uplift is caused by magmatic underplating in response to the passive upwelling of the mantle and the flexural isostatic effects of erosion throughout the syn-rift phase.

The primary objective has been to quantify the amount of uplift and erosion associated with the breakup unconformity / breakup megasequence boundary. This is of particular importance in hydrocarbon exploration as it quantifies the potential loss of old reservoirs and predicts the provenance of new reservoir clastics.

Two data sets, from the Grand Banks and the Northwest Shelf of Australia, have been studied. In both cases there are multiple breakup events and breakup megasequence boundaries form part of a complex tectono-stratigraphy. Regional seismic lines have been interpreted, depth converted and modelled using a new technique of combined reverse post-rift and forward syn-rift modelling. The results of this process, together with seismic megasequence analysis, show that the morphology of the breakup megasequence boundary varies systematically across a passive margin. It is strongly erosional at about 70 km landward of the continent-ocean boundary, where regional "breakup" uplift outweighs extensionally controlled subsidence, but may be depositional on either side of this zone.

A coupled, quantitative magmatic-tectonic model has been constructed by combining the Bickle-McKenzie melt generation model with the flexural cantilever model for continental extension. The magnitude of underplating can be estimated using the Bickle-McKenzie model, in which the amount of melt produced is controlled by the extension factor, $\beta$, and the proximity of a mantle plume convection cell.

## ACKNOWLEDGEMENTS

These acknowledgements were originally going to be brief, not because I am ungrateful for all the help I have received, but because I wanted to avoid over-sentimental references to individuals. My idea was to thank my supervisors and then mention "everybody who knew me at Liverpool" including academics, researchers, departmental staff, friends in general, publicans, tea ladies . . . . and so the list went on. But it would appear that people like to see their names in print, so here goes. Firstly, I am deeply indebted to Nick Kusznir, whose assistance and supervision has been incalculable. Secondly, Mike Daly is acknowledged for his help in obtaining first class data sets from B.P. and for many useful discussions on the work in progress. My thanks also go to Paul Caban, whose patience I tried on too many occasions, but who still gave me his reference list editor. To Clare Milsom, for her chats at tea-time and to Simon Day, for coming to see me when nobody else in their right minds would be in the department. Lastly, to Derek Hendrie, Simon Norris and Phil Nadin without whom this thesis would be merely a pile of A4 paper.

The research for this thesis was undertaken while in receipt of a N.E.R.C. - B.P. C.A.S.E. award.

# CONTENTS

## *VOLUME I*

## CHAPTER 1

## INTRODUCTION AND THESIS PLAN



## CHAPTER 2

## THE FLEXURAL CANTILEVER MODEL FOR CONTINENTAL EXTENSION

## CHAPTER 3

## MELT GENERATION DUE TO EXTENSION OF THE LITHOSPHERE.



## CHAPTER 4

## THE COMBINED MAGMATIC-TECTONIC MODEL FOR CONTINENTAL EXTENSION

## CHAPTER 5

## THE TECTONO-STRATIGRAPHY OF THE GRAND BANKS, OFFSHORE NEWFOUNDLAND



## CHAPTER 6

## THE MORPHOLOGY OF BREAKUP MEGASEQUENCE BOUNDARIES BASED ON SEISMIC SECTIONS ACROSS THE GRAND BANKS

# CHAPTER 7

## MODELLING PHILOSOPHY AND THE RESULTS OF THE APPLICATION TO THE GRAND BANKS

*VOLUME II*

## CHAPTER 8

## THE TECTONO-STRATIGRAPHY OF THE NORTHWEST SHELF OF AUSTRALIA.



## CHAPTER 9

## SEISMIC MEGASEQUENCE ANALYSIS ON THE NORTHWEST SHELF OF AUSTRALIA.

## CHAPTER 10

## MODELLING RESULTS FROM THE NORTHWEST SHELF OF AUSTRALIA.



## CHAPTER 11

## GLOBALLY SYNCHRONOUS MEGASEQUENCE BOUNDARIES.



## CHAPTER 12



## BIBLIOGRAPHY

## APPENDIX A



## APPENDIX B
## APPENDIX C
## APPENDIX D

# CHAPTER 1

## INTRODUCTION AND THESIS PLAN.

The concept of an unconformity, thought to form during the final uplift phase prior to seafloor spreading, was first proposed by Falvey (1974), based on seismic data from the S. Australian passive margin. It was termed the "breakup unconformity" and it forms the most important break in the stratigraphy of all passive margins, linking the sequence stratigraphy to the tectonic evolution of the margin. In tectono-stratigraphic terms, it marks the end of the rift phase and the onset of post-rift thermal subsidence.

When Falvey first defined the breakup unconformity, he envisaged that "active" upwelling of the mantle asthenosphere was responsible for the uplift. Such upwelling is now usually considered to be a passive response to continental extension leading to breakup, as defined by McKenzie (1978). This model, however, does not predict uplift above sea level and cannot be used to predict the location of subaerial erosion. In this thesis, the flexural cantilever model for continental extension and rift-basin formation is taken as a starting point, which predicts localised uplift in the footwalls of major planar faults in the upper crust. Various other mechanisms produce regional uplift, required from our knowledge of breakup megasequence boundary morphology, the most important of which is magmatic underplating.

The thesis plan in Figure 1.1 shows that introductory chapters 2 and 3 cover the flexural cantilever and melt generation models respectively, while Chapter 4 shows how they can be united in the combined magmatic-tectonic model for continental extension. This model has been applied to the large scale passive margin

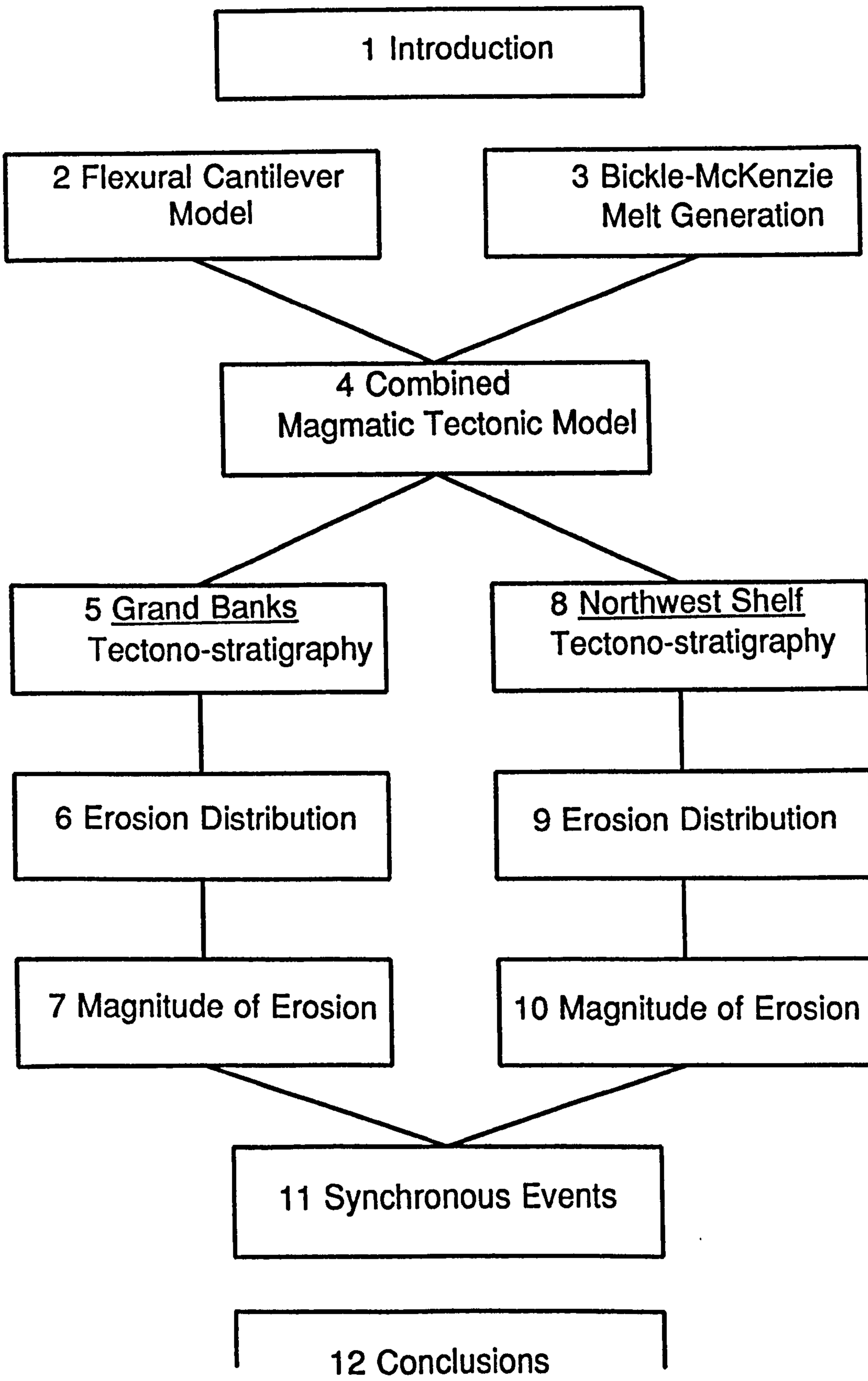


**Figure 1.1** Thesis Plan.

geometry (including an underplating wedge) but modelling results also predict the details of breakup megasequence boundary morphology.

The research undertaken for this thesis has three fundamental objectives:-

1) To determine the timing of breakup and deduce the tectono-stratigraphic framework for the two passive margins studied.

2) To analyze the spatial distribution of subaerial uplift and erosion associated with each breakup event.

3) To calculate the magnitude of breakup uplift, in order to better understand the mechanisms that are operating on passive margins at the rift to drift transition.

These fundamental objectives are essentially the answers to three basic questions concerning the subaerial uplift and erosion forming the breakup unconformity; When?, where?, and by how much?. The central portion of this thesis (Figure 1.1) has been arranged such that a chapter is devoted to each of these questions respectively:- Chapters 5, 6 and 7 for the Grand Banks study area, offshore Eastern Canada and Chapters 8, 9 and 10 for the Northwest Shelf of Australia. To achieve the third objective a modified form of flexural backstripping has been applied to the passive margins. By reverse modelling the post-rift phase, forward modelling the syn-rift phase and comparing the two, a quantitatively determined profile of the end of rift phase can be derived and the initial conditions of the model constrained.

The structure and evolution of passive margins in general is further outlined in this chapter, the breakup unconformity is formally defined and the mechanisms that have been proposed to explain its generation are discussed.

## 1.1 The formation of passive continental margins.

The formation of a passive margins has been explained in terms of two end-member models which differ in the distribution of stretching within the lithosphere: pure-shear and simple-shear models.

**Pure-shear models** - in which extension is distributed throughout the lithosphere. Figure 1.2a shows the McKenzie (1978) model in which the lithosphere is thinned by a single factor Beta ($\beta$) such that the original crustal thickness, $t_c$, reduces to $t_c/\beta$. Note the simplicity of the model - there are no faults and the Beta profile, in the upper part of the diagram, has an simple trapezoidal shape. More importantly, the rift flanks stay at, or below, sea level and the model cannot therefore be used to predict the location of subaerial uplift and erosion. Decompression of the upwelling asthenosphere causes partial melting (Figure 1.2b) and, if magma segregates and collects at the Moho, an "apparent stretching factor, $\beta_*$" can be defined. In Figure 1.2c, from Royden & Keen (1980), the rift flanks are uplifted as a result of hot, low density asthenosphere upwelling beneath un-thinned crust. Two separate stretching factors have been defined ($\beta$ for the crust and $\delta$ for the asthenosphere - the dotted line in the upper part of Figure 1.2a) hence the name depth dependent extension.

All of the models in Figure 1.2 assume local, or Airy type, isostatic equilibrium. By contrast, this thesis prefers to use the concept of flexural isostasy as explained in the next chapter. It is noted here that, by combining flexural rigidity with a depth dependent stretching model, Watts & Thorne (1984) were able to model the post-rift coastal onlap of a passive margin with reasonable accuracy (Figure 1.3).

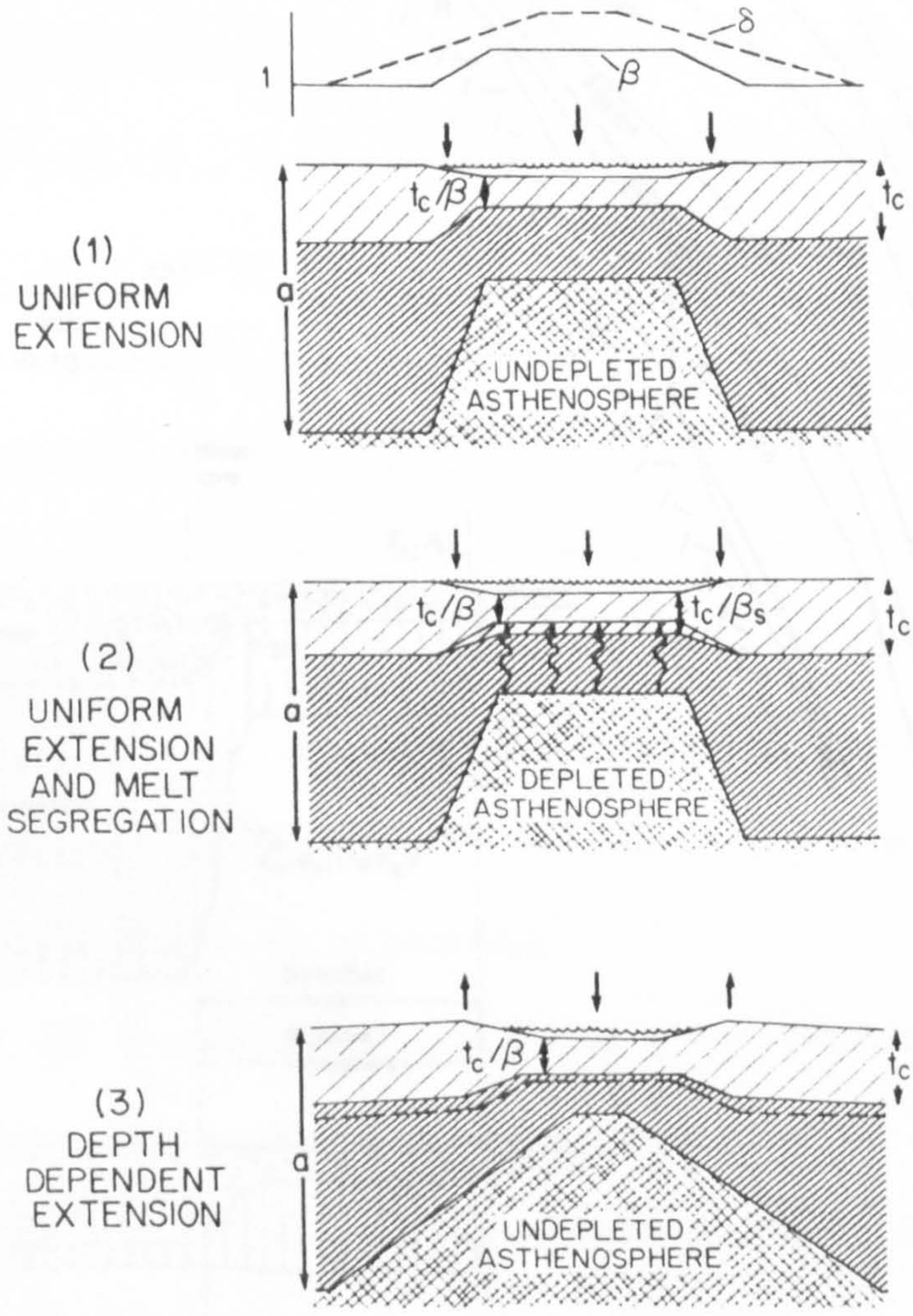


**Figure 1.2** (1) The McKenzie Model for uniform pure-shear thinning of the lithosphere with a crustal stretching factor β. (2) As with (1) but showing partial melting of the asthenosphere. (3) Depth dependent extension with a crustal stretching factor β and a lower lithosphere factor δ. Note the arrows marking the uplift of the rift shoulders.

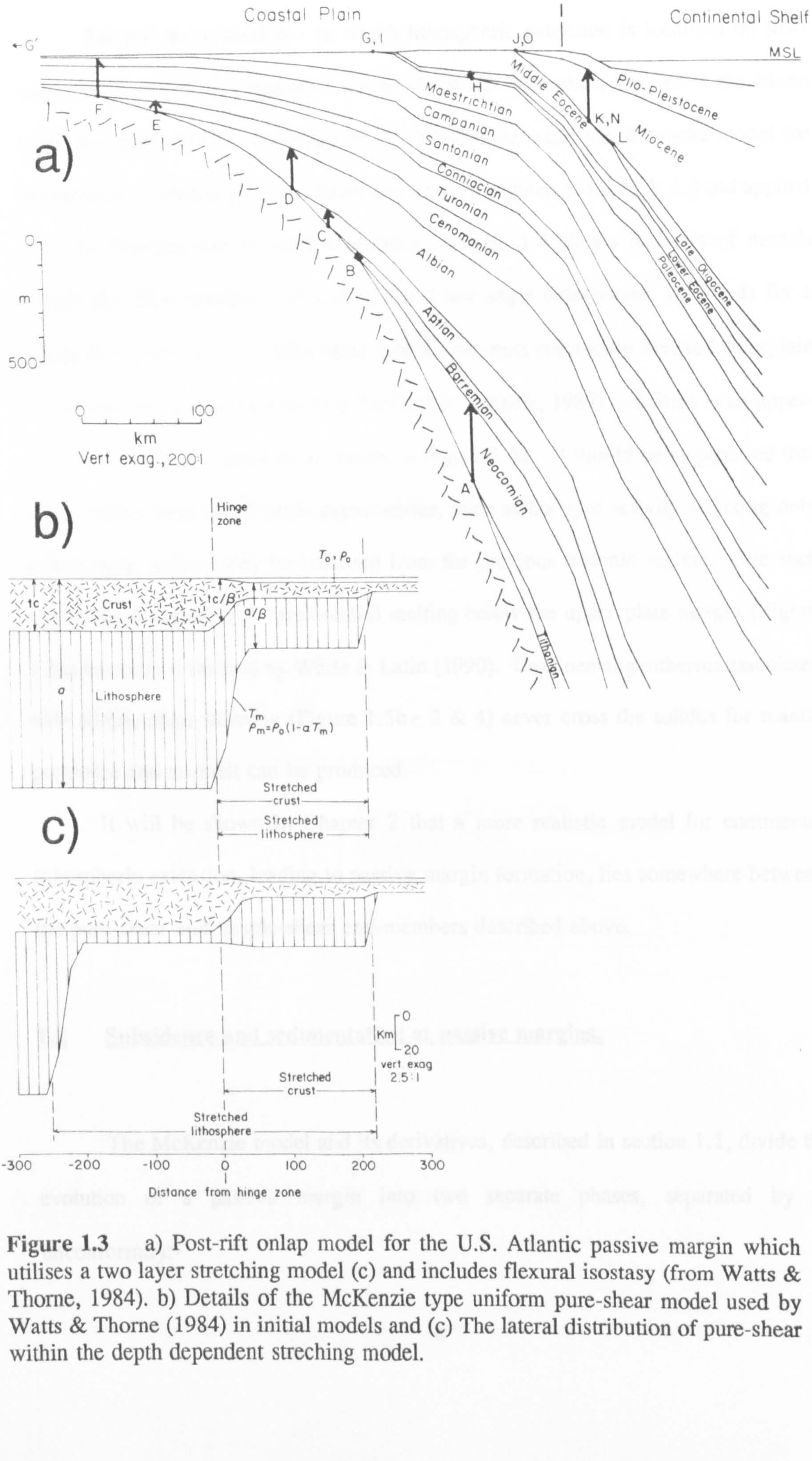


**Figure 1.3** a) Post-rift onlap model for the U.S. Atlantic passive margin which utilises a two layer stretching model (c) and includes flexural isostasy (from Watts & Thorne, 1984). b) Details of the McKenzie type uniform pure-shear model used by Watts & Thorne (1984) in initial models and (c) The lateral distribution of pure-shear within the depth dependent streching model.

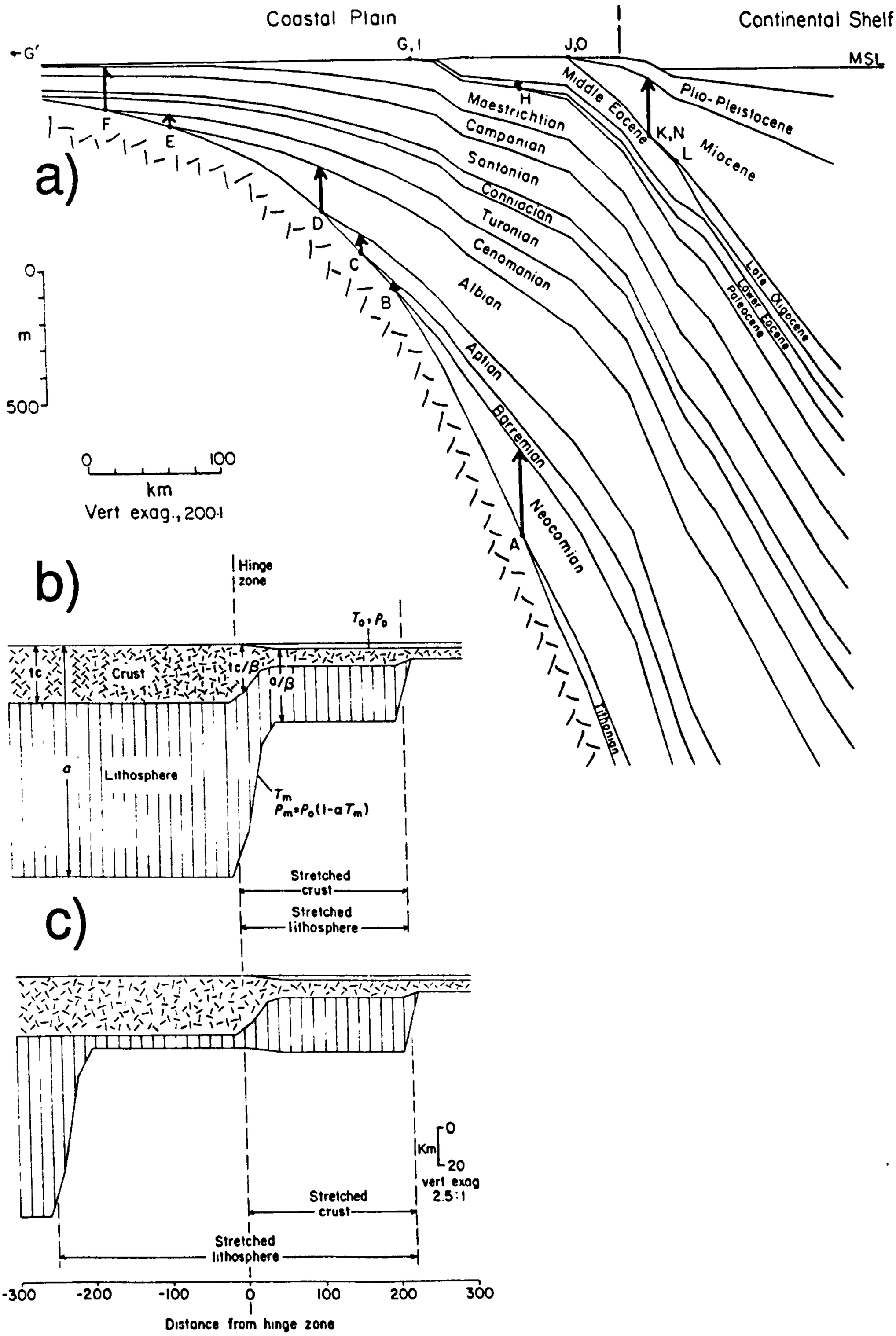


**Figure 1.3** a) Post-rift onlap model for the U.S. Atlantic passive margin which utilises a two layer stretching model (c) and includes flexural isostasy (from Watts & Thorne, 1984). b) Details of the McKenzie type uniform pure-shear model used by Watts & Thorne (1984) in initial models and (c) The lateral distribution of pure-shear within the depth dependent streching model.

**Simple-shear models** - in which lithospheric extension is localised on low-angle faults which may penetrate the whole of the lithosphere and offset the Moho (e.g. Wernicke, 1985). Etheridge et al. (1989) have taken the Wernicke model for lithospheric extension (e.g. the Basin and Range Province of the U.S.A.) and applied it to the development of passive margins. Figure 1.4 shows two sets of models before and after breakup - a) and b) for a low-angle detachment, c) and d) for a "ramp-flat" geometry. Simple-shear models are most commonly invoked to explain conjugate margin asymmetries (e.g Tankard & Welsink, 1987) and fitted to an upper-plate/lower-plate framework, as shown in Figure 1.5a. It should be emphasised that other mechanisms could cause asymmetries, such as hot-spot activity affecting only one margin, or they may be inherited from the previous tectonic regime. One such hypothetical asymmetry - preferential melting below the upper plate margin (Figure 1.5a) has been dismissed by White & Latin (1990). Continental geotherms associated with simple-shear thinning (Figure 1.5b - 2 & 4) never cross the solidus for mantle peridotite and no melt can be produced.

It will be shown in Chapter 2 that a more realistic model for continental lithospheric extension, leading to passive margin formation, lies somewhere between the pure-shear and simple-shear end-members described above.

## 1.2 Subsidence and sedimentation at passive margins.

The McKenzie model and its derivatives, described in section 1.1, divide the evolution of a passive margin into two separate phases, separated by an unconformity:-

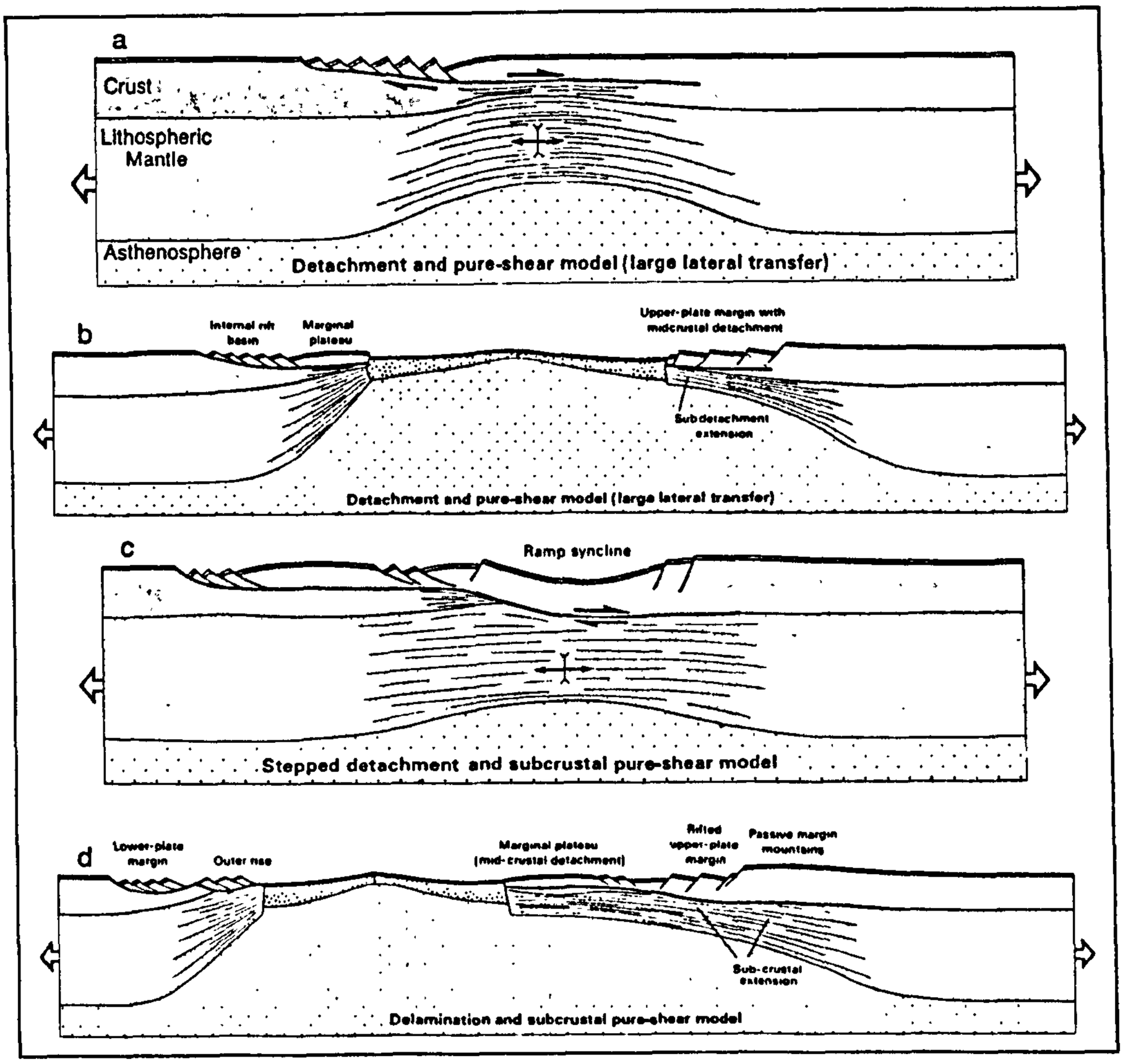


**Figure 1.4** Simple-shear models for passive margin development, before and after breakup. (a) and (b) With a listric geometry and inter-crustal detachment. (c) & (d) With a ramp-flat geometry and subcrustal detachment. (From Etheridge et al., 1989)

a)

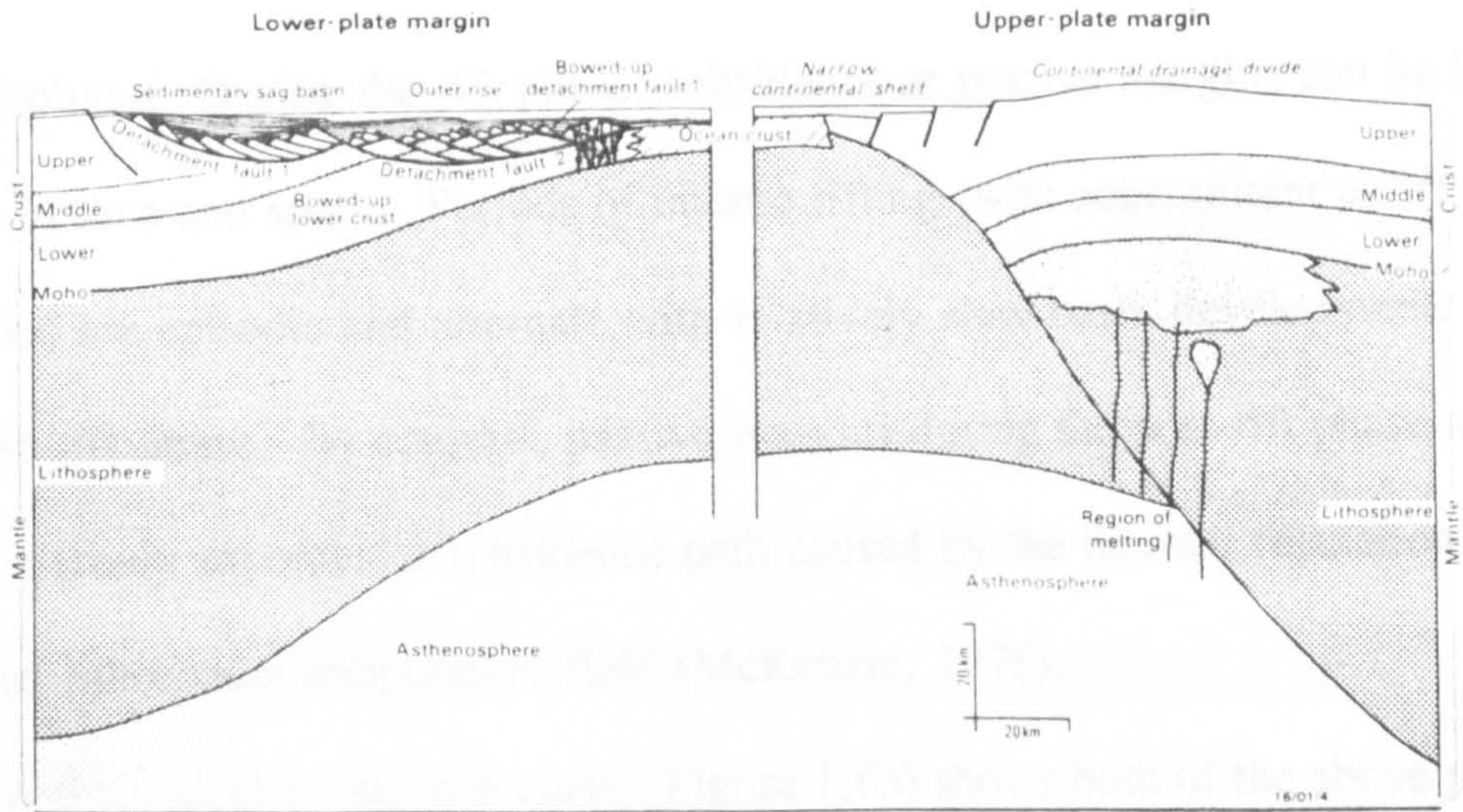


b)

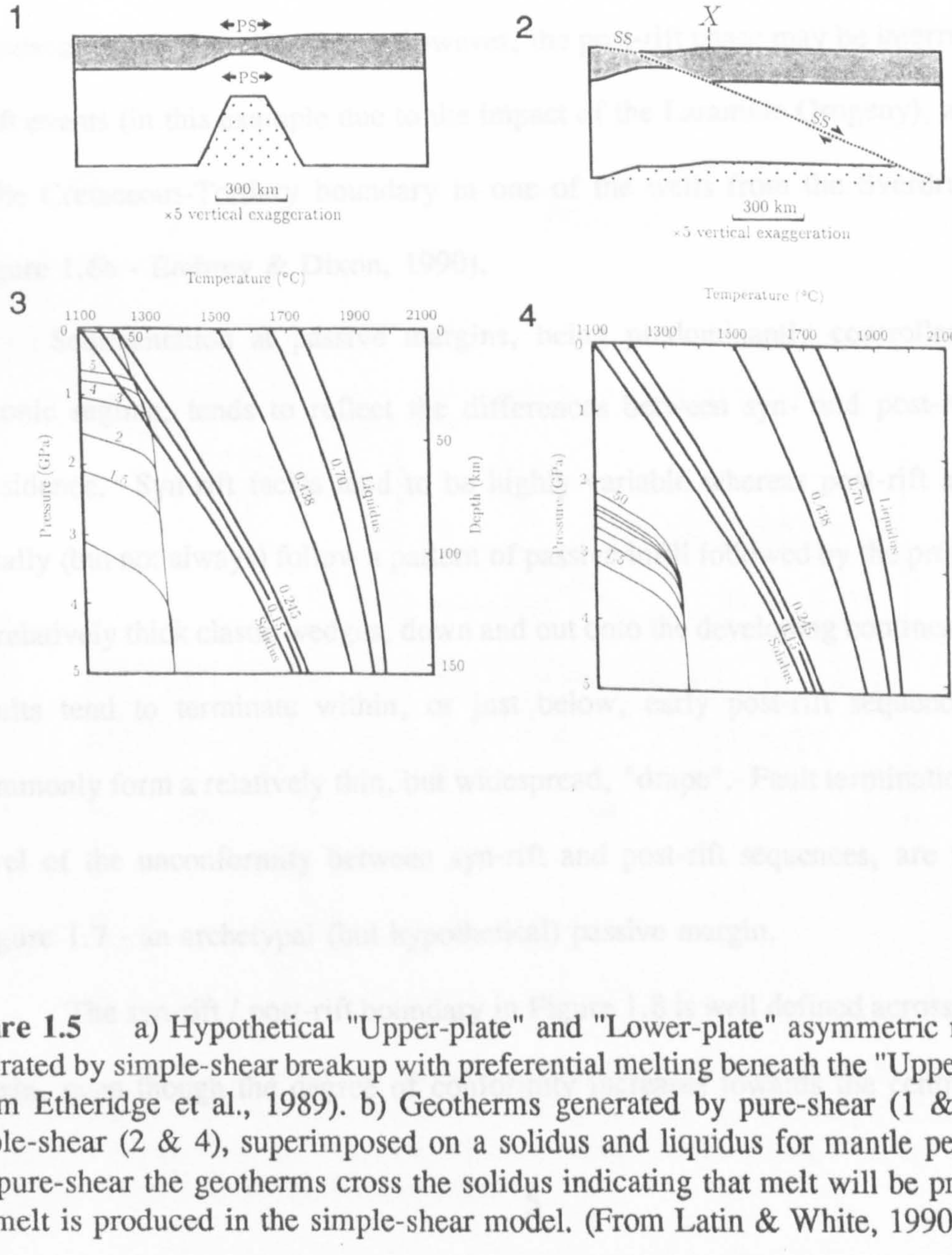


**Figure 1.5** a) Hypothetical "Upper-plate" and "Lower-plate" asymmetric margins generated by simple-shear breakup with preferential melting beneath the "Upper-plate" (From Etheridge et al., 1989). b) Geotherms generated by pure-shear (1 & 3) and simple-shear (2 & 4), superimposed on a solidus and liquidus for mantle peridotite. For pure-shear the geotherms cross the solidus indicating that melt will be produced. No melt is produced in the simple-shear model. (From Latin & White, 1990)

**The rift phase.** During the rift phase, subsidence at passive margins can be highly variable in time and space. Periods of intense rifting (with concomitant uplift of the rift flanks) are episodic and alternate with relatively slow basin development.

**The post-rift phase.** By contrast, passive margins during the post-rift phase usually follows a steady exponential subsidence path caused by the thermal relaxation of the perturbed lithosphere temperature field (McKenzie, 1978).

A theoretical subsidence curve (Figure 1.6a) shows both of the above phases, separated by an inflection point associated with breakup. Variable rates of tectonic subsidence (and uplift) during the syn-rift contrasts with the smooth thermal subsidence in the post-rift phase. However, the post-rift phase may be interrupted by uplift events (in this example due to the impact of the Laramide Orogeny), as shown at the Cretaceous-Tertiary boundary in one of the wells from the Sverdrup Basin (Figure 1.6b - Embrey & Dixon, 1990).

Sedimentation at passive margins, being predominantly controlled by the tectonic regime, tends to reflect the differences between syn- and post-rift phase subsidence. Syn-rift facies tend to be highly variable whereas post-rift sequences usually (but not always) follow a pattern of passive infill followed by the progradation of relatively thick clastic wedges, down and out onto the developing continental slope. Faults tend to terminate within, or just below, early post-rift sequences which commonly form a relatively thin, but widespread, "drape". Fault terminations, at the level of the unconformity between syn-rift and post-rift sequences, are shown on Figure 1.7 - an archetypal (but hypothetical) passive margin.

The syn-rift / post-rift boundary in Figure 1.8 is well defined across the entire basin, even though the degree of conformity increases towards the centre. If this

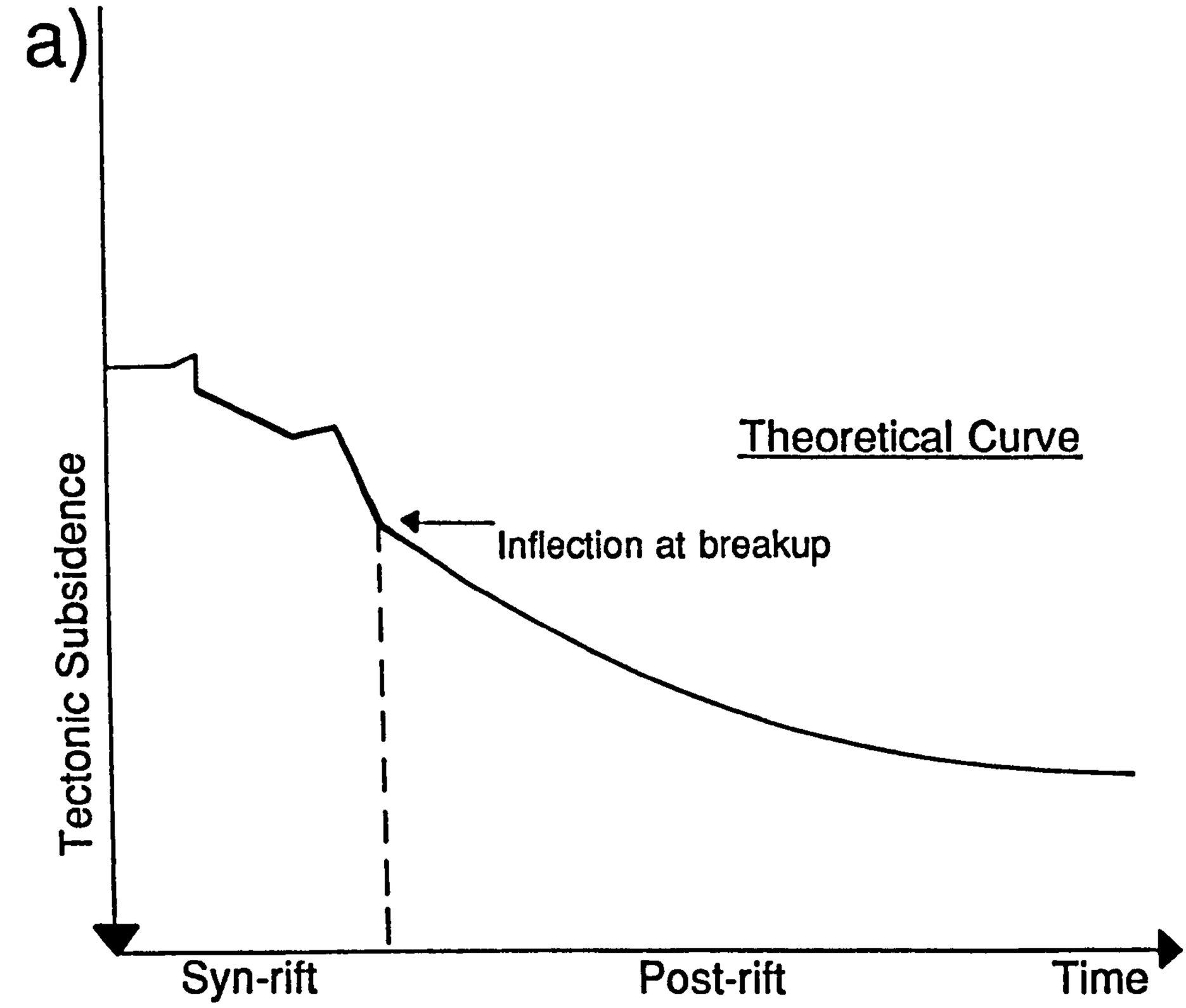


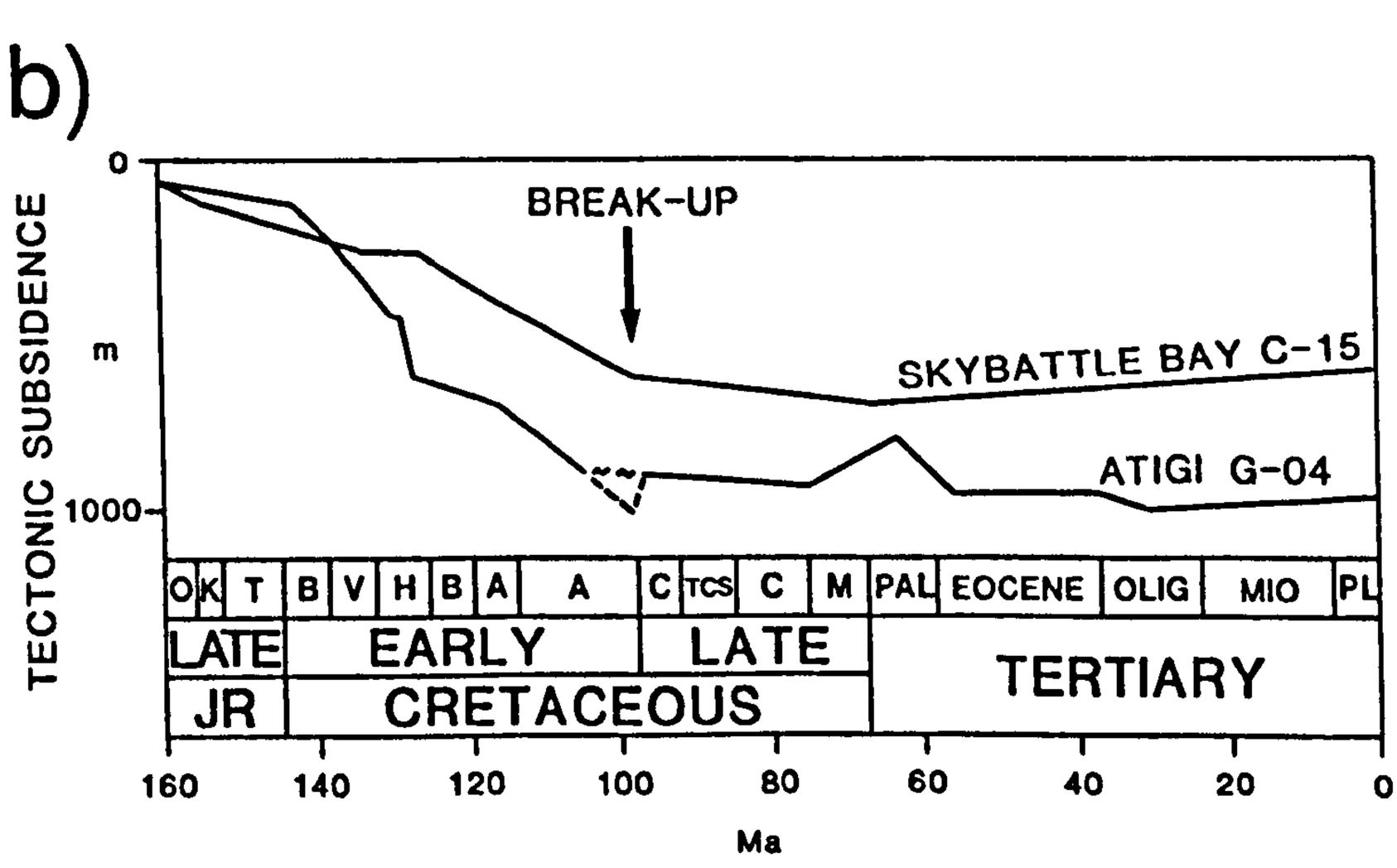


**Figure 1.6** a) Hypothetical subsidence curve showing the contrast between syn- and post-rift phases with breakup marked by an inflection. b) Breakup inflections on subsidence curves from the Amerasian Basin, Arctic Ocean. (From Embrey & Dixon, 1990). Note uplift at 65 Ma on Atigi G-04.

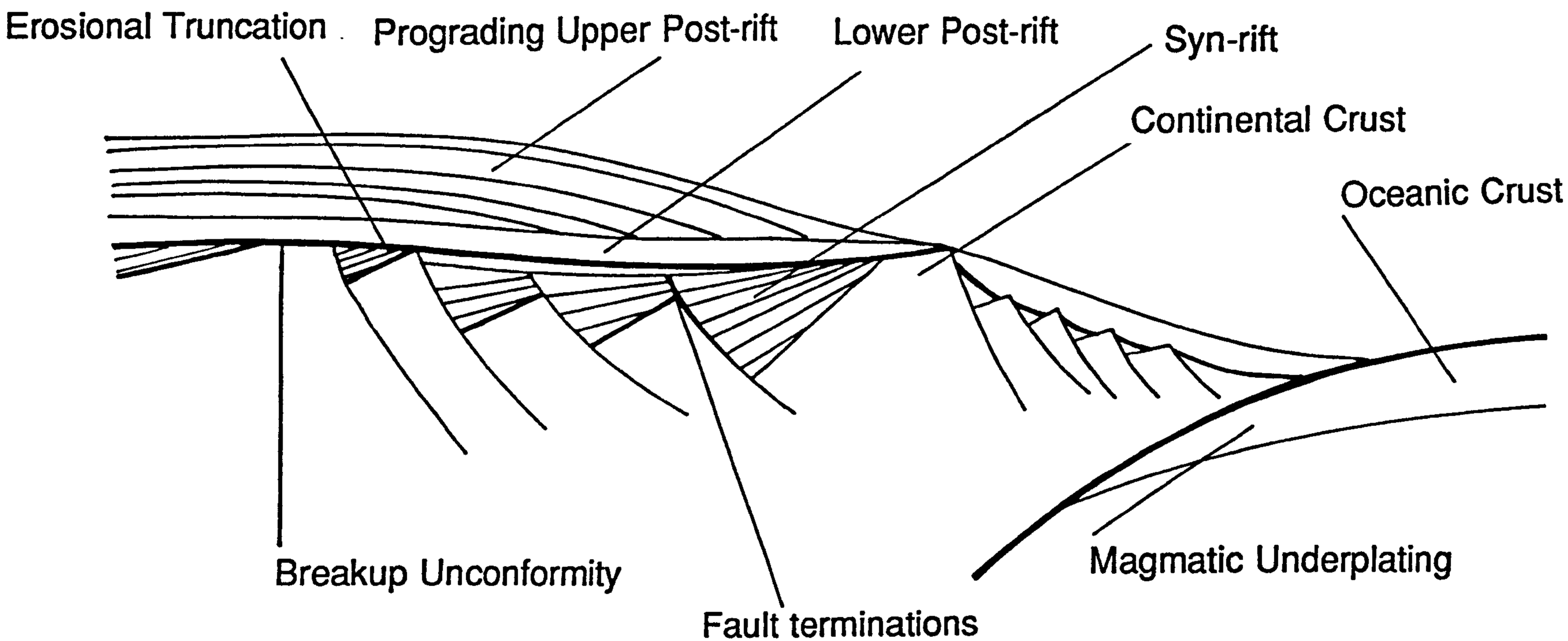


**Figure 1.7** An archetypal passive margin showing a breakup unconformity separating rotated syn-rift sediments from two overlying post-rift megasequences. Note the progradational nature of the upper layer, the lack of faulting above the breakup unconformity and the magmatic underplating landward of the continent ocean boundary.

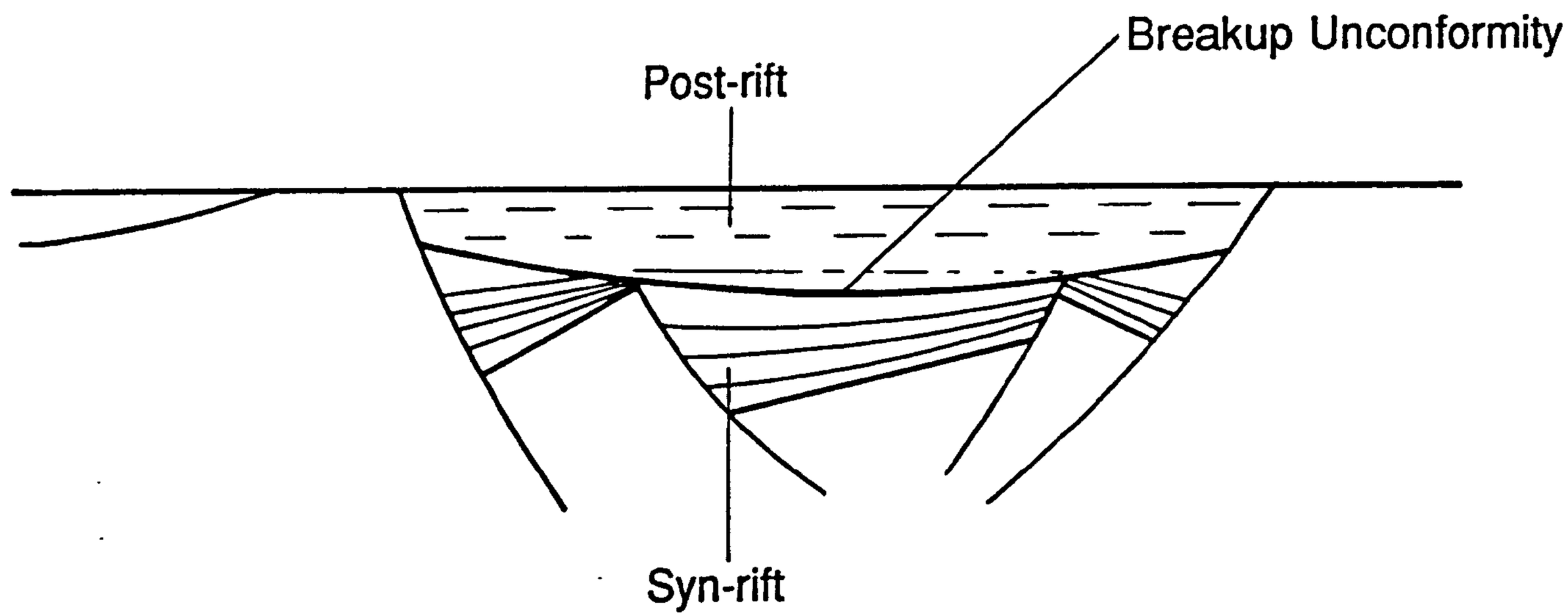


**Figure 1.8** Passive post-rift infill of palaeo-bathymetry generated by the syn-rift phase. Note the change in internal characteristics above and below the breakup unconformity.

were not the case (e.g. on a seismic section where the acoustic impedance contrast was small) the passive post-rift infill could be mistakenly included with the underlying syn-rift to produce a thick, wedge-shaped sequence. Prosser (Pers. Com) has emphasised that the internal characteristics of the sequences should be contrasted, i.e. the difference between parallel post-rift reflectors and dipping syn-rift reflectors defining growth sequences.

Rift / post-rift boundary definition may be poor when there is a large amount of palaeo-bathymetry at the end of the rift phase, on a sediment starved margin. By contrast, areas which have been largely subaerial during the syn-rift phase are often overlain by evaporites, deposited during the initial flooding at the start of the post-rift phase (Figure 1.9). In other cases, igneous activity associated with the onset of sea floor spreading leaves a layer of volcanic extrusives between the syn- and post-rift sequences.

### 1.2.2 Criteria for the Recognition of the Breakup Megasequence Boundary.

Embrey & Dixon (1990) and Sinclair (1988) have recognised that several criteria for the recognition of the breakup unconformity can be defined by the pattern of subsidence and sedimentation at passive margins. Briefly, summarising the previous section, these are:-

1) An inflection in the subsidence curve - relatively fast syn-rift subsidence changes to slower thermal subsidence which can be fitted to the theoretical hyperbolic McKenzie curves for various beta factors (Figure 1.6).

2) The termination of faults at the breakup megasequence boundary, marking the end of the rift phase (Figure 1.7).

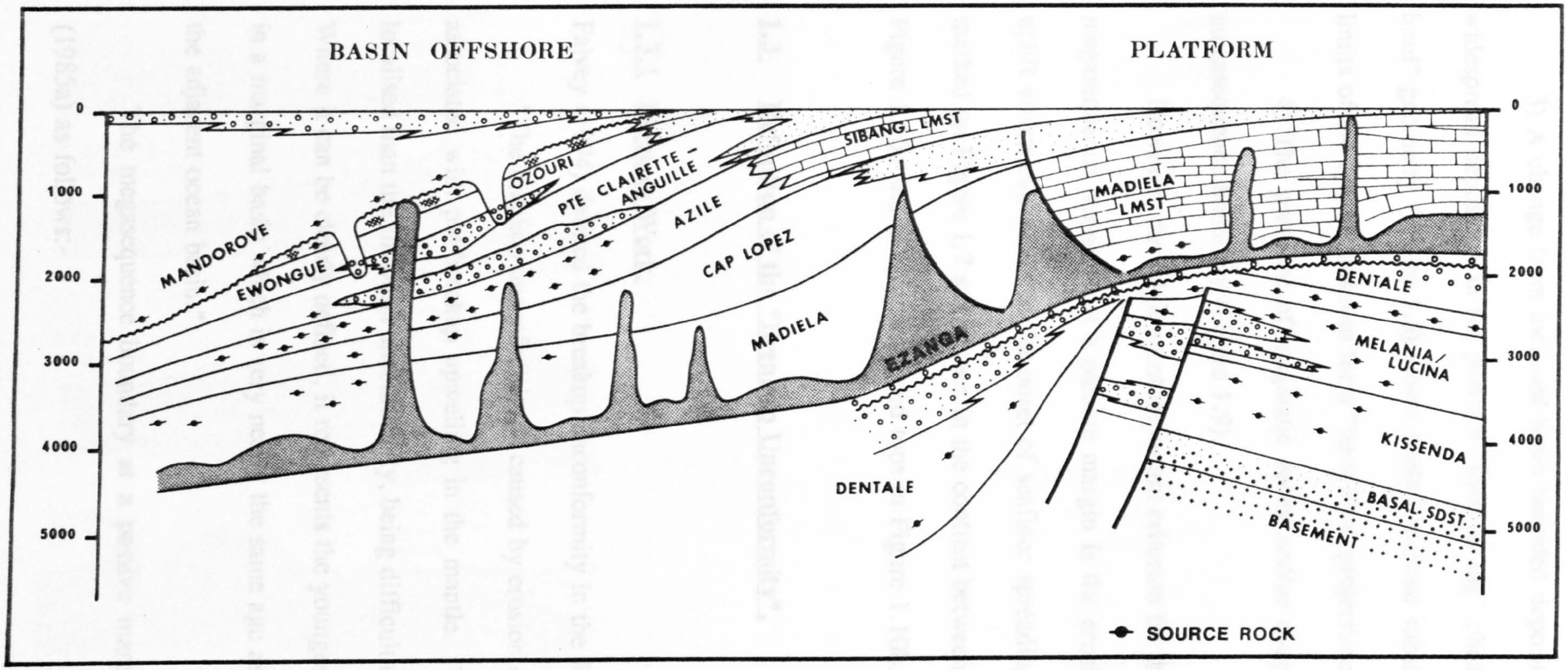


**Figure 1.9** Salt deposited directly above the breakup unconformity may have a dramatic effect on the post-rift evolution of the margin. From offshore Gabon (Teisserenc & Villemin, 1989)

3) A change from localised basin bounded deposition (i.e. syn-rift) to more widespread deposition in the post-rift "thermal sag" phase, i.e. the classic "steers-head" geometry (Figure 1.8) where further thermal subsidence extends beyond the limits of the syn-rift basin to form "horn-like" projections.

4) The presence of magmatic rocks and/or evaporites at the level of the megasequence boundary (Figure 1.9).

However, the single most important criterion for the recognition of a breakup megasequence boundary at a passive margin is the erosional truncation caused by uplift which culminates at the onset of seafloor spreading. Erosional truncation is marked on Figure 1.7 and is seen in the contrast between the "pointed" footwalls in Figure 1.10a and the planar eroded tops in Figure 1.10b.

## 1.3 Definition of the "Breakup Unconformity".

### 1.3.1 Previous Work.

Falvey (1974) defined the breakup unconformity in the following way:-

"The breakup unconformity is caused by erosion during the final uplift pulse associated with pre-breakup upwelling in the mantle. This unconformity is more localised than the rift onset unconformity, being difficult to define in troughs ....."."

Where it can be clearly defined, it represents the youngest cycle of subaerial erosion in a marginal basin which is very nearly the same age as the oldest oceanic crust in the adjacent ocean basin."

The megasequence boundary at a passive margin is defined by Hubbard (1985a) as follows:-

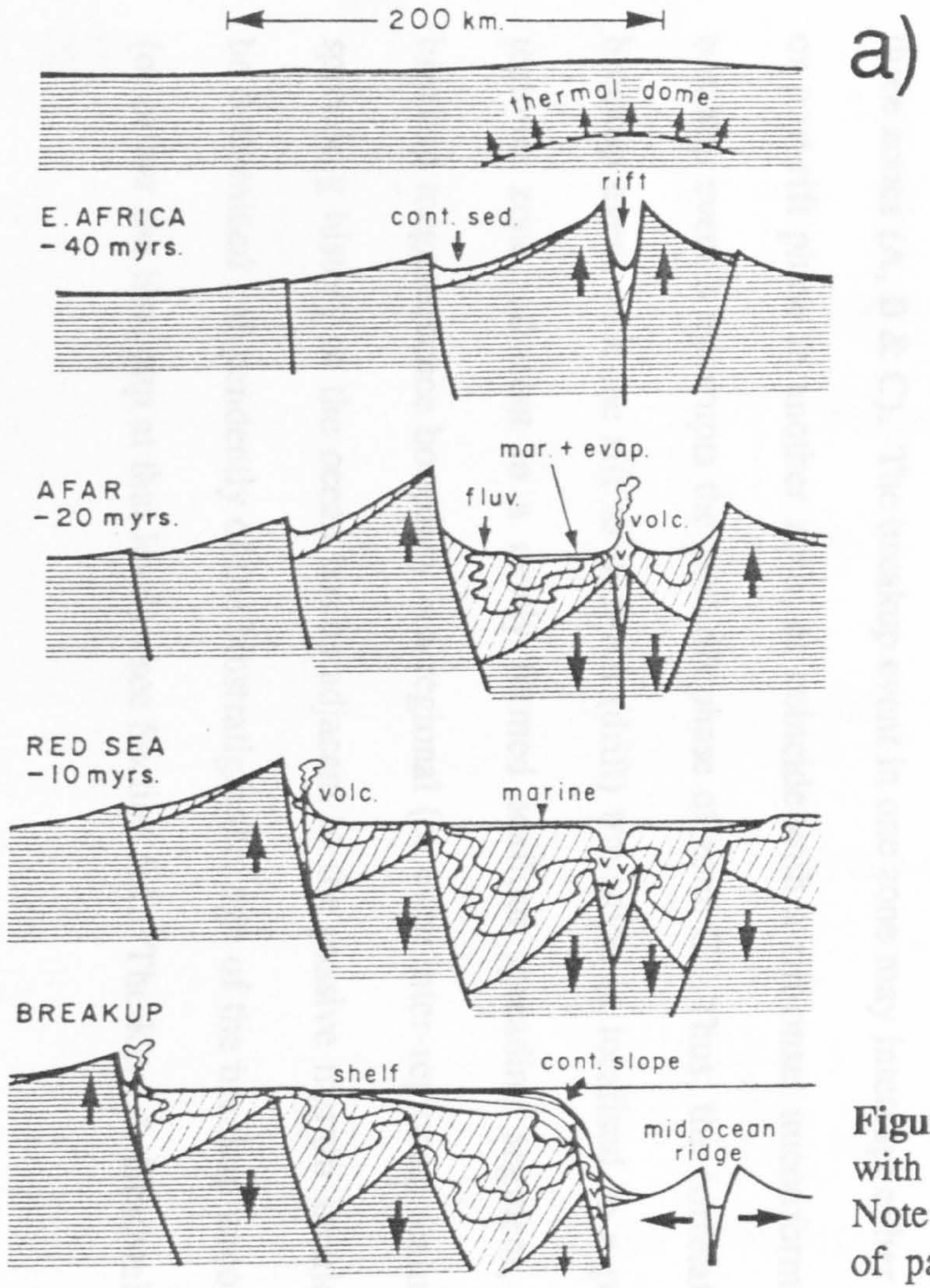


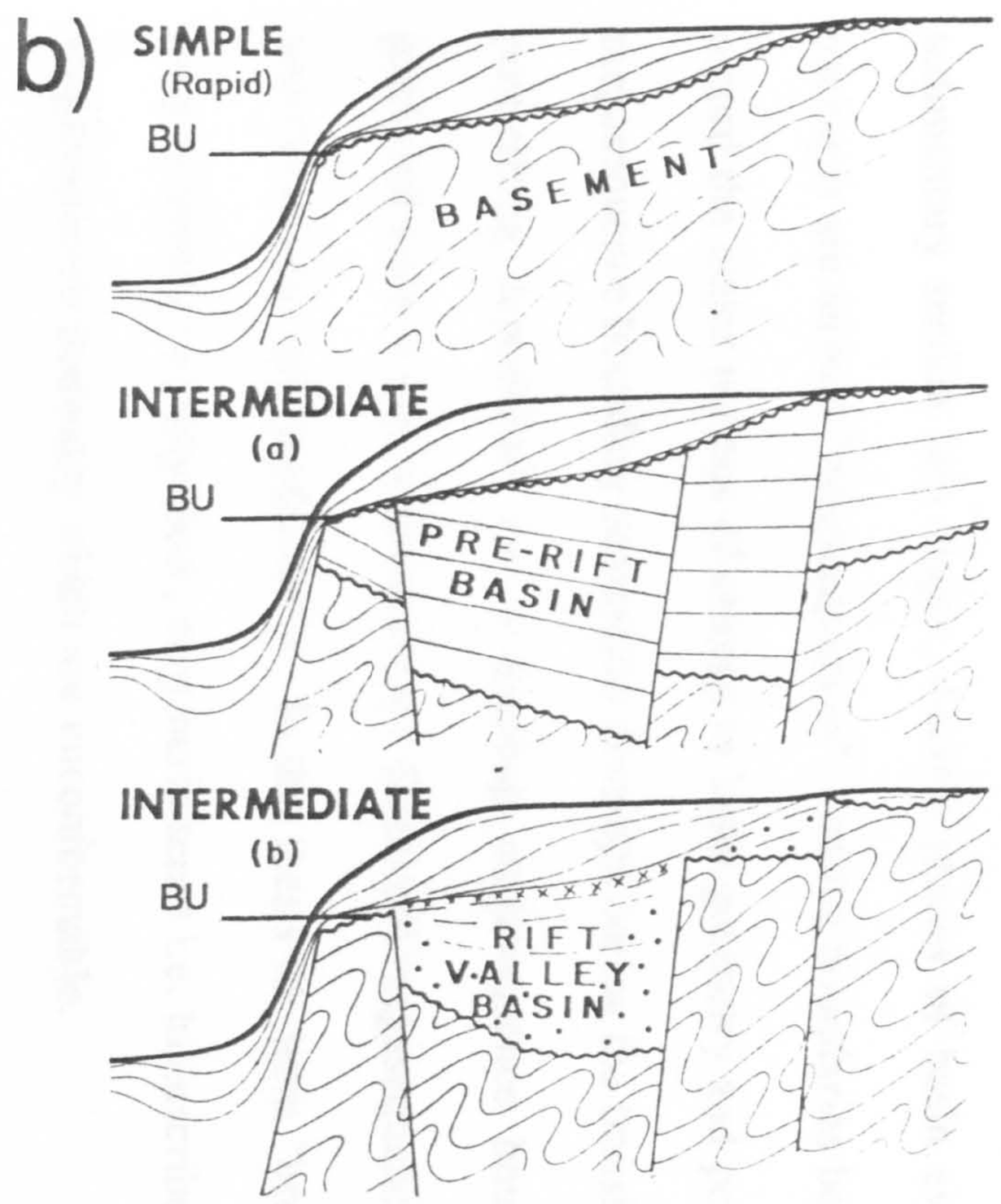


**Figure 1.10** a) The evolution of a passive margin as envisaged by Falvey (1974) with respect to time since the onset of rifting and by analogy to modern analogues. Note that this is an "active rifting model" initiated over a thermal dome. b) Definition of passive margin types depending on the extension rate (Falvey, 1974). BU = Breakup Unconformity.

"....the most prominent regional unconformities that separate the total sedimentary section into major, discrete phases of basin evolution. These major packages are termed "megasequences", and the boundaries between them are seen to record the major periods of change in basin geometry and polarity. For example, a megasequence boundary commonly develops during the transition from syn-rifting to post-rifting deposition" i.e. a breakup megasequence boundary. This term is preferred since it will be shown that a (breakup) megasequence boundary can be both unconformable and conformable. In this thesis the term "breakup unconformity" is only retained in a fairly loose, or generic sense i.e. to describe those parts of breakup megasequence boundary which are unconformable.

It is important to emphasise synchroneity with the onset of seafloor spreading, as the term "breakup" is sometimes used (mistakenly) to indicate the onset of an intense period of rifting (Bond, 1990). Figure 1.11 shows that this situation is complicated in an area of multiple breakup - three separate breakups (1, 2 & 3) in three zones (A, B & C). The breakup event in one zone may interrupt either the syn- or post-rift phase in another zone, or coincide with a rift-onset unconformity, e.g. breakup event 3 interrupts the post-rift phase of zone C. Thus, the correlation of a breakup event with the rift to post-rift (drift) transition is localised to a particular tectonic zone, adjacent to a newly formed seafloor spreading segment, but the breakup megasequence boundary is a regional (or even inter-regional) feature. The spreading history of the ocean basins adjacent to the passive margin should always be determined independently of the biostratigraphic age of the breakup unconformity (or rather the time gap at that level) - see Section 5.1. The Kent & Gradstein (1986)

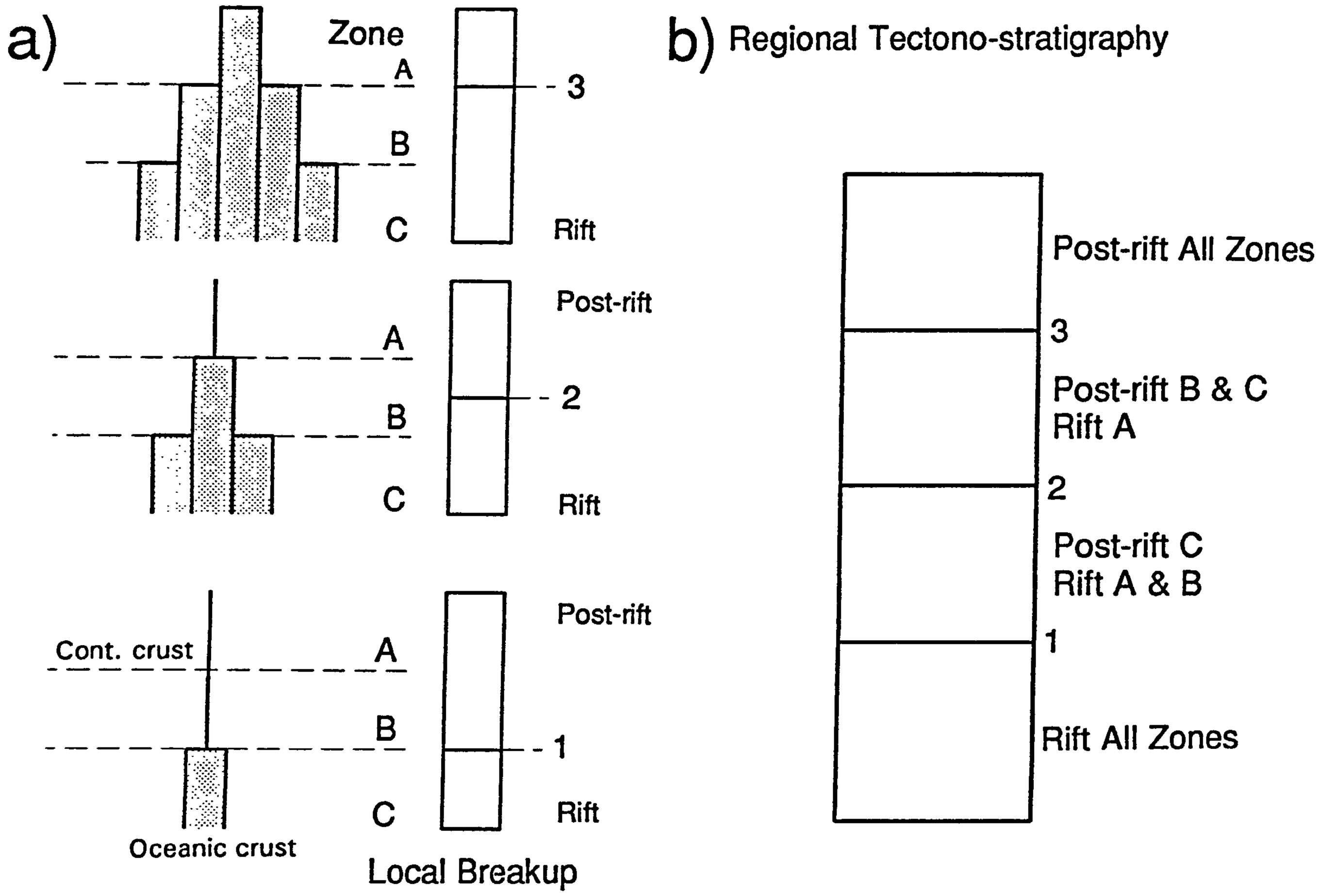


**Figure 1.11** a) Schematic sequential breakup. Columns at the right side of a) show the rift to drift transition in three tectonic zones. In part b) the three breakup events are superimposed in the regional tectono-stratigraphy. e.g. Breakup 2 in zone B interrupts the post-rift phase of zone A.

timescale is used throughout the thesis but this is not the case with some the more important references (e.g. Sinclair, 1988).

### 1.3.2 Sequence Stratigraphic Philosophy of the Breakup Megasequence Boundary as a Single Event.

In this study, the breakup megasequence boundary is considered to be a single horizon, linked genetically to the geologically rapid onset of seafloor spreading. Figure 1.12 shows that the breakup megasequence boundary may vary in character, from a strongly angular and erosional unconformity to a depositional conformity. It always marks the division between syn-rift (1 & 2) and post-rift (3) erosional products of breakup uplift.

Post-rift clastic deposits, derived by erosion at the level of the breakup megasequence boundary, should not be classified as a "transitional sequence" with an implied genetic link to a gradual change in tectonic regime at the rift to drift transition. Continued post-rift erosion has two important consequences:-

i) Chronostratigraphic correlation between the unconformity and its basinward conformity (a fundamental tenet of sequence stratigraphy, as defined by Vail, 1977), is only strictly valid at the instant of breakup (Cartwright, Pers. Com.). Figure 1.12 shows that the geometry of the source area is subsequently altered during the post-rift phase.

ii) The flexural isostatic response to post-rift erosion may produce several second order unconformities, amalgamated with the main breakup megasequence boundary or beyond the limits of seismic resolution.

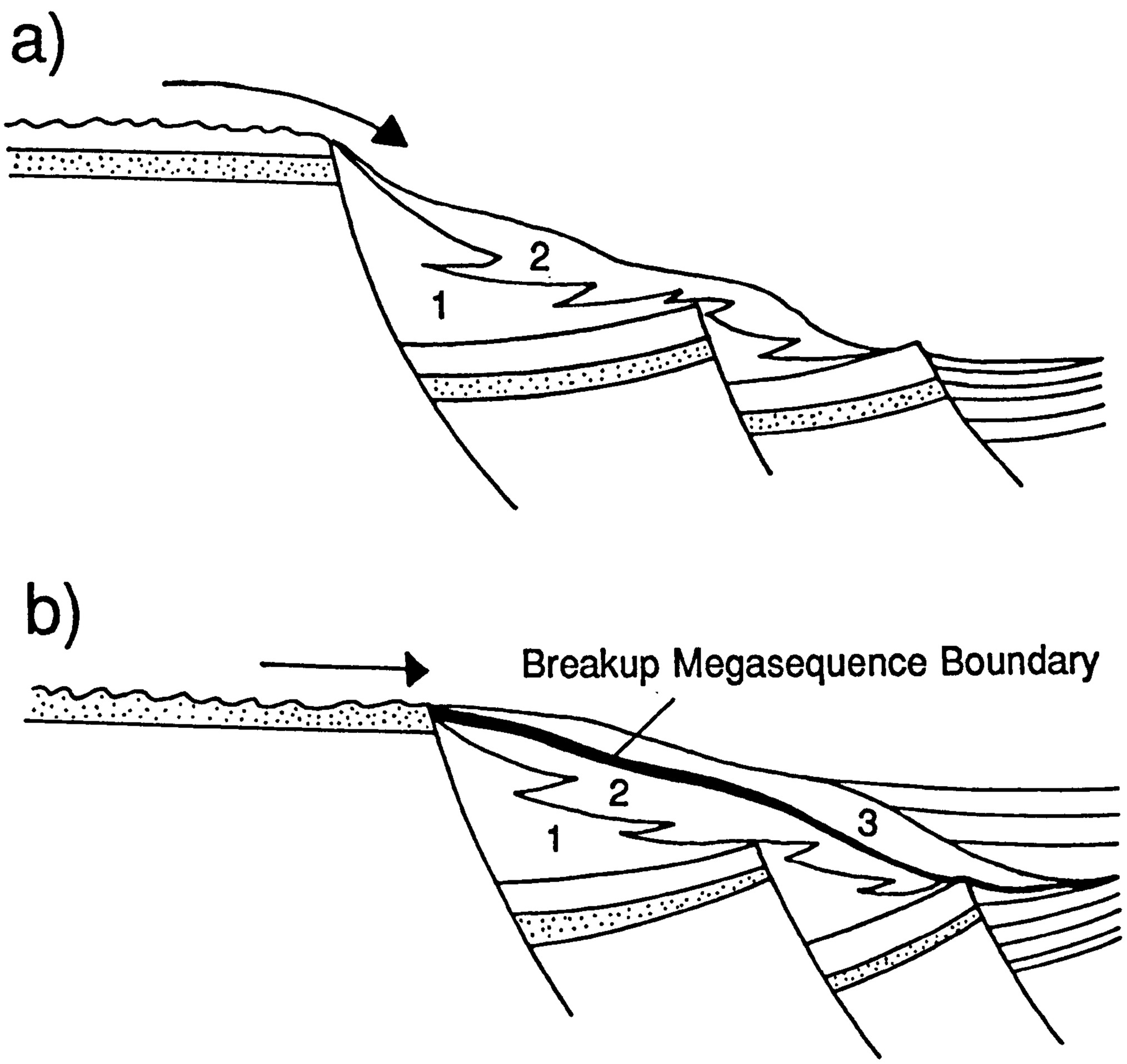


**Figure 1.12** The breakup megasequence boundary (B.M.B) as a discrete event. Rift sequences 1 & 2 and post-rift sequence 3, derived by erosion from the rift flank, could be mistakenly combined into a "transitional sequence". They are separated by the B.M.B.

There are a few instances in which the term "transition sequence" is appropriate. For example, Moore (1992) has shown that in the Porcupine Basin, offshore southwest Ireland, a failed rift-system terminates up to 35 Ma before the onset of seafloor spreading between North America and Europe. The sequence between the end-rift unconformity and the true breakup megasequence boundary may be described as "transitional" since post-rift thermal subsidence appears to be delayed until after the later event.

## 1.4 Review of the Mechanisms That Have Been Proposed to Explain the Generation of the Breakup Megasequence Boundary.

### 1.4.1 Introduction.

Several uplift mechanisms have been identified as being important at passive continental margins. These are :-

1) The flexural isostatic effects of tectonic unloading (i.e. footwall uplift).

2) Thermal uplift due to an increase in geothermal gradient during extension.

3) The flexural isostatic effects of erosion.

4) Magmatic underplating.

5) Stress concentration towards the centre of the rift zone.

6) Small scale convection cells causing flanking uplift.

7) Thermal uplift due to lateral heat transfer from newly formed mid-ocean ridges.

8) A change in intraplate stress/strength at the rift to drift transition.

The timing of uplift is important in that the first six of these uplift mechanisms occur throughout the rift phase and culminate at the rift to drift transition whereas the last two occur only at the onset of seafloor spreading.

In subsequent chapters it will be shown that the magnitude of uplift, produced by the first four mechanisms, far exceeds anything possible from the latter four. Thermal uplift due to an increase in geothermal gradient during extension (mechanism 2) forms an integral part of both the McKenzie and flexural cantilever models for continental extension tectonics and is therefore included in Chapter 2. It should be noted that this mechanism is incapable of producing subaerial uplift on its own (c.f. Falvey, 1974).

The remainder of this chapter reviews the possible contribution of the other mechanisms that have been proposed. It is emphasised that although they are of lesser importance in terms of the magnitude of uplift, they produce the "modification" of breakup uplift which is required to generate a megasequence boundary in areas where deposition would otherwise be continuous.

### 1.4.2 Stress Concentration Towards the Centre of the Rift Zone.

Veirbuchen et al. (1982) have described a dynamic, finite element model which can be thought of as a variant of the Royden and Keen depth dependent model for continental extension (see section 1.1). This is a constant force model with constant flow laws and constant temperatures for each layer. Instead of two layers it has ten (L1-L10), each with their own thickness (T), time-dependent rheologies and $\beta$ factors, as summarised in Table 1.1:-

| L | T (km) | Rheology | L | T (km) | Rheology |
|---|---|---|---|---|---|
| 1 | 1 | Sediment | 6 | 10 | Ductile Crust |
| 2 | 5 | Brittle Crust | 7 | 20 | Ductile Mantle |
| 3 | 5 | " | 8 | 25 | " |
| 4 | 5 | " | 9 | 25 | " |
| 5 | 10 | Ductile Crust | 10 | 25 | " |

Table 1.1

Partial melting is predicted by the model and was used to define the time at which extension was terminated. Slight necking at the centre of the model produced the necessary instability required to act as a stress concentrator for the power law creep. The isostatic consequences of the stretching, thinning and thermal loads were calculated using Airy isostasy, with the basin three-quarters full of sediment. In addition, any material uplifted above sea level was immediately removed by erosion.

Figure 1.13 shows that, as previously described in section 1.2, uplift occurs where mantle lithosphere is thinned but the crust is not. Stress concentration occurs because the upper crustal boundary of the deformed zone moves out at a slower rate than deeper layers. The magnitude of axis uplift is optimised when the initial mantle strain rate is 5-10 times less than the crustal strain rate.

In more recent applications of the constant force, finite element model for continental extension, an even greater dependence on strain rate has been shown to exist (Caban, pers com. 1991). If the strain rate is fast then advective heat transfer dominates (the Peclet number is large), the rheology and viscosity are decreased and stress concentration accelerates. A slow strain rate allows conductive heat loss from the system, which decreases the viscosity and increases the strength of the upper lithosphere. No necking occurs and the width of the rift zone tends to increase. In

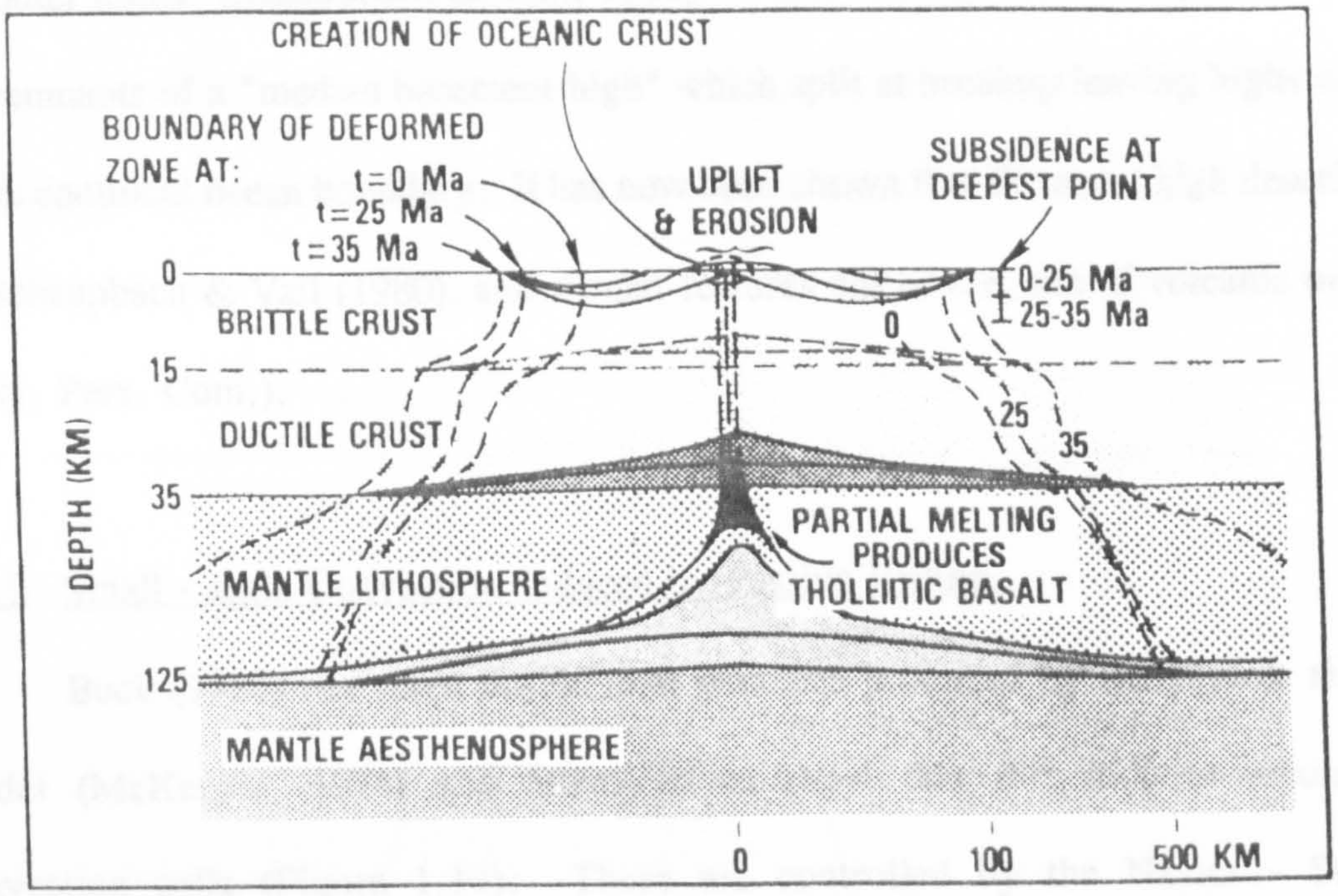


**Figure 1.13** Stress concentration towards the centre of the rift zone causing uplift and erosion due to the thermal effect of mantle upwelling. Extreme thinning of the mantle dominates at the axial position, 25-35 Ma after rift onset. Partial melting is shown but uplift due to magmatic underplating is not included. (From Veirbuchen, George and Vail, 1982).

this thesis, necking of the lithosphere (assuming a fast strain rate) is modelled somewhat less rigorously by adding a second amount of pure-shear, in a narrow zone at the axis of the rift.

The original objective of Veirbuchen et al. (1982) was to explain the origin of "outer highs" (Scheupbach & Vail, 1980). These features had been postulated as the remnants of a "median basement high" which split at breakup leaving highs close to the continent ocean boundary. It has now been shown that the outer high described by Scheupbach & Vail (1980), and similar features elsewhere, are of volcanic origin (Daly, Pers. Com.).

### 1.4.3 Small - scale Convection Induced by Passive Rifting.

Buck (1986) has taken the thermal structure produced by the passive rifting model (McKenzie, 1978) and attempted to show that this induces secondary convection cells (Figure 1.14). These are controlled by the Navier - Stokes equations, and the study utilized a finite difference method. The all-important parameter - viscosity - is defined either as a function of temperature (T) and pressure (P) or with an extra strain rate term (ė):-

$$\mu(T, P) = A \exp[(E+PV) / RT] \qquad (1.1)$$

or

$$\mu(T, P, e) = \frac{\mu(T, P)}{1 + A_e[\mu(T, P) \cdot e]^{2/3}} \qquad (1.2)$$

where A is an average viscosity and E controls the temperature dependence on viscosity. The value of initial viscosity at 150 km depth ($\mu_{ref}$) varies between 1.0 and

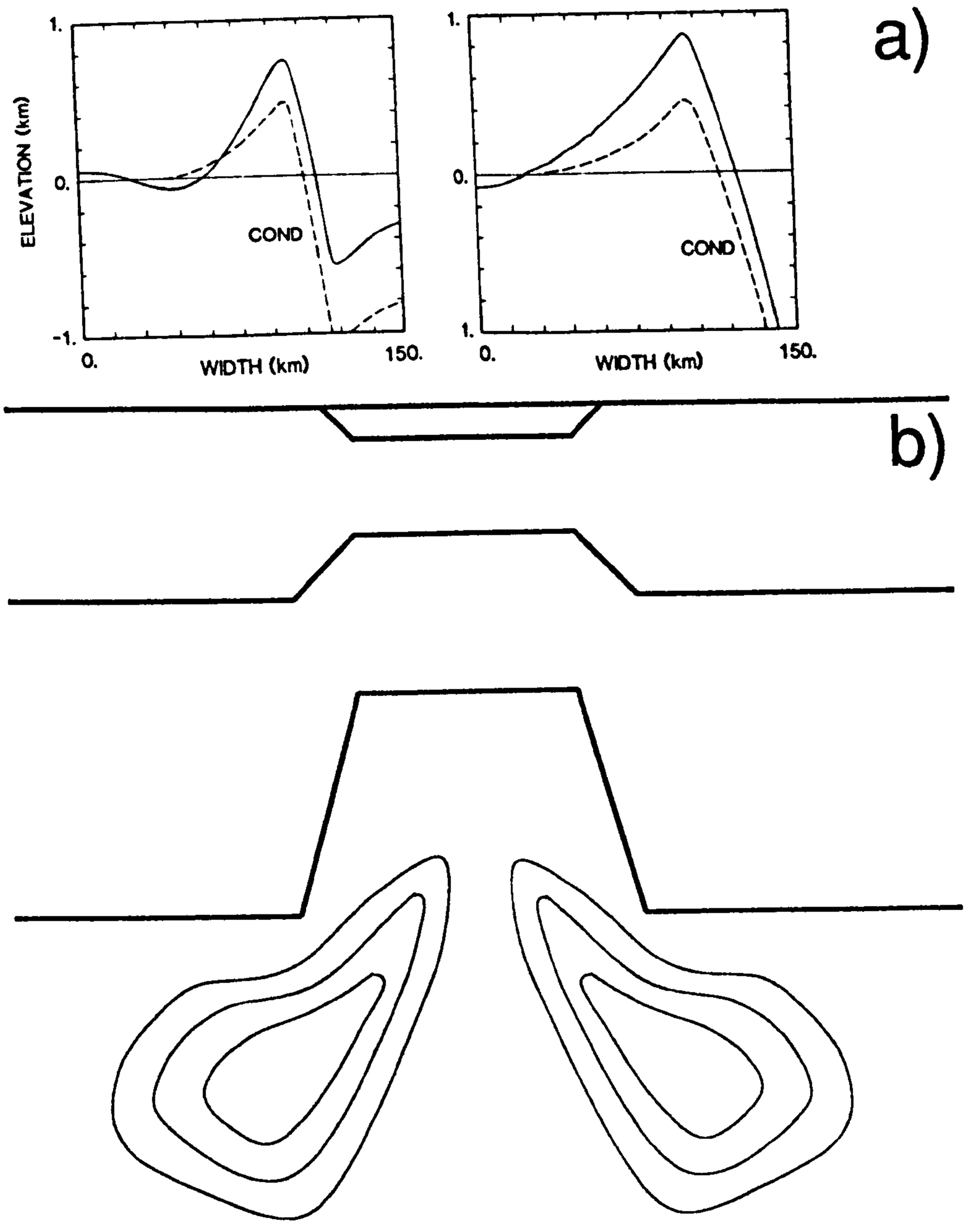


**Figure 1.14** Rift-shoulder uplift (a) resulting from small scale convection cells (b). (Redrawn from Buck, 1986). In the topmost diagrams the uplift due to conduction (COND -dashed lines) is compared with a convective model (solid lines) for two different thermal anomaly geometries.

$5.0 \times 10^{18}$ Pa. Figure 1.14a shows an application of the model to the formation of rift flanks adjacent to the Red Sea Basin (Buck, 1986). Maximum uplift of 500 m is thought to be possible over the rift flanks as a result of convective heat flow from the upwelling asthenosphere (Figure 1.14b).

The Buck model has been criticised by McKenzie (Pers. Com., 1991) for requiring low viscosities (for convection) at densities which are too low to complete the down-going part of the convection cell i.e. the upwelling asthenosphere is too buoyant to convect at this scale. The rift flanks in the adjacent to the Red Sea can be explained just as well by flexural isostatic footwall uplift (see Chapter 2). Similarly, differences in melt generation and extrusion on the Northwest shelf of Australia can be explained, without resorting to a small scale convection cell mechanism, as a Hopper et al. (1992) have done (see Chapter 8). The small scale convection cell mechanism is therefore not considered further in this thesis.

### 1.4.4 Thermal Uplift from Newly Formed Mid-ocean Ridges.

The thermal uplift effect of a newly formed mid-ocean ridge has been investigated, in a fairly simple way, using a finite difference method. A temperature grid is set up, at To, with two adjacent blocks - one oceanic with a temperature of 1333° C at every node, and the other, continental block, with a geothermal gradient (Figure 1.15a). Heat flows from the relatively hot oceanic block into the adjacent continent causing thermal uplift which decreases away from the margin. Figure 1.15b shows that around 100m of uplift remains after 10 million years. In this thesis it is considered that this mechanism is automatically included in the thermal load since 2-D heat transfer is always calculated.

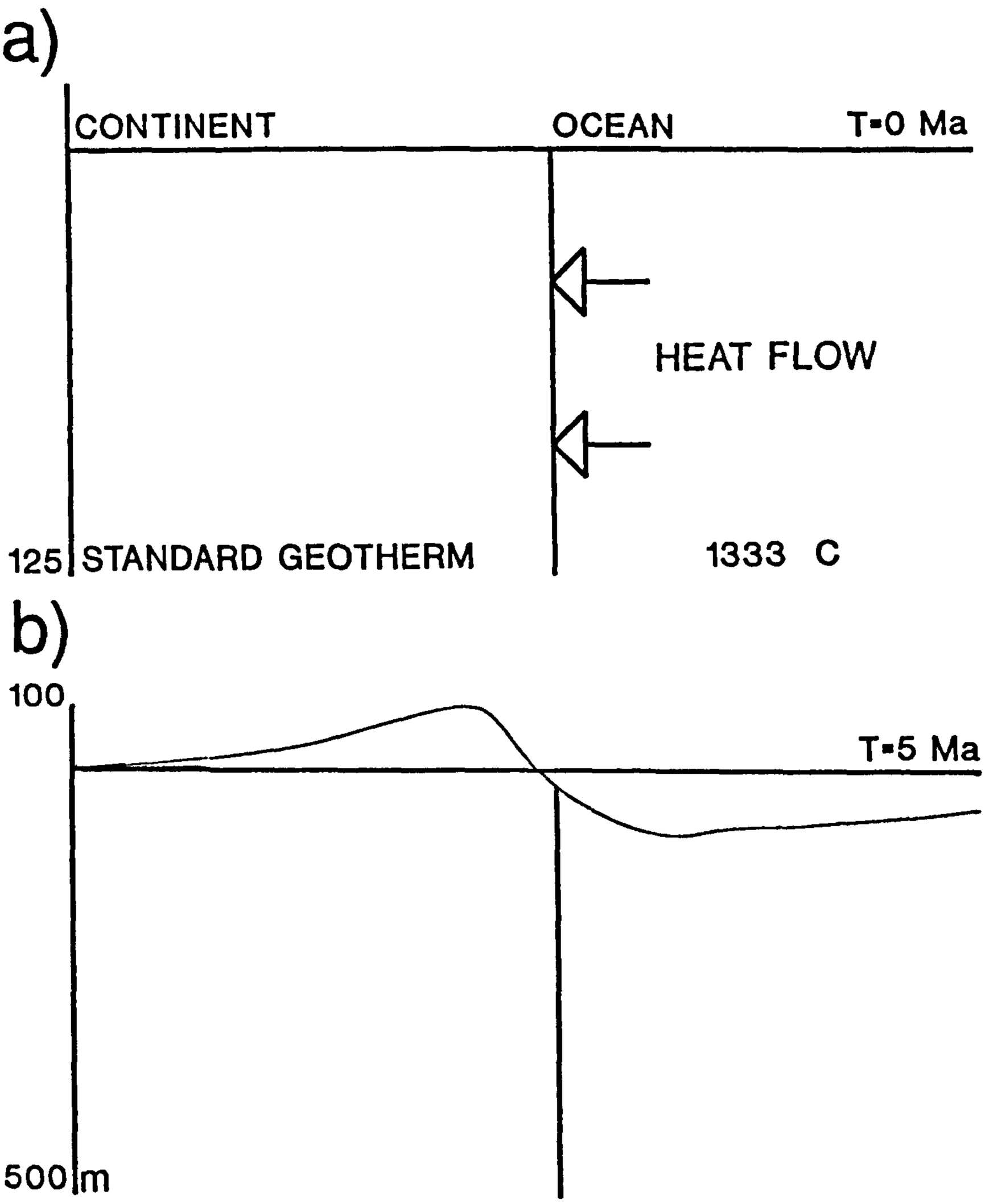


**Figure 1.15** A simple model for the thermal uplift resulting from the early phases of sea-floor spreading. a) The initial condition with a continental block (standard geotherm) adjacent to an oceanic block (assumed to be at 1333 °C throughout). b) After 5 Ma sufficient heat has conducted into the continental block to uplift the area by over 100m. (Note vertical scales).

### 1.4.5 A Change in Intra-plate Stress and Strength at the Rift to Drift Transition.

Figures 1.16a & b show the effect of instantaneously reducing the intraplate stress from 130 MPa to zero at a breakup event (22 Ma), as calculated by Braun & Beaumont (1989). The basin is uplifted by up to 200 m while the rift shoulder subsides by a similar amount (Figure 1.16a). Breakup related inflections on subsidence curve, for three points (A, B and C) along the model profile, are shown in Figure 1.16b. Braun & Beaumont (1989) have noted that the polarity of the effect of a reduction in tensional intra-plate stress depends on the depth of flexural isostatic compensation - and thus on the necking geometry of the lithosphere. When the depth of compensation is reduced, by asymmetric necking above and below a "strong layer" (diagonal shading in Figure 1.16c ii & iv), the polarity of the result is the same as Figure 1.16a. Lowering tensional intraplate stress after symmetrical necking of the lithosphere causes rift shoulder uplift and basin subsidence (Figure 1.16c i and iii). This effect explains the modelling results of Lambeck et al. (1987) where 100 MPa horizontal compression (equivalent to an equal reduction in tensional intra-plate stress) gives flanking uplift and basin subsidence (the dashed line in Figure 1.16d). Note that the magnitude of the effect in the Lambeck model is only of the order of a few tens of metres.

The fundamental parameter which affects the viability of this mechanism is the magnitude of the horizontal stress. In models discussed above the horizontal, in-plane tensile stress varies between 100 and 130 MPa, distributed over a 100 km thick lithospheric plate ( $\equiv$ 10 - 13 $\times$ $10^{12}$ $Nm^{-1}$ ). This is significantly greater than stresses predicted lithospheric stresses, such as those caused by slab pull (3 - 5 $\times$ $10^{12}$ $Nm^{-1}$). For this reason, and because of the magnitude discrepancy of the two models

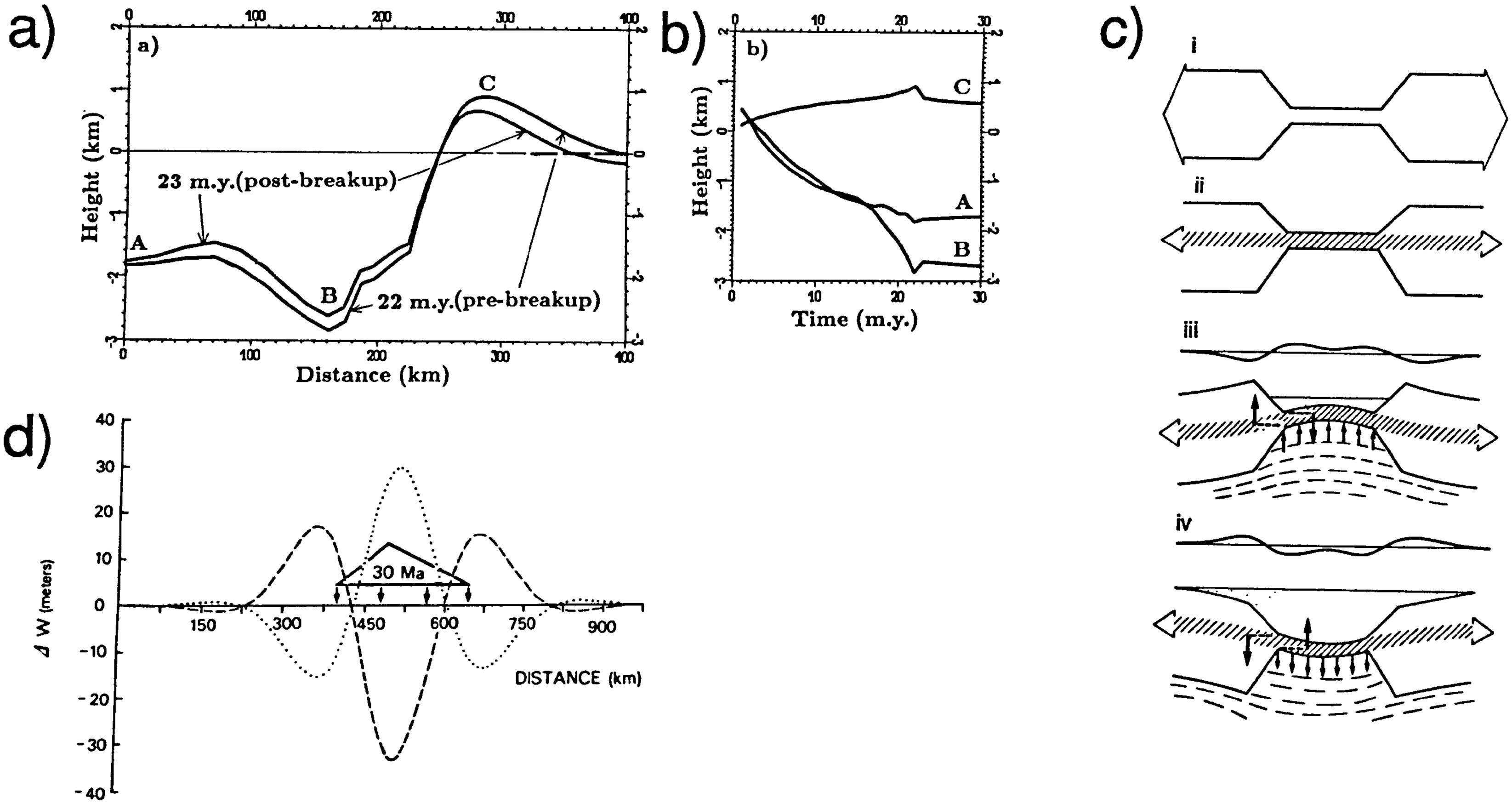


**Figure 1.16** a) & b) Changes in intra-plate stress before (130 MPa) and after (0 MPa) a breakup event at 22 Ma. Uplift = 200m (approx) in the basin (with downwarping of rift-flanks by a similar amount). c) The polarity of the effect depends on the necking geometry - see text for details (From Braun & Beaumont, 1989). d) The effect of 100 MPa in-plane compression (dashed line) and tension (dotted line) on a marginal basin loaded with a sedimentary wedge. (From Lambeck et al., 1987). Note the maximum uplift (+ve) is 20m.

described above, intraplate stress is not considered further in this thesis. Its relevance (if any) lies not in its ability to provide more uplift, but rather to cause the differential vertical movements that may help to create a breakup megasequence boundary.

# CHAPTER 2

# THE FLEXURAL CANTILEVER MODEL FOR CONTINENTAL EXTENSION.

## 2.1 Introduction to the Flexural Cantilever Model.

Observations of extensional terrains on deep seismic sections show that the brittle upper crust extends on planar faults. An example, the DRUM line from the NW shelf of the U.K. (Figure 2.1a) shows several en-echelon sub-planar faults which are clearly defined in the upper crust but which pass into a diffuse zone of extension above the Moho (McGeary & Warner, 1986; Kusznir & Mathews, 1988). From Figure 2.1b it can be seen that the Outer Isles Fault is planar after depth conversion. These observations are consistent with earthquake seismology from the Aegean (Jackson, 1987) and the Basin and Range, western U.S.A. (Stein & Barrientos, 1985) where focal-plane solutions indicate that faults are planar and source locations lie within the upper 8 - 10 km of the crust (Figure 2.2).

In addition to the focal-plane solution, Stein & Barrientos (1985) measured the co-seismic deformation of the Borah Peak earthquake (Figure 2.2). For a single event the footwall was uplifted by 0.2 m and the hangingwall subsided by 1.0 m. This post-seismic geometry could be accurately determined using elastic dislocation theory for a planar fault dipping at 60°. A rift basin grows by the summation of many such co-seismic events, as modelled by Walsh & Watterson (1987). The model described in this chapter calculates the long term isostatic consequences of

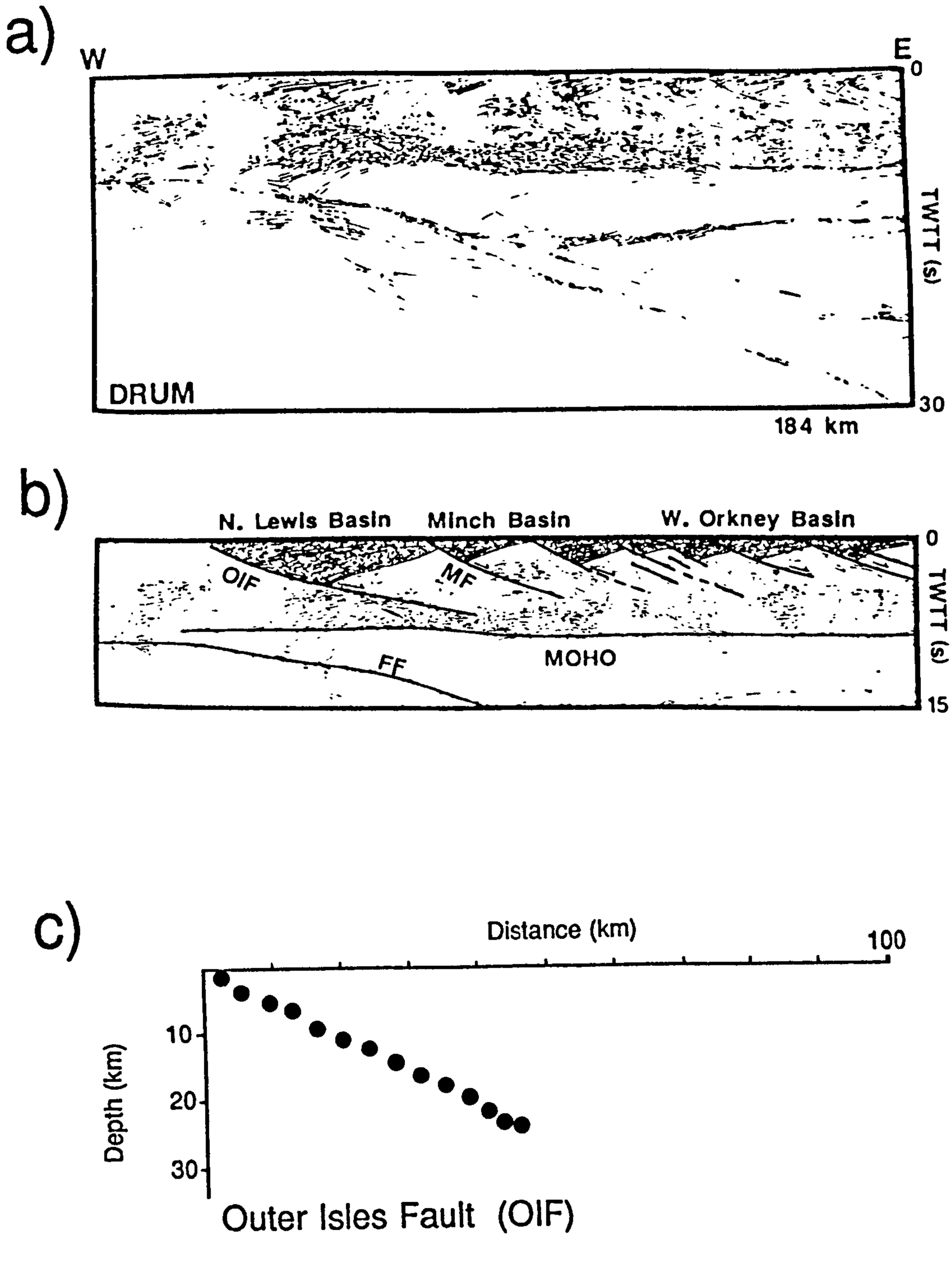


**Figure 2.1** The DRUM deep seismic line from the northwest shelf of the U.K. a) Un-interpreted, vertical Scale to 30 seconds T.W.T.T. (V = H). b) Interpreted, vertical scale to 15 seconds (V = H). Note that faults in the upper crust are approximately planar and that they cannot be traced down to offsets of the Moho but terminate within the highly reflective lower crust (From McGeary & Warner, 1986). c) Depth conversion of the Outer Isles Fault (redrawn from Marsden, 1990) showing it to be planar.

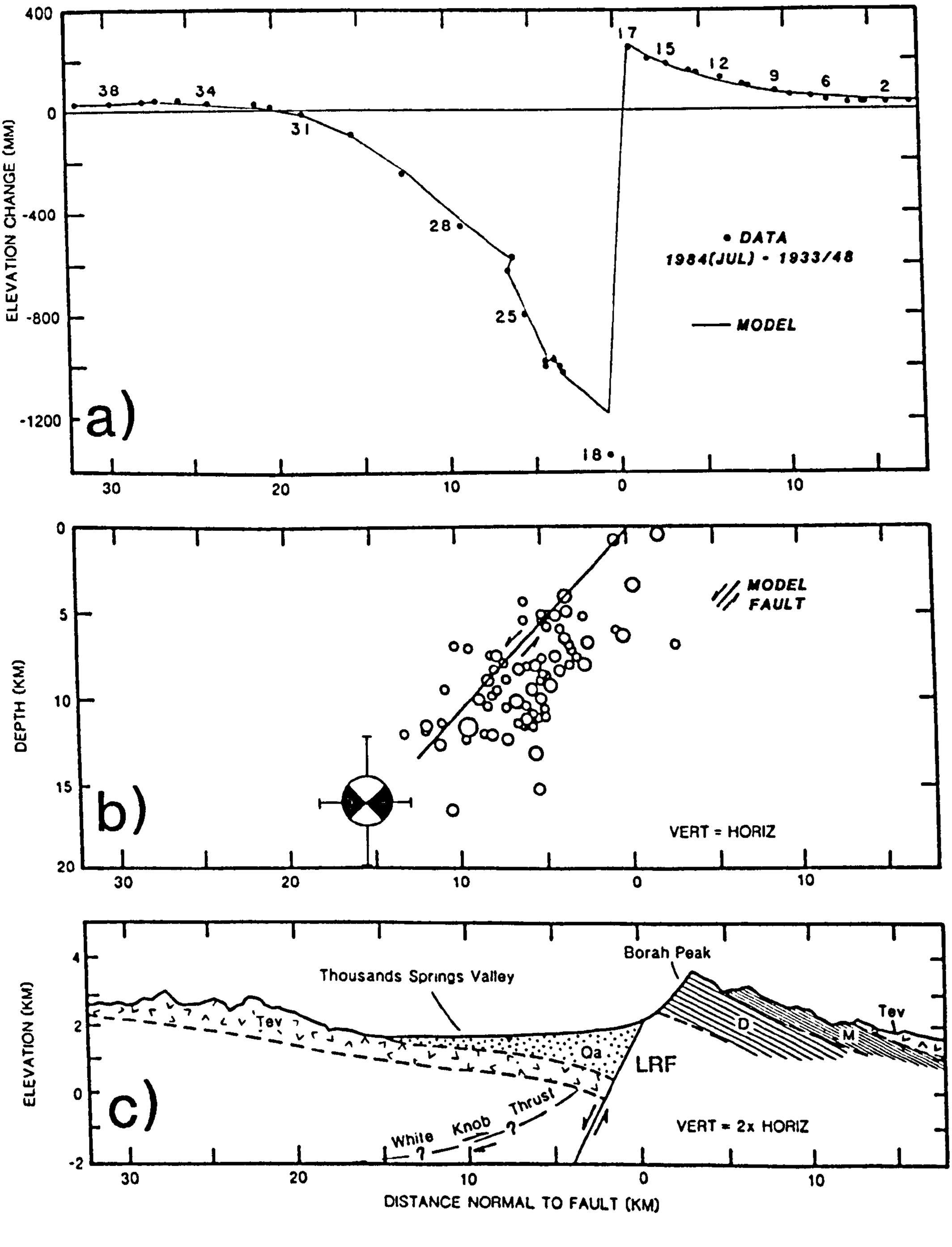


**Figure 2.2** The 1983 Borah Peak earthquake (from Stein & Barrientos, 1985). a) Coseismic deformation in the order of a few cm. b) Aftershock focal points defining a planar fault, dipping westwards at 50°. c) Geological cross-section of the region on either side of the Lost River Fault (LRF).

lithospheric extension and is applicable over larger timescales - of the order 0.1 to 1.0 Ma.

Lithospheric flexure is best exemplified by the bending of oceanic crust on either side of ocean islands, (Figure 2.3a), where the oceanic plate responds to a simple vertical load (the weight of the ocean island). In a more complex tectonic regime, flexure of the continental crust produces foreland basins in response to thrust-stacking loads (Figure 2.3b). The models in this thesis assume that during extension, the continental crust also retains a certain flexural strength. Combining the flexural isostatic effects of basin formation, adjacent to planar faults in the upper crust, with the downloading response to the upwelling of dense mantle due to pure-shear extension of the lower crust and mantle, produces a coupled simple-shear pure-shear model known as the flexural cantilever model (Figure 2.4). Lithospheric strength varies above and below the brittle - ductile transition and extension on planar faults in the upper crust contrasts with the distributed nature of pure-shear in the lower crust and mantle. In addition to the flexural isostatic response to crustal thinning loads, the thermal uplift due the elevation of the geotherm during extension is incorporated within the flexural cantilever model.

## 2.2 The Flexural-isostatic Response to Geometric Loads Generated by Extension of the Lithosphere.

The flexural cantilever model can be described, in simple terms, by first considering the simple-shear extension on planar faults in the upper crust and then adding the corresponding pure-shear extension in the lower crust and mantle.

a)


b)

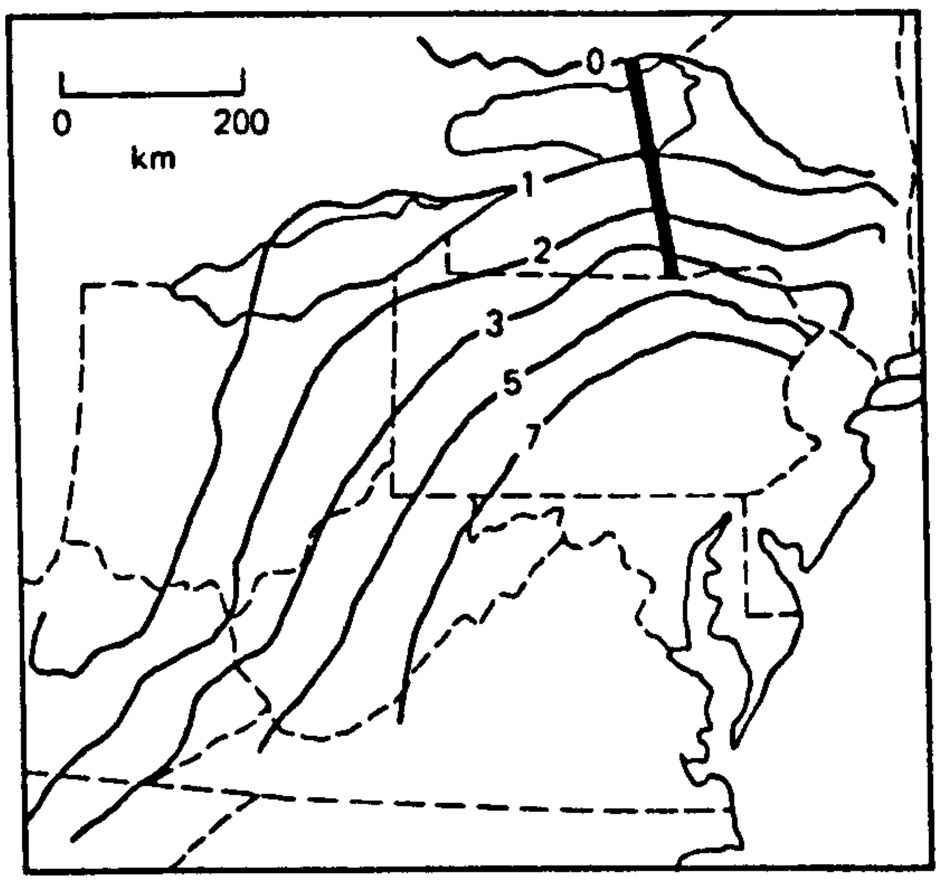


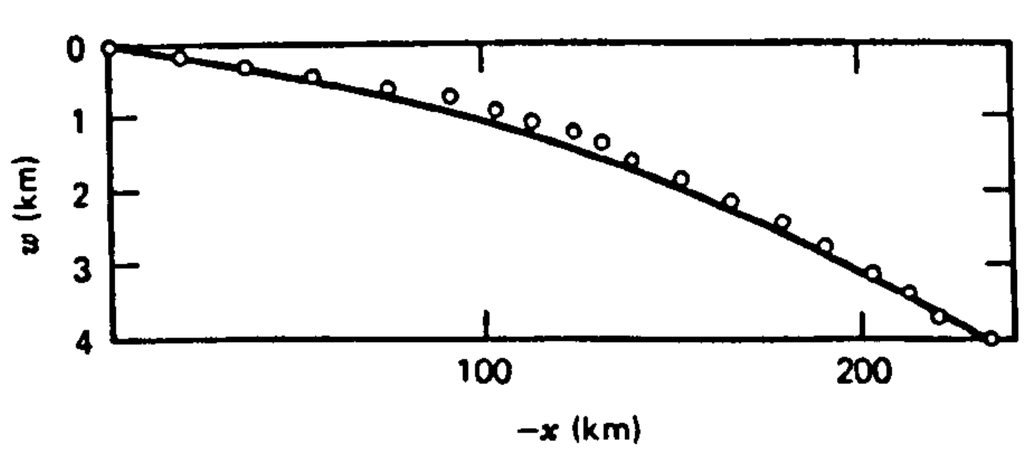


**Figure 2.3** a) The flexural isostatic response of the oceanic crust to a load (the ocean island created over the Hawaiian hot spot. b) Contour map and cross section of the flexural bending of continental crust in the foreland Appalachian Basin (From Turcotte & Schubert, 1982).

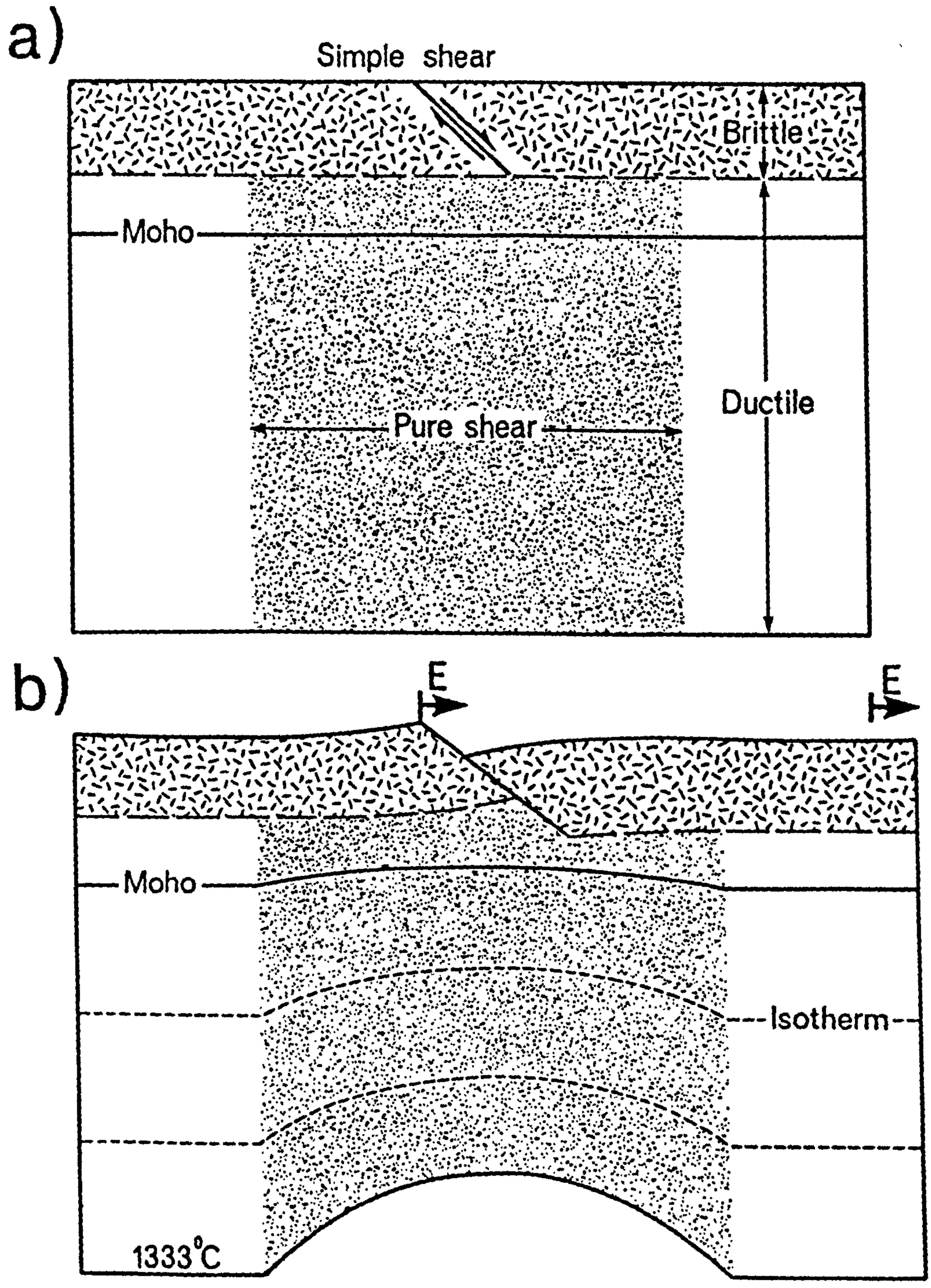


**Figure 2.4** Schematic representation of the coupled simple-shear / pure-shear flexural cantilever model for continental extension (Kusznir et al., 1991). a) Initial condition - a planar fault in the brittle upper crust and distributed pure-shear in the ductile lower crust and mantle. b) Footwall uplift and hangingwall rollover after extension of 10 km on the planar fault. Moho topography and a perturbation of the lithosphere temperature field result from pure-shear in the lower crust and mantle.

### 2.2.1 The Buoyancy Force Generated by Extension on a Planar Fault in the Upper Crust and its Flexural-isostatic Response.

Figure 2.5a shows a single planar fault, extending wholly crustal material, with the hanging-wall moving down over the footwall by simple-shear until a horizontal displacement $E$ is achieved (Kusznir, Marsden & Egan, 1991). In this purely geometric construction it is assumed that gravity has been "switched off" and that the fault continues to infinite depth. Above the hangingwall, air replaces crust, creating a buoyancy force (load $l_1$) whose magnitude is given by Equation 2.1:-

$$l_1(x) = -h\rho_c g \qquad (2.1)$$

where $\rho_c$ is the crustal density, $g$ is gravitational acceleration and $h$ is the depth of any point on the crustal surface below datum.

When gravity is "switched on" again the buoyancy force will cause an upward displacement of the upper crustal surface which can be calculated using the flexure equation derived in Appendix A. Vertical flexure can be calculated in the wavenumber domain by calculating:-

$$U(k) = R(k) \cdot L_1(k) \qquad (2.2)$$

using an isostatic response function *R(k)*:-

$$R(k) = 1/((\rho_c - \rho_a) g + Dk^4) \qquad (2.3)$$

$D$ is the flexural rigidity, $k$ is the wavenumber $= 2\pi/\lambda$ and $\rho_a$ is the density of air. $U(k)$ and $L_1(k)$ are the Fourier transforms of the uplift and buoyancy load respectively. The justification for using $(\rho_c - \rho_a)$ is discussed in Appendix A. Uplift in the space domain, $u(x)$ (Figure 2.5b), can be obtained from the reverse transform

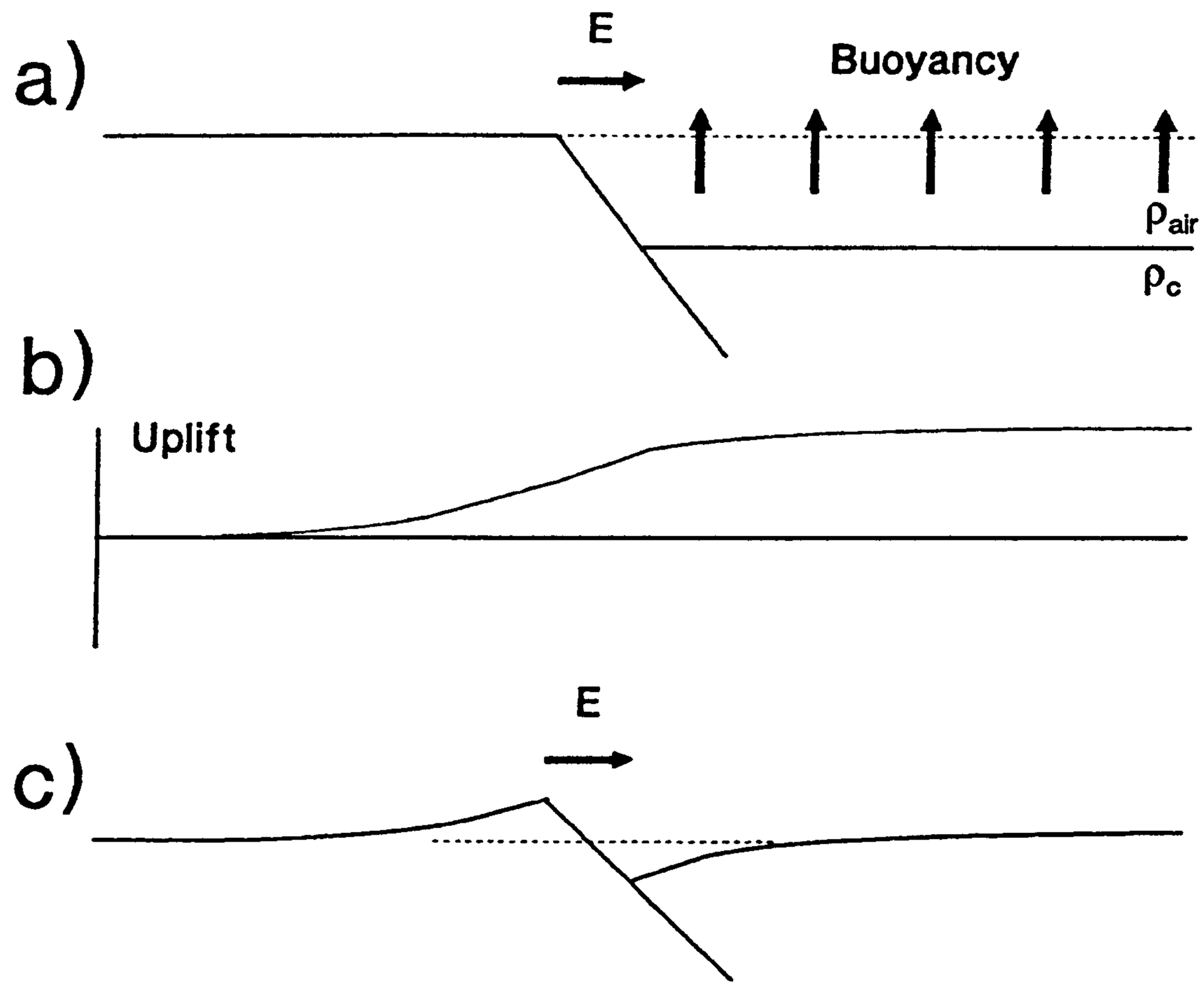


**Figure 2.5** The flexural isostatic response to the geometrical load generated by extension of the lithosphere (Kusznir et al., 1991). a) After extension (E), with gravity "switched off", generating an air filled basin. The single planar fault in the upper crust dips 60°. Datum = sea level. b) The flexurally distributed uplift in response to the buoyancy force when gravity is "switched back on". c) The resultant basin geometry after adding the uplift to the profile shown in a).

of *u(k)* and added to the crustal surface *h(x)* to give the resultant geometry *s(x)* shown in Figure 2.5c:-

$$s(x) = h(x) + u(x) \tag{2.4}$$

The magnitude of the buoyancy force is such as to return the right-hand end of the profile to its original upper crustal surface level. However, the flexural isostatic distribution of the load also causes footwall uplift and a corresponding collapse of the hangingwall rollover (Figure 2.5c). Figure 2.6 shows additional features of the resultant basin geometry across the profile including proximal footwall subsidence and a "hangingwall flexural bulge" in a distal position relative to the rollover. Because at this stage it has been assumed that the basin is air-loaded during extension, the area of footwall uplift exactly matches the hangingwall rollover. This symmetry is seen as evidence of the equivalent behaviour of footwall and hangingwall (cf. Chevron construction).

In addition to the response of the upper crustal surface, the flexurally distributed buoyancy force also acts on the fault plane. The increase in the magnitude of the flexural isostatic restoring force across the fault plane has the effect of uplifting the bottom of the fault more than the top and the fault plane therefore undergoes a net rotation. Buck (1988) has shown that flexural rotation of normal faults may explain many of the features of the Basin & Range Province where very large values of extension give rise to a low angle, listric geometry after rotation of initially planar faults.

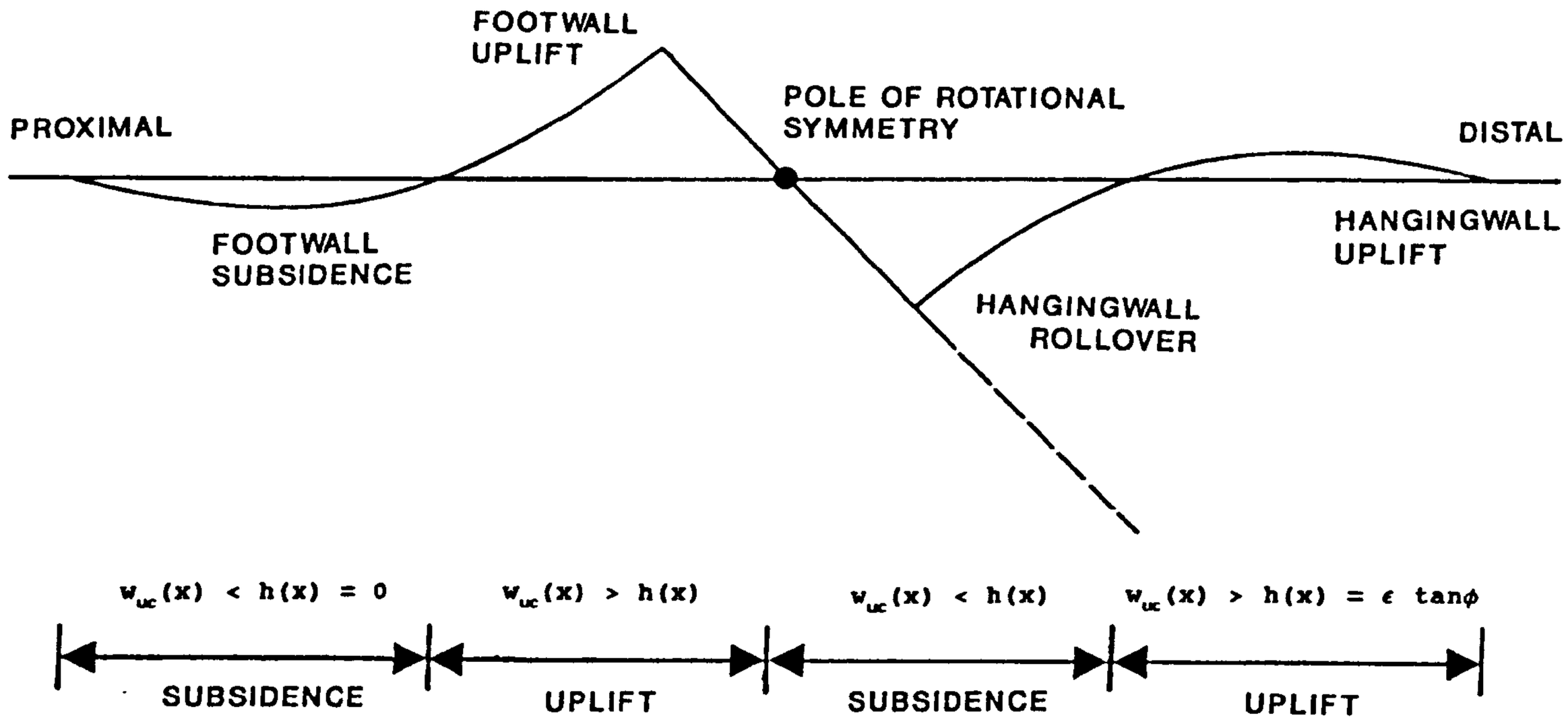


**Figure 2.6** Details of the topography generated by extension of 10 km on a planar fault including a hangingwall "flexural bulge" and footwall basin (From Marsden, 1990).

### 2.2.2 The Load Caused by the Generation of Moho Topography and its Flexural-Isostatic Response.

Extension of the continental crust leads to the generation of Moho topography, which has two components - the true pure-shear extension in the lower crust and the "pseudo pure-shear" (Kusznir, Marsden & Egan, 1991) resulting from the conservation of area at the brittle-ductile transition.

A fundamental assumption of the coupled simple-shear pure-shear model is that extension in the upper, brittle crust is exactly matched by pure-shear extension below the brittle ductile transition (Kusznir et al., 1991). As a result of the ductile nature of the lower crust, the pure-shear extension is likely to be of a distributed nature and has been given a sinusoidal distribution such that:-

$$\beta = 1 + C\sin(\pi x / W) \tag{2.5}$$

where $1 + C$ is the maximum stretching factor $\beta$, $W$ is the width of the pure-shear region and $x$ is the horizontal distance from the start of the sinusoidal distribution. If the pure-shear extension must match $E$ in the upper crust then:-

$$E = \int_0^{W'} (\beta(X) - 1)\, dx \tag{2.6}$$

$$= \int_0^{W'} C\sin(\pi x / W)\, dx \tag{2.7}$$

where $W'$ is the pre-extension pure-shear width. The constant $C$ in Equation 2.5 can be determined from the integral in Equation 2.7:-

$$E = 2CW'/\pi \tag{2.8}$$

or

$$C = (\pi E) / (2\,(W-E)) \tag{2.9}$$

The sinusoidal pure-shear stretching factor, given by Equation 2.5, has been used to determine the geometry of the Moho in Figure 2.7a. The real pure-shear extension in the lower crust, which acts on a thickness (*d-t*), is given by:-

$$RPS(x) = -(d-t)\,(1-1/\beta_{lc}(x)) \tag{2.10}$$

where *d* is total crustal thickness and *t* is the thickness of the brittle upper crust.

Consideration of the conservation of area in Figures 2.7a & b shows that the upper crustal area *E.t* , created by the extension, must be balanced by an area (*C-D*), at the base of the brittle layer beneath the fault, in order to conserve area. To avoid generating an empty space, the ductile lower crust flows up into the area (*C-D*) as shown in Figure 2.7c. Upwelling of the mantle, to replace the upward flow of ductile lower crust, is termed "pseudo pure-shear" (Kusznir, Marsden & Egan, 1991). Like real pure-shear, the "pseudo pure-shear" has a sinusoidal distribution (Figure 2.7c), but acts on a ductile layer whose thickness is equal to that of the upper crust (*t*):-

$$PPS(x) = -t(1-1/\beta_{uc}(x)) \tag{2.11}$$

The real and "pseudo" pure-shears are assumed to have the same lateral distribution and may be combined, such that $\beta_{uc}(x) = \beta_{lc}(x)$, and the total pure-shear acts on the total thickness of the crust (Figure 2.7d):-

$$PS(x) = -d(1-1/\beta(x)) \tag{2.12}$$

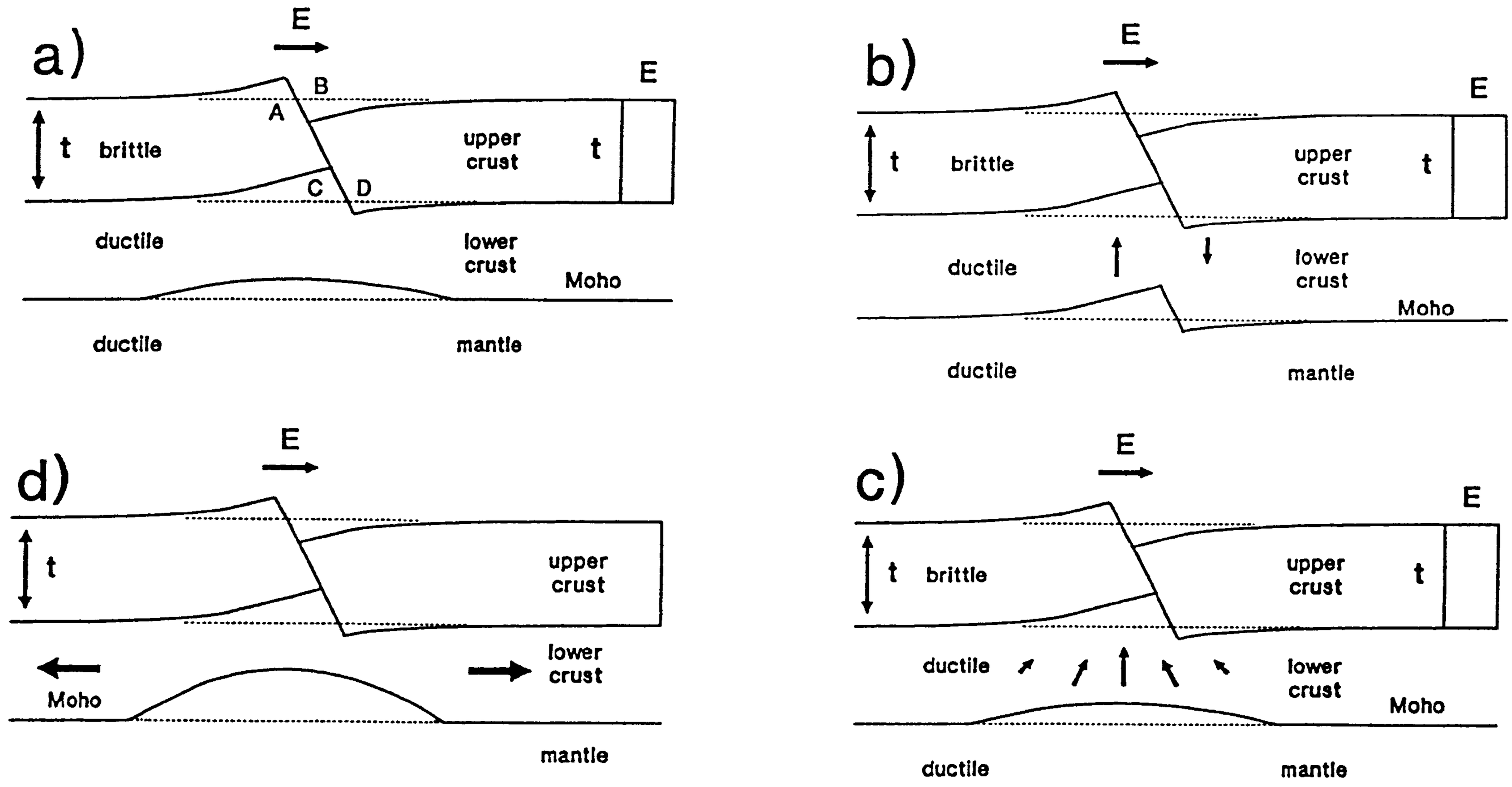


**Figure 2.7** Generation of Moho topography by distributed pure-shear in the ductile lower crust (modified from Kusznir et al., 1991). a) Real pure-shear matching the simple-shear extension (E) in the brittle upper crust, distributed over 75 km and offset 20 km behind the footwall cut-off. b) Hypothetical Moho geometry which exactly matches the brittle ductile transition. c) "Pseudo pure-shear" geometry, distributed sinusoidally as in a). d) Total Moho topography combining real and pseudo pure-shear.

Replacing lower crust by mantle generates a downward load, ($l_2$), given by:-

$$l_2(x) = PS(x)\ (\rho_c - \rho_m)\ g \qquad (2.13)$$

where $\rho_m$ is the mantle density at asthenospheric temperature.

The flexural isostatic response to this load involves the full thickness of the lithosphere. Therefore, although it is calculated in the same way as the buoyancy load, a different response function is used (see Appendix A):

$$R(k) = 1/((\rho_m - \rho_{air})\ g + Dk^4) \qquad (2.14)$$

The flexural isostatic response is added to the crustal surface, fault geometry and the Moho topography (which actually causes the load).

## 2.3 Thermal Uplift due to the Syn-rift Perturbation of the Lithosphere Temperature Field.

During continental extension, upwelling of hot, low density mantle material due to the elevation of the lithosphere/asthenosphere boundary, with a corresponding increase in the geothermal gradient, causes thermal uplift (Figure 2.8). It should be emphasised that this asthenosphere upwelling is a purely passive response to the whole-lithosphere pure-shear extension which matches the pure-shear in the ductile lower crust. For the thermal buoyancy load, simple-shear temperature perturbations in the upper crust can be neglected since calculations show that the effects, once flexurally distributed, are negligible. The thermal load ($l_3$) can be calculated relatively simply by considering the reduction in mantle density due to the increase

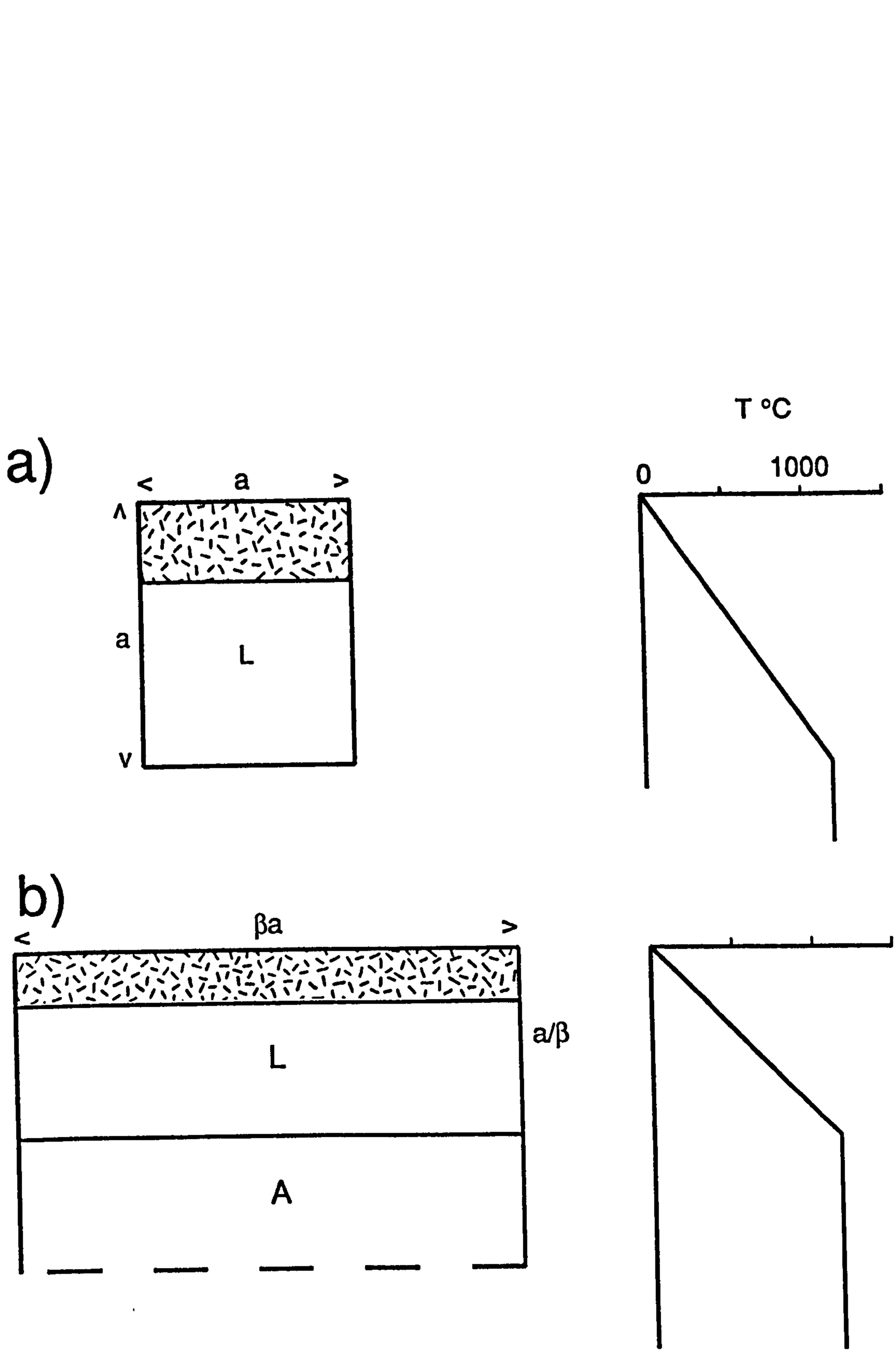


**Figure 2.8** a) The standard, linear geotherm down to a uniform asthenosphere temperature of 1333 °C. b) The perturbed geotherm for lithosphere (L), extended by a constant factor β, and upwelling of the asthenosphere (A). In the flexural cantilever model a separate geotherm is calculated for each value of Beta across the profile.

in temperature between the old and new geothermal gradients using the coefficient of thermal expansion, $\alpha$.

Temperatures (Ti) on the initial geotherm are given by the following equation:-

$$T_i = \frac{T_0 z}{A} \qquad (2.15)$$

where z is depth, A is the depth of the lithosphere and $T_0$ is the asthenosphere temperature (1333° C). Temperatures (Tp) on the perturbed lithospheric geotherm are given by:-

$$T_p = \frac{T_0 z}{A} \cdot \beta(x) \qquad \left(z \leq \frac{A}{\beta(x)}\right) \qquad (2.16)$$

where $\beta$(x) is the value of the Beta factor at each location across the profile. The region of upwelled asthenosphere is assumed to have a temperature of 1333° C:-

$$T_p = 1333 C^\circ \qquad \left(z > \frac{A}{\beta(x)}\right) \qquad (2.17)$$

The thermal buoyancy load is calculated by integrating the product of the temperature change $\Delta$T, thermal expansion coefficient ($\alpha$) and density with respect to depth:-

$$l_3(x) = -\int_0^{\lambda} \Delta T . \alpha . \rho_z . g \, dz \qquad (2.18)$$

where $\Delta T = (T_p - T_i)$ and $\rho_z$ is the depth dependent density (of either crust or mantle). The thermal load, like the load due to Moho topography, is considered to be regionally compensated and the flexural isostatic response is calculated in the

wavenumber domain by multiplying the response function (Equation 2.14) and the Fourier transform of the thermal load:-

$$U(K) = L_3(k) \times R(k) \qquad (2.19)$$

The reverse transform of *u(k)* is then added to the crustal surface, fault geometry and the Moho.

## 2.4 Sediment Loading by Iterative Basin Fill.

### 2.4.1 Sediment Infilling to Sea Level.

The process of modelling basin infilling, with either water, of density $\rho_w$, or sediment, of density $\rho_s$, is iterative and is accomplished by several steps (Figure 2.9). In the initial step, sediment fills the basin to sea level and generates a load ($l_4$):-

$$l_4(x) = h(x)\,\rho_s\,g \qquad (2.20)$$

where h(x) is the initial depth of the basin below sea level. The flexural isostatic response to this load is determined, in the wavenumber domain, and added to the profile. After this calculation, the upper surface of the first layer of sedimentary infill is below sea level and a second fill to sea level is required (Figure 2.9b). This process is repeated until the sediment filled basin reaches flexural isostatic equilibrium - usually around 30 iterations (Figure 2.9c).

### 2.4.2 Sediment Infilling to Finite Bathymetry.

Palaeo-bathymetry can be added very simply to the flexural cantilever model, by specifying the depth of water to be left after infilling (Pb). This value can be varied laterally, Pb(x), or kept constant across the basin. If $\rho_w$ is the density of water

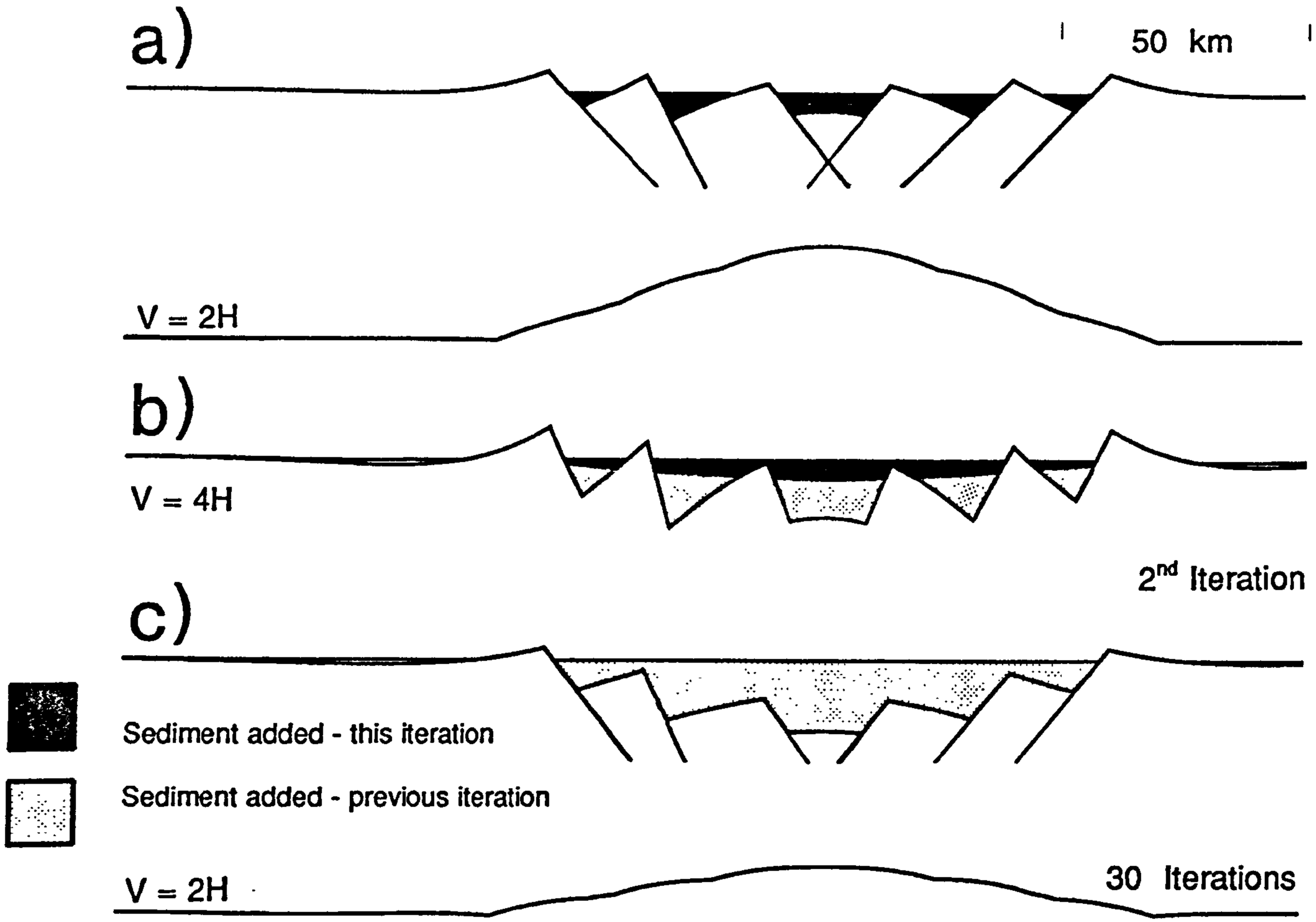


**Figure 2.9** The iterative process of modelling sediment infilling. a) The initial water-filled basin. b) Sediment loading from the first iteration causes broad downwarping and more sediment is required to fill the basin to sea level. c) The full basin after 30 iterations.

then Equation 2.20 can be modified so that the load at each step comprises both sediment and water:-

$$l_4(x) = (h(x) - Pb)\,\rho_s\,g + Pb\,\rho_w\,g \qquad (2.21)$$

## 2.5 Application of the Flexural Cantilever Model with a Single Fault.

Two fundamental parameters controlling the geometry of basins adjacent to a single fault are the amount of extension and the angle of the fault. Figure 2.10 shows that as the extension is increased from 2 to 10 km the basin becomes progressively wider and deeper. Moho topography and footwall uplift also increases as the amount of extension rises.

The effects of increasing the initial fault angle, while extension remains constant, are shown in Figure 2.11. With an initial fault angle of 25° a broad but shallow basin is generated. As the angle of the fault increases the basin deepens and the amount of footwall uplift is greater while the overall width of the basin decreases slightly.

## 2.6 Multiple Planar Faults.

### 2.6.1 Fault Spacing and its Effect on the Flexural Cantilever Model with Multiple Faults

So far the simple-shear extension on only a single fault in the brittle upper crust has been considered. With several planar faults, the resultant basin geometry is determined by the mutual interference of the flexural isostatic responses to these

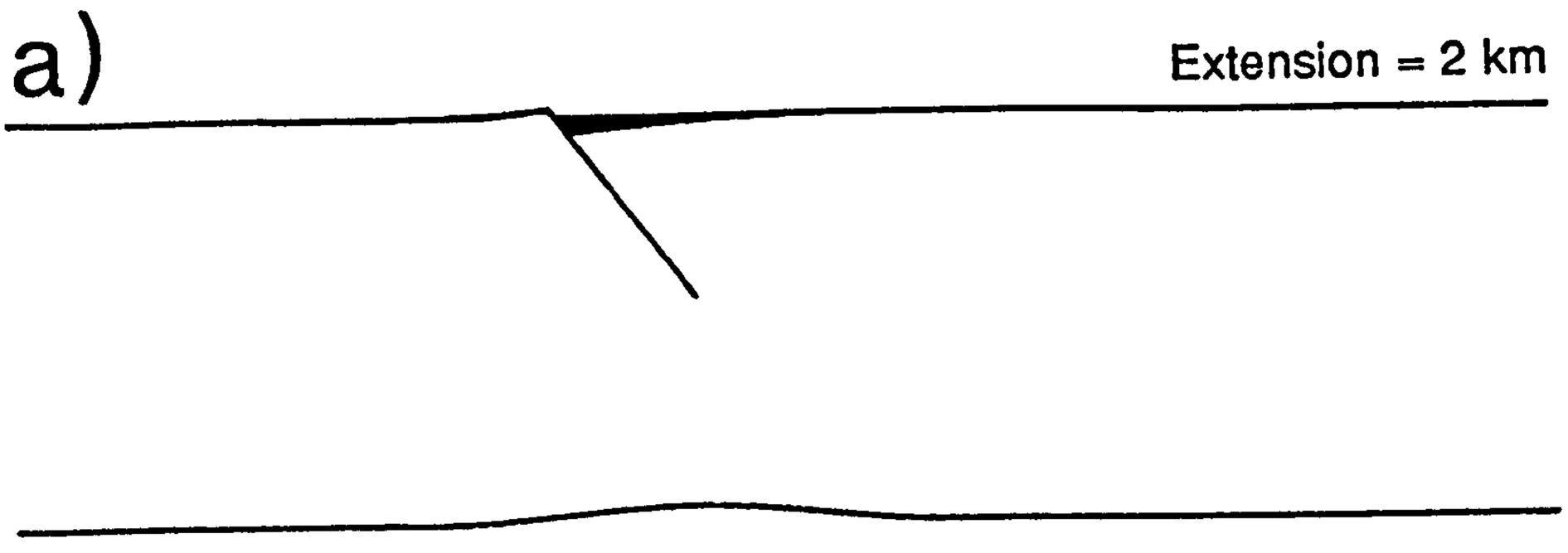


**Figure 2.10** Increasing extension. As extension is increased from 2 km (a) to 5 km (b) and then 10 km (c) the basin becomes progressively deeper and wider. Moho topography also increases.

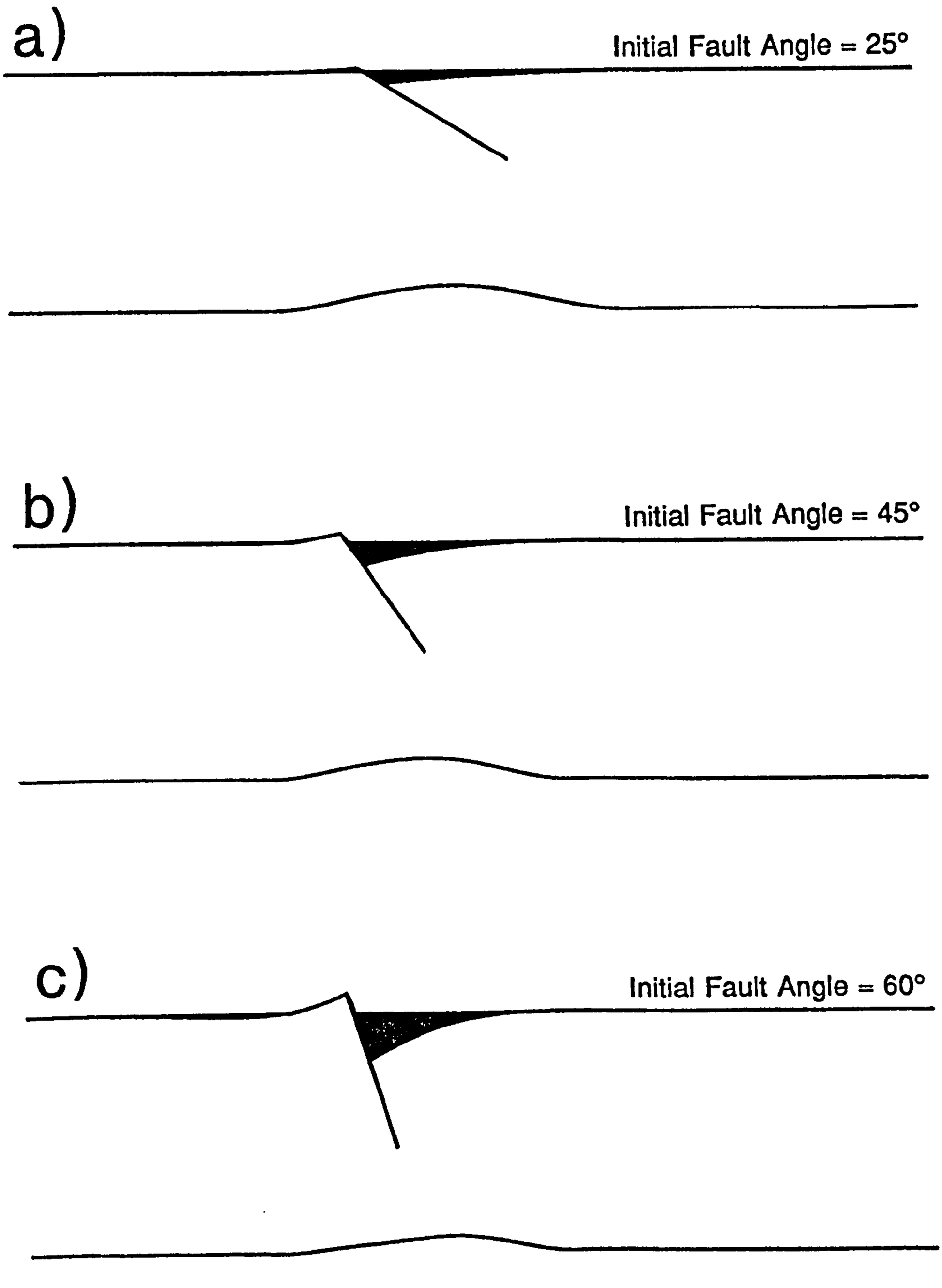


**Figure 2.11** Increasing the initial fault angle. As the angle of dip is increased: a) - 30°; b) - 45°; c) - 65°) the basin becomes progressively deeper and the region of footwall uplift more accentuated. Extension remains constant in all of the models.

faults. Figure 2.12 shows four planar faults, each with an extension of 5 km and fault spacings of 20, 40 and 60 km respectively. The upper crustal surface between the two widely spaced faults has a characteristic sigmoidal geometry, comprising the hangingwall rollover to fault number two and the footwall uplift of fault three. However the surface between the closely spaced faults is approximately planar. The upper crustal block between the two faults has first been flexed down in the hangingwall of fault number one and then subsequently flexed back up in the footwall of fault number two. The net effect is to rotate the crustal block, but by a process of bending and unbending, rather than as a rigid body.

### 2.6.2 Comparison of the Flexural Cantilever Model with the "Domino-style" Models for Lithosphere Extension

By increasing the number of faults in the flexural cantilever model, profiles such as those in Figure 2.12 begin to resemble the familiar "domino-style" of crustal faulting. Previous models for this style of faulting either have space problems (Jackson & McKenzie, 1983) or require an unrealistic fault geometry at one end (Barr, 1987). Jackson (1987) has attempted to reconcile whole lithosphere pure-shear with simple-shear extension on planar faults by including the rotation of the "domino" fault blocks (Figure 2.13a). Largely because of the assumption that the fault blocks remain undeformed as they rotate, the Jackson model cannot predict the geometry at either end of the "domino" fault system and it continues to infinity. Barr (1987) has attempted to eliminate the large voids in the crust at either end of the profile, but uses a listric geometry (Figure 2.13b) which is unrealistic for the reasons given in section

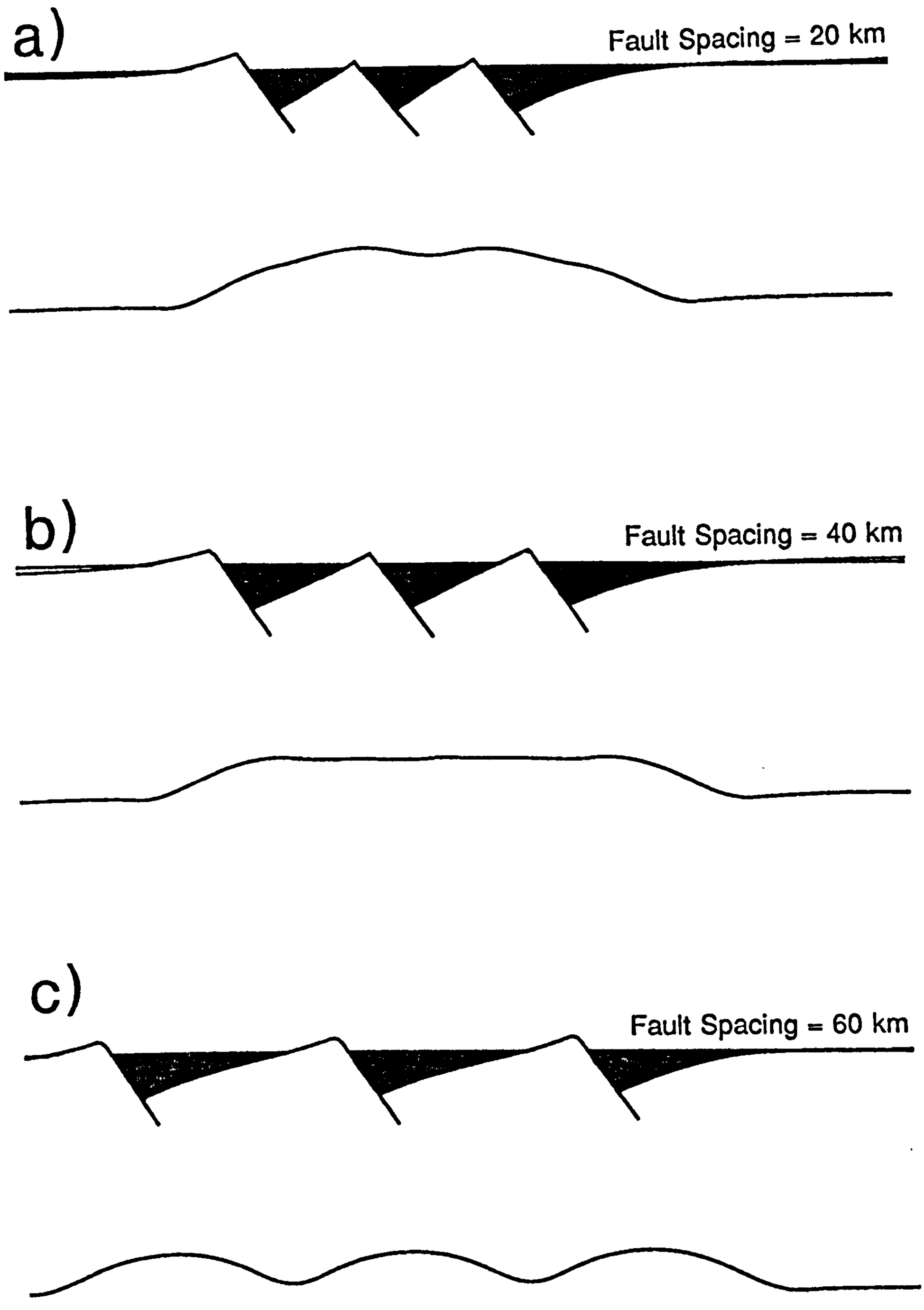


**Figure 2.12** Fault spacing and the flexural cantilever model. Faults get progressively further apart between a) 20 km b) 40 km and c) 60 km. The upper crustal surfaces of the fault blocks are planar in a) and b). At larger spacings the flexural interference mechanism breaks down and a sigmoidal upper crustal surface joins the hangingwall rollover to the footwall uplift.

a)

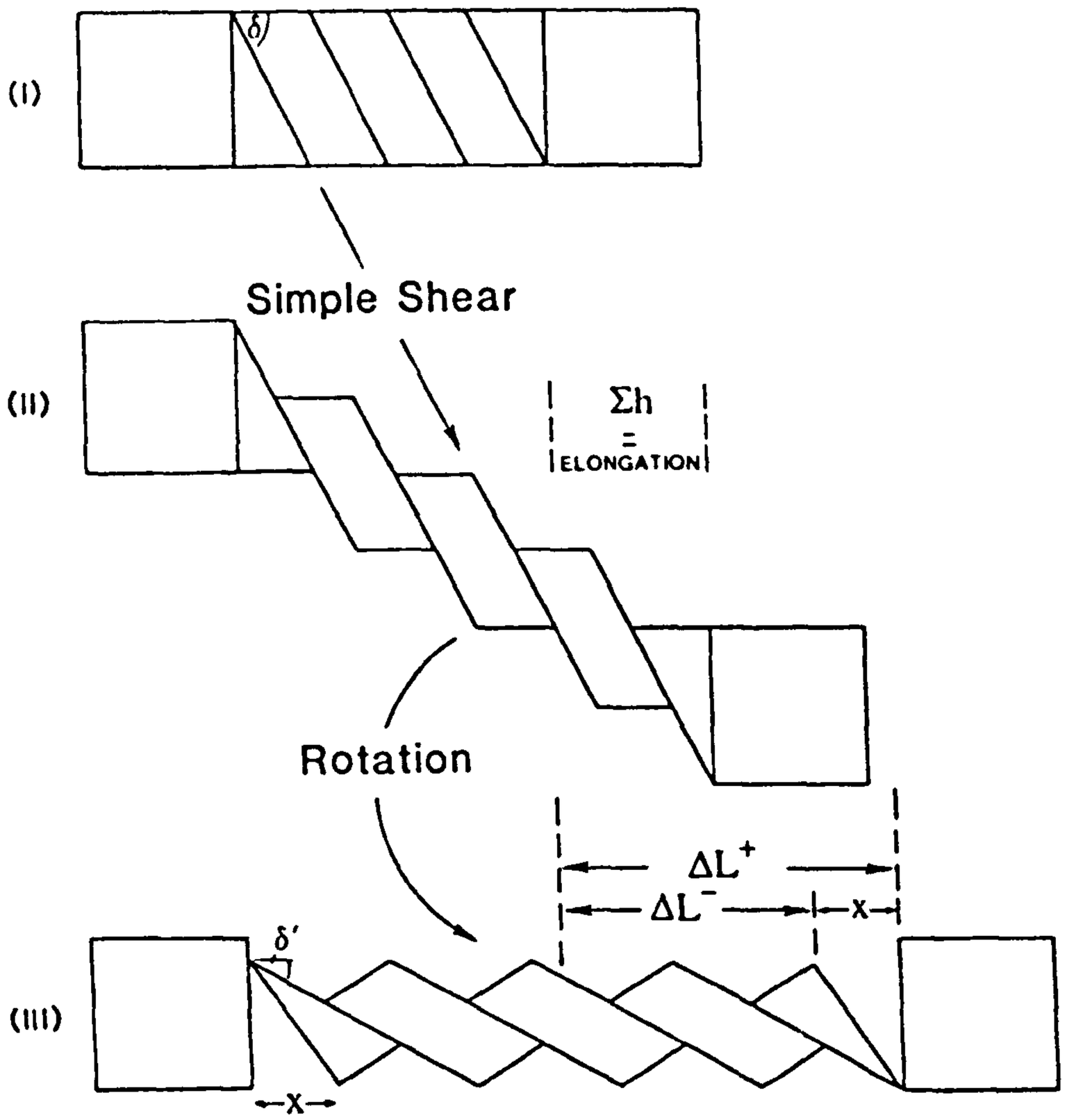


b)

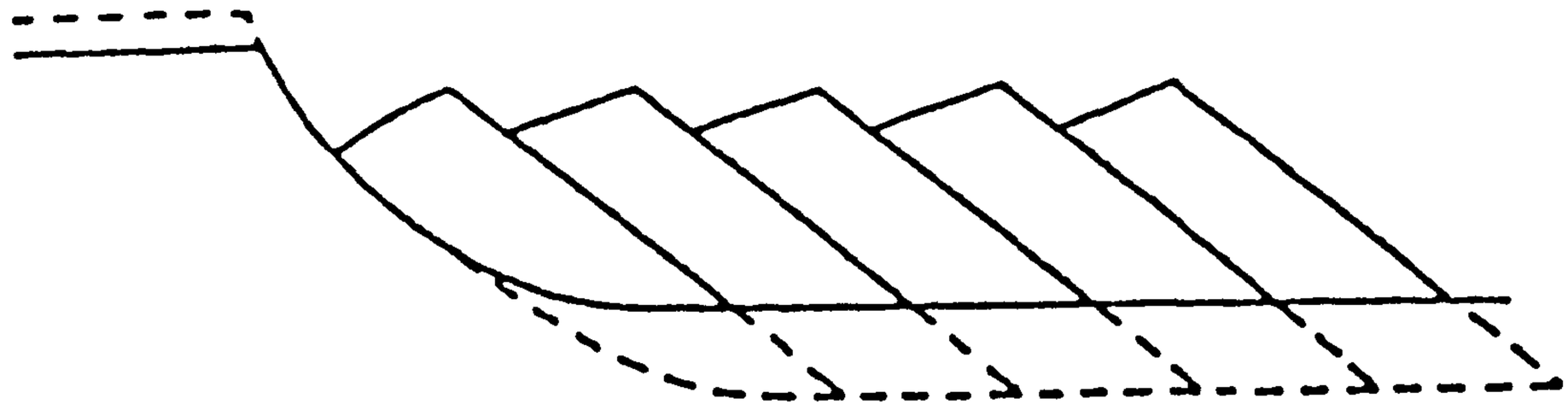

**Figure 2.13** a) The "Domino" style of extension. Rigid block rotation after simple-shear is equivalent to pure-shear (From Jackson, 1987). Note the space problems at either end of the model. b) The Barr (1987) model, in which the "domino" style fault blocks are separated from the footwall by a listric fault.

2.1. The flexural cantilever model has no such space problems and the area of "domino" style faulting is bounded either by footwall uplift or hangingwall rollover.

## 2.7 The Effective Elastic Thickness Parameter Te.

### 2.7.1 The Relationship Between Effective Elastic Thickness and the Depth of the Brittle Ductile Transition.

The effective elastic thickness (Te) can be defined as the thickness of an unbroken, perfectly elastic plate that would have the same effective flexural rigidity as the lithosphere (Kusznir et al. 1991). Te is quite well constrained by forward modelling lithospheric extension because it controls the angle of dip of fault-block tops and it can be varied until a best fit is achieved. It will be shown that the values of Te, used in Equation A15, are usually much less than the thickness of the brittle upper crust (10-15 km) as suggested by earthquake seismology (Jackson, 1987) or rheological arguments (Kusznir & Park, 1987).

Figure 2.14 shows that the reduction in flexural rigidity with extension is the direct consequence of brittle failure caused by bending stresses exceeding the brittle failure envelope of the upper crust (Kusznir et al., 1991). An unstretched plate begins with a flexural rigidity which corresponds to the thickness of the brittle upper crust. The flexural response to extension creates bending stresses which cause fracturing of the upper crust (Figure 2.14c), thus lowering its effective rigidity. As extension is increased the resultant bending stresses further exceed the brittle failure envelope causing even more fracturing which significantly reduces the effective elastic thickness. Figure 2.14d shows a plot of Te against extension, for bending stress

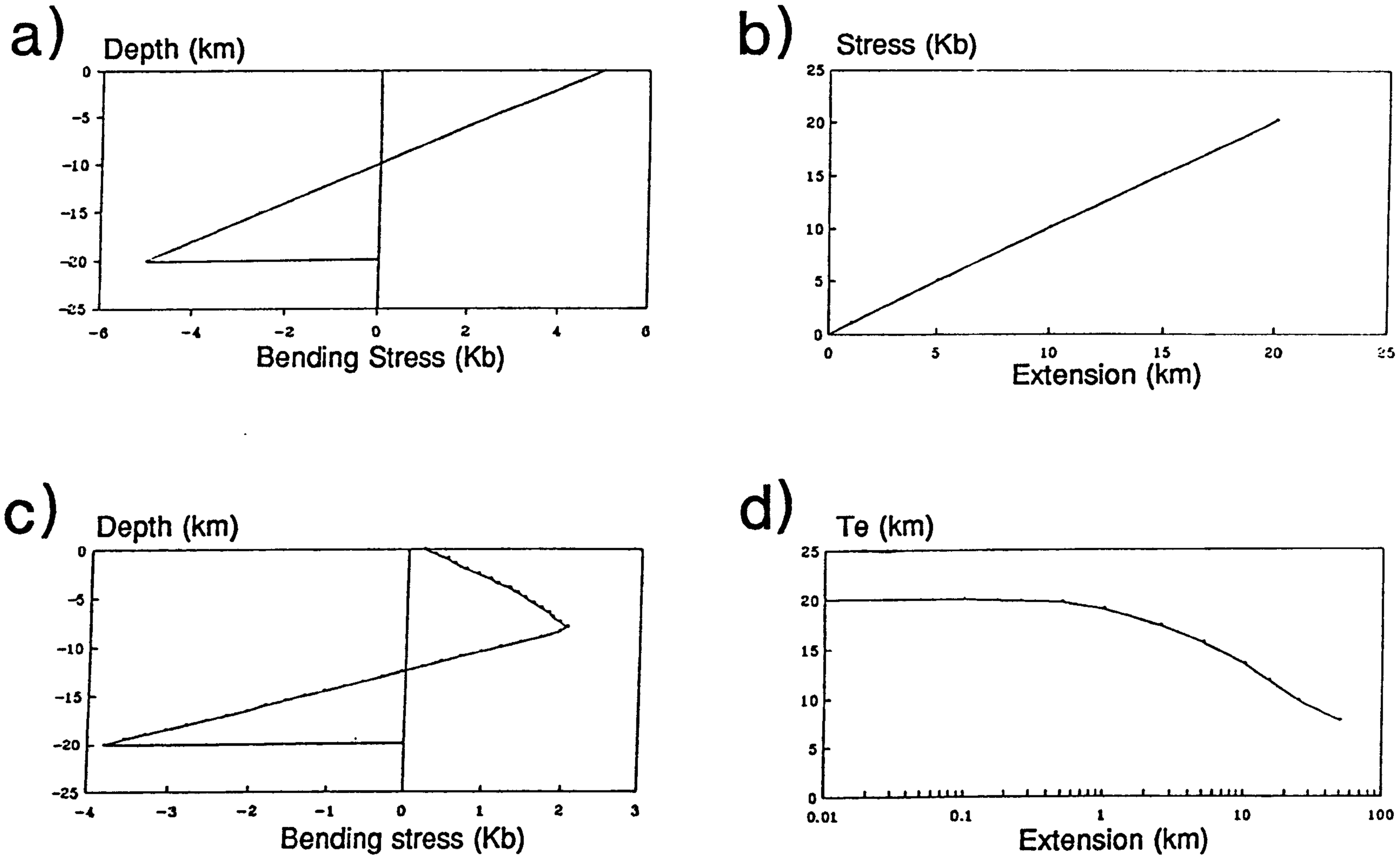


**Figure 2.14** The effective elastic thickness parameter Te (from Kusznir et al., 1991). a) Bending stresses up to 5 Kb generated when Te equals the thickness of the upper crust (20 km). b) Bending stresses increase linearly with extension until they exceed the brittle failure envelope. c) Fractures in the upper crust release the bending stress. d) Te reduces with extension due to the loss of strength in the upper crust (N.B. Log scale).

released by brittle failure only. When the effect of bending stress release by creep in the lower crust is included, Te is further reduced but is still high compared to values derived from the modelling (3 to 4 km). This discrepancy is thought to be a caused by using laboratory estimates for the flexural strength of the lithosphere (Kusznir, in press). Further reductions in Te, caused by progressive dyke intrusion close to the continent ocean boundary, are discussed in Chapter 4.

### 2.7.2 The Control of the Effective Elastic Thickness Parameter on Rift Basin Geometry

Figure 2.15 shows that the effective elastic thickness parameter controls the interference mechanism which affects the geometry of sub-basins across the profile. At low values of Te, the flexural isostatic response to extension on each fault is restricted to a narrow zone adjacent to the fault (Figure 2.15a). Sub-basin geometry is therefore independent for each fault, producing a characteristic sigmoidally shaped upper crustal surface. At higher values of Te the mutual interference of the flexural isostatic responses produces the "domino-style" extensional geometry with systematic variations in sub-basin depth and geometry across the profile. The footwall at the proximal end of the profile is uplifted by the flexural isostatic response to extension on all three faults while the distal sub-basin is deeper than the other two (Figure 2.15b & c).

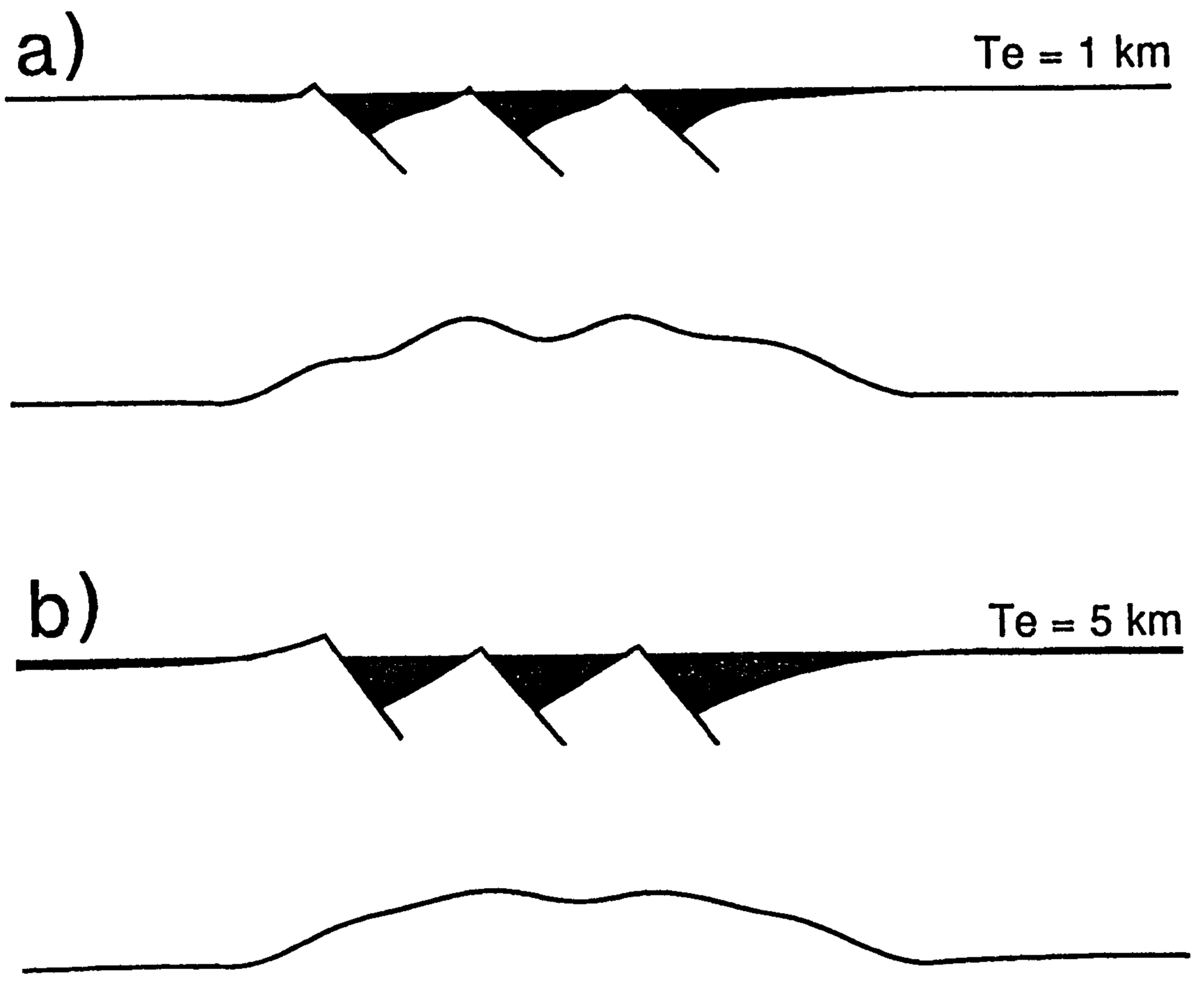


**Figure 2.15** Effective elastic thickness and the flexural cantilever model. As Te increases ( a) 1km; b) 5 km; c) 10 km ) the basin geometry is strongly affected by the flexural interference mechanism. At low values of Te (A) the flexural wavelength is low by comparison with the basin width and sigmoidal fault-block surfaces are generated between narrow basins. As Te increases, the basin width increases and fault-block surfaces become planar.

## 2.8 Post-rift Thermal Subsidence.

### 2.8.1 Lithosphere Loading due to Thermal Cooling and Contraction of the Lithosphere.

Before an application of the flexural cantilever model to basin formation can be considered, the post-rift thermal subsidence must be calculated. An outline is sufficient because in subsequent chapters the forward models only the syn-rift geometry is calculated.

It is assumed that the thermal perturbations produced by instantaneous rifting gradually decay as the geotherm returns to its pre-extension position. Appendix B shows how the new post-rift temperature field is calculated using a finite difference solution of the two-dimensional heat conduction equation:-

$$\frac{\partial T}{\partial t} = \frac{k}{\rho C_p}\left(\frac{\partial^2 T}{\partial x^2} + \frac{\partial^2 T}{\partial Z^2}\right) \qquad (2.22)$$

A downward load is generated by virtue of the increase in density due to the thermal contraction of the lithosphere (since $\Delta T$ is negative). The integral for the thermal load, generated in a given time interval, is given by:-

$$l_5(x) = -\int_0^A \Delta T . \alpha . \rho_z . g \, dx \qquad (2.23)$$

The flexural isostatic response to the post-rift thermal load is calculated using a response function which assumes compensation within the asthenosphere (Equation 2.14). Once the new profile is calculated, any part of the basin which has subsided below sea level, or below a specified value of palaeo-bathymetry, is infilled with

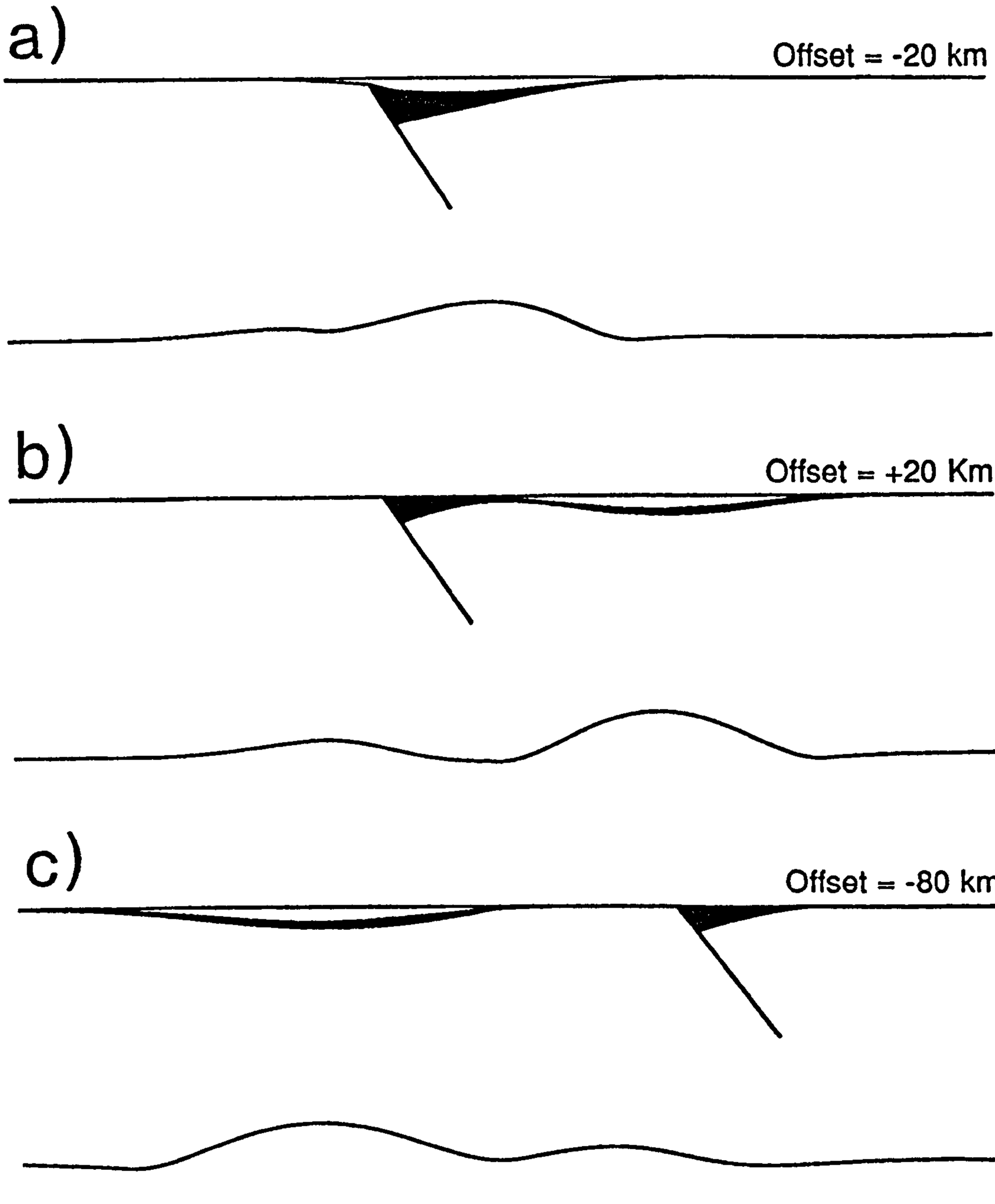


**Figure 2.16** The effect of pure-shear location on post-rift thermal subsidence. a) Pure-shear distributed over 75 km and offset 20 km West of the footwall cut-off superimposes the maximum thermal subsidence over the deepest part of the rift basin. b) Pure-shear offset 20 km East of the footwall cut-off generating an off-axis thermal subsidence basin. c) A footwall basin generated by pure-shear offset 80 km west of the fault cut-off.

sediment using the iterative process described in section 2.4. Figure 2.16a shows the resultant basin geometry after 150 Ma of post-rift thermal subsidence.

Theoretically the lateral distribution of post-rift thermal subsidence could be affected by variations of the pure-shear width. However, finite element modelling of lithospheric extension by Caban (1991) has shown that, for each fault, the pure-shear width within the ductile lower crust is independent of the strain rate and the pre-rift thermal gradient. In nearly all cases, perturbations of the Moho are distributed over 75 km and this value of pure-shear width is used throughout the thesis.

Caban (1991) has also shown that the overall pure-shear width of a rift system cannot be related simply to the overall width of the zone of faulting in the brittle upper crust. However, in the flexural cantilever model, the total pure shear width is derived from the product summation of the pure shear envelopes of each individual fault in the system.

### 2.8.2 The Effect of Pure-shear Lateral Distribution on Post-rift Thermal Subsidence.

An important attribute of the flexural cantilever model is that, although the pure-shear in the ductile lower crust and mantle is "coupled" to the extension on planar faults in the brittle upper crust, the sinusoidal distribution of the pure-shear is, in theory, independent of the fault position. This is important because it is the location of the pure-shear, and therefore the upwelling of hot mantle material, that controls the position of the post-rift thermal sag. In theory, this could lead to "off-axis" thermal subsidence basins (Figure 2.16b and c), but the preferred pure-shear distribution (75 km, offset 20 km behind the footwall cut-off of the fault) has the

effect of superimposing the maximum thermal subsidence over the deepest part of the rift basin (Figure 2.16a).

## 2.9 The Flexural Isostatic Effect of Erosion.

Removal by erosion of the footwall induces an isostatic response to the unloading which is flexurally distributed over an area which includes the basin fill. Like basin infilling, the modelling of erosion, and the isostatic rebound it causes, is an iterative process. Figure 2.17 shows that the flexural isostatic response to removal of the footwall brings the entire basin to a shallower level and tilts the sedimentary surface towards the hangingwall. In some cases, syn-rift sediments are also eroded and subsequent iterations must take account of the different densities of unloaded material until the region reaches flexural isostatic equilibrium. Although the end result in Figure 2.17 is shown after 60 iterations, adequate convergence is usually obtained with 30 or 40 iterations.

## 2.10 Application of the Flexural Cantilever Model.

The parameters which may vary for any given application of the flexural cantilever model are given below:-

1) The effective elastic thickness of the lithosphere.

2) The amount of extension.

3) The number of faults

4) Fault positions.

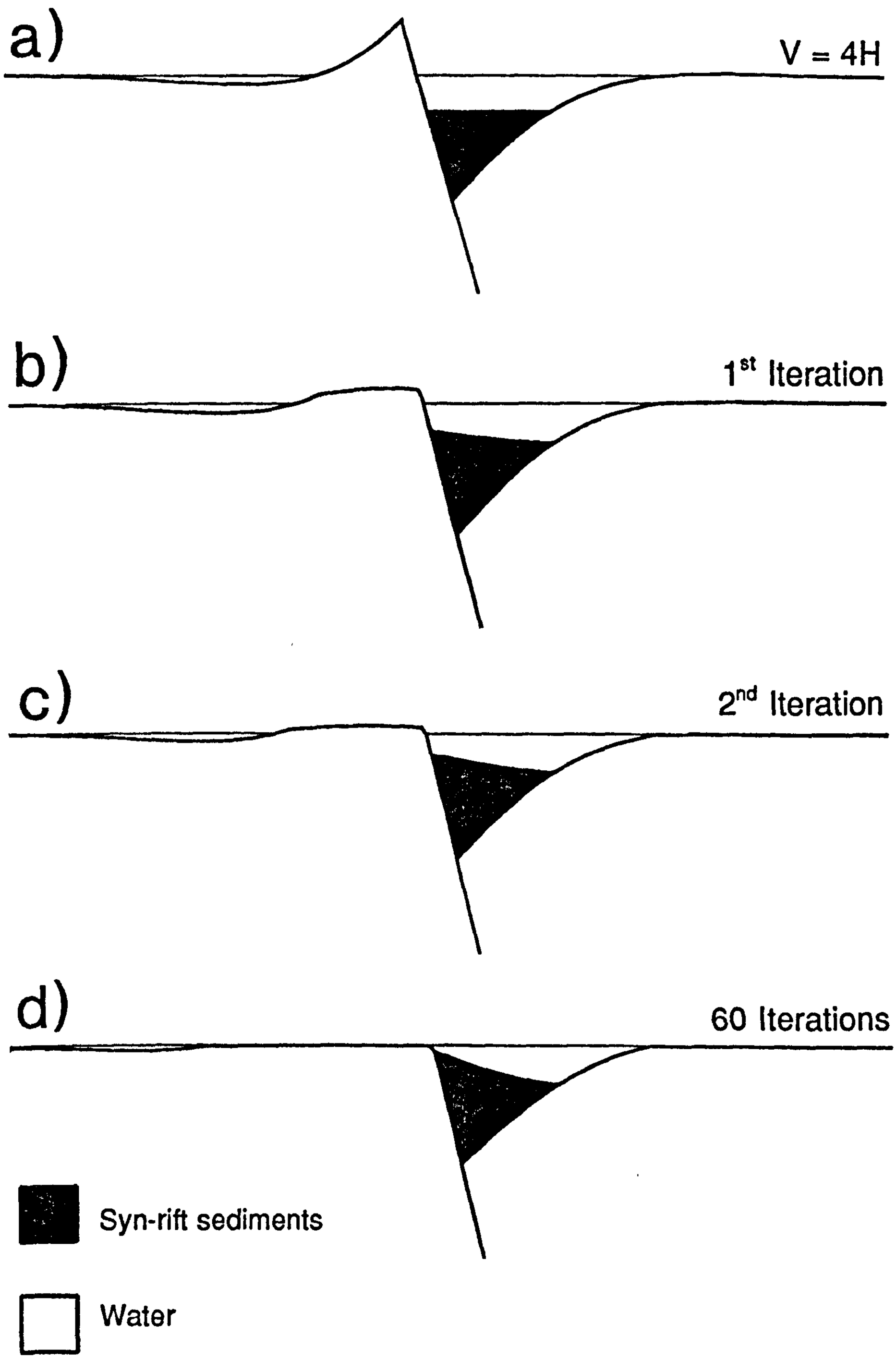


**Figure 2.17** The flexural isostatic effects of erosion.

5) The width and lateral position of the pure-shear in the lower crust and mantle.

6) The location of the pure-shear in the lower crust and mantle.

6) Crustal thickness

7) Depth of the brittle-ductile transition.

8) The pre-extension angle of each fault.

The Jeanne d'Arc basin on the Grand Banks off the eastern coast of Newfoundland was chosen to test the flexural cantilever model, in its early development, because of the control provided by deep seismic data (Keen et al., 1987). The Moho is imaged on several profiles at 12 s T.W.T.T., corresponding to a crustal thickness of 35 km. Tankard & Welsink (1987) have suggested that faults on the Grand Banks detach at 26 km, and this value is used to delimit the depth of the brittle-ductile transition, even though the detachment model itself has now been discredited (Kusznir & Egan, 1989). The bounding faults of the Jeanne d'Arc basin have a deceptively listric appearance on deep seismic time sections, notably the southern portion of the Murre Fault. When depth converted, however, these faults are all shown to be planar (see section 7.3), with post extension dips of around 50°. The location of the pure-shear can be specified by an abrupt change in the gradient of Moho reflectors, at two points along the profile where they are particularly strong. These two points are assumed to mark the lateral extent of Moho topography created below the Jeanne d'Arc basin during extension.

Figure 2.18 shows the two depth sections - profiles 1 and 2 - from Tankard et al. (1990), which were modelled by Kusznir & Egan (1989). In an initial model

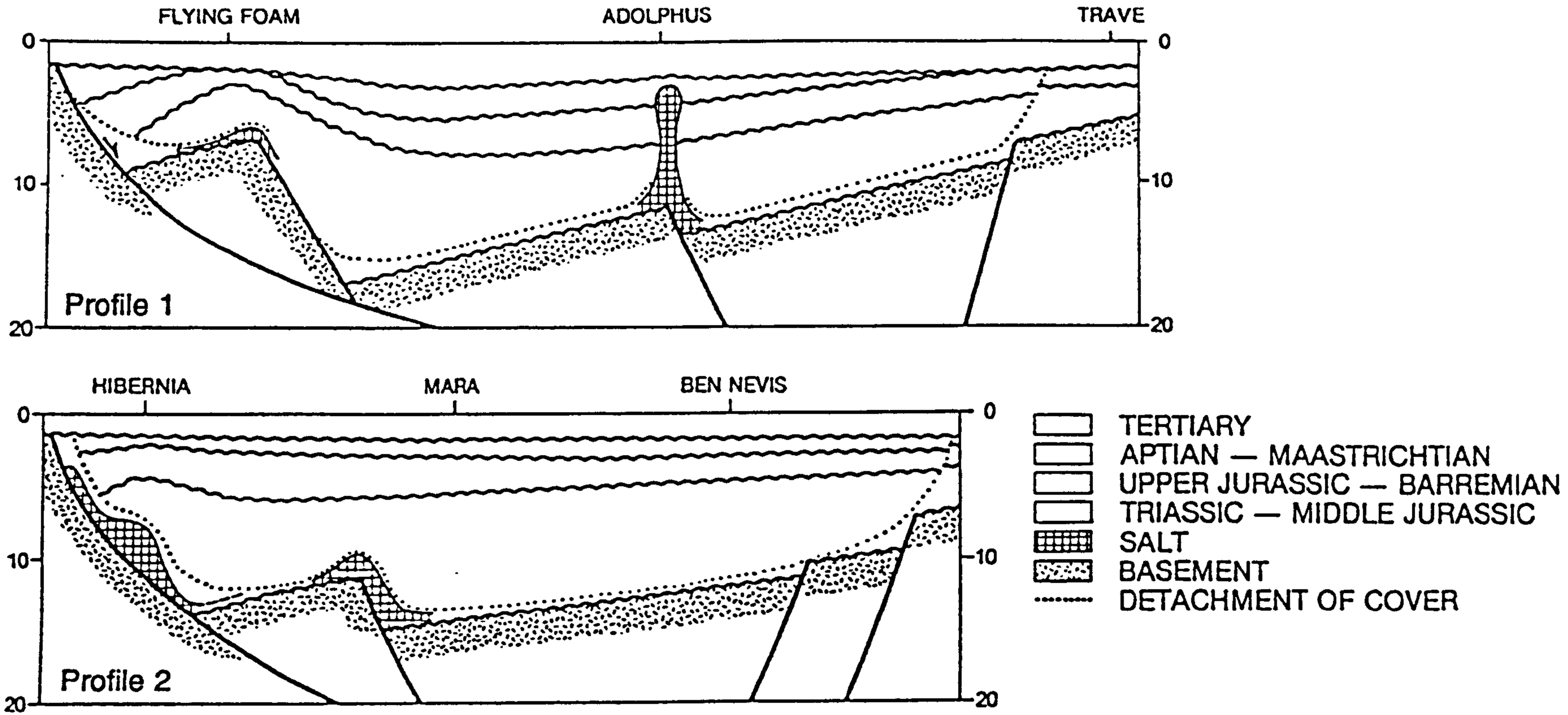


**Figure 2.18** Depth converted sections across the Jeanne d'Arc basin, Grand Banks. 1 and 2 (from Tankard et al., 1989)

of profile 1 the values of extension used on two planar faults (5.5 km and 6.5 km) were measured directly from the section. The resultant total basin depth, after 100 Ma of post-rift thermal subsidence is only 14 km, rather than the observed 17 km. Kusznir & Egan (1989) found that the basin could be deepened by increasing the extension on the major basin bounding fault, which produced significant amounts of footwall uplift. However, on seismic profiles the footwall region is almost perfectly flat, and it was concluded that the footwall uplift had been completely eroded.

Figures 2.19 and 2.20 show the preferred models for profiles 1 and 2 respectively (Kusznir et al., 1991). In all cases Te = 10 km and pure-shear is distributed over a width of 75 km, offset 20 km behind the footwall cut-off. Figure 2.19a shows that the extension on the main basin bounding fault has been nearly doubled to 12 km. After erosion, only a certain proportion of this extension is preserved (Figure 2.19b). The total basin subsidence is calculated after 100 Ma post-rift thermal subsidence (Figure 2.19c) and compared directly with the observed depth section at a more detailed scale (dots in Figure 2.19c). The preferred model of the second profile (Figure 2.20) has more extension on the bounding fault (14 km) and much less on the secondary fault (2.5 km) but the same value of Te (10 km) again gave the best fit (Kusznir et al. 1991).

## 2.11 Discussion: The Flexural Cantilever Model with Erosion and the Generation of the Breakup Megasequence Boundary.

In terms of modelling the breakup megasequence boundary, it is the footwall uplift that is of direct importance. However, it should be emphasised that this is a

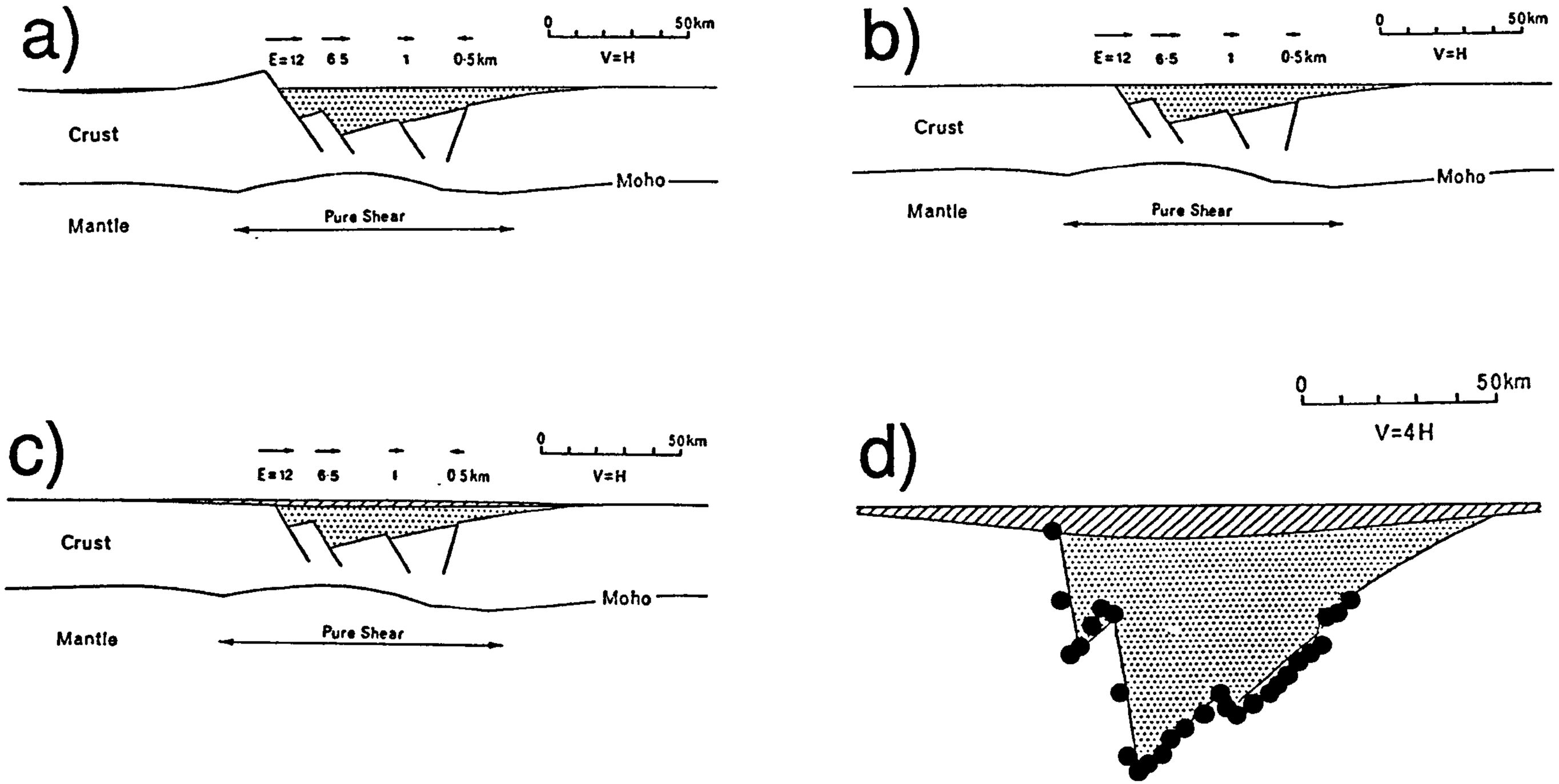


**Figure 2.19** Preferred flexural cantilever model for profile 1 (Kusznir et al., 1991). a) Before erosion. b) After erosion. c) After thermal subsidence (100 Ma). d) Comparison of model results (solid lines) with the observed depth section (dots).

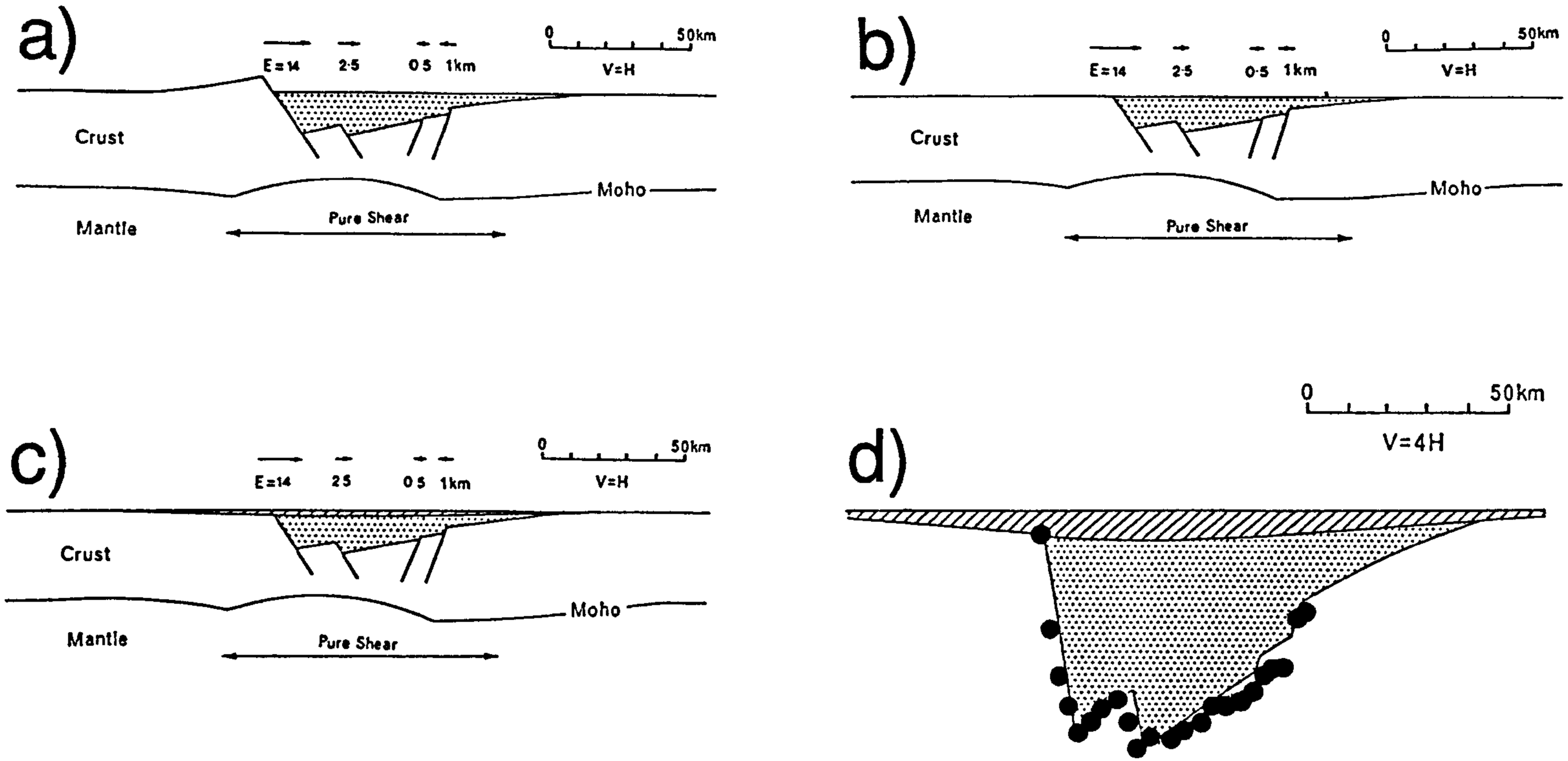


**Figure 2.20** Preferred flexural cantilever model for profile 2 (Kusznir et al., 1991). a) Before erosion. b) After erosion. c) After thermal subsidence (100 Ma). d) Comparison of model results (solid lines) with the observed depth section (dots).

localised effect (Figure 2.21a, b & c) and is inadequate to explain all of the features of the uplift, especially its regional nature, as described in Chapter 1. Extra mechanisms, which augment regional uplift, increase the lateral extent of erosion associated with breakup (Figure 2.21d, e & f). An erosional megasequence boundary across the entire region can be produced, but only by assuming that the basin is full at the end of the rift phase. This is relatively unlikely, especially in the sediment starved outer basins of passive margins.

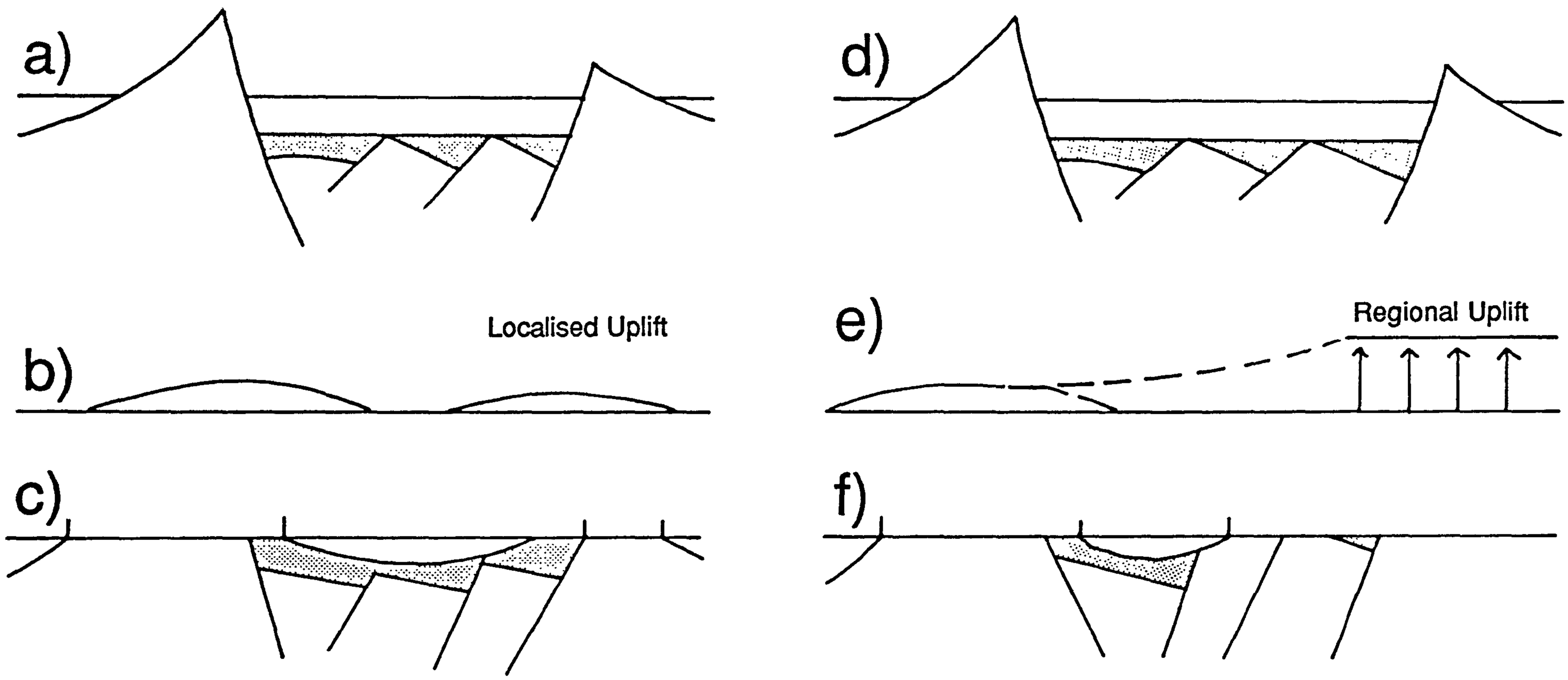


**Figure 2.21** a) and d) Hypothetical basin with flanking uplift and palaeo-bathymetry. b) The localised flexural isostatic effect of eroding footwall uplift. c) The unconformity resulting from b). e) Additional regional uplift added to the model. f) Closer approximation to the breakup unconformity.

# CHAPTER 3

# MELT GENERATION DUE TO EXTENSION OF THE LITHOSPHERE.

## 3.1 Introduction.

Using a combination of seismic reflection and refraction techniques, White et al. (1987) have shown that the Hatton Bank margin, off northwest Britain, is underlain by a wedge of anomalously high, lower crustal, seismic velocity. They interpret this high velocity zone as a thick layer of igneous rock which has underplated the continental crust. Some of the melt reached the surface and can be seen as seaward-dipping lava flows on seismic sections (Figure 3.1a). Figure 3.1b shows a NW-SE profile across the Hatton Bank, on which iso-velocity contours have been superimposed (White et al. 1987). The velocity structure is derived from synthetic-seismogram modelling of expanding-spread profiles (White et al. 1987). Deep seismic reflection studies across the Grand Banks margin (Figure 3.2) have identified landward dipping reflectors (marked L) which are interpreted as the upper and lower boundaries of a magmatic underplating wedge (Keen & DeVoogd, 1988).

The observations, described above, form the basis of a growing consensus that basaltic melt is produced during the rift phase, due to the adiabatic decompression of upwelling asthenosphere and that this melt underplates the continental crust (White and McKenzie, 1990; White et al. 1987; Keen & deVoogd, 1988). However, it is not yet clear how much additional melt underplates the margin as a result of lateral accretion during the initial stages of organised sea-floor spreading.

a)

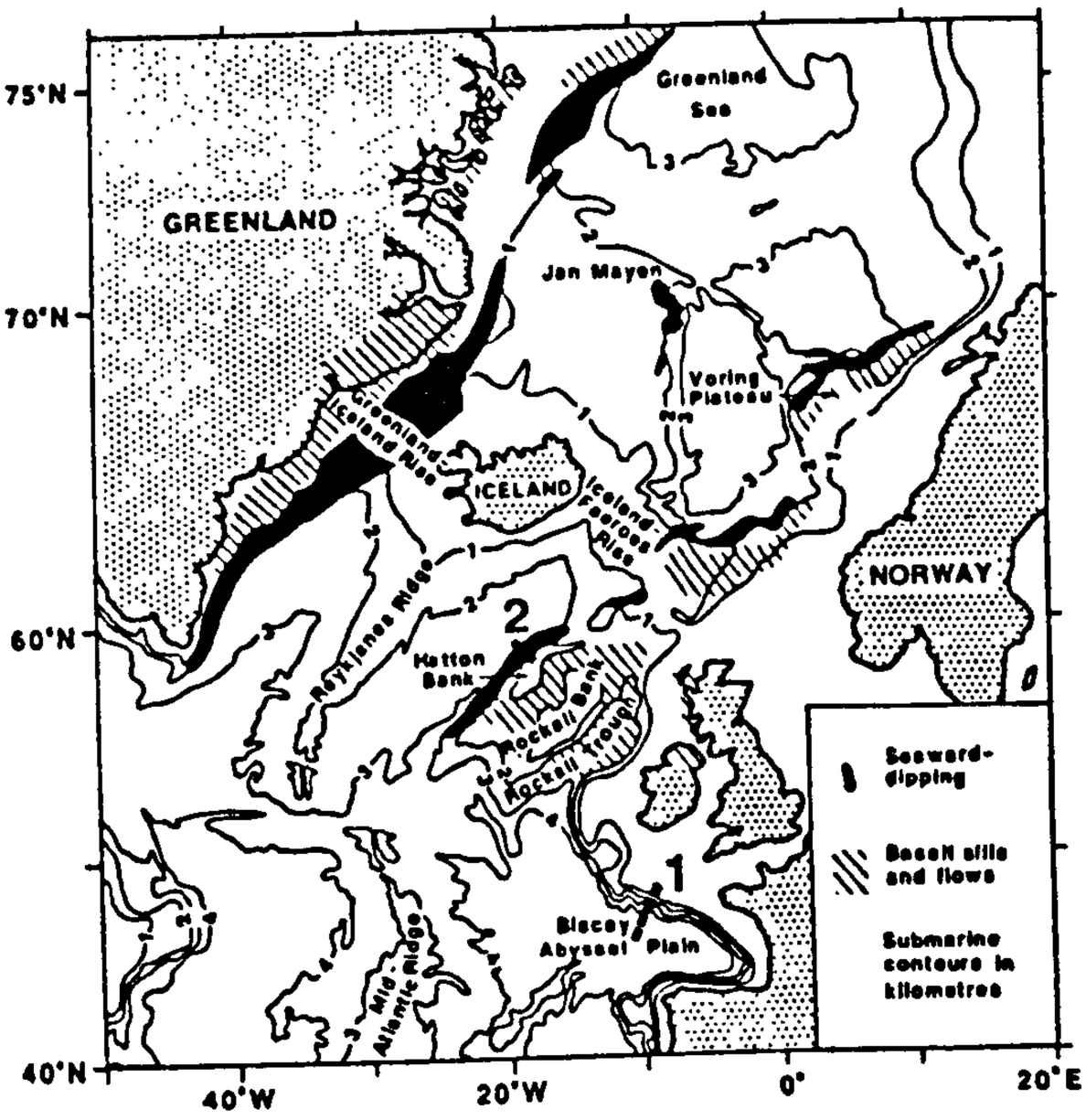


b)

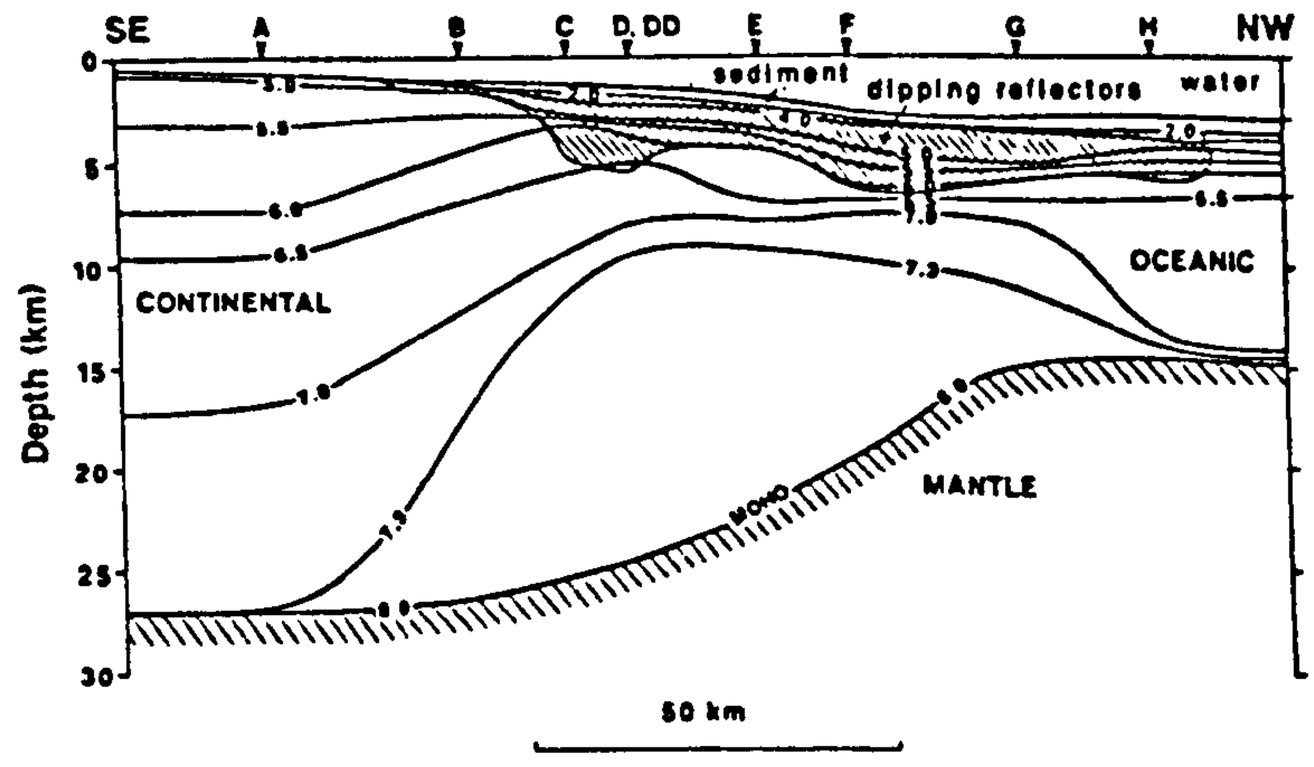


**Figure 3.1** Magmatic underplating at the NW European passive margin in the vicinity of the Hatton Bank. a) Location map - note the location of line 2. b) Iso-velocity contours on the continental crust beneath the Hatton Bank margin (line 2) showing a high velocity zone expanding southeastwards from the C.O.B. (White et al., 1987).

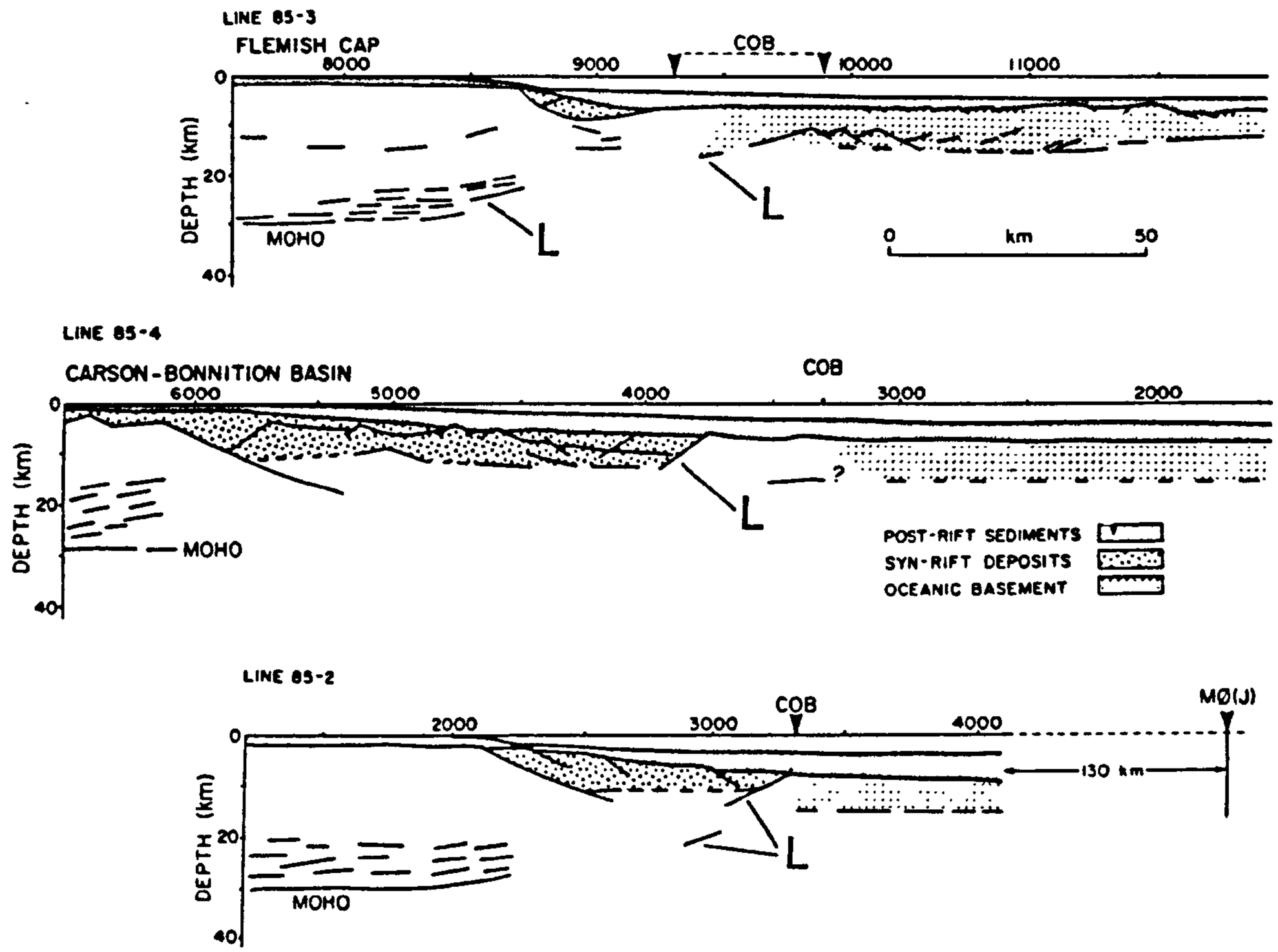


**Figure 3.2** Magmatic underplating wedges imaged on the Lithoprobe deep seismic profiles across the Grand Banks margin (Keen & de Voogd, 1988). L = Landward dipping reflectors, above and below the underplating wedge.

In this chapter, the genesis of partially molten rock during lithosphere extension, and the subsequent extraction of melt, will be quantified using the theoretical models of McKenzie (1984) and McKenzie & Bickle (1988). The extraction of melt requires it to move relative to the matrix and McKenzie (1984) has set out the governing equations for this mechanism, based on the assumptions of conservation of mass, momentum and energy for two phase flow.

## 3.2 The McKenzie-Bickle Model for Melt Generation by the Extension of the Lithosphere.

The underlying principles behind the McKenzie-Bickle model are relatively simple and the basic concepts have been outlined by earlier workers e.g. Foucher et al., 1982. A continental geotherm is superimposed on a solidus and liquidus for mantle peridotite. Where the geotherm temperature exceeds the solidus temperature, a partial melt is generated whose melt fraction depends on the temperature and pressure. Figure 3.3 shows that there are three circumstances in which these conditions are met:-

a) Extension of the lithosphere brings the normal temperature of upwelling asthenosphere above the solidus at shallow depths.

b) Elevation of asthenosphere temperature by mantle plume convection cells take the geotherm over the solidus.

c) Volatiles such as water and $CO_2$ lower the temperature of the solidus for mantle peridotite while the geotherm remains unchanged.

Partial melt production during extension leading to lithosphere rupture and

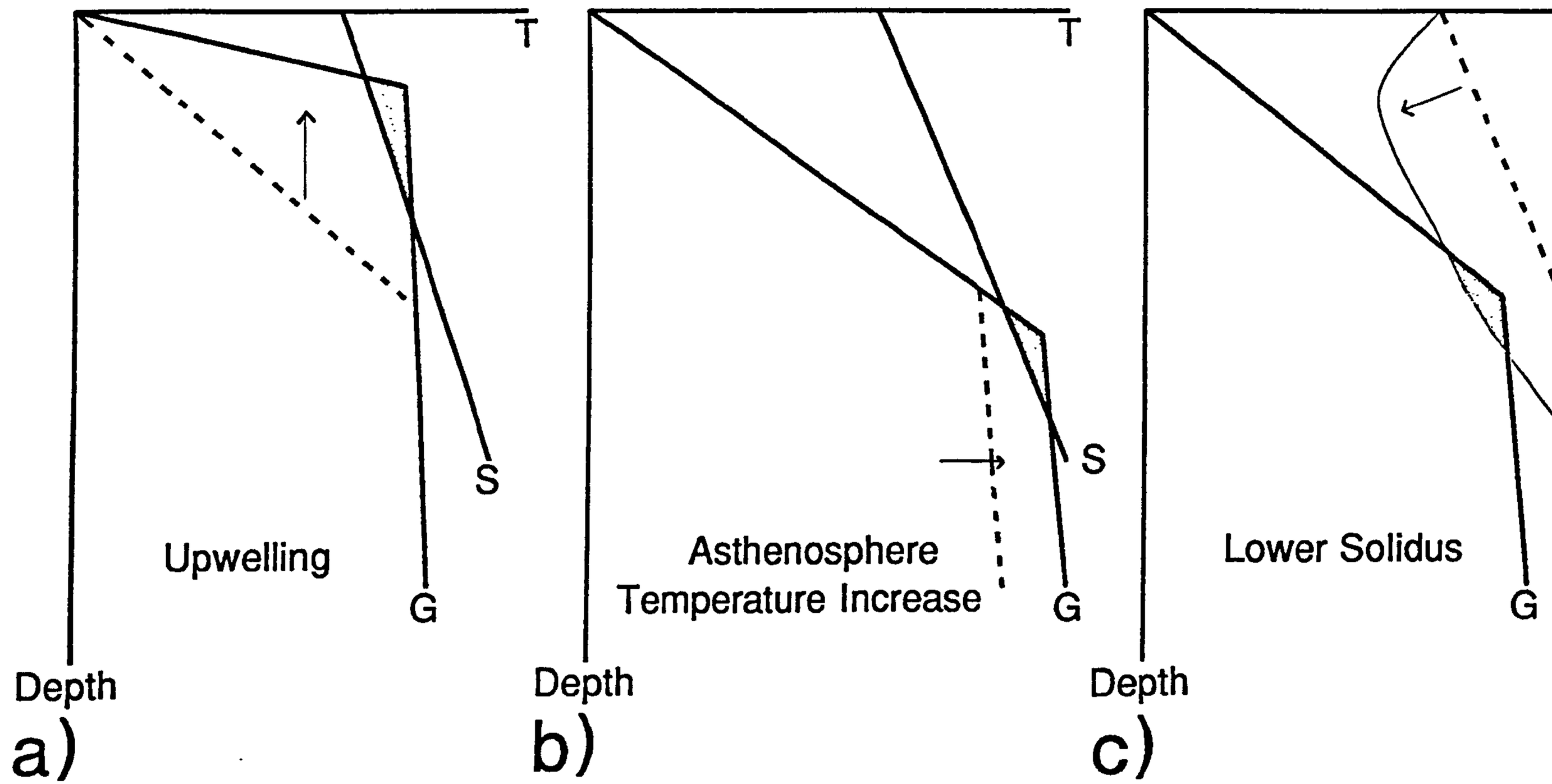


**Figure 3.3** Schematic representations of the three possible mechanisms for melt generation :- a) Upwelling and pressure release allowing the geotherm to intersect the solidus at lower temperatures. b) An increase in the asthenosphere temperature due to hot spot activity. c) Lowering solidus temperatures by the introduction of volatile elements into the system. (After Latin, 1990).

seafloor spreading is dominantly controlled by the first mechanism at normal asthenosphere temperatures. The underlying cause for the variation in asthenosphere temperature variation is considered towards the end of the chapter since it links well with Chapter 4 where hot-spot activity is described in detail.

The McKenzie - Bickle model provides mathematical formulations for the geotherm, solidus and liquidus and the paramaterisation of the melt fraction. A geotherm is constructed, using both conductive and convective considerations, and is shown to be critically controlled by the lithosphere / asthenosphere structure. The solidus and liquidus for mantle peridotite, and the parameterisation of the melt fraction between them, are derived empirically from experimental results.

Because the Bickle-McKenzie model is concerned with the adiabatic upwelling of a compressible material, differences in temperature are not simply proportional to differences in original heat content. As mantle rises it decompresses and loses temperature to maintain entropy, even though none of the original heat is lost (the Peclet number for the system is large and conduction can be neglected, Bickle & McKenzie, 1988). This situation is analogous to the rapid expansion, and cooling, of gas in a cylinder as a piston is withdrawn (Figure 3.4). By defining a "potential temperature", Tp, which is the temperature that the asthenosphere would have at the surface (i.e. at a reference pressure of 0 GPa) the original heat content can be compared directly. The equation which relates potential temperature $T_p$ to real temperature $T$, as given by McKenzie & Bickle (1988) is:-

$$T_p = T \exp\left(-\frac{g\alpha z}{C_p}\right) \qquad (3.1)$$

where $\alpha$ is the coefficient of thermal expansion and z is the depth. The potential

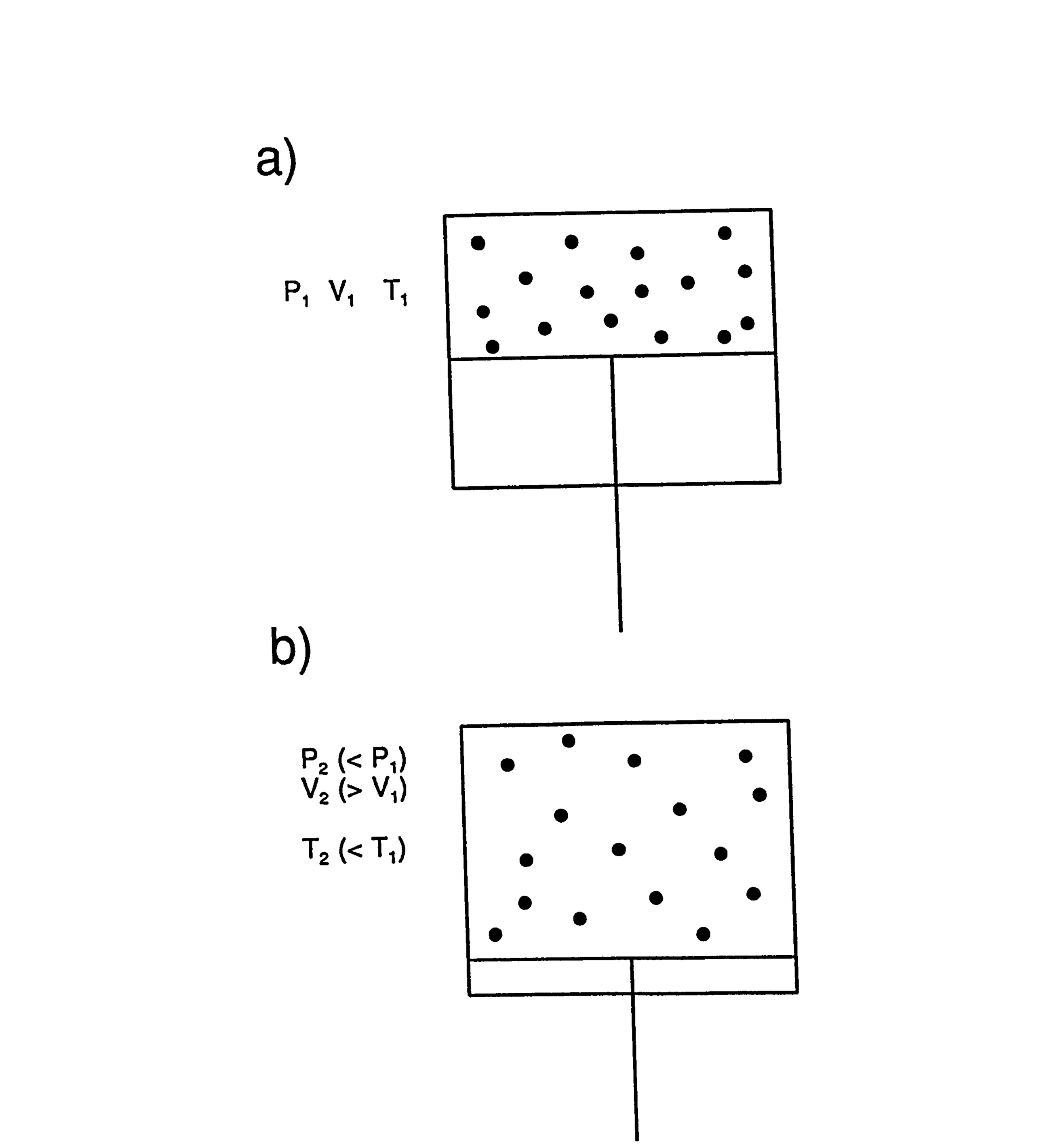


**Figure 3.4** Schematic representation of adiabatic decompression, by analogy to the rapid expansion, and cooling, of gas in a cylinder as the piston is withdrawn.

temperature is unchanged by adiabatic upwelling. By applying Equation 3.1 a real temperature of 1333 °C at 125 km depth corresponds to a potential temperature of 1280° C.

Table 3.1 lists all of the thermodynamic parameters and notation used in this chapter, together with their dimensions, from McKenzie (1984). If not otherwise stated, all other parameters have S.I. units.

| Parameter | Meaning | Value | Dimensions |
|---|---|---|---|
| $C_p$ | Specific heat at constant pressure | $10^3$ | J $kg^{-1}$ $K^{-1}$ |
| g | Acceleration due to gravity | 9.81 | m $s^{-2}$ |
| k | Thermal conductivity | 3.11 | W $m^{-1}$ $K^{-1}$ |
| $\kappa$ | Thermal diffusivity | $10^{-6}$ | $m^2$ $s^{-1}$ |
| $\Delta S$ | Entropy change on melting | 250 | J $kg^{-1}$ $K^{-1}$ |
| $\Delta V$ | Volume change on melting | 4.34 E-5 | $m^3$ $kg^{-1}$ |
| $\alpha_f$ | Thermal expansion coefficient of melt | 6.8 E-5 | $K^{-1}$ |
| $\alpha_s$ | " " of matrix | 4.0 E-5 | $K^{-1}$ |
| $\rho_f$ | density of melt | 2.8 E+3 | kg $m^{-3}$ |
| $\rho_s$ | density of matrix | 3.3 E+3 | " |
| $\upsilon$ | Mantle viscosity | 4.0 E+15 | Pa s |

Table 3.1

## 3.3 Lithosphere - Asthenosphere Structure Assumed by the Bickle-McKenzie Melt Generation Model.

Unlike the flexural cantilever model, in which the definition of the lithosphere conforms to the thermal model of Parsons & Sclater (1977), the McKenzie-Bickle model provides no unique definition of the lithosphere. Instead, the continental crust and upper mantle are divided into three layers (Figure 3.5):-

1) An upper mechanical boundary layer, dominated by conductive heat transfer.

2) A thermal boundary layer which is usually dominated by conduction, but which is periodically replaced by hotter, convecting mantle.

3) An adiabatic interior, dominated by vigorous convection.

The great advantage of this system is that it provides, in the thermal boundary layer, a smooth transition from the inner convective layer to the outer conductive part. Convection, within the thermal boundary layer, also explains Parsons & Sclater's observation that the horizontal 1333 °C isotherm, for oceanic lithosphere, does not continue to deepen away from a spreading ridge. Latin (1990) has noted that the Bickle-McKenzie model retains a substantive link with the plate model because the assumption of a real temperature of 1333.4 °C at a depth of 125 km is used to determine the value for normal potential temperature (1280 °C). This link is retained in this thesis (see section 3.4).

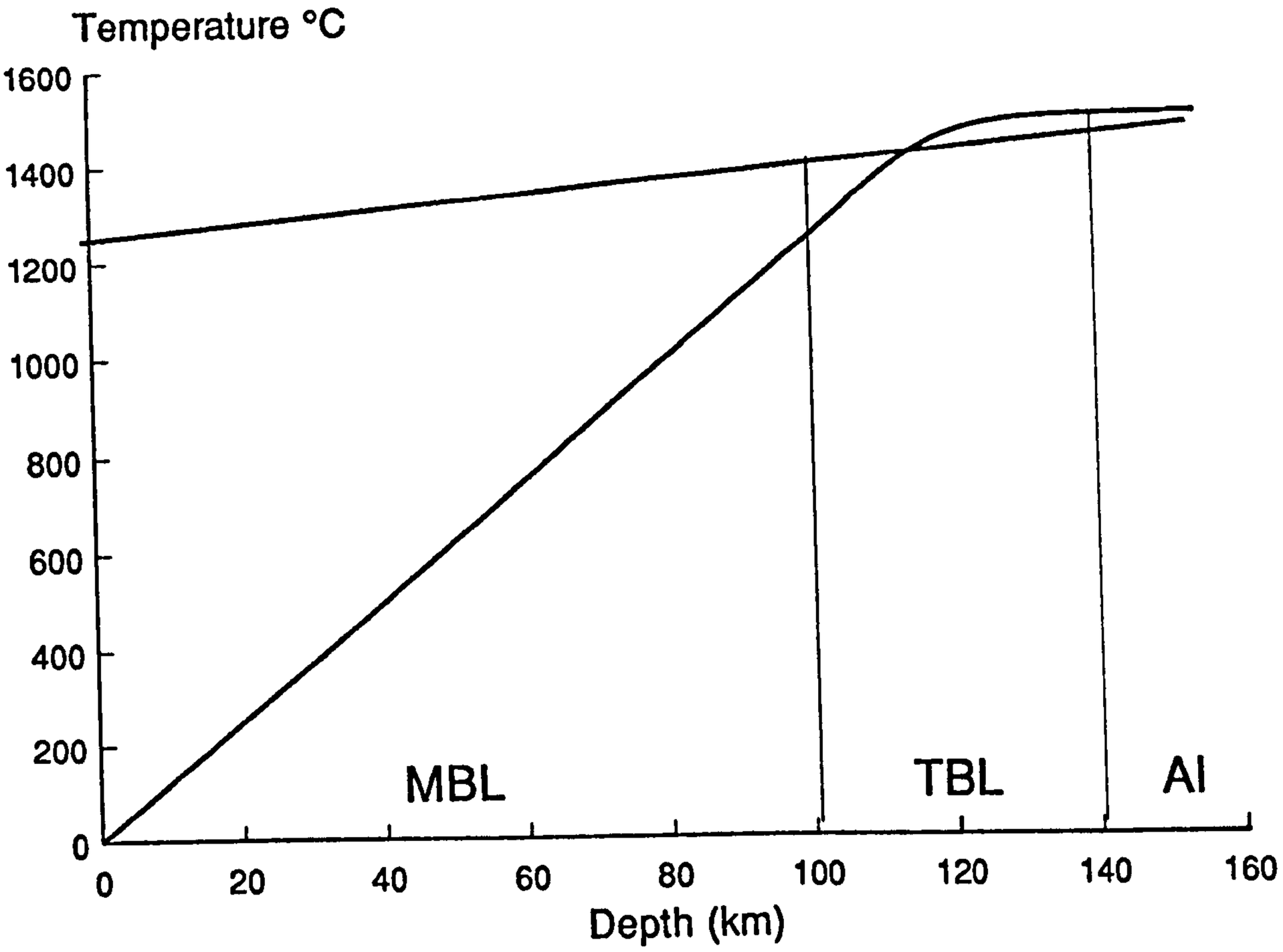


**Figure 3.5** The Lithosphere - Asthenosphere structure used in the McKenzie-Bickle model. MBL = Mechanical boundary layer - conductive, TBL = Thermal boundary layer - poorly convective, AI = Adiabatic interior.

## 3.4 The Geotherm.

The upper two boundary layers, as defined in section 3.3, control the geotherm used in the McKenzie-Bickle model. The equation for the temperature increase, $\Delta T(z)$, from the base of the mechanical boundary layer (Figure 3.6) includes a Rayleigh number term, $Ra_F$, for the convective heat flow within the thermal boundary layer and adiabatic interior:-

$$\Delta T=\left(\frac{Fd}{k}\right)Ra_F^{-0.219}\left(1.84+e^{-\bar{z}}\sum_{n=0}^{4}a_n\bar{z}^n\right) \qquad (3.2)$$

with

$a_0 = -1.84$ $\quad a_1 = -1.18$

$a_2 = -0.22$ $\quad a_3 = 0.1$

$a_4 = 0.01$

Where:-

$$Ra_F=\frac{g\alpha d^4 F}{k\kappa\upsilon} \qquad (3.3)$$

and

$$\bar{z}=1.45\,Ra_F^{0.219}\left(\frac{z}{d}\right) \qquad (3.4)$$

The depth, z, used to defined $\bar{z}$, the appropriate stretched variable for the convective cell (Richter & McKenzie, 1981), is measured from the base of the mechanical boundary layer and d is the depth of the convecting layer (700 km, McKenzie & Bickle, 1988).

Equation 3.2 is solved by assuming that the conductive heat flux, F, through

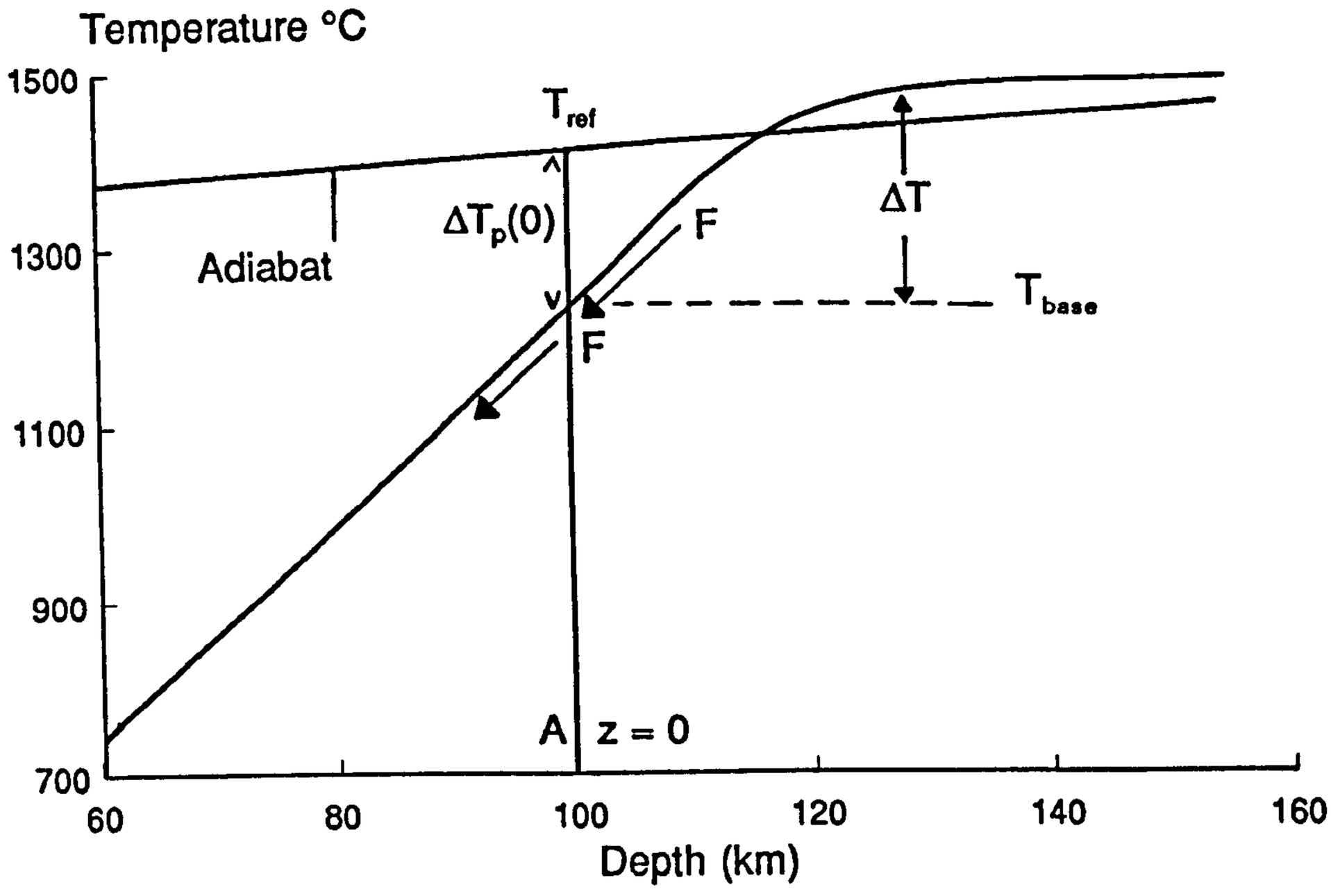


**Figure 3.6** Schematic representation of the heat flow balance at the MBL - TBL interface, used to solve Equation 3.6 and derive the geotherm. (F = Heat Flux, $T_{ref}$ = Adiabatic temperature at the base of the MBL, $\Delta T$ = Increase in real temperature from the base of the MBL.

the mechanical boundary layer is matched by the convective heat flux at the top of the thermal boundary layer. Figure 3.6 shows a diagrammatic representation of this heat flow balance. The heat flux F through the mechanical boundary layer is given by:-

$$F = \frac{T_{base} \cdot k}{A} = \frac{(T_{ref} - \Delta T_p(0)) \cdot k}{A} \qquad (3.5)$$

where A is the depth to the base of the mechanical boundary layer, $T_{base}$ is the real temperature at A and $T_{ref}$ is the temperature on the adiabat at A. The same value of heat flux, F, is substituted into Equation 3.2 for $\Delta T$ at the top of the thermal boundary layer (z = 0), which then becomes:-

$$\Delta T_p(0) = \frac{\left(\frac{(T_{ref} - \Delta T_p(0)) \cdot k}{A}\right) \cdot d}{k} Ra_F^{-0.219} \times 1.84 \qquad (3.6)$$

Numerical iteration can then be used to solve Equation 3.6 for $\Delta T(0)$ and Equation 3.5 then gives the heat flux F. When F is known, the increase in potential temperature from the base of the mechanical boundary layer, $\Delta T_p(z)$, can be calculated (using Equation 3.2). Potential temperature is converted to the real temperature using:-

$$\Delta T(z) = \Delta T_p(z) \exp\left(\frac{g\alpha z}{C_p}\right) \qquad (3.7)$$

where z is now measured from the surface. Any temperature on the geotherm, below the base of the mechanical boundary layer, is then given by :-

$$T(z) = T_{base} + \Delta T(z) \qquad (3.8)$$

The remainder of the geotherm is purely conductive and depends on the thickness of the mechanical boundary layer (and thus also on the Beta stretching factor). Figure 3.7 shows four geotherms, and the relationship of two of them to the adiabatic gradient, for potential temperatures between 1280 and 1580 °C.

The shape of the geotherm within the thermal boundary layer is controlled by viscosity (through the $\upsilon$ term in Equation 3.3). At relatively low viscosities (Figure 3.8a) the transition from conduction to convection is sharply defined, but takes place over a progressively wider zone as the viscosity is increased (Figure 3.8b). The thickness of the mechanical boundary later can also be varied and is assumed to be thicker under ancient cratonic interiors. An M.B.L. thickness of 100 km and a viscosity of $4 \times 10^{15}$ PaS are used throughout this thesis.

## 3.5 The Solidus and Liquidus for Mantle Peridotite.

As a result of the thermodynamic complexity of the multi-phase multi-component mantle system, McKenzie and Bickle (1988) prefer a simple, empirical approach to provide a quantitative theory of melting. Analytical expressions for the solidus and liquidus are obtained by plotting the experimental results of several authors in T-P space (Figure 3.9). Data which constrains the position of the solidus includes the pressure (GPa), the highest temperature at which no melt is present and the lowest temperature at which melt is present. By a least squares minimisation of the magnitude of the difference between the observed temperature and the temperature calculated from the mathematical expression, $|T_{obs}-T_{calc}|$, the following expression has

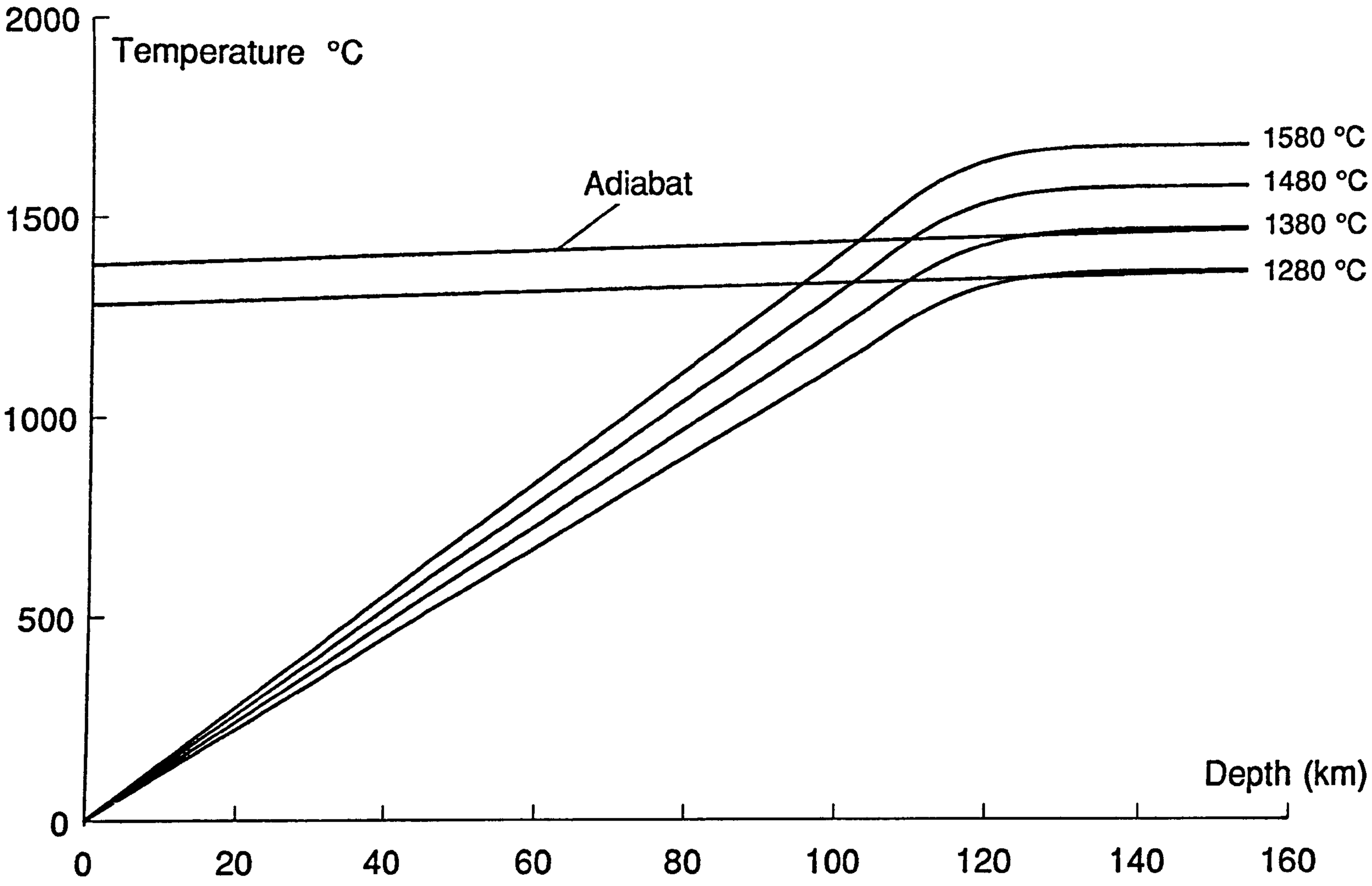


**Figure 3.7** Geotherms for Potential Temperatures ranging between 1280 °C and 1580 °C calculated with respect to an adiabatic temperature gradient which does not take account of heat loss due to partial melting.

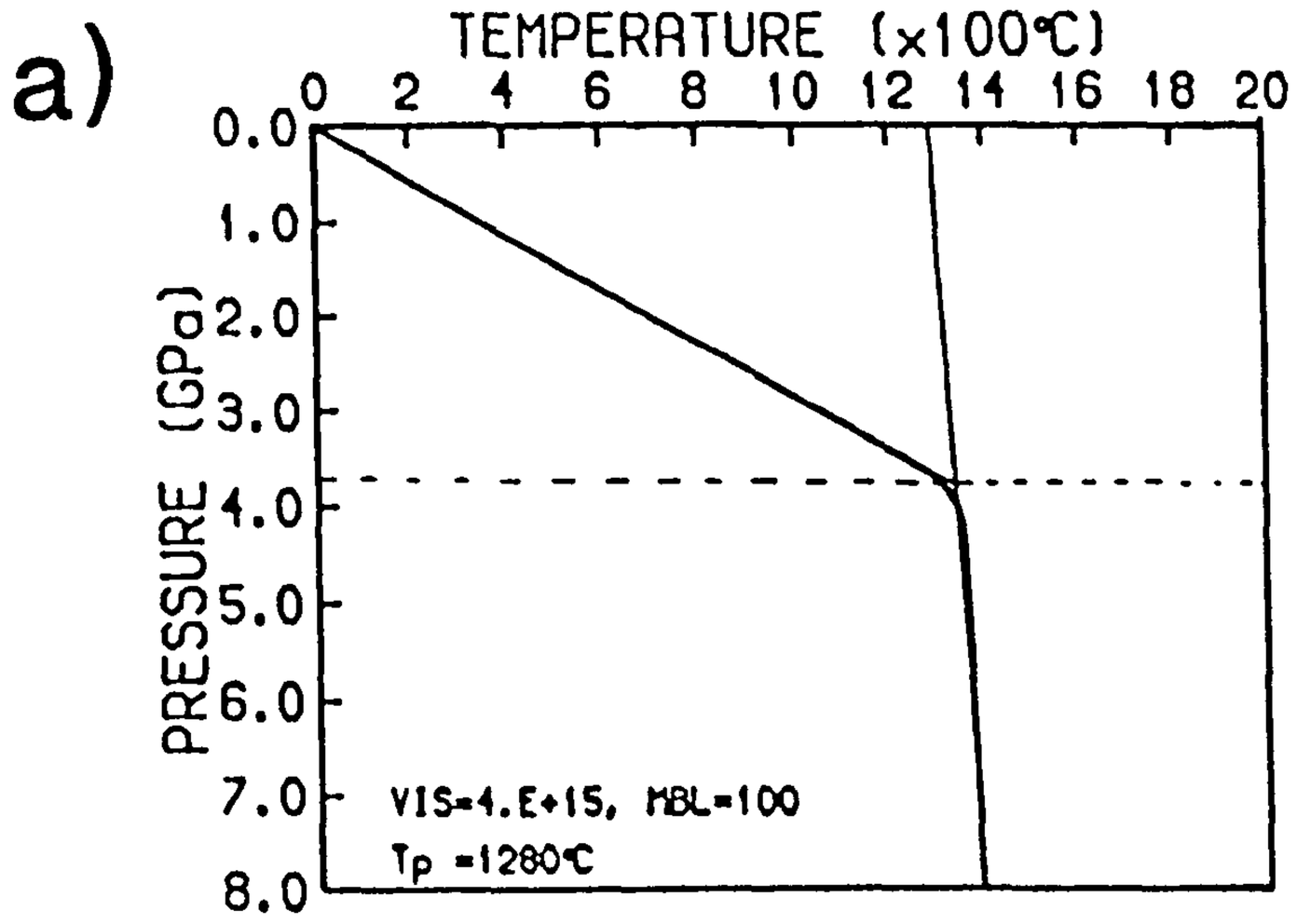


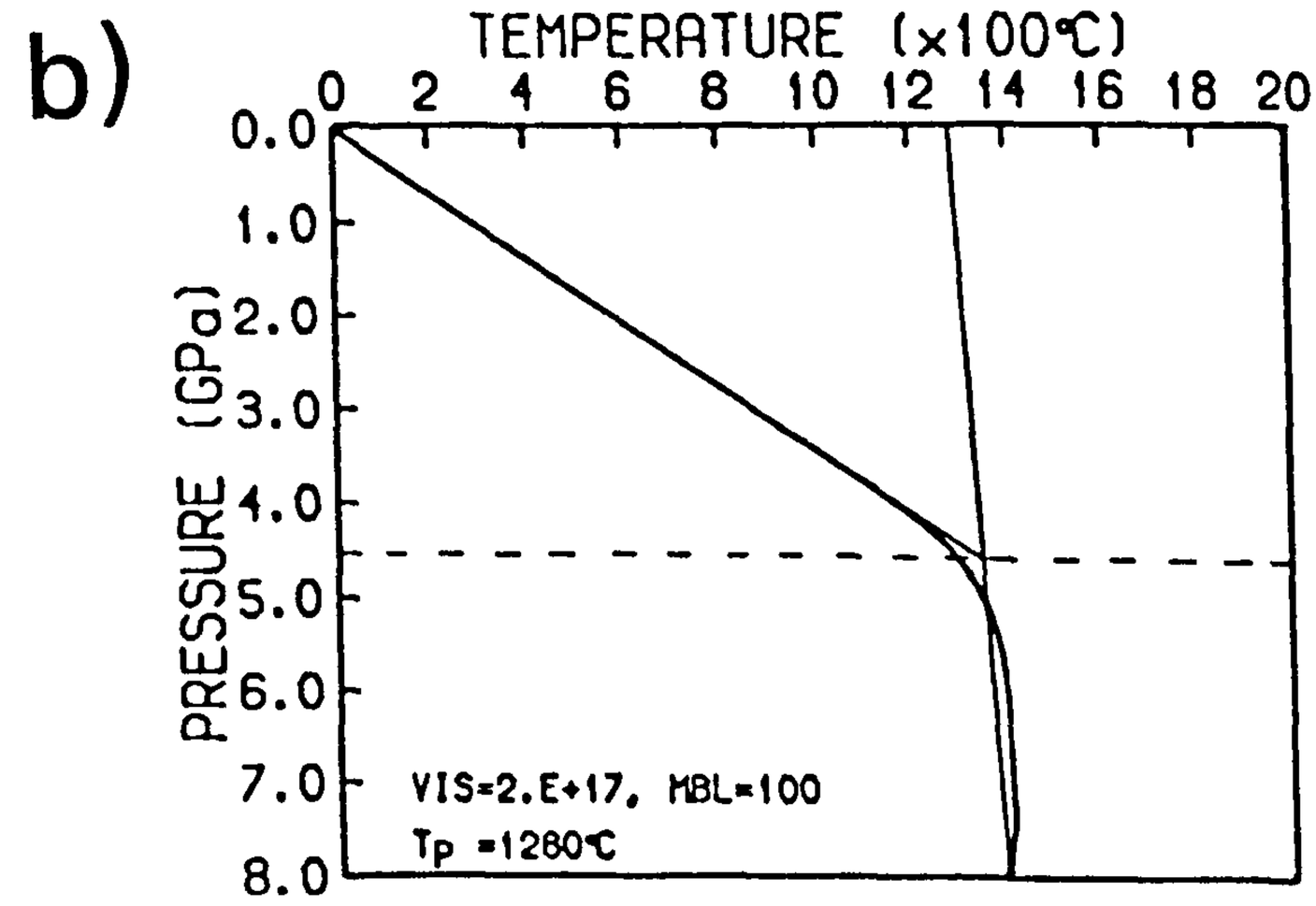


**Figure 3.8** Two conductive-convective geotherms showing the effect of varying the viscosity of the TBL and adiabatic interior:- a) Viscosity = $4 \times 10^{15}$ $m^2s^{-1}$. b) Viscosity = $2 \times 10^{17}$ $m^2s^{-1}$. (From Latin, 1990)

been determined:-

$$P=(T_s-1100)/136+4.968\times10^{-4}\exp(1.2\times10^{-2}(T_s-1100)) \quad (3.9)$$

Note that numerical iteration must be used to obtain solidus temperature, T, in °C, as a function of pressure, P in GPa.

Figure 3.9 shows that the liquidus is poorly constrained by seven points (McKenzie & Bickle, 1988) and only three complete data sets, Viz. - pressure (GPa), maximum temperature at which melting was incomplete and the minimum temperature at which melting was complete. Again. by minimising $|T_{obs}-T_{calc}|$, Bickle & McKenzie (1988) determined the following expression for liquidus temperature, $T_l$ in °C, as a function of pressure P in Gpa:-

$$T_l=1736.2+4.343P+180\tan^{-1}(P/2.2169) \quad (3.10)$$

It can be shown that the lack of data constraining the liquidus is relatively unimportant since it is the position of the solidus, and low melt fractions above it, that primarily controls magma generation at normal and slightly elevated potential temperatures.

## 3.6 Paramaterisation of the Melt Fraction Between Solidus and Liquidus.

McKenzie & Bickle (1988) have shown that the parameterisation of the melt fraction as a function of temperature and pressure, X(T,P), is facilitated by first defining a dimensionless temperature, T´ between the solidus and liquidus. Using Equation 3.11 the solidus temperature is normalised to T´ = -0.5 and the liquidus temperature becomes T´ = 0.5 :-

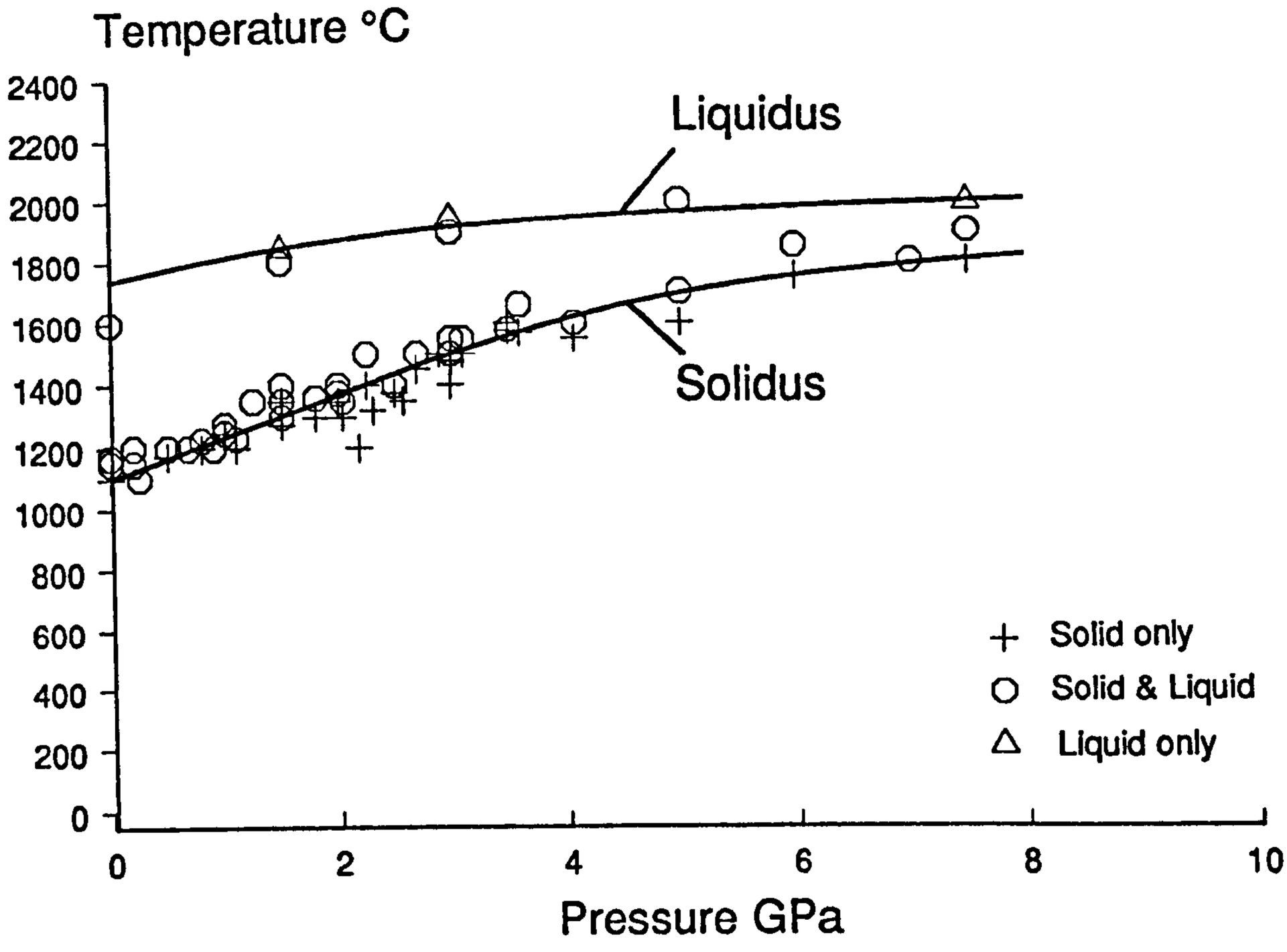


**Figure 3.9** The solidus and liquidus for mantle peridotite derived by curve-fitting experimental results and minimising $|T_{obs} - T_{calc}|$ (Redrawn from McKenzie & Bickle, 1988).

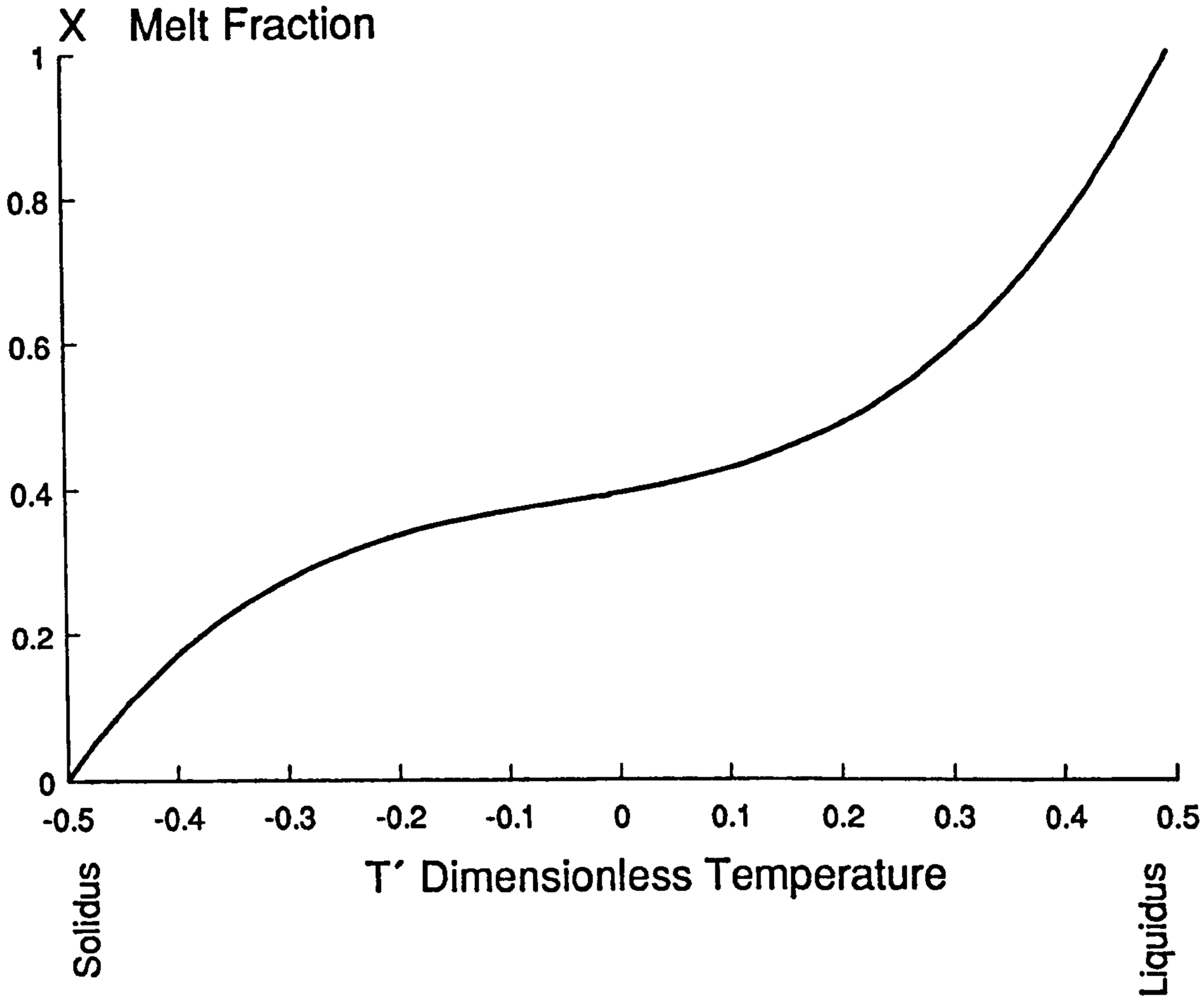


**Figure 3.10** Parameterisation of the melt fraction (X) between the solidus and liquidus by plotting X against a dimensionless temperature T′. (See text for the definition of the dimensionless temperature).

$$T' = \frac{(T - (T_s + T_l)/2)}{T_l - T_s} \qquad (3.11)$$

Knowing that the numerical expression for X(T´) must pass through (-0.5,0), at the solidus, and (0.5,1) at the liquidus, a polynomial has been fitted to experimental results by minimizing $|X_{calc.}-X_{obs.}|$. From the data available to McKenzie & Bickle (1988) the following expression has been obtained:-

$$X - 0.5 = T' + (T'^2 - 0.25)(a_0 + a_1 T'^2 + a_2 T'^2 .....) \qquad (3.12)$$

where

$$a_0 = 0.4256 \quad a_1 = 2.9880$$

Figure 3.10 shows the result of plotting the melt fraction, X, against dimensionless temperature, T´.

Since a single expression fits the normalised data, McKenzie & Bickle concluded that the only control that pressure has on the melt fraction, X(T,P), is through the variation of solidus and liquidus temperatures (which are used to calculate T´). However, recent studies by Takahasi (pers com., 1992), using improved experimental techniques, have shown that partial melting between solidus and liquidus is in fact strongly pressure dependent. The low pressure McKenzie & Bickle parameterisation is still adopted throughout this thesis and the implications of the Takahasi result are further discussed in section 3.10.

## 3.7 Heat Loss Due to Partial Melting.

Probably the most important attribute of the McKenzie-Bickle model, and the factor which most distinguishes it from its precursors, is the correction made for heat

lost due to partial melting above the solidus i.e. the latent heat of fusion of the mantle material. Figure 3.11 shows the adiabatic temperature gradients for various potential temperatures after this correction.

McKenzie (1984, Appendix D) starts with the assumption of constant entropy during adiabatic upwelling.

$$dS=\left(\frac{\partial S}{\partial X}\right)_{P,T}dX+\left(\frac{\partial S}{\partial T}\right)_{X,P}dT+\left(\frac{\partial S}{\partial P}\right)_{X,T}dP=0 \qquad (3.13)$$

Where X is the melt fraction by weight of the partial melt. According to McKenzie (1984), Equation 3.13 can be converted to the following by using Maxwell's relationships and other thermodynamic identities :-

$$\Delta S\,dX+\left[(1-x)\,C_p^s+XC_p^f\right]\frac{dT}{T}-\left[\frac{\alpha_s}{\rho_s}+\left(\frac{\alpha_f}{\rho_f}-\frac{\alpha_s}{\rho_s}\right)X\right]dP=0 \qquad (3.14)$$

Which (if $C^f_p = C^s_p$) can be rearranged to give :-

$$\frac{dX}{dP}=\frac{-\frac{C_p}{T}\left(\frac{\partial T}{\partial P}\right)_X+\frac{\alpha_s}{\rho_s}+\left(\frac{\alpha_f}{\rho_f}-\frac{\alpha_s}{\rho_s}\right)X}{\Delta S+\frac{C_p}{T}\left(\frac{\partial T}{\partial X}\right)_P} \qquad (3.15)$$

When the geotherm crosses the solidus, into the zone of partial melting, Equation 3.15 is integrated using a fourth order Runge-Kutta method. It is very important to note that the partial derivatives ($\delta T/\delta P$) and ($\delta T/\delta X$) should *not* be obtained by differentiating the simple linear relationship between T, X and P within the solidus - Equation D8 of McKenzie (1984). Instead, they are derived by the partial differentiation of the equations for solidus, liquidus and melt fraction:-

By rearranging Equation 3.11, the following expression for T can be

a)

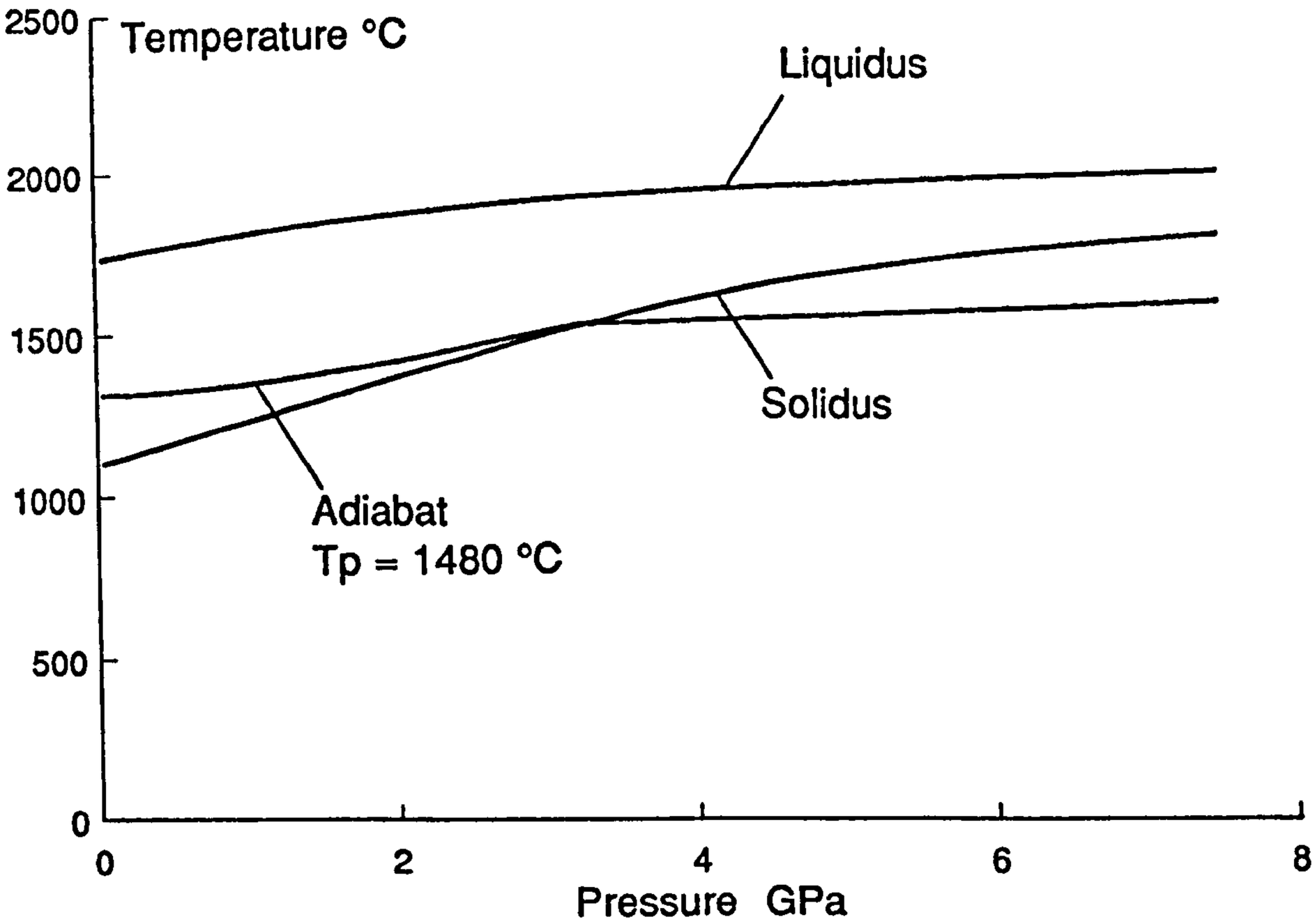


b)

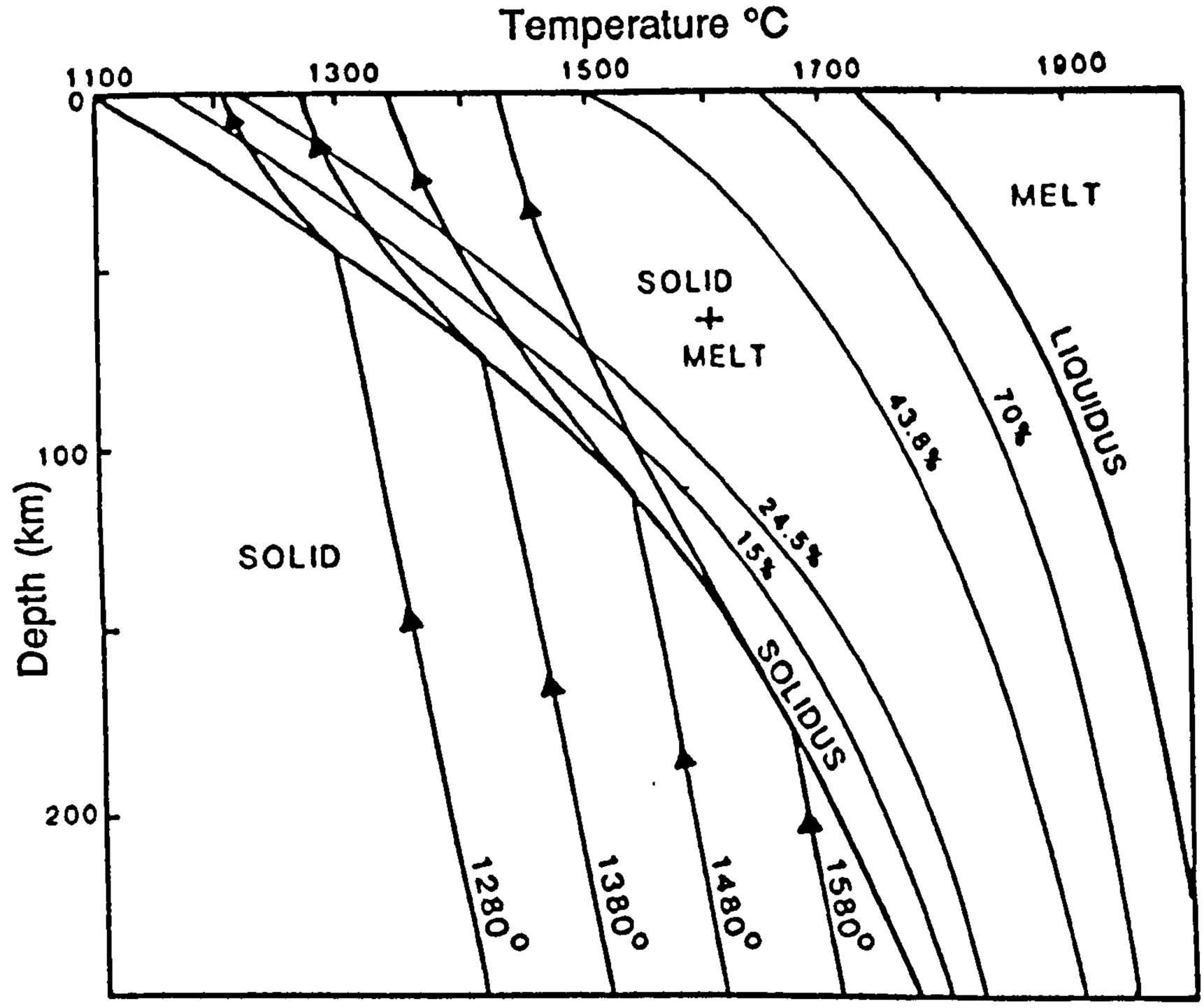


**Figure 3.11** Curved adiabatic temperature gradients within the solidus. a) For a single potential temperature (1480 °C) and plotted against pressure. b) Adiabatic gradients for a range of potential temperatures plotted against depth (From Bickle & McKenzie, 1988). Beta = ∞ in all cases

obtained:-

$$T = T' . (T_L - T_S) + \frac{(T_S + T_L)}{2} \quad (3.16)$$

which, after partial differentiation gives:-

$$\frac{\partial T}{\partial T'} = T_L - T_S \quad (3.17)$$

Partial differentiation (by products) of Equation 3.12 yields:-

$$\frac{\partial X}{\partial T'} = 1 + (T'^2 - 0.25) . (a_1 + 2a_2 T') + (2T') . (a_0 + a_1 T' + a_2 T'^2) \quad (3.18)$$

and since

$$\frac{\partial X}{\partial T} = \frac{\partial X}{\partial T'} . \frac{\partial T'}{\partial T} \quad (3.19)$$

then:-

$$\frac{\partial X}{\partial T} = \left[1 + (T'^2 - 0.25) . (a_1 + 2a_2 T') + (2T') . (a_0 + a_1 T' + a_2 T'^2)\right] . \frac{1}{(T_L - T_S)} \quad (3.20)$$

and the reciprocal can be taken.

The partial derivative $\delta T/\delta P$ in the McKenzie-Bickle (1988) computer model is derived from the pressure equivalent of Equation 3.19:-

$$\frac{\partial P}{\partial T} = \frac{\partial P}{\partial T'} . \frac{\partial T'}{\partial T} \quad (3.21)$$

The partial differential $\delta T'/\delta T$ is given by the reciprocal of Equation 3.17 and $\delta P/\delta T'$ is obtained from the reciprocal of the partial differential of Equation 3.11 with respect to pressure, i.e:-

The partial differentials of $T_L$ and $T_s$, with respect to pressure, are obtained directly

$$\frac{\partial T'}{\partial P} = \frac{\partial}{\partial P}\left(\frac{(T-(T_s+T_l)/2)}{T_l-T_s}\right) \tag{3.22}$$

from Equations 3.9 and 3.10:-

$$\frac{\partial P}{\partial T} = 1/136 + 4.968\times1.2\times10^{-2}.\ EXP(1.2\times10^{-2}.(T_S-1100)) \tag{3.23}$$

$$\frac{\partial T_S}{\partial P} = 1/(\partial P/\partial T) \tag{3.24}$$

and:-

$$\frac{\partial T_L}{\partial P} = 4.343 + (180/2.2169)/(1.+(P/2.2169)^2) \tag{3.25}$$

## 3.8 Superimposition of the Geotherm on the Solidus and Liquidus.

At each step down in pressure the melt fraction X is calculated, and, since the solidus and liquidus temperatures are known, the temperature of the partially molten rock can be derived by the iterative solution of Equation 3.15. Thus, in a rather complex formulation, the geotherm temperature is lowered, to take account of the heat loss due to partial melting, with reference to the iterative intersection of an adiabatic P-T gradient with the solidus. Figure 3.12 shows the perturbed geotherms for various Beta factors (increasing from 1 to 5) and Tp = 1480 °C. It can be seen that in an area corresponding to temperatures above the solidus the iterative solution of the equation in section 3.7 do not give a "smooth" result. This is largely a function of the size of the pressure step used in the computer program, whereby a smaller step produces a smoother curve but takes unreasonable amounts of time in

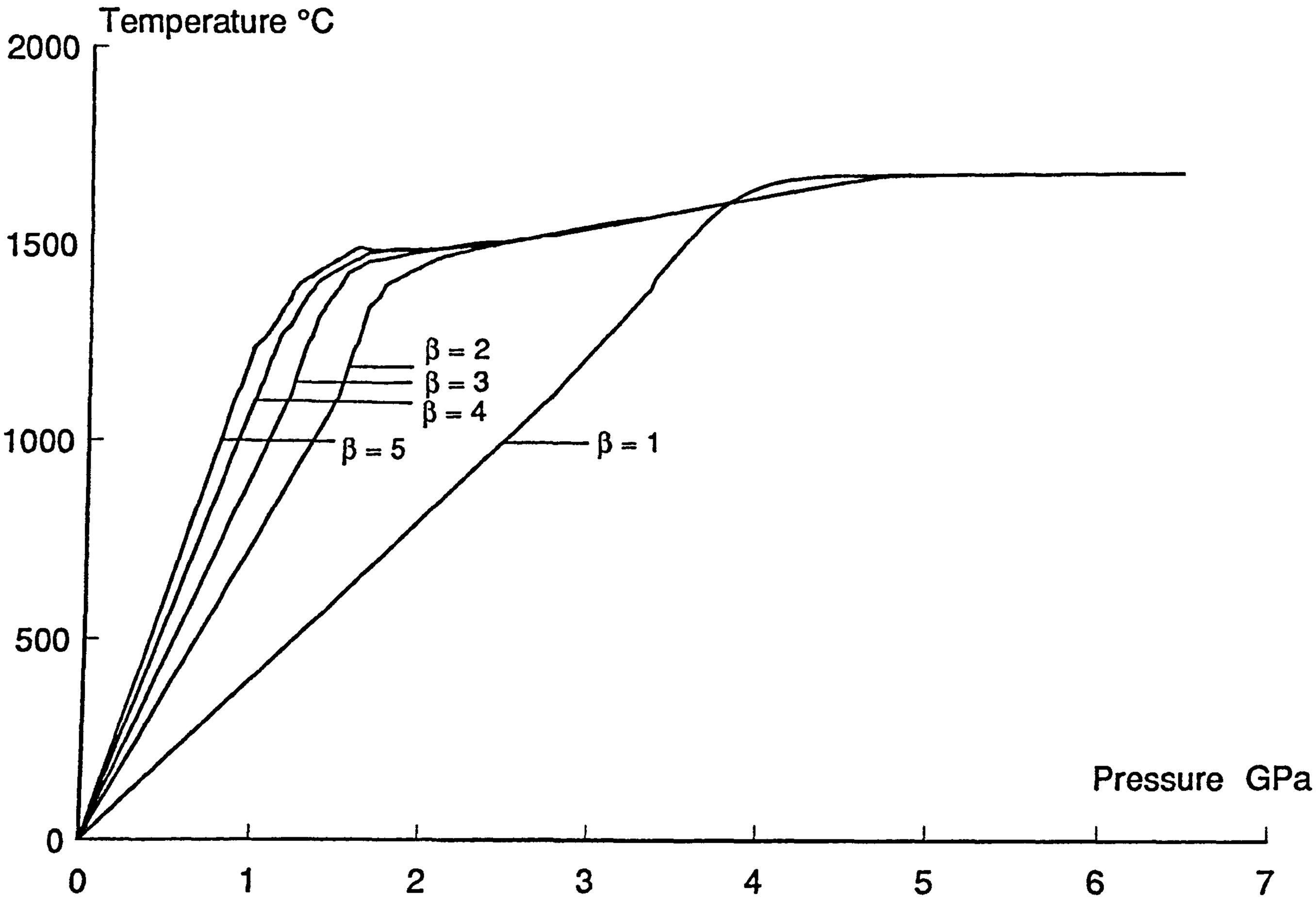


**Figure 3.12** Perturbed geotherms for Beta factors between 1 and 5, corrected for heat loss due to partial melting. (N.B. the incremental pressure step - 0.03 GPa - causes some instability in the solution for the geotherm above the solidus).

later applications.

The melt fraction, by weight, is then converted to the volume melt fraction $\phi$ using:-

$$\phi = \frac{X\rho_s}{\rho_f + X(\rho_s - \rho_f)} \tag{3.26}$$

and then integrated, with respect to depth, to give the total thickness (Figure 3.13).

## 3.9 Extraction of Melt from the Asthenosphere and Magmatic Underplating

One of the most important conclusions of McKenzie (1984) is that the majority of the melt, produced in the upwelling asthenosphere, can be expelled from the parent mantle. The details of the self-compacting mechanism, by which melt is expelled, are beyond the scope of this thesis, but, in broad terms, it can be shown that the compaction rate depends critically on three matrix properties (McKenzie, 1984):-

i) Permeability.

ii) Bulk viscosity.

iii) Shear viscosity.

These parameters can, in turn, be related to the "dihedral angle" - the angle between grain-melt interfaces (Figure 3.14). Laboratory experiments suggest that the dihedral angle for partially molten rock remains below 60°. Below this critical value "the porosity network remains interconnected at all values of porosity" (McKenzie, 1984) and the melt produced at grain-grain interfaces can always escape.

The mechanism by which the melt rises through the mechanical boundary layer remains obscure. In this thesis it is assumed that it all rises vertically and underplates

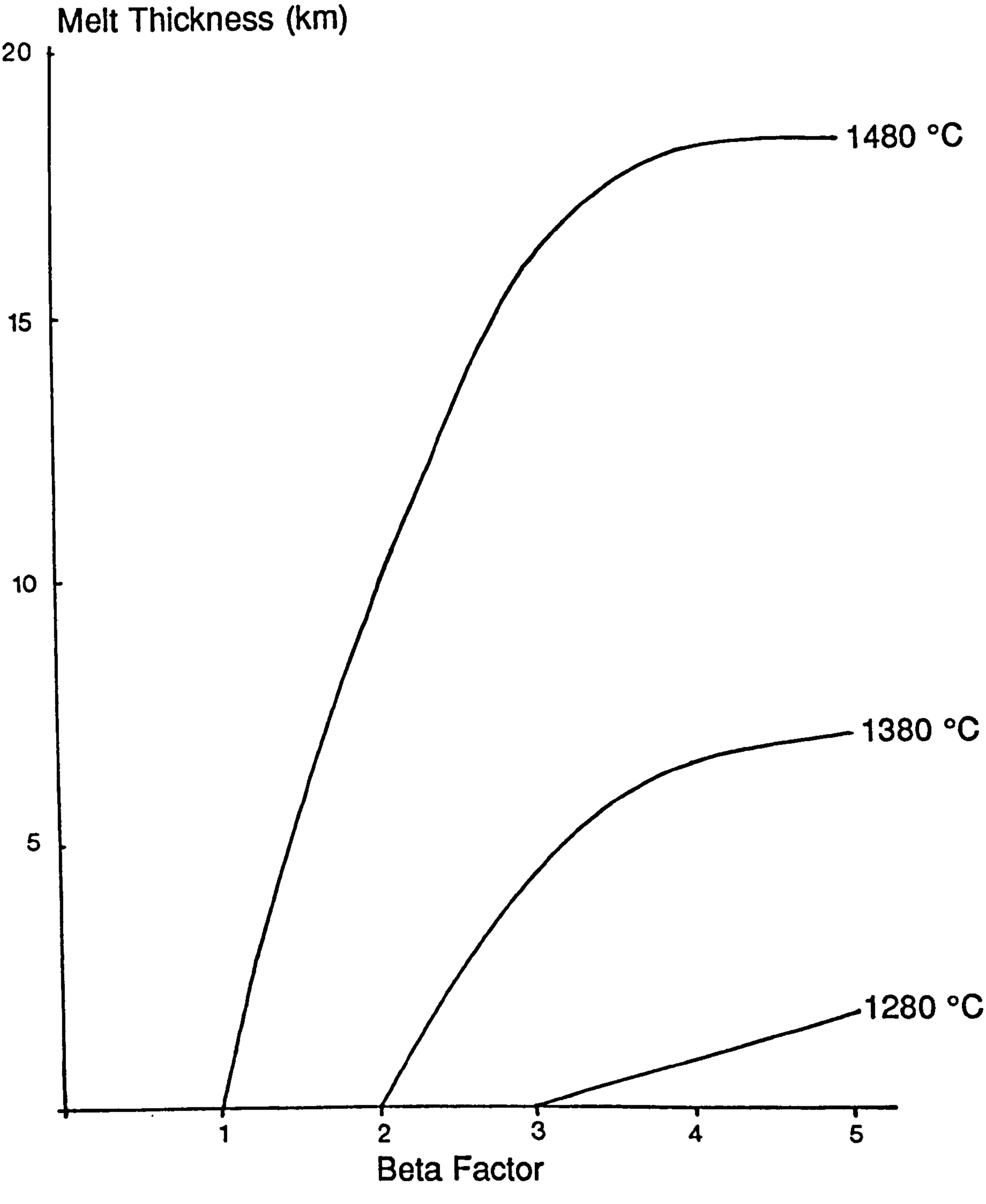


**Figure 3.13** The total melt thickness, predicted by the Bickle - McKenzie Model, controlled by the mantle potential temperature (Tp) and stretching factor Beta (1 to 5).

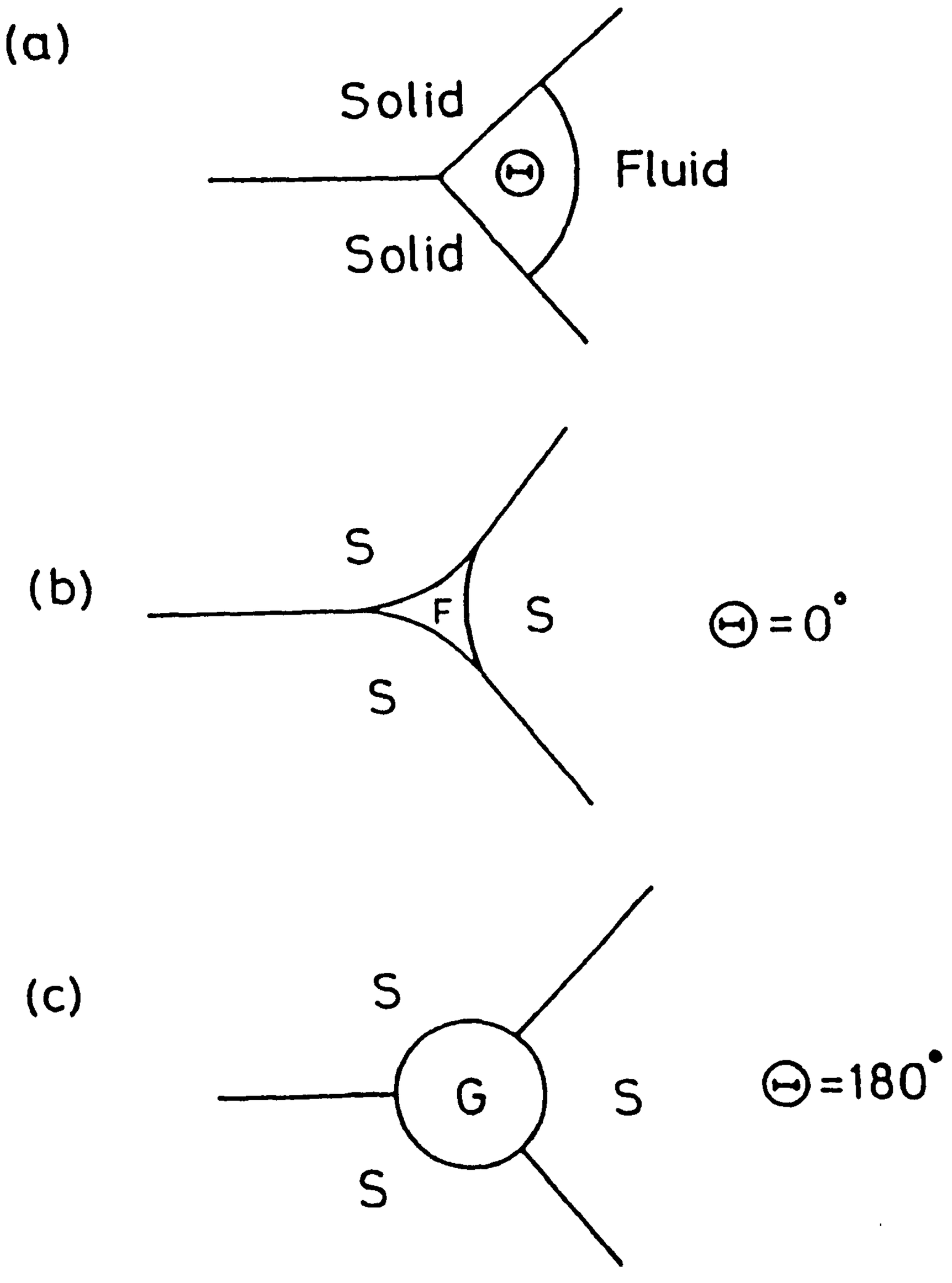




**Figure 3.14** a) The dihedral angle parameter (Θ) which controls the extraction of melt from mantle peridotite. b) Small Θ - solid-fluid boundaries are concave c) Large Θ - solid-gas boundaries are convex. (From McKenzie, 1984).

the lower crust, although the introduction of a coefficient to partition the melt between underplating and extrusion is briefly discussed in Chapter 4.

## 3.10 Limitations of the Bickle - McKenzie Melt Generation Model.

The Bickle-McKenzie model has been criticised for the lack of constraint at relatively small melt fractions (Latin & Waters, *in press*) because of the lack of experimental data that constrains the curve shown in Figure 3.10. Recent work by Takahasi (pers. com., 1992) has confirmed that the Bickle-McKenzie melt parameterisation is too simplistic and that the mathematical expression is only strictly valid at relatively low pressure. Fortunately, melt generation at passive margins (up to 4.5 GPa) should not be greatly affected by this additional pressure dependency, but it severely limits the accuracy of the model in an intra-continental setting where Beta stretching factors are relatively small. The net effect is to significantly reduce the amount of melt produced at elevated potential temperatures (and high pressure) beneath slightly thinned lithosphere.

A further limitation of the Bickle-McKenzie model is the accuracy of the value of latent heat of fusion of mantle peridotite, $\Delta S$, used in the equation controlling heat loss due to partial melting. Latin (1990) notes that McKenzie & Bickle (1988) give no quantitative justification for using a value of 250 J $kg^{-1}K^{-1}$ and states that "for consistency McKenzie & Bickle (1988) have assumed the value of 1333 °C [for the normal, real asthenosphere temperature] and have adjusted the value of $\Delta S$ to produce the correct volume of melt (7 km) [beneath a spreading ridge] at this temperature". From thermodynamic considerations, the most accurate determination of $\Delta S$ comes

from the relationship between the gradient of the solidus and the volume change on melting (McKenzie, 1984):-

$$\frac{dT}{dP} = \frac{\Delta V}{\Delta S} \qquad (3.27)$$

By using the best estimates available for dT/dP and $\Delta V$, McKenzie (1984) obtained a value of 362 J $kg^{-1}$ $K^{-1}$ for $\Delta S$. The uncertainty in the values of $\Delta S$ are matched by the range in thickness of oceanic crust (4.5 to 8.5 km; White, 1984) and Latin (1990) has calculated that the combined error on the normal value of Tp is 1280 °C $\pm$ 40 °C.

## 3.11 Variation in Potential Temperature and the Effect of Hot Spots.

Figure 3.13 shows that the melt thickness predicted for a normal potential temperature of 1280 °C, and a Beta factor of 5, is 2 km - i.e. melt is always produced at breakup. Definitions of "volcanic" (and "non-volcanic") margins are therefore purely arbitrary (c.f. Hopper et al., 1992) and the term "plume related margin" is preferred. As the potential temperature rises, the melt thickness increases to 7 km (Tp = 1380 °C) and 17 km (1480 °C). Such large quantities of melt are at present produced at hot-spots such as Iceland. White & McKenzie (1989) emphasise the scale of mantle plume hot-spots (Figure 3.15). Although the central column of the plume may be 100-200 km in diameter, the "mushroom" head of the convection cell elevates Tp over an area of diameter 2000 km. In the past, such plumes have produced massive outpourings of flood basalt e.g. 1-2.5 million $km^3$ extruded over the Deccan Traps in only 0.5 Ma (Courtillot & Cisowski, 1987). The margins

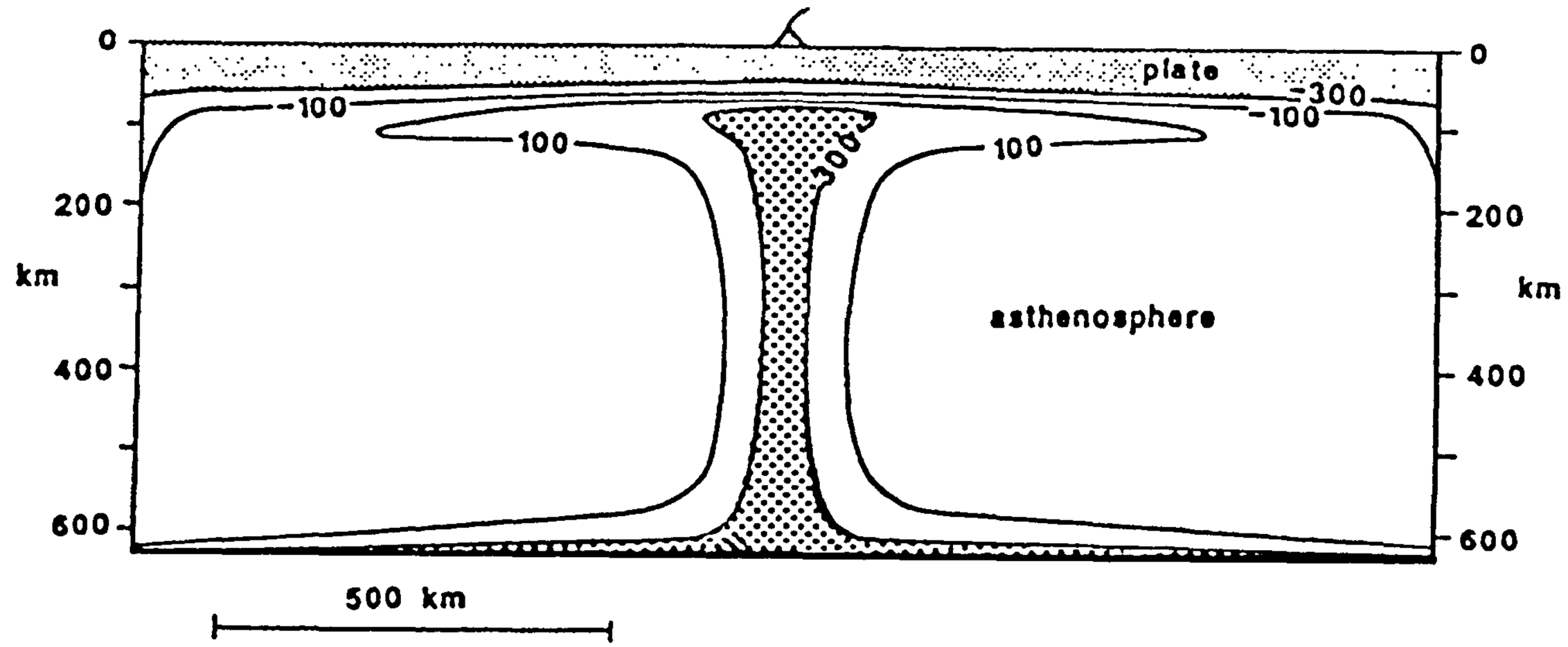


**Figure 3.15** The modelled mantle plume convection cell for the Cape Verde hot spot with the temperature anomaly below the mechanical boundary layer contoured every 200 °C (From White & McKenzie, 1990).

studied in this thesis were associated with more modest plumes, later in their history, where temperatures rarely exceeded 1480 °C.

# CHAPTER 4

# A COMBINED MAGMATIC-TECTONIC MODEL FOR CONTINENTAL EXTENSION.

## 4.1 Introduction.

In recent years a controversy has arisen concerning the nature of the Palaeocene (Top Danian) sequence boundary in the North Sea (Knox et al. 1981) and many other basins of the northwest European continental margin. Previous work has concentrated on the subsequent "anomalous" Eocene subsidence (Milton et al. 1990) but it is argued here that the origin of the Palaeocene (and earlier) uplift is of prime importance. It will be shown that uplift is associated with a major igneous event in the British Tertiary volcanic region associated with the onset of Iceland hot spot activity. The northern and central North Sea is therefore chosen as an example of the regional effect of a mantle plume convection cell which is well constrained in time and space.

Over-thickening of oceanic crust in the North Atlantic adjacent to the Grand Banks, from anomaly M4 (127 Ma) onwards (Tucholke & Ludwig, 1982), implies that the potential temperature may have been elevated at this time. A sequence boundary at the top of the Hauterivian may correlate temporally with this event since it cannot be explained either as a breakup or rift-onset megasequence boundary. However, it will be shown in Chapter 5 that, in general, hot spot activity associated with the Grand Banks-Iberia breakup is less constrained than in the Palaeocene of Northwest Europe.

White & McKenzie (1989) have made a detailed study of the effects of mantle plumes with the primary aim of explaining the genesis of huge quantities of flood basalts associated with continental extension leading to breakup. Perhaps the most important result of this study is that mantle plumes, which were previously visualised as relatively narrow zones of upwelling, elevate the potential temperature of the asthenosphere over an area of diameter 2000 km.

In Chapter 3 it was shown that the McKenzie - Bickle melt generation model predicts magmatic underplating for a normal potential temperature of 1280° C. When the potential temperature is elevated by a plume, even more melt is produced. Any model which attempts quantify regional breakup uplift, at a passive margin, must therefore include the effects of magma accumulating beneath the extending continental crust.

According to White & McKenzie (1989), uplift results from the isostatic response to hot, low density melt replacing mantle, the response of a reduction in the density of the mantle residue, the thermal uplift caused by an increase in the temperature at the base of the lithosphere and the dynamic support from the mantle plume convection cell. The first (and third) of these mechanisms has been added to the flexural cantilever model to produce the combined magmatic-tectonic model for continental extension. The other mechanisms, being less well constrained, are considered in a semi-quantitative manner.

For passive margins, two end-member geometries have been identified and theoretical model profiles constructed, for a "pure-shear breakup" and a "dyke injection breakup". It is supposed that most passive margins comprise a geometry somewhere between these two end members.

## 4.2 Observations of the Sequence Stratigraphic Response to Hot Spot Activity and Magmatic Underplating.

Figure 4.1a shows a clearly defined boundary, between Danian chalk (Lower Palaeocene) and the overlying coarse sandstones and reworked chalk, on well logs from the Central North Sea. Biostratigraphic data suggests that the boundary is close to the Danian - Thanetian boundary (Knox et al. 1981) giving an age of 62 Ma on the timescale of Kent & Gradstein (1986). According to Mussett et al. (1988) and White & McKenzie (1989) the oldest dates obtained from volcanics of the British Tertiary Igneous Province cluster around 60 Ma (Figure 4.2b). In addition, Green (1986) has shown that fission tracks from granites sampled in Northern England have been annealed by a thermal event at 60 Ma, associated with uplift and erosion on the kilometre scale.

The observations outlined above can be explained as the distal effects of the Iceland hot spot - elevation of mantle potential temperatures over a wide area, melt generation and regional uplift (Figure 4.3). There are two possible timescales over which the hot spot activity could affect the area. White (1989) has suggested that the Iceland hotspot initiated rapidly at 62 Ma, in which case the discrete sequence boundary could be a direct result of this event. Alternatively, the sequence boundary at 62 Ma could be a rift-onset megasequence boundary for the North Atlantic superimposed on plume-related uplift throughout the Late Cretaceous - Early Tertiary. (It should be emphasised that it is not proposed that the Central North Sea underwent any extensional reactivation in the Palaeocene). Subsidence curves (Figure 4.1b) appear to show that uplift occurred over a period of several million years, but this

a)

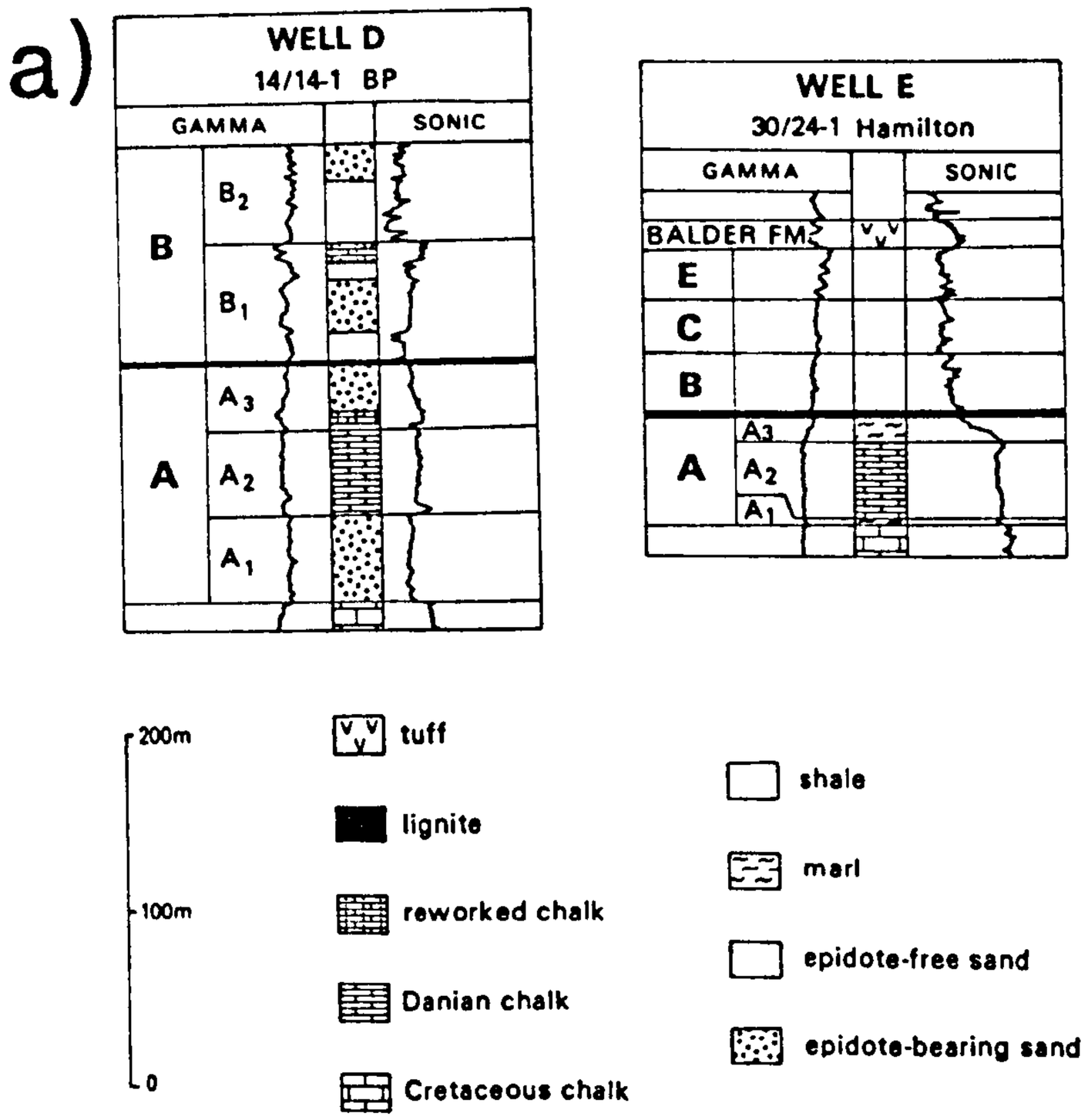


b)

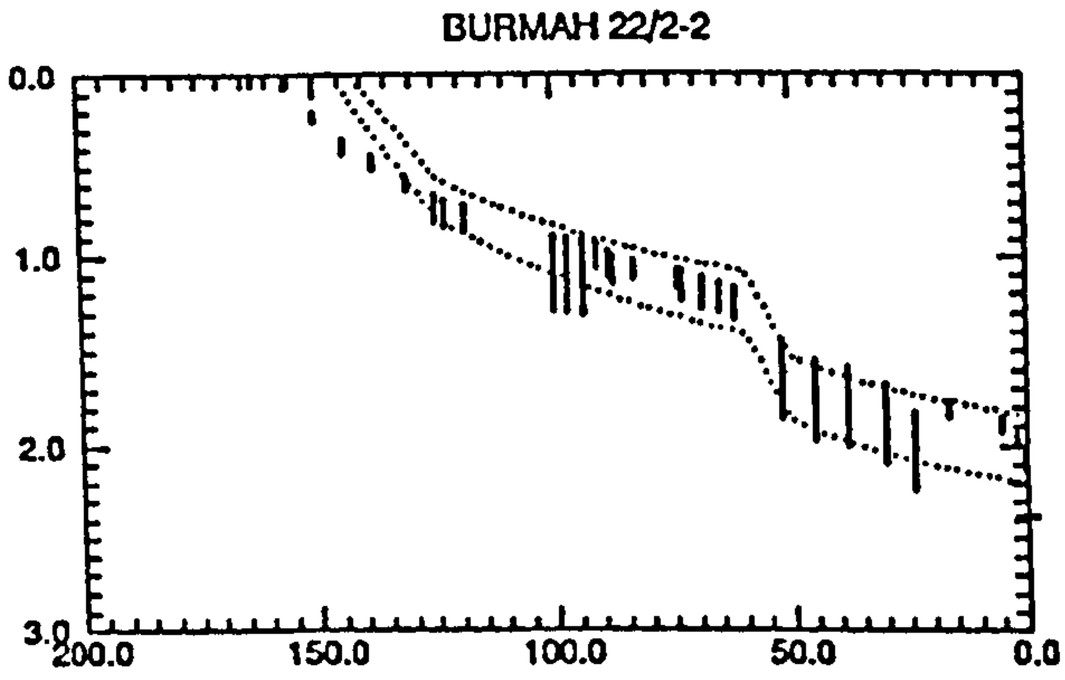


**Figure 4.1** a) Well logs from the Outer Moray Firth area of the North Sea showing the influx of clastic material in the mid Palaeocene (Knox et al., 1981).
b) Representative subsidence curve for the North Sea showing slow subsidence in the late Cretaceous and a rapid increase in the subsidence rate in the Palaeocene (White & Latin, in press).

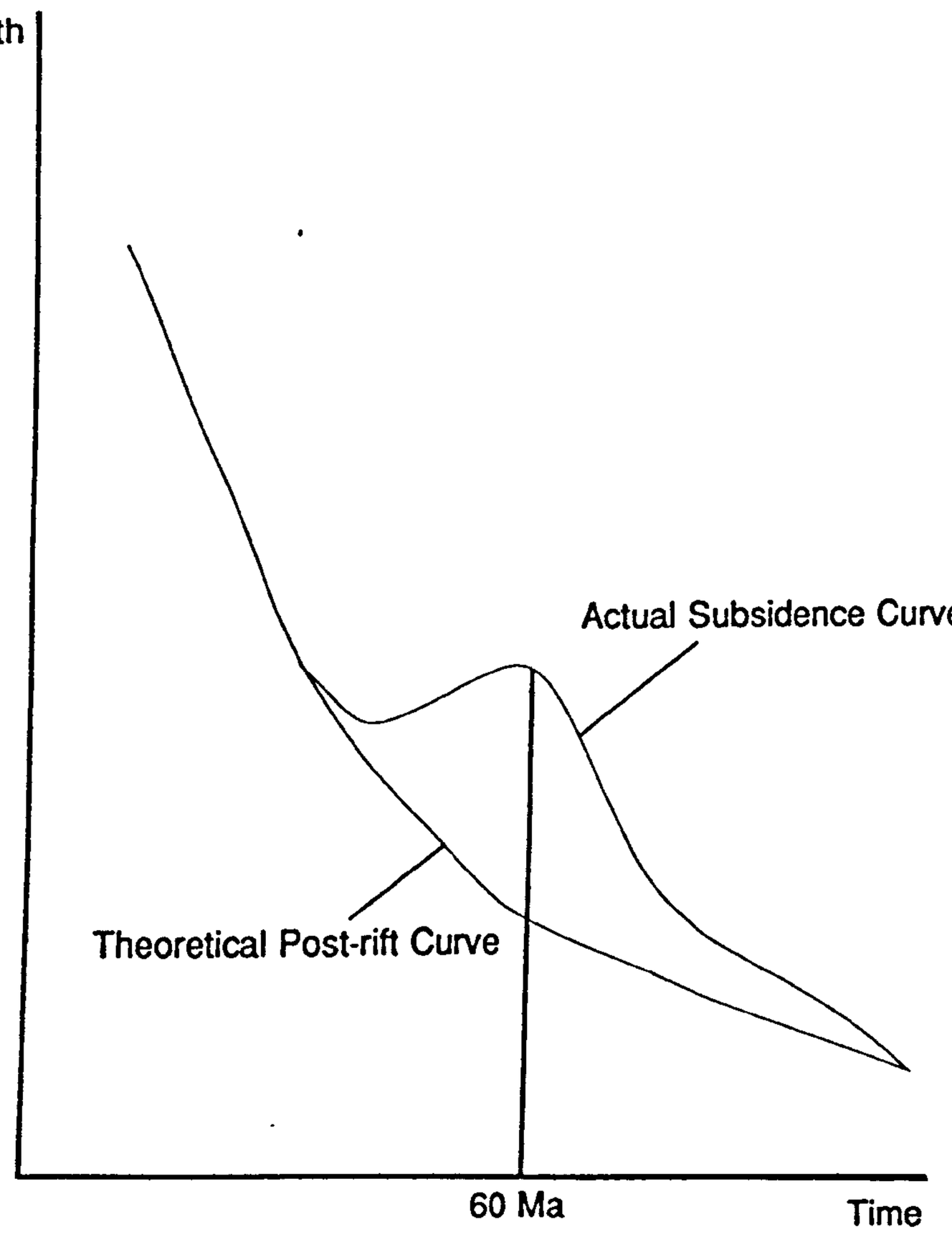


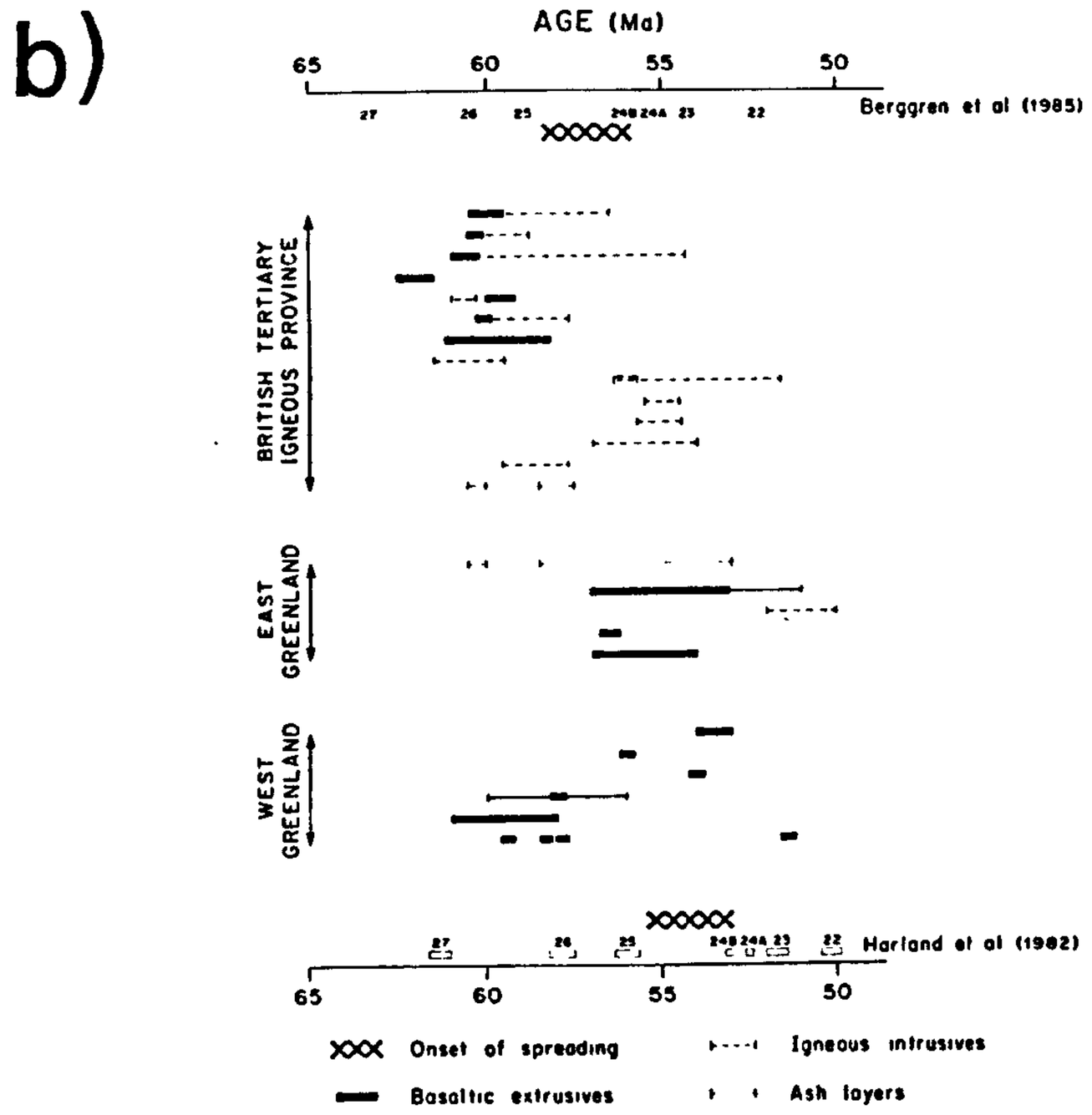


**Figure 4.2** a) Theoretical subsidence curve showing the effect of a mantle plume convection cell impinging on the base of the lithosphere below a thermally subsiding basin. b) The age of igneous activity in the British Tertiary Igneous Province and Greenland, showing a strong temporal link with the mid-Palaeocene rift event in the North Atlantic (White & McKenzie, 1989).

a)

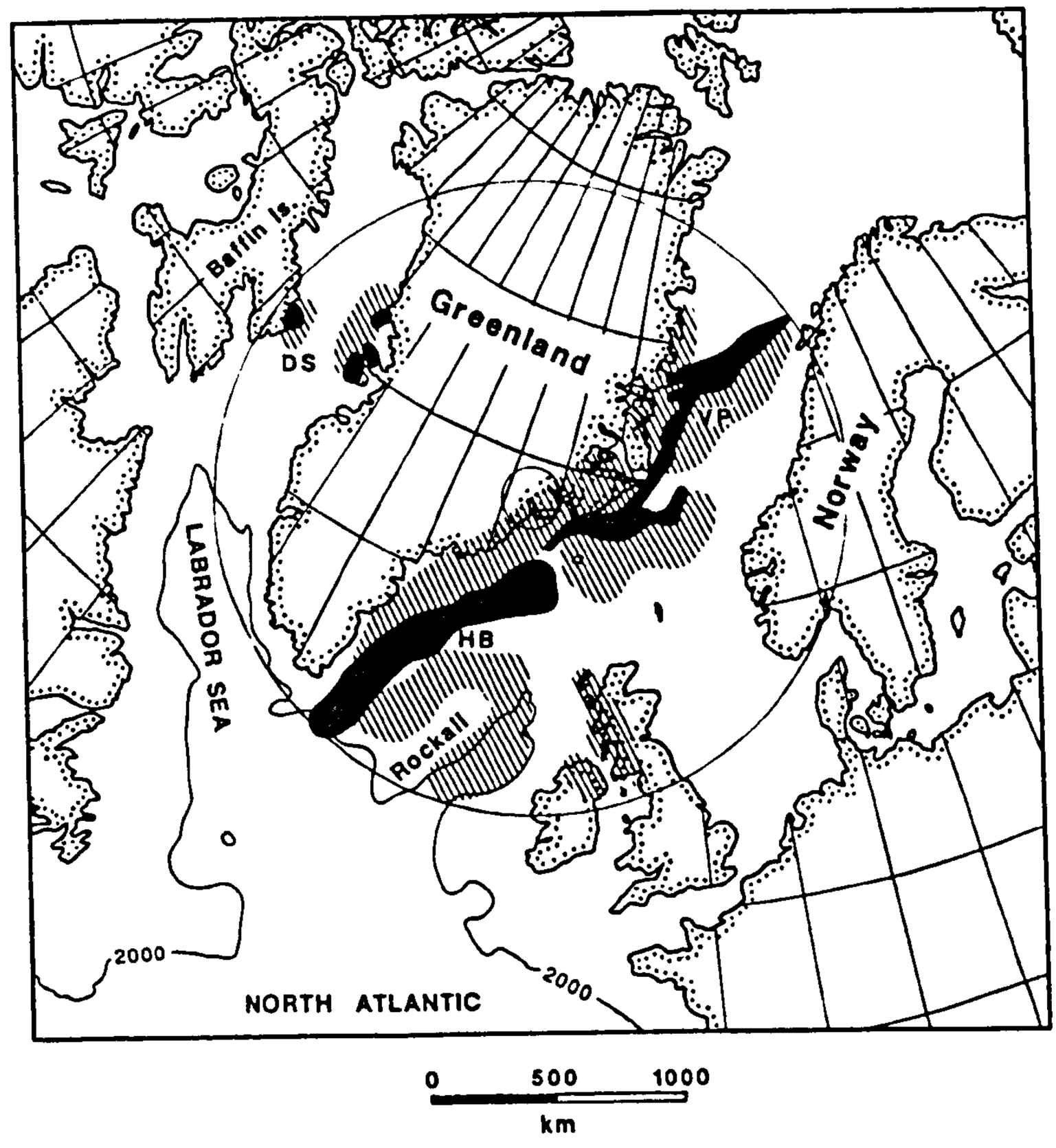


b)

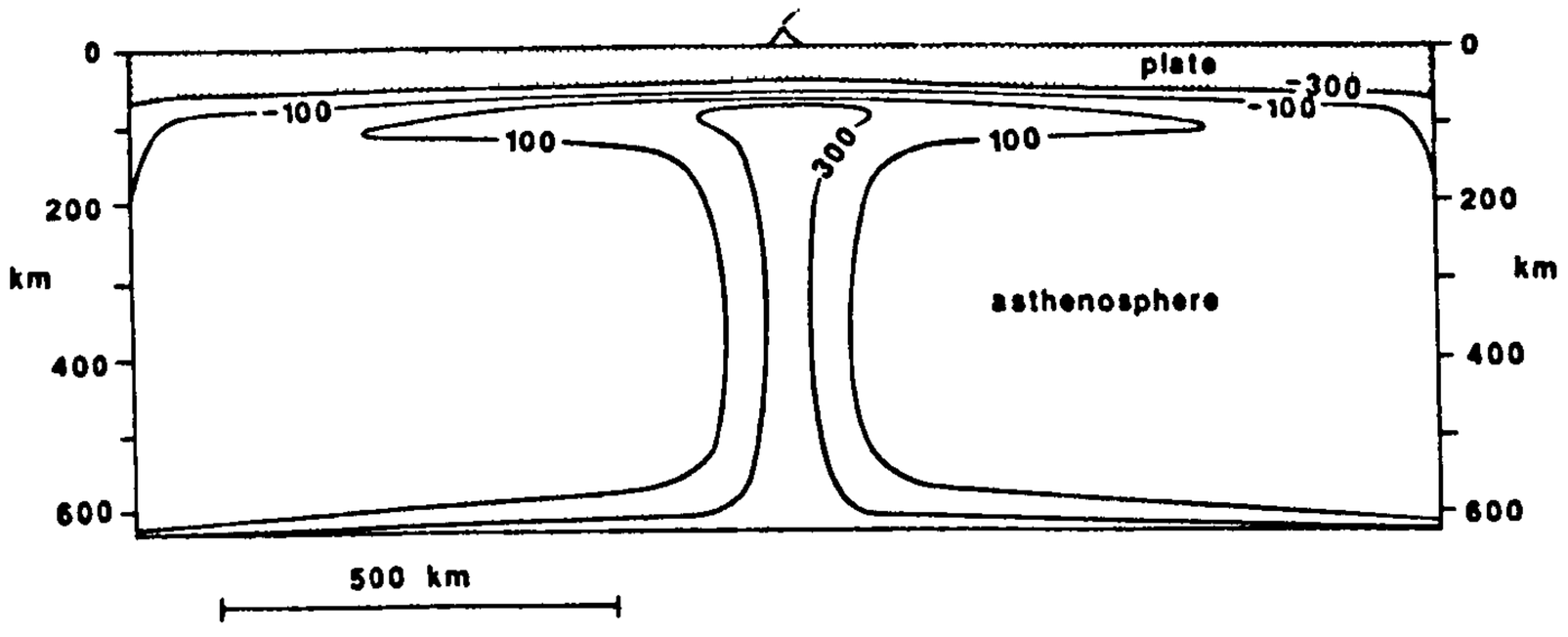


**Figure 4.3** a) North Atlantic reconstruction showing the inferred position of the Iceland hot spot below eastern Greenland just prior to breakup. The area within the circle is underlain by anomalously hot asthenosphere. Large scale basaltic extrusives are marked by solid shading and diagonal lines mark other areas of igneous activity. (White & McKenzie, 1989). b) A typical "mushroom-shaped" mantle plume based on the asthenosphere temperature variations required to model the thermal anomaly over the Cape Verde Rise (White & McKenzie, 1989).

may be an artefact of ignoring the flexural isostatic effects of erosion. A longer plume build-up time is also supported by late Cretaceous igneous activity in West Greenland (Roberts, 1993 pers. com.). In either case, Eocene subsidence (after excluding the important effect of sediment loading) most probably results from the entrainment of the Iceland hot-spot in the newly formed North Atlantic, reducing the diameter of the thermal anomaly (White and McKenzie, 1989). During the Tertiary the subsidence curves usually return to their normal post-rift trajectories (Figure 4.2a) - this is not the case in Southern North Sea and Channel Basin, which were affected by synchronous Alpine related reactivation.

## 4.3 Uplift Mechanisms Associated with Melt Generation and Plumes.

### 4.3.1 Introduction

In Figure 4.4 the crustal thickness ($t_c$) and the thickness of the crust-plus-underplating ($t_{c+m}$) are plotted against $\beta$ for potential temperatures ranging from 1280 °C to 1480 °C. At the highest value of potential temperature the Moho topography has been almost entirely filled with melt. This result has fundamental consequences for the nature and composition of the lower crust.

White & McKenzie, (1989), have shown that there are two uplift mechanisms associated with melt fractionation and magmatic underplating:-

1) The isostatic consequence of hot, low density melt replacing mantle.

2) The isostatic consequence of a decrease in density of the mantle residue after partial melting.

In addition, mantle plume convection cells also have two effects:-

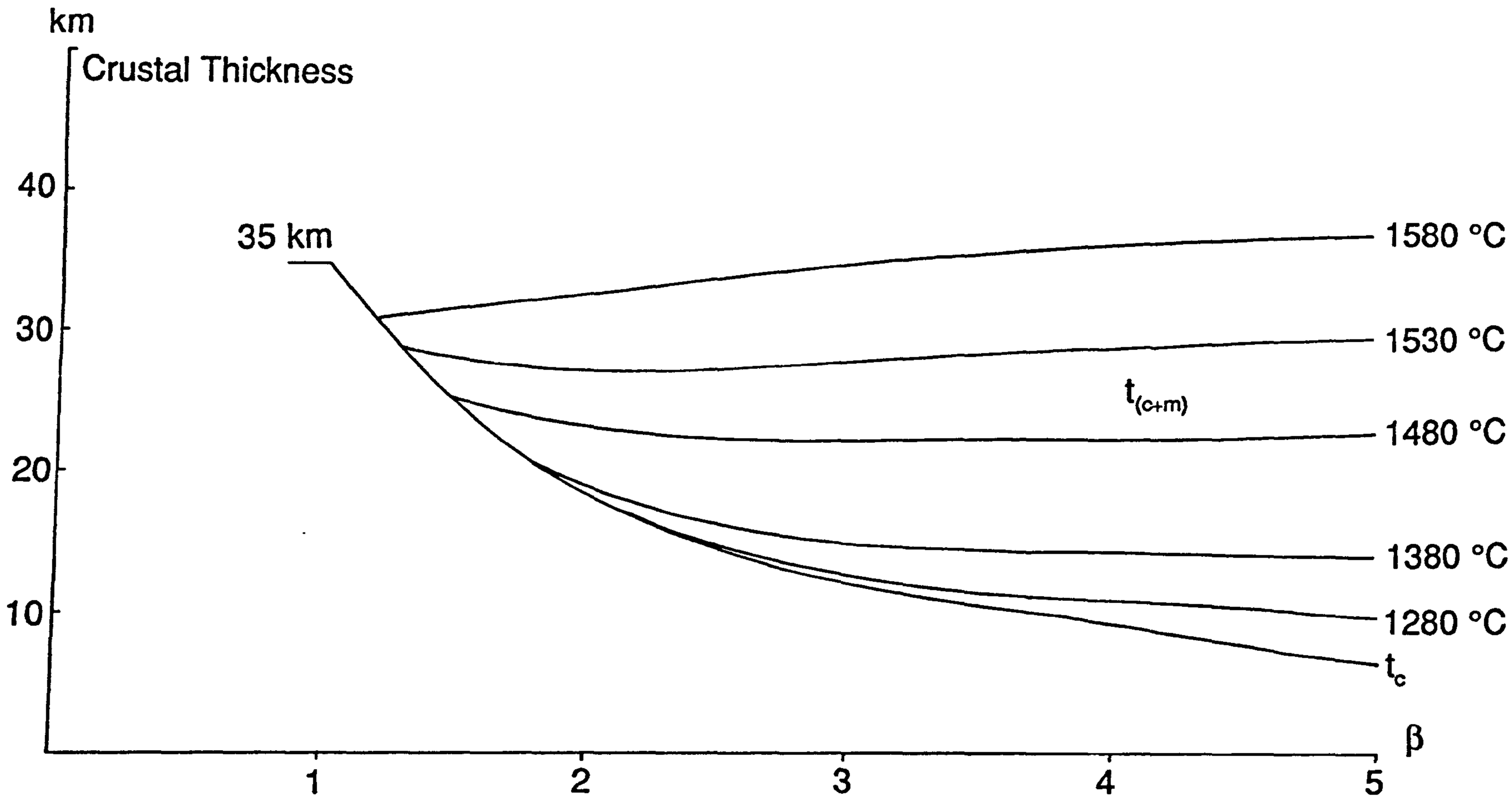


**Figure 4.4** Plots of the thickness of crust and crust+melt against the stretching factor Beta showing the gradual filling of Moho topography with magma as the potential temperature is increased. At a potential temperature of 1580 °C the thickness of crust+melt initially decrease but as stretching increases the total thickness gradually increases back to the original crustal thickness - 35 km.

3) The thermal uplift caused by an increase in the base lithosphere temperature.

4) The dynamic support of the mantle plume convection cell.

The second of these mechanisms is poorly constrained, mainly by the lack of experimental data, but the magnitude of the fourth has been calculated by Courtney & White (1986) above the Cape Verde hot-spot. About a kilometre of uplift is possible, directly above a plume, and should be included in models with very high potential temperatures. In this thesis, the first and third mechanism has been added to the flexural cantilever model to produce a combined magmatic-tectonic model for continental extension.

### 4.3.2 Uplift Caused by Hot, Low Density Material Replacing Mantle.

For a given melt thickness, h, underplating the continental crust, the load generated is given by:-

$$LOAD = h.(\rho_{upm} - \rho_{mantle}).g \qquad (4.1)$$

Where $\rho_{upm}$ is the density of the underplated material, which can be assumed to be either solidified or molten, and $\rho_{mantle}$ is the density of the original mantle material from which the melt is derived. White & McKenzie (1989) use a variety of values for the density of the solidified melt, $\rho_{upm}$, which depend on the potential temperature at which the melt formed (Figure 4.5b). The magnitude of uplift, or rather the reduction in initial subsidence, due to magmatic underplating at various potential temperatures is shown in Figure 4.5a. For a potential temperature of 1380° C, and

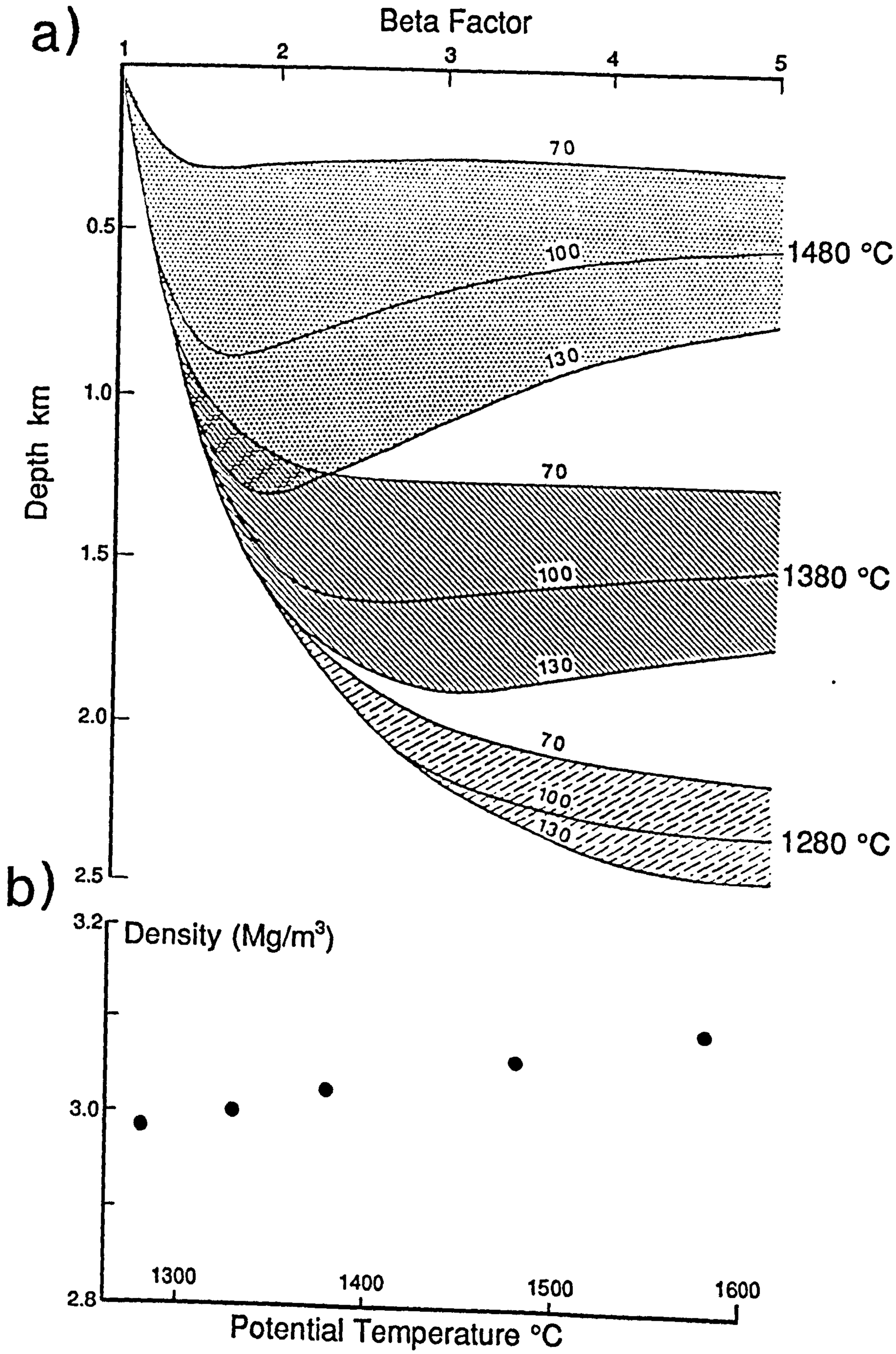


**Figure 4.5** a) Uplift (subsidence reduction) due to magmatic underplating only, using the solid densities given in b). For each temperature the mechanical boundary layer thickness is also varied - 70, 100 and 130 km. b) Variation of solidified melt density with the potential temperature of formation. (White & McKenzie, 1989).

a Beta factor of 5, 800 metres of uplift is predicted. At the same Beta factor and a highly elevated potential temperature (1480° C), towards the centre of a mantle plume, the uplift increases to 1800 m. It should be emphasised that White & McKenzie (1988) assume local, or Airy, isostatic compensation in all their calculations.

### 4.3.3 Uplift Caused by a Decrease in the Density of Mantle Residue and thermal uplift associated with the plume.

White & McKenzie (1989) state that "The uplift caused by the density change of the mantle as it becomes depleted by the removal of melt is the most uncertain of the corrections, but it is also the smallest". It is theoretically possible to calculate the density of the residue after the extraction of a known amount of melt, which results in a known residual composition, for a given potential temperature. In practise, White & McKenzie (1989) adopt a much simpler approach, by which the density difference between lherzolite and residual harzburgite ($\Delta\rho \approx 20$ kg $m^{-3}$) is used to give an average uplift of the order of 300 m. In Figure 4.6 the solid lines represent the uplift associated with magmatic underplating and the thermal uplift caused by an increase in the base lithosphere temperature. The maximum uplift (dashed lines) includes the effect of a decrease in the density of the residual mantle (White & McKenzie, 1989).

### 4.3.4 Uplift Caused by the Dynamic Support of the Mantle Plume Convection Cell.

From a detailed study of the heat flow and geoid anomaly across the Cape Verde hot-spot in the North Atlantic, Courtney & White (1986) have constrained both

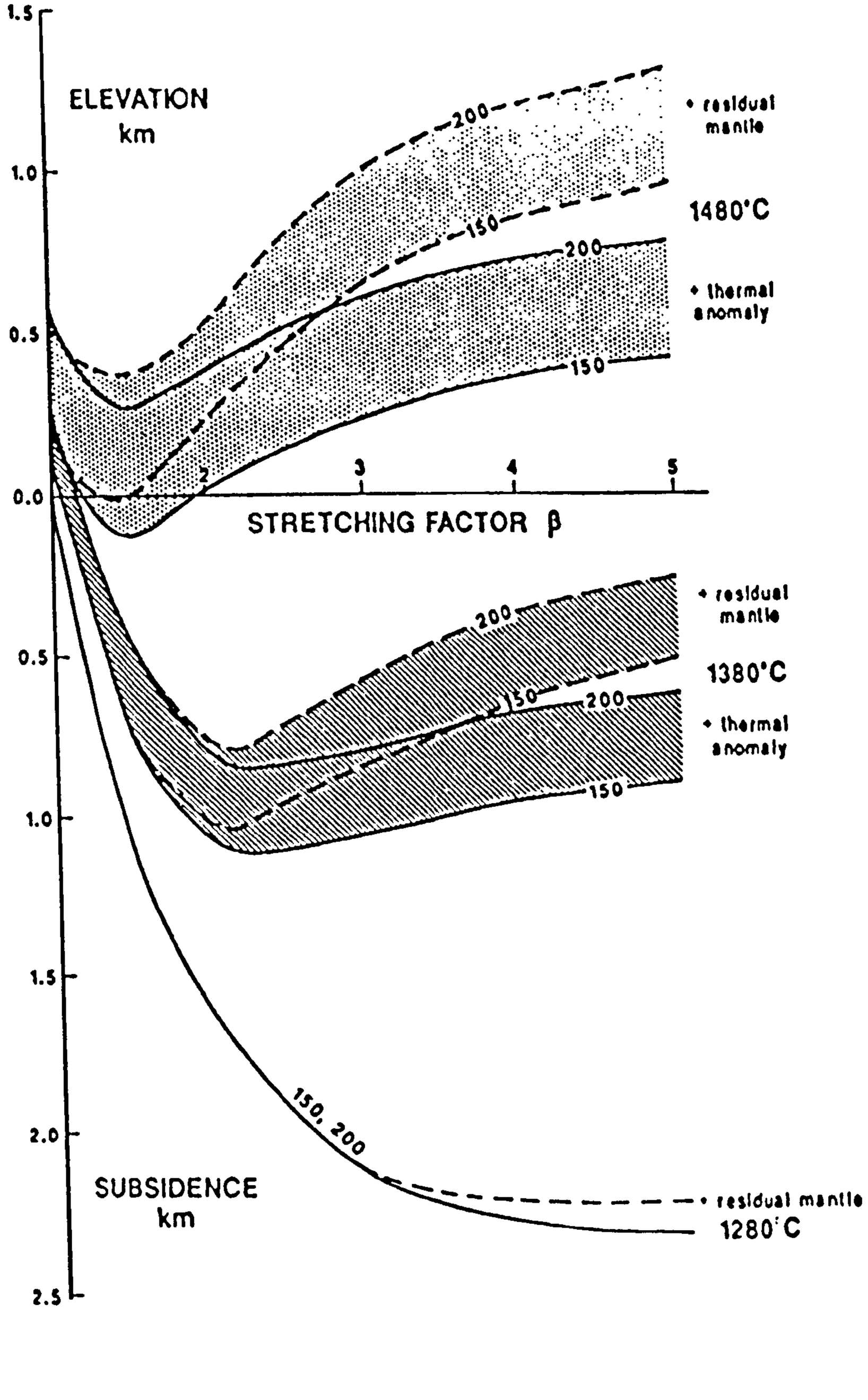


**Figure 4.6** Uplift resulting from the thermal anomaly associated with the mantle plume convection cell (solid lines) - and with the effect of a reduction in the density of the mantle residue (dashed lines) - both in addition to magmatic underplating. Mechanical boundary layer - 150 km and 200 km thick. (White & McKenzie, 1989).

b)

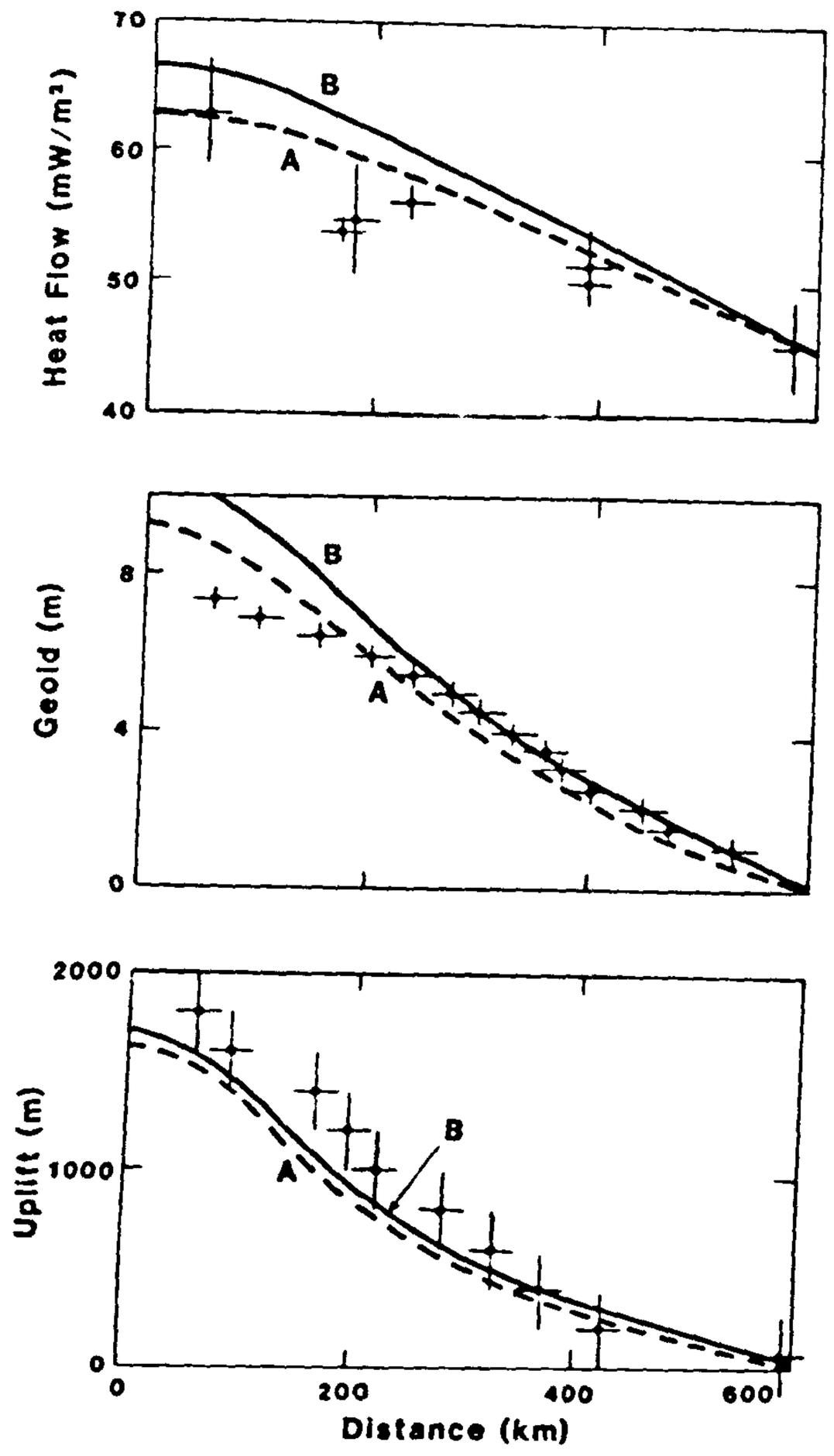


a)

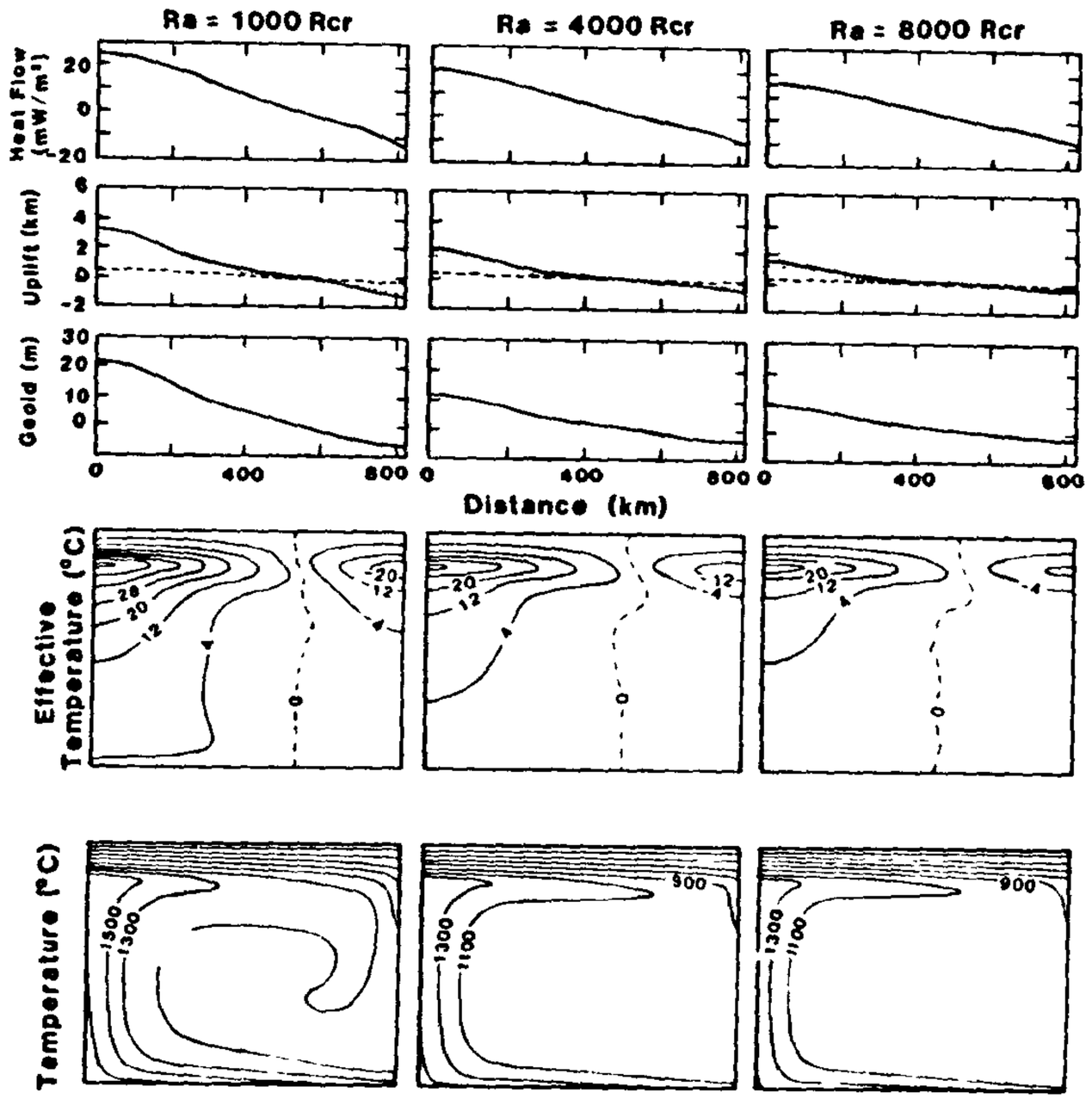


**Figure 4.7** a) Modelling the Cape Verde Rise thermal plume as an axisymmetric convection cell for various Rayleigh Numbers. b) Predicted heat flow, geoid anomaly and uplift for two convective models:- A - Ra = 8000 $R_{cr}$, viscosity = $1.8 \times 10^{20}$ Pa. B - Ra = 4000 $R_{cr}$, viscosity = $3.6 \times 10^{20}$ Pa. Note the modelled smooth decay of heat flow across the Cape Verde Rise. (Courtney & White, 1986).

the convection model and the magnitude of the dynamic support from the mantle plume. Their preferred model involves complex mathematical formulations which solve the equations of motion and energy within an "axisymmetric" convection cell, overlain by a conductive lid (Courtney & White, 1986). Figure 4.7a shows that the geometry of the convection cell is critically dependent on the Rayleigh number (Ra), the mantle viscosity and $\alpha$, the coefficient of thermal expansion. It can be seen that in all cases the total uplift (solid line) is dominated by the convective component of uplift (dotted line) i.e. the dynamic support from the plume. In Figure 4.7b the heat flow, geoid anomaly and uplift, predicted by a two convective models A & B (with different viscosities), are compared with data from the Cape Verde hot-spot (Courtney & White, 1986). All other models fail to model the smooth decrease in heat flow across the profile. The total uplift predicted at the centre of the Cape Verde plume is nearly 2 km.

## 4.4 The Combined Magmatic-Tectonic Model for Continental Extension.

### 4.4.1 Introduction.

In this model, the distributed pure-shear, which controls the Moho topography, is used to define the beta factor at all points across the profile (Figure 4.8). For a given potential temperature, these beta factors control the melt thickness generated by asthenosphere upwelling, which is then added at the Moho, and the isostatic response to the underplating is calculated. It is assumed that melt generated in the asthenosphere rises vertically to enable underplating of the continental crust.

The combined magmatic-tectonic model includes the uplift caused by hot low

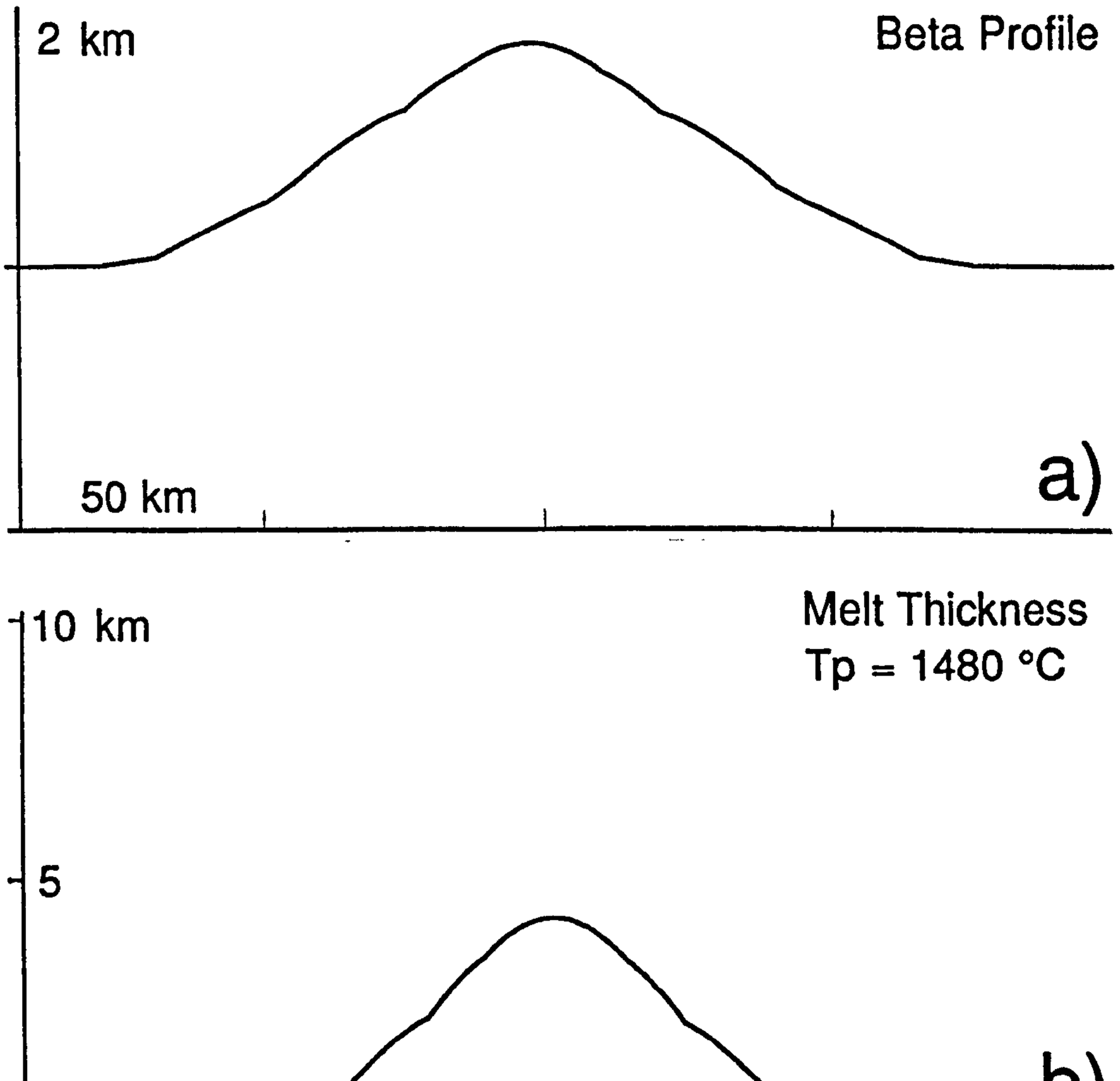


**Figure 4.8** Definition of the Beta stretching factor profile used to define the amount of melt produced in the combined magmatic-tectonic model.

density material underplating the crust. This material can either be assumed to be molten ($\rho_{upm}$ = 2800 kg $m^{-3}$) or solidified - in which case the temperature dependent densities of White & McKenzie (1989) are used (see section 4.3.2). When the density of molten rock is used, the magnitude of uplift is augmented because $\Delta\rho$ is larger. This can compensate for the fact that the uplift due to a reduction in the density of mantle residue is not included in the combined magmatic-tectonic model.

Unlike the calculations of White & McKenzie (1989), the combined magmatic-tectonic model assumes that the crust retains flexural rigidity during extension. This affects both the magnitude and distribution of the uplift across the model section. A very important consequence of this is that underplating, close to the continent ocean boundary, is capable of uplifting the passive margin in a landward direction.

### 4.4.2 Thermal Uplift Caused by an Increase in the Base Lithosphere Temperature.

Figure 4.9 shows the thermal uplift effect of an increase in the potential temperature associated with a mantle plume convection cell. The profiles are calculated by assuming a simple linear geotherm down to the relevant base lithosphere temperature - dotted line = 1333 °C and solid line = 1533 °C. Thermal uplift is calculated in the same way as described in Chapter 2. The difference between the two profiles is plotted (at a different vertical scale) in Figure 4.9b. An elevation of 200 °C produces up to 800 m of uplift.

### 4.4.3 Uplift Generated by Hot Low Density Melt Replacing Mantle: Variation with Potential Temperature.

Figures 4.10 and 4.11 show the effect of increasing the potential temperature

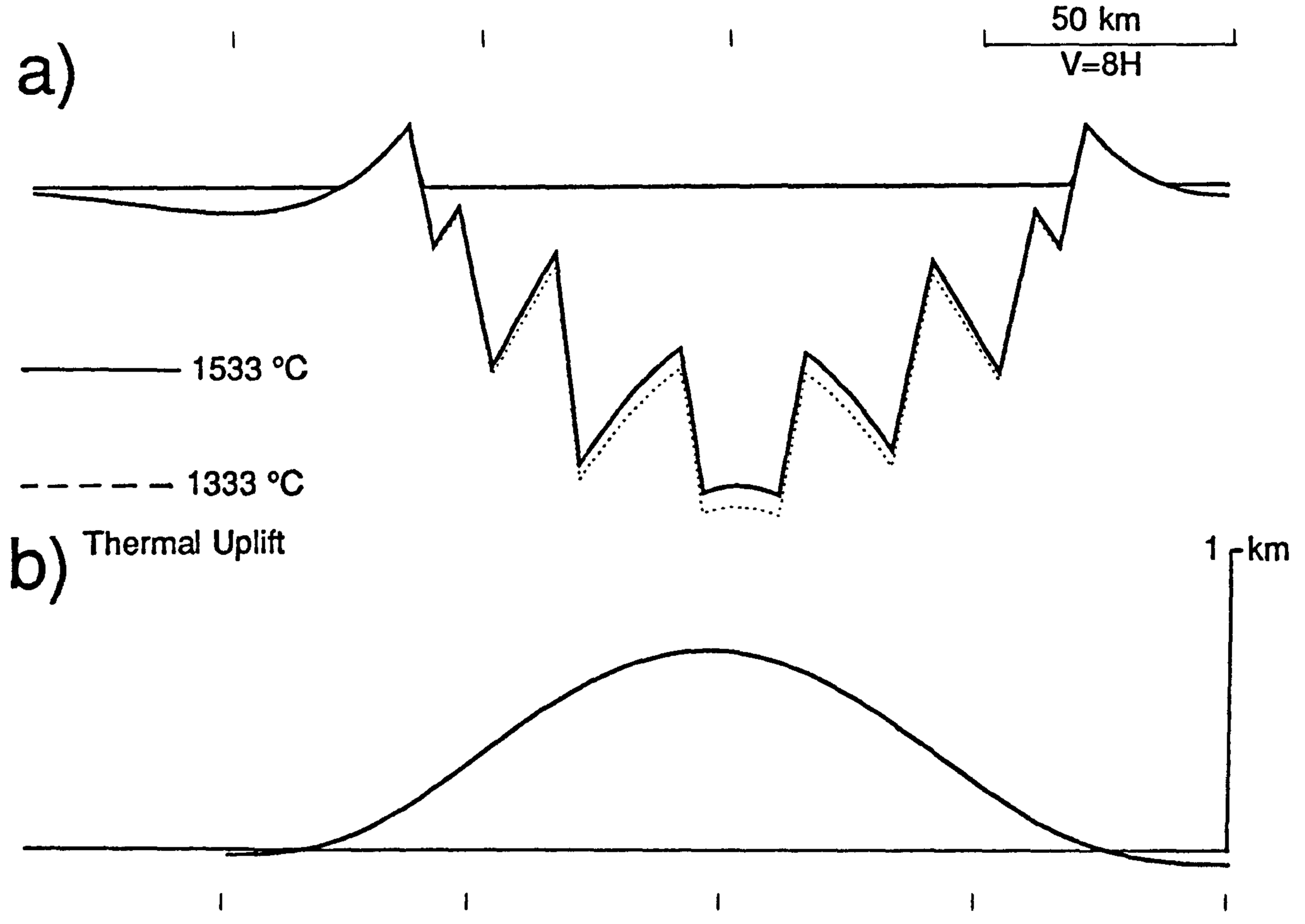


**Figure 4.9** The effect of the thermal anomaly alone. Mantle plume convection cells raise the base lithosphere temperature. a) Basin profile. b) The difference between the solid (1533 °C) and dotted lines (1333 °C), plotted at a greater vertical exaggeration.

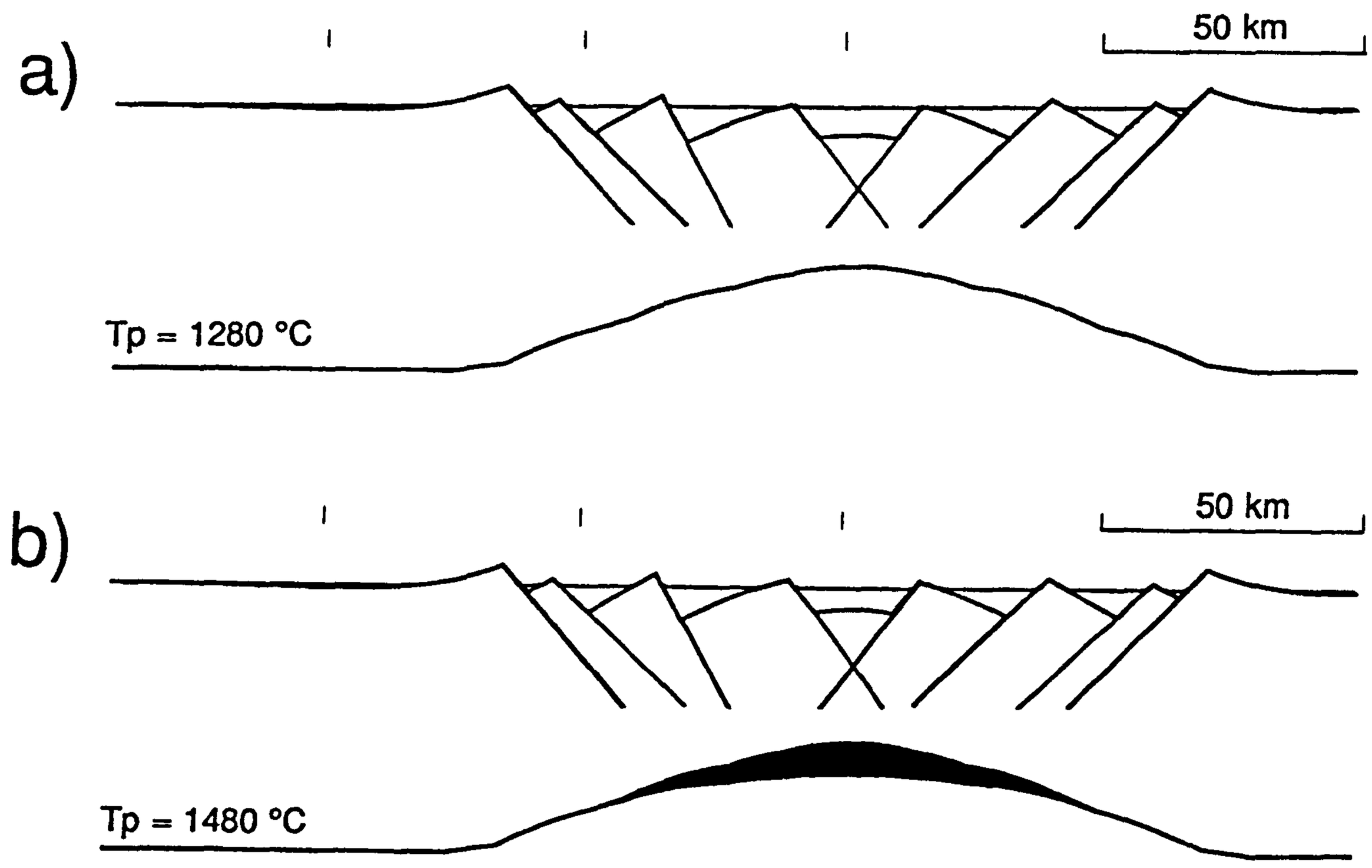


**Figure 4.10** The effect of varying the mantle potential temperature and magmatic underplating for water loaded profiles.

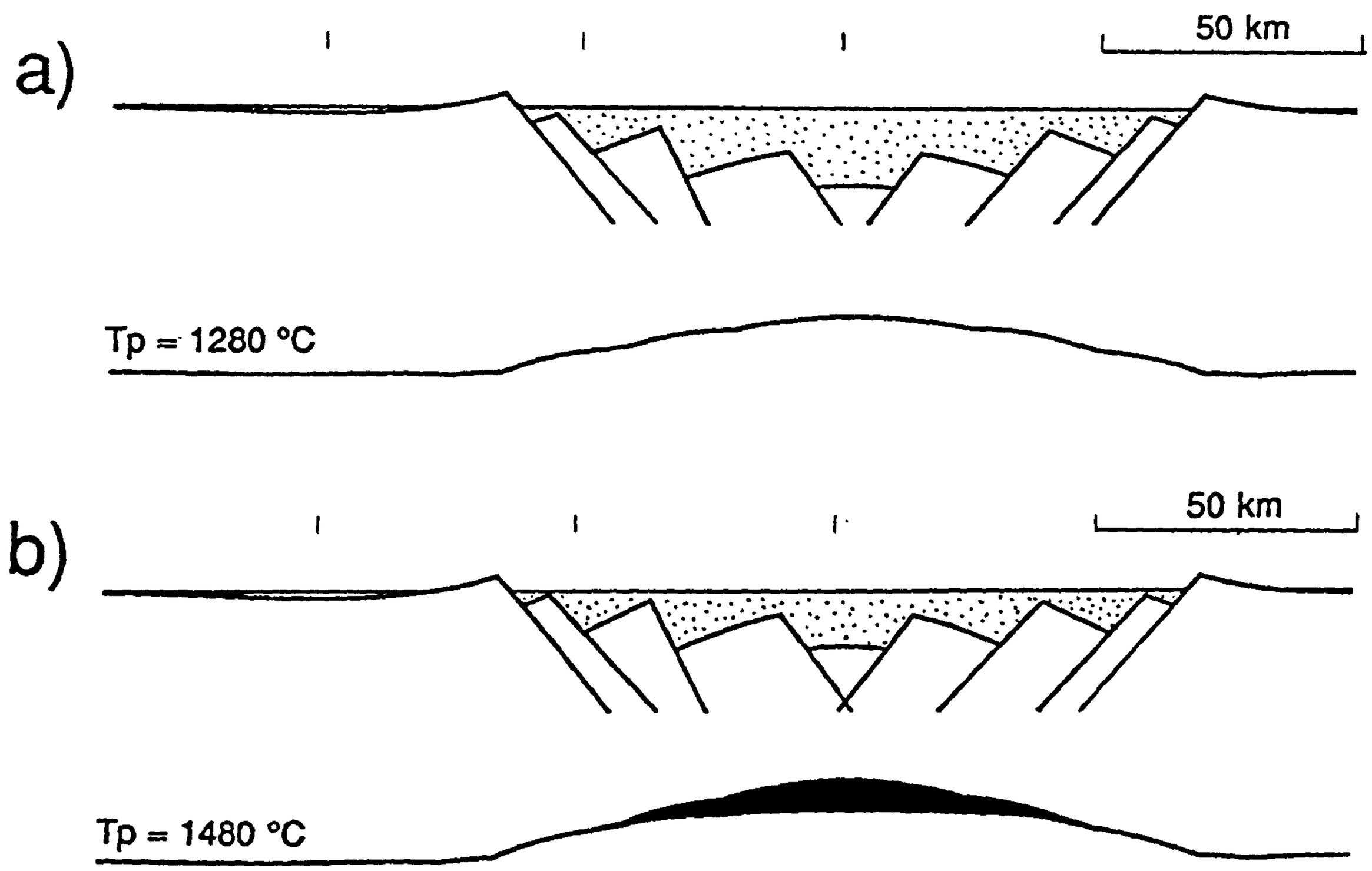


**Figure 4.11** The effect of varying the mantle potential temperature and magmatic underplating for sediment loaded profiles.

of the asthenosphere below a simple, symmetrical graben. In both cases Te = 5 km and up to 5 km of melt is produced and underplated when the potential temperature is elevated by 200 °C. Figure 4.10 shows water loaded profiles, but the effect of underplating is even more pronounced on sediment loaded profiles (Figure 4.11). The results can be described in loose terms as the development of a "rift-related dome". Plume related pre-rift thermal doming, as defined by Ziegler (1982) and Le Bas (1971), is greatly accentuated by magmatic underplating during the latter stages of the rift phase.

### 4.4.4 Partition of Melt Between Underplated Intrusives and Extrusives.

So far it has assumed that *all* of the melt, produced as a result of asthenosphere upwelling, underplates the continental crust at the Moho. However, it is known that an extrusive component may also be important. At its most extreme, massive outpourings of flood basalts cover volcanic passive margins associated with mantle plumes (e.g. The Deccan Traps). For passive margins above more moderately elevated potential temperatures, the proportion of melt extruded probably reflects the complex interplay between extension rate, the magnitude of tensional stress and the rate of melt production (Gudmundsson, 1990). This relationship would explain the fact that the majority of extrusion of the Deccan Traps takes place over a remarkably short period of time, at the onset of plume activity when the melt generation rate is at a maximum (Courtillot et al., 1988; Whitehead, 1986).

In order to partition the melt, an "extrusion coefficient", $E_c$, can be defined such that the proportion of the total melt thickness $T_t$ allowed to reach the surface is given by $E_c.T_t$ and the underplated thickness becomes $(1-E_c).T_t$ (Figure 4.12a). For

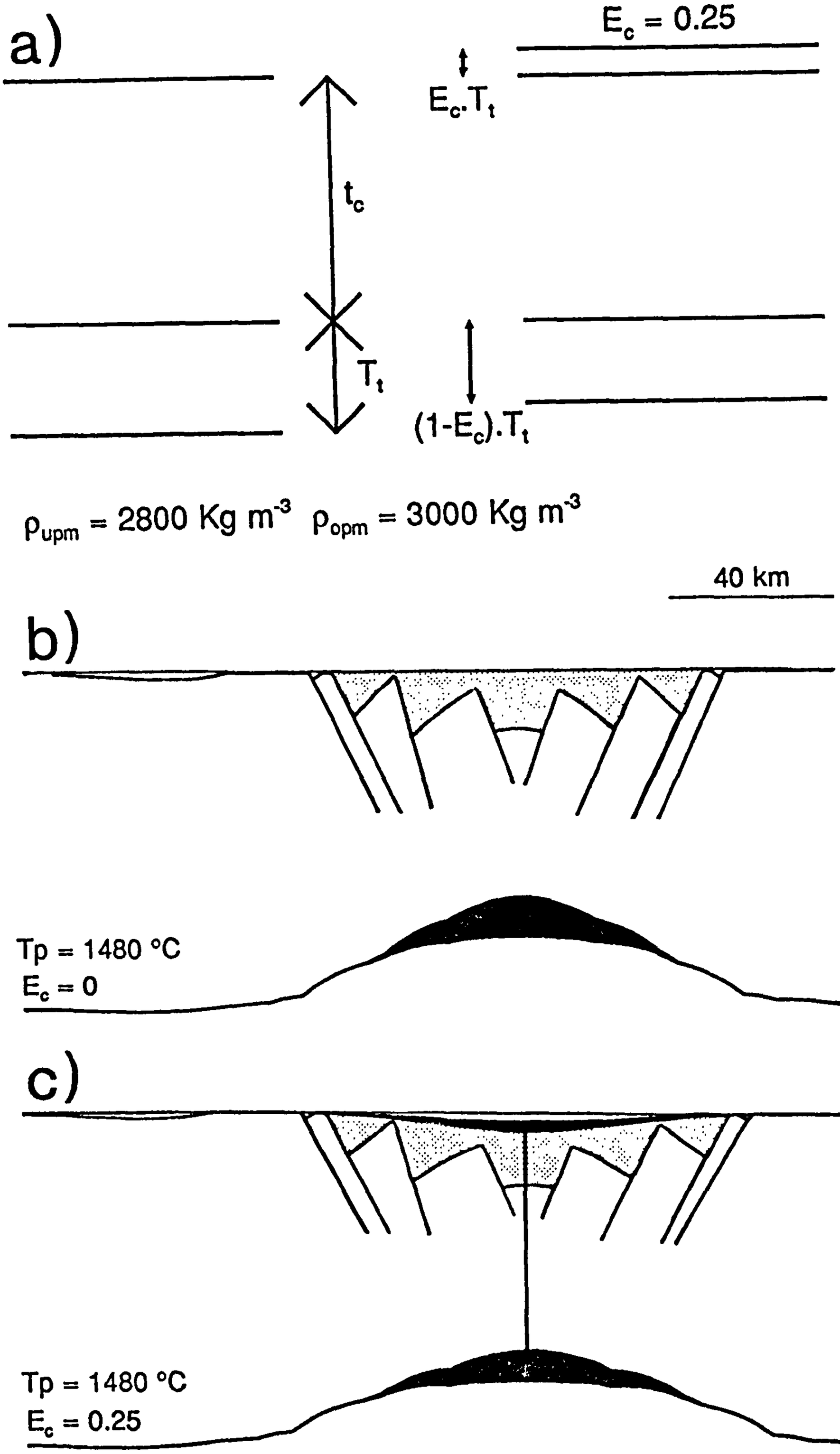


**Figure 4.12** The theoretical effect of magmatic overplating. a) New density structure - $E_c$ = Extrusion coefficient. b) The combined magmatic-tectonic model without melt partition. Tp = 1480 °C. c) With magmatic under- and over-plating. $E_c$ = 0.25.

moderately elevated potential temperatures an extrusion coefficient of 0.25 has been suggested (Cox, *pers. com.*). It also seems convenient to call the extrusion process "magmatic overplating".

The flexural isostatic effect of magmatic overplating is to load the continental crust and reduce the uplift caused by underplating. When calculating the load:-

$$LOAD = h \cdot \rho_{opm} \cdot g \qquad (4.2)$$

the temperature dependent (solid) densities of White & McKenzie (1989) are used for the overplated material ($\rho_{opm}$).

Figure 4.12 shows an example of the combined magmatic-tectonic model, with a $T_p$ of 1480 °C, before (b) and after extrusion (c). The extrusion coefficient $E_c = 0.25$. It can be seen that the extruded material has a significant down-warping effect and it is concluded that uplift (and erosion) is greatly reduced when large amounts of melt leak to the surface.

### 4.4.5 Application of the Combined Magmatic Tectonic Model to an Intra-Continental Rift System.

Figure 4.13 shows an application of the combined magmatic-tectonic model to an intra-cratonic rift basin. The model has been made more realistic by including 200 m palaeo-bathymetry, a relatively high Te (7 km) and the flexural isostatic effect of erosion (Figure 4.13b). The degree of extension is not excessive and only 3 km of melt is produced when the potential temperature is elevated.

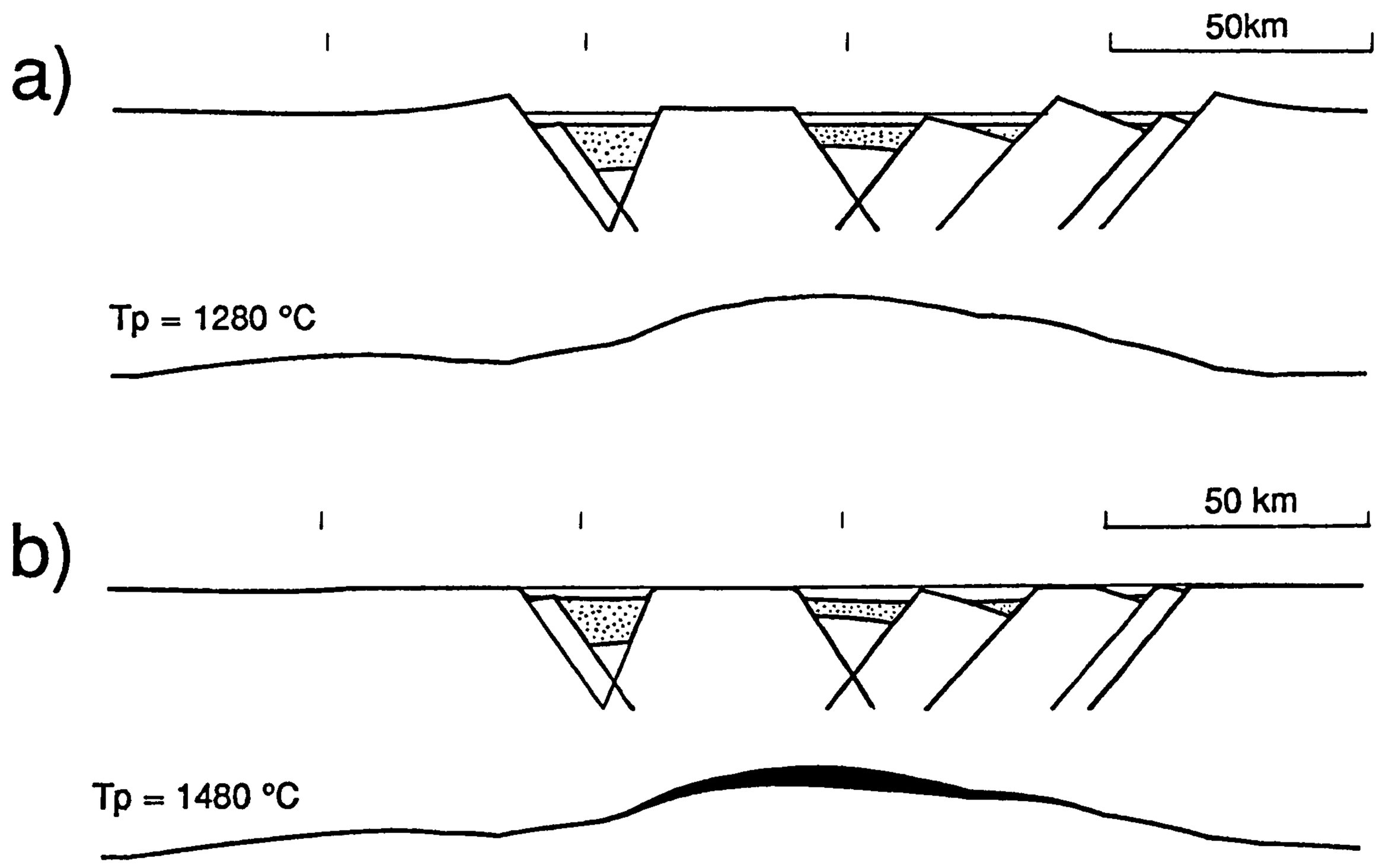


**Figure 4.13** Theoretical example of the combined magmatic-tectonic model in an intra-continental setting:- a) With sediment loading to a constant level of palaeo-bathymetry (1 km), but before erosion (Tp = 1280 °C). b) With magmatic underplating (Tp = 1480 °C) and after erosion of any blocks above sea level.

## 4.5 The Combined Magmatic-Tectonic Model at Passive Margins.

### 4.5.1 Introduction.

The tectonic evolution of the central/southern Red Sea remains controversial and two end-member models have been proposed which exemplify the possible range in passive margin morphology (Figure 4.14). The model favoured here (Figure 4.14b) is that of Girdler & Styles (1974) in which virtually the entire width of the basin is underlain by oceanic crust and the Moho rises steeply such that oceanic crust abuts nearly normal thickness continental basement. This model is most consistent with the magnetic anomaly pattern in the southern Red Sea. Although the other model (Figure 4.14a) does not match the tectonic evolution of this part of the Red Sea, it can be applied to other passive margins where the crust thins over a broad zone (up to 150 km wide) e.g. the highly attenuated Bay of Biscay margin (Avedik et al., 1982). In the following sections two mechanisms are proposed which explain the differences in passive margin morphology.

### 4.5.2 Theoretical "Pure-Shear Breakup" at Passive Margins.

The passive margin models in Figure 4.15 have been generated by including extension on numerous faults which, when summed together produce a broad pure-shear thinning over 100 km at the right-hand end of the profile. Note that extreme rotation of initially planar faults has resulted in the evolution of low angle detachments with a curvilinear geometry. A simple, water loaded, symmetrical graben and broad horst are included at the left-hand end of the profile. The only difference between the model input is in the potential temperature. No melt is

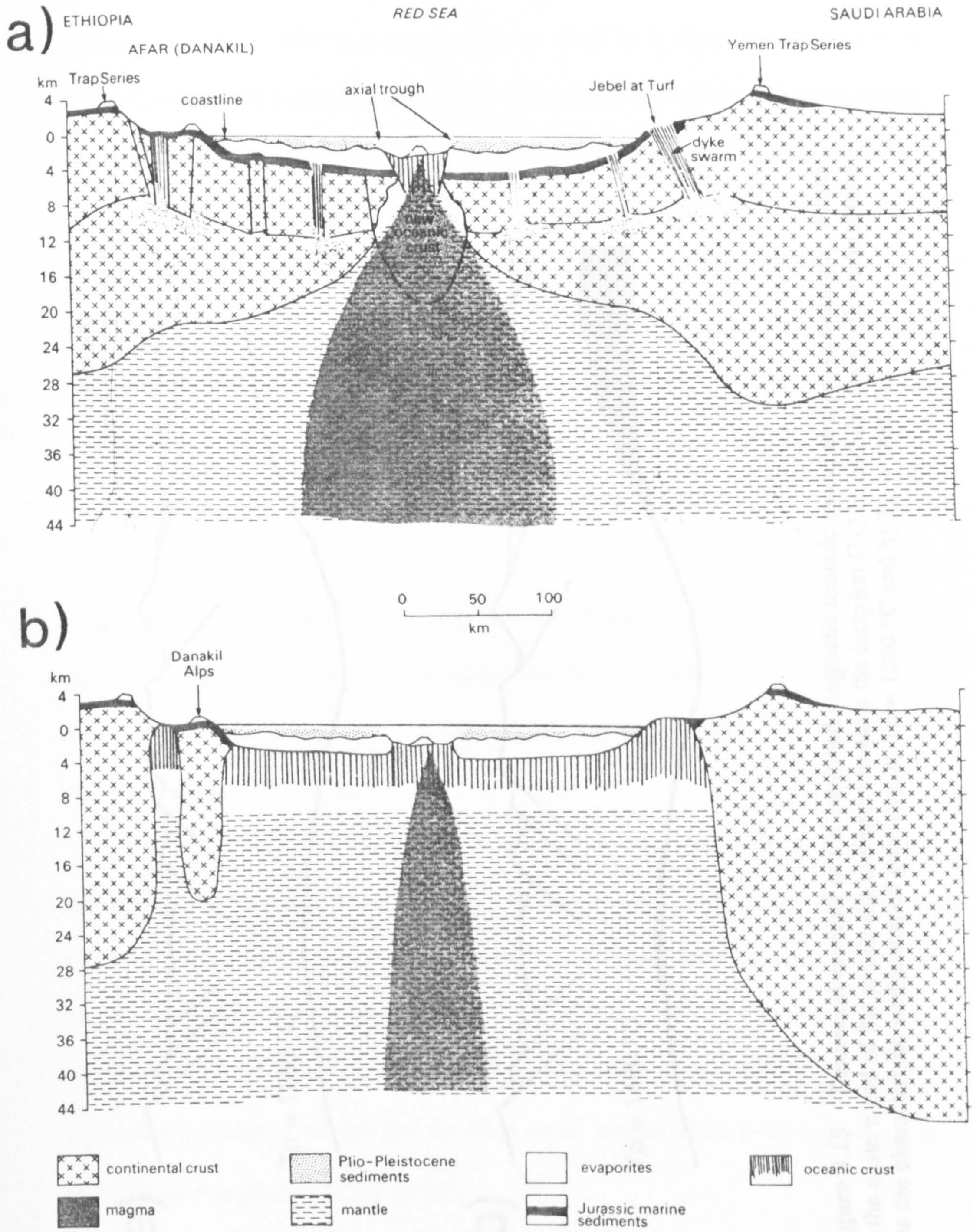


**Figure 4.14** The variation of passive margin geometry based on two models for the Red Sea. a) Continental crust extending out to the axial part of the Red Sea and b) Based on magnetic anomaly data, model b suggests that the majority of the basin is underlain by oceanic crust and that the Moho at the C.O.B. rises steeply over a very narrow zone, consistent with a "dyke injection breakup" (From Gass & Styles, 1980).

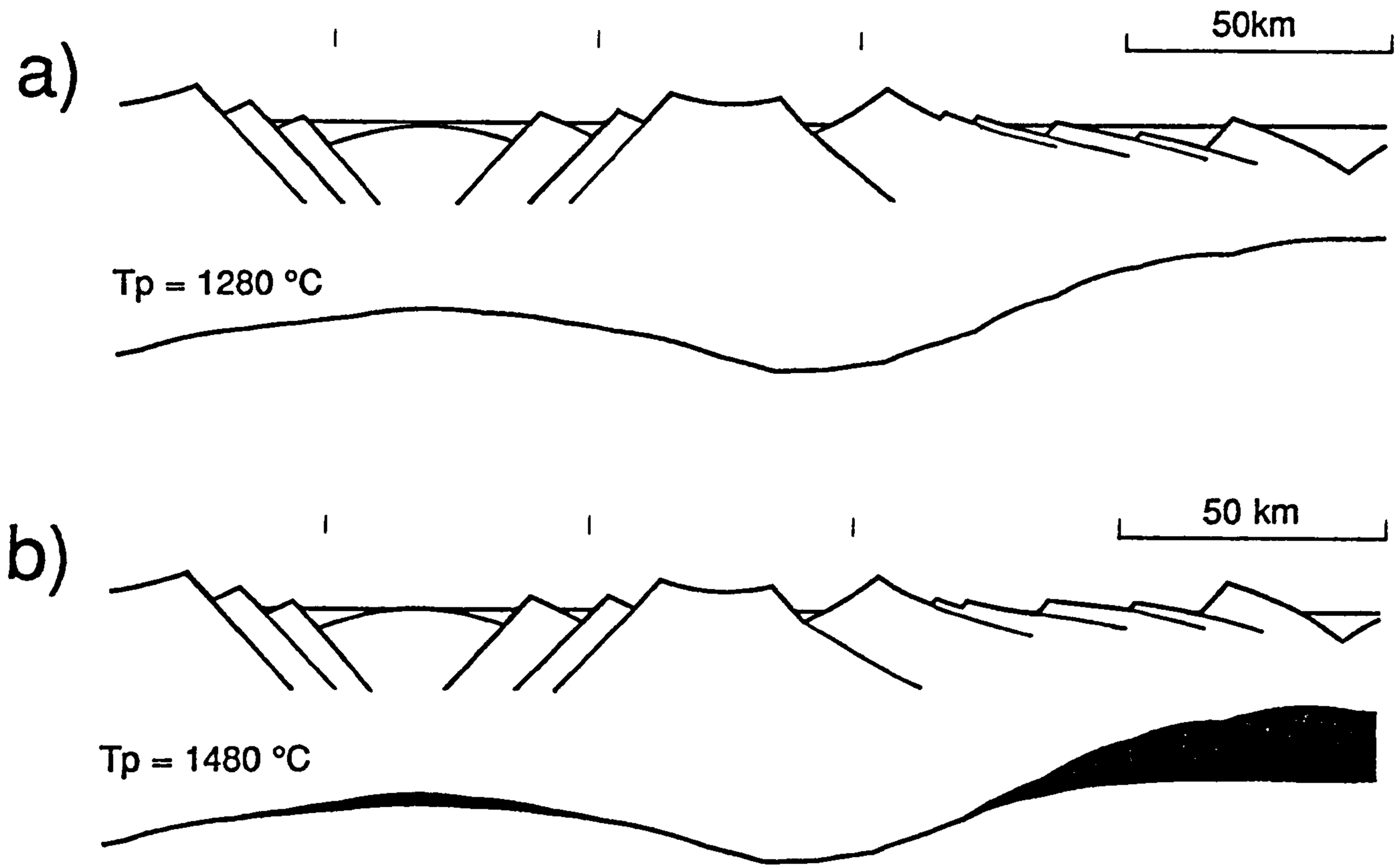


**Figure 4.15** Theoretical example of the combined magmatic-tectonic model at a passive margin. Faults at the eastern end of the profile dip uniformly towards the incipient C.O.B. and the magmatic underplating has the characteristic wedge-shaped geometry. a) Tp = 1280 °C and b) Tp = 1480 °C.

predicted with Tp = 1280 °C (Figure 4.15a) but when Tp is elevated a large amount of melt (about 8 km) is produced, close to what would become the continent ocean boundary in Figure 4.15b. Continental crust remains above sea level right out to the edge of margin above anomalously hot asthenosphere (Figure 4.15b), but subsides several kilometres when there is no underplating (Figure 4.15a).

It should be noted that the continental crust in Figure 4.15 remains 10 km thick at the right-hand end of the profile i.e. the breakup event has not been modelled to completion. The main reason for this is that the pure-shear component, which balances extension on the conjugate margin, but whose spatial distribution overlaps the proximal margin, has not been added to the profile. This situation is shown schematically in Figure 4.16 where the spatial distribution of pure-shear from the two margins are separated. Ideally, composite sections should be constructed across both margins and modelled together, but, alternatively, extra pure-shear can be added to the highly attenuated profile.

Figure 4.17 shows the effect of adding the contribution to the extension coming from the conjugate margin. For direct comparison with Figure 4.15, no sediment loading is calculated. Both profiles have been modelled by an extra amount of pure-shear, equivalent to extension of 60 km, located 50 km east of the profile and distributed up to 75 km west of this point. It can be seen that the magmatic underplating wedge is thicker and the crust much thinner when extra pure-shear is added at the eastern end of the model.

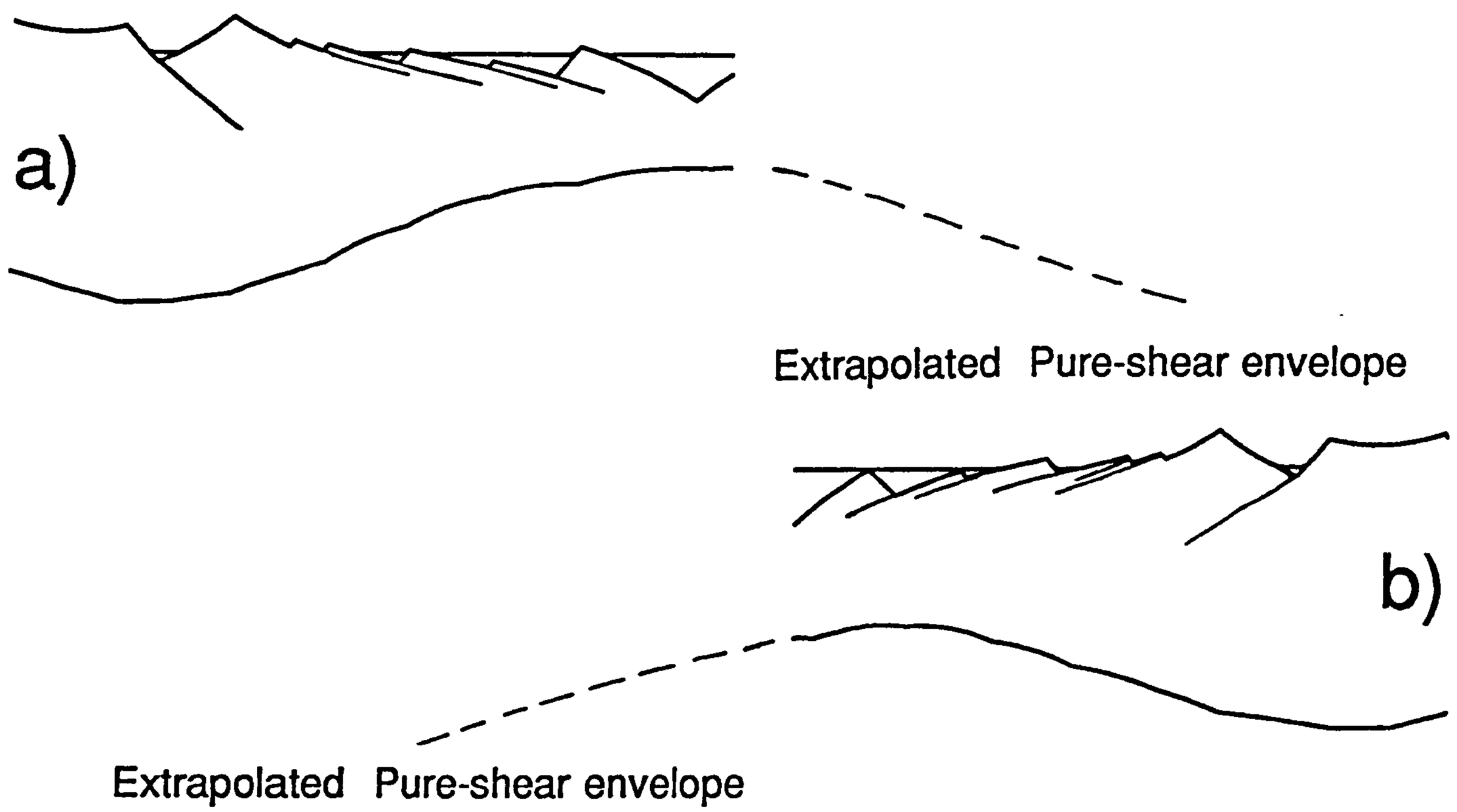


**Figure 4.16** Schematic section of two conjugate passive margins, just prior to breakup. The total pure-shear in the lower crust and mantle is the result of the superposition of pure-shear required to balance the extension of both margins. i.e. the pure-shear envelope for margin A overlaps margin B.

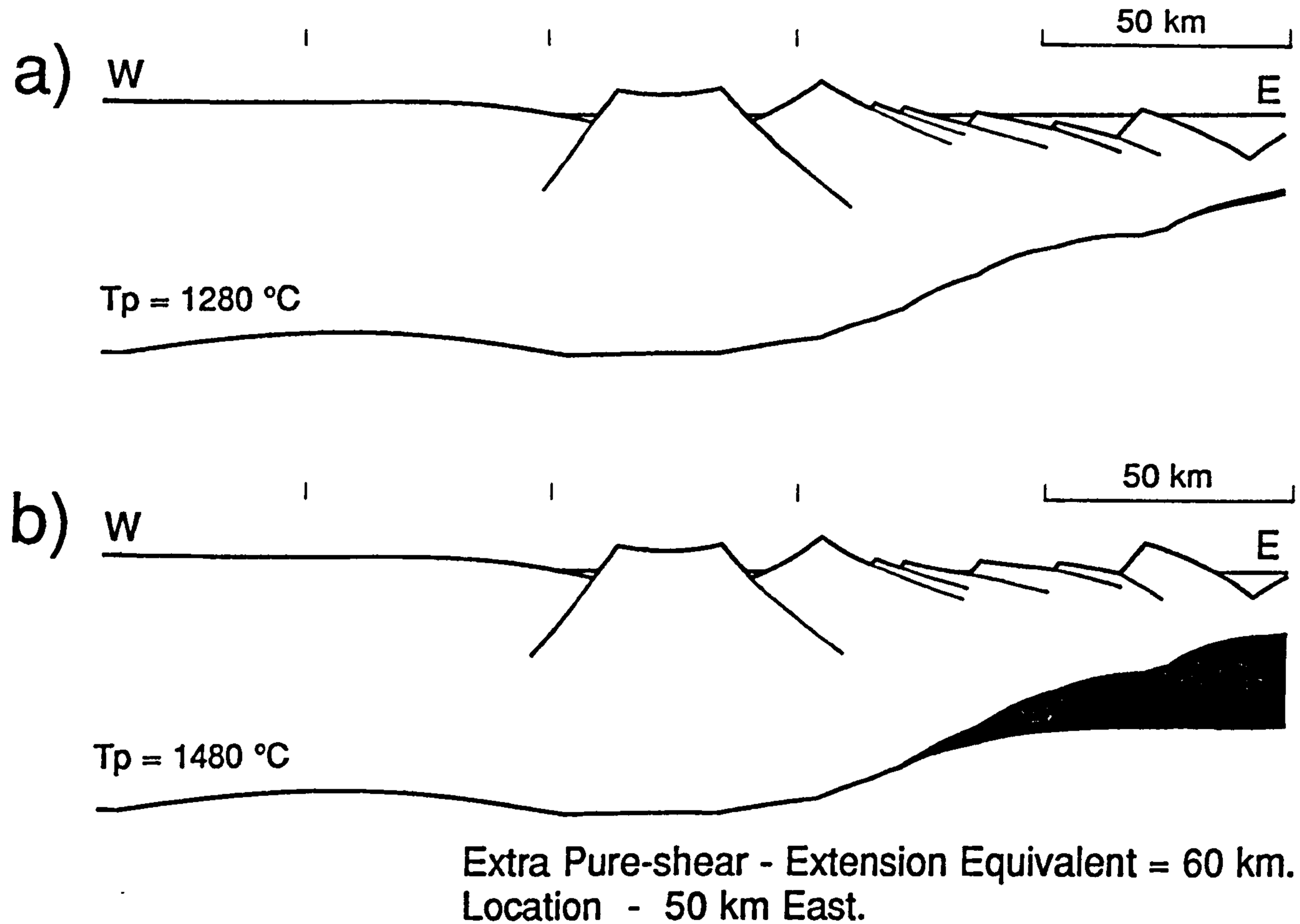


**Figure 4.17** Theoretical example of the combined magmatic-tectonic model (as for Figure 4.15) but with added pure shear equivalent to 60 km extension and a sinusoidal distribution over 75 km located 50 km East of the footwall cut-off. a) Tp = 1280 °C and b) Tp = 1480 °C.

### 4.5.3 Theoretical Dyke Injection / Lithosphere Rupture Breakup.

Figure 4.18a shows a simple, water loaded model in which the lithosphere has been partially thinned by extension on planar faults and, since the potential temperature is elevated, a certain amount of melt has been produced. No further pure-shear takes place, the thinned crust is ruptured and a 10 km wide dyke emplaced between the two continental blocks (Figure 4.18b). The height of the dyke, at this potential temperature, is calculated from the Bickle - McKenzie model using an infinite Beta factor. The magnitude of uplift, on either side of the dyke, is affected by the assumption of zero flexural rigidity for the zone of intrusion. Two halves of the model no longer mutually support each other and the centre of the rift basin subsides. Similar effects are expected in the case of Te reduction, due to progressive intrusion of dykes, leading to breakup. It is emphasised again that pure-shear breakup and dyke injection breakup, as described in this section, are end member models. Dyke injection, through highly attenuated crust, is likely to be a common phenomenon close to the "final break" of the lithosphere.

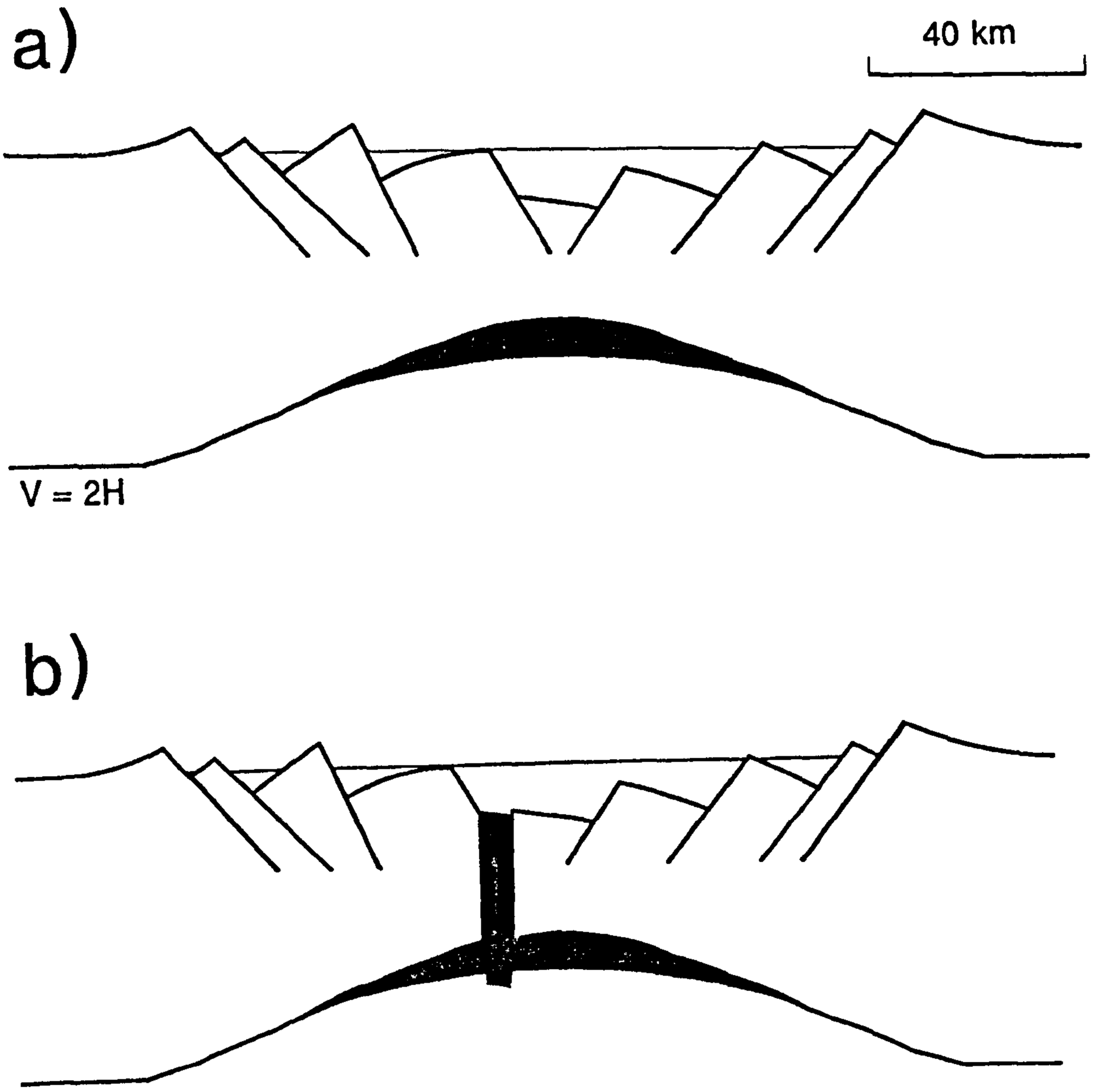


**Figure 4.18** Theoretical example of the combined magmatic-tectonic model applied to a "dyke-injection breakup". a) Small amount of extension with melt production due to the elevated Tp. b) Injection of a 10 km wide dyke into a zone of zero effective elastic thickness.

# CHAPTER 5

# THE TECTONO-STRATIGRAPHY OF THE GRAND BANKS, OFFSHORE NEWFOUNDLAND.

## 5.1 Introduction.

The methodology adopted in this thesis to determine the timing of breakup is, wherever possible, to date the continent ocean boundary independently of the biostratigraphic gap at the breakup megasequence boundary, using data from the adjacent oceanic basin (Figure 5.1). This approach avoids circular arguments when discussing the causative link between the onset of seafloor spreading and the uplift and erosion at the level of a particular megasequence boundary. However, once a causative link between a certain breakup event and a megasequence boundary has been established, by a temporal correlation, the precise timing of breakup is obtained biostratigraphically. It should be emphasised that interpretations of seismic data, obtained for this study, listed in Appendix C, and described in Chapter 6, allows objective conclusions to be drawn from the review of the tectonic evolution of the North Atlantic. The resultant tectono-stratigraphic framework for the Grand Banks is new, particularly with respect to the southeastern margin.

The Grand Banks lie adjacent to Newfoundland on the eastern coast of Canada (Figure 5.2a) and can be defined as the area bounded by the 3000m isobath (Figure 5.3). The present day basin architecture results from a long rifting history, including two main phases in the Late Triassic-early Jurassic and the second in the Late Jurassic-early Cretaceous. Figure 5.3 shows the main tectonic elements of the Grand

a)

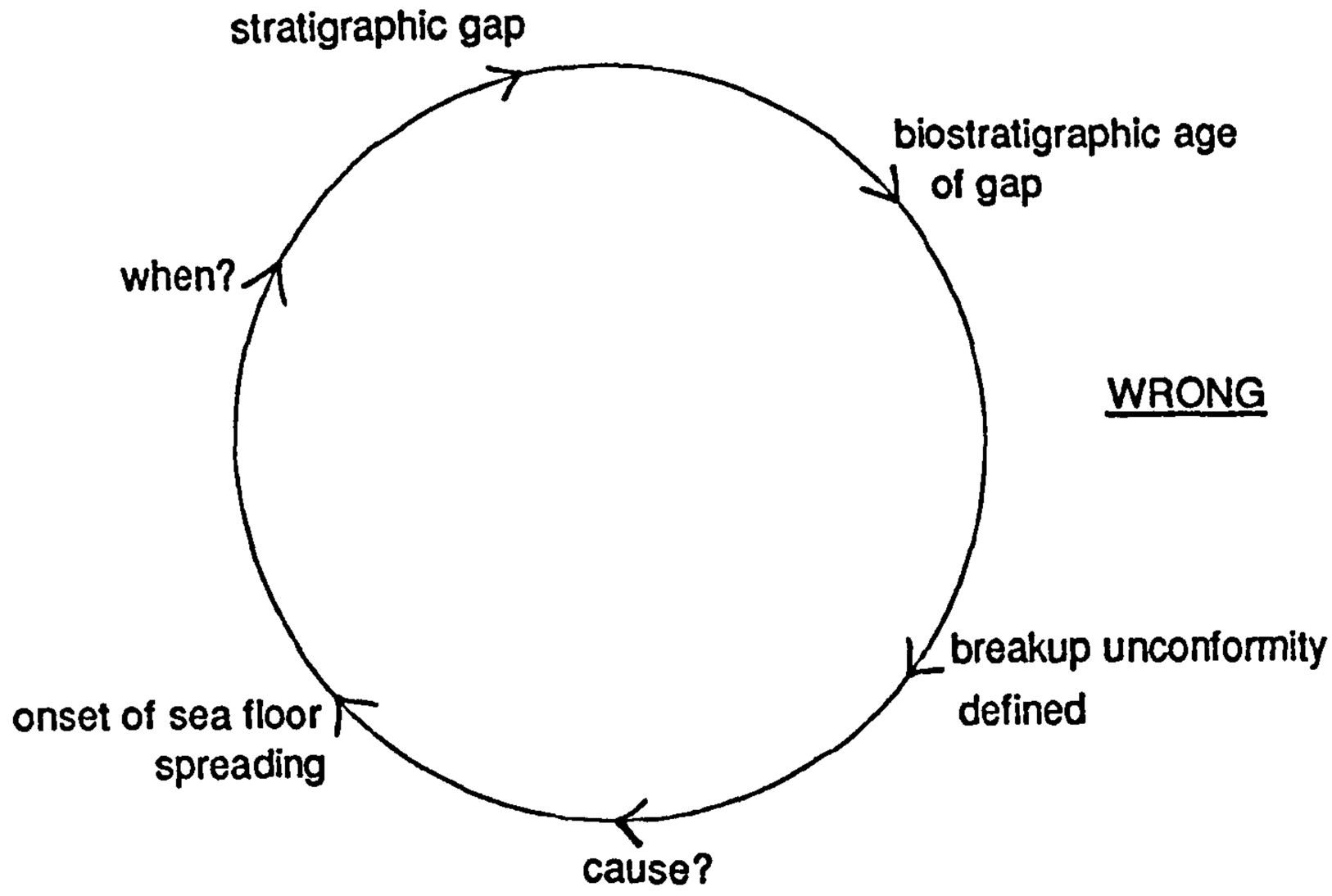


b)

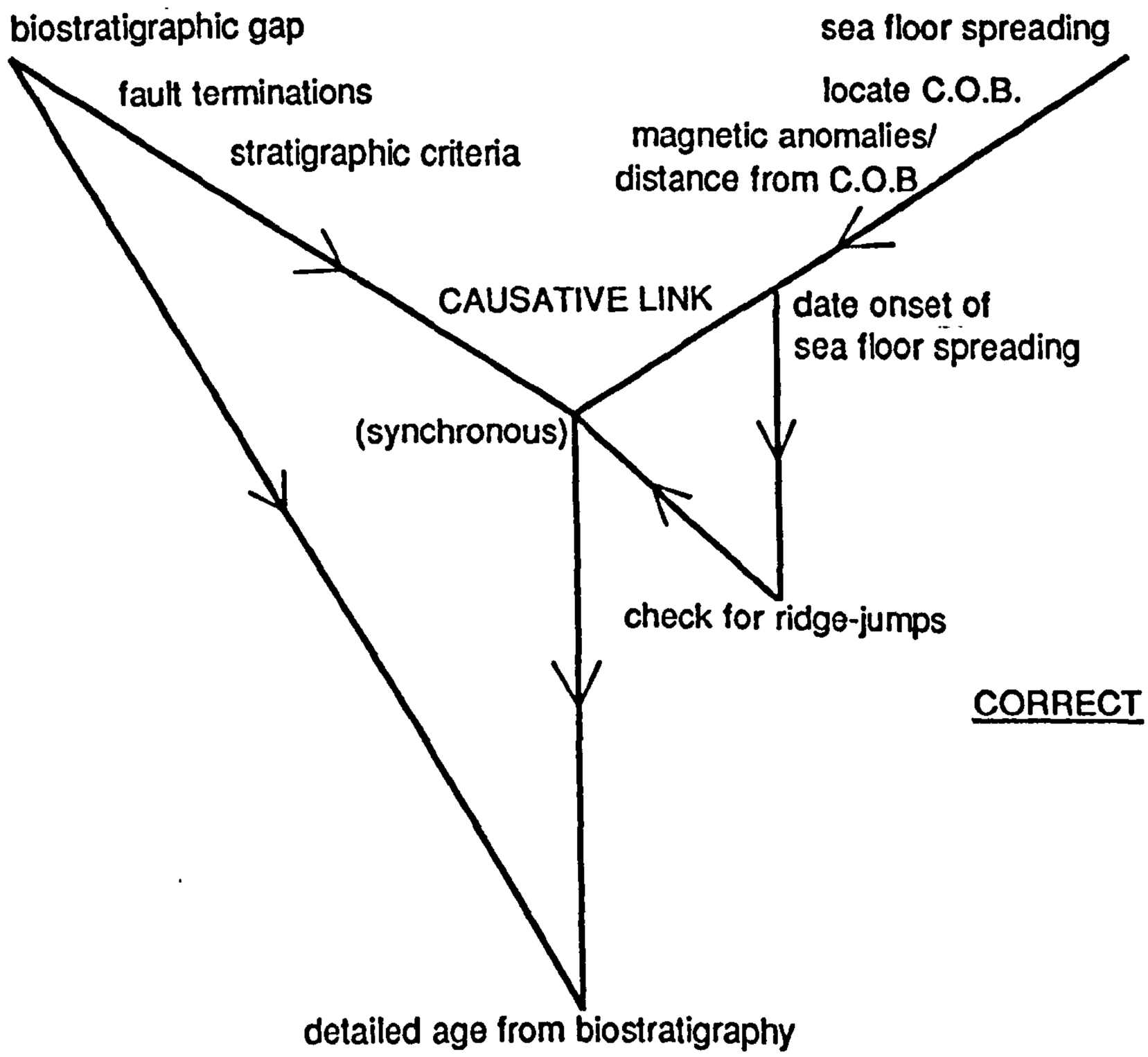


**Figure 5.1** Methodology adopted in this thesis for the age determination of a particular breakup megasequence boundary.

a)


b)

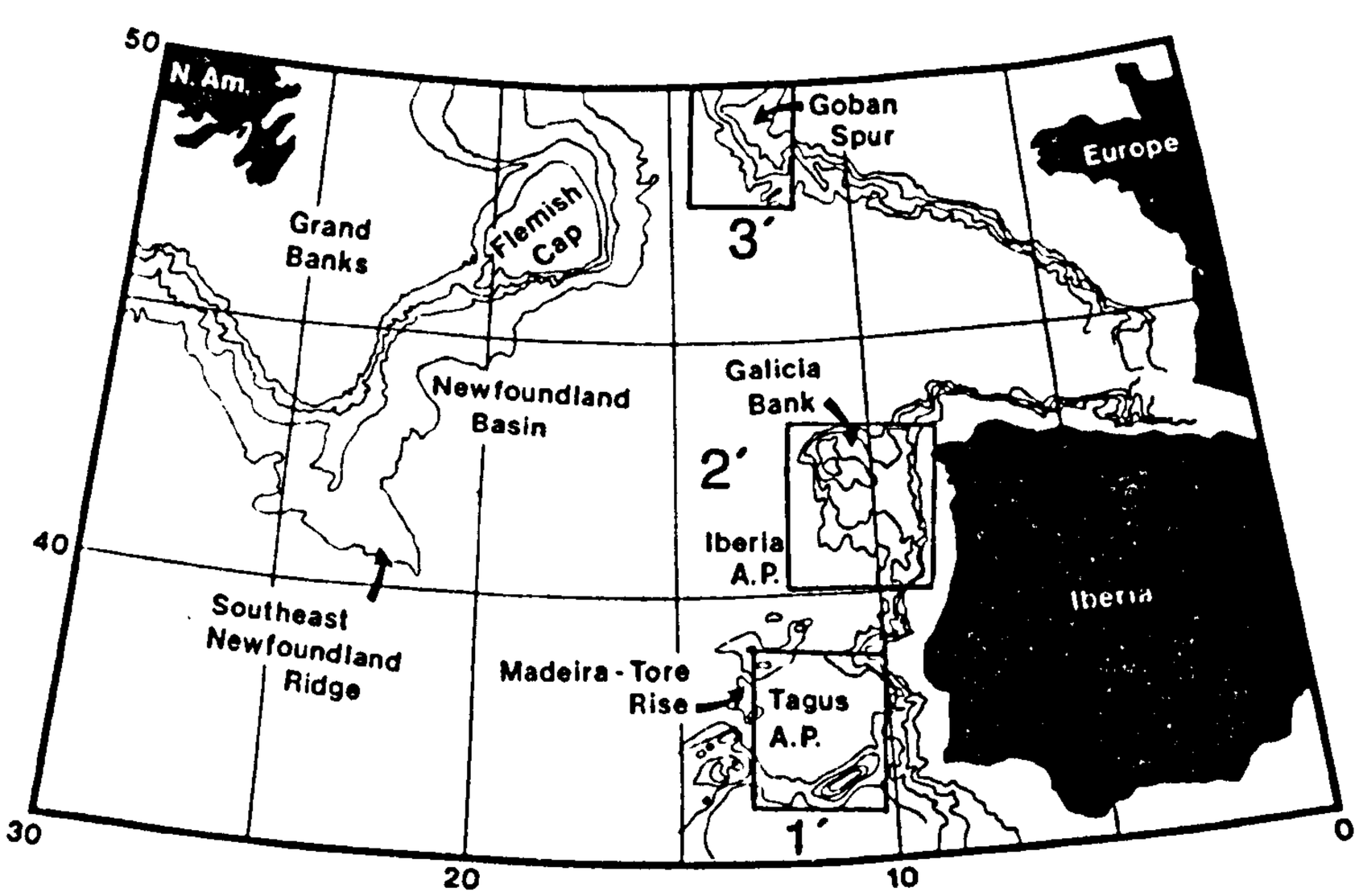


**Figure 5.2** a) Location of the Grand Banks (shaded) adjacent to Newfoundland on the eastern coast of Canada. b) Location map of the three conjugate margins studied in this chapter; The Tagus Abyssal Plain, Galicia Bank and Goban Spur (Masson & Miles, 1985).

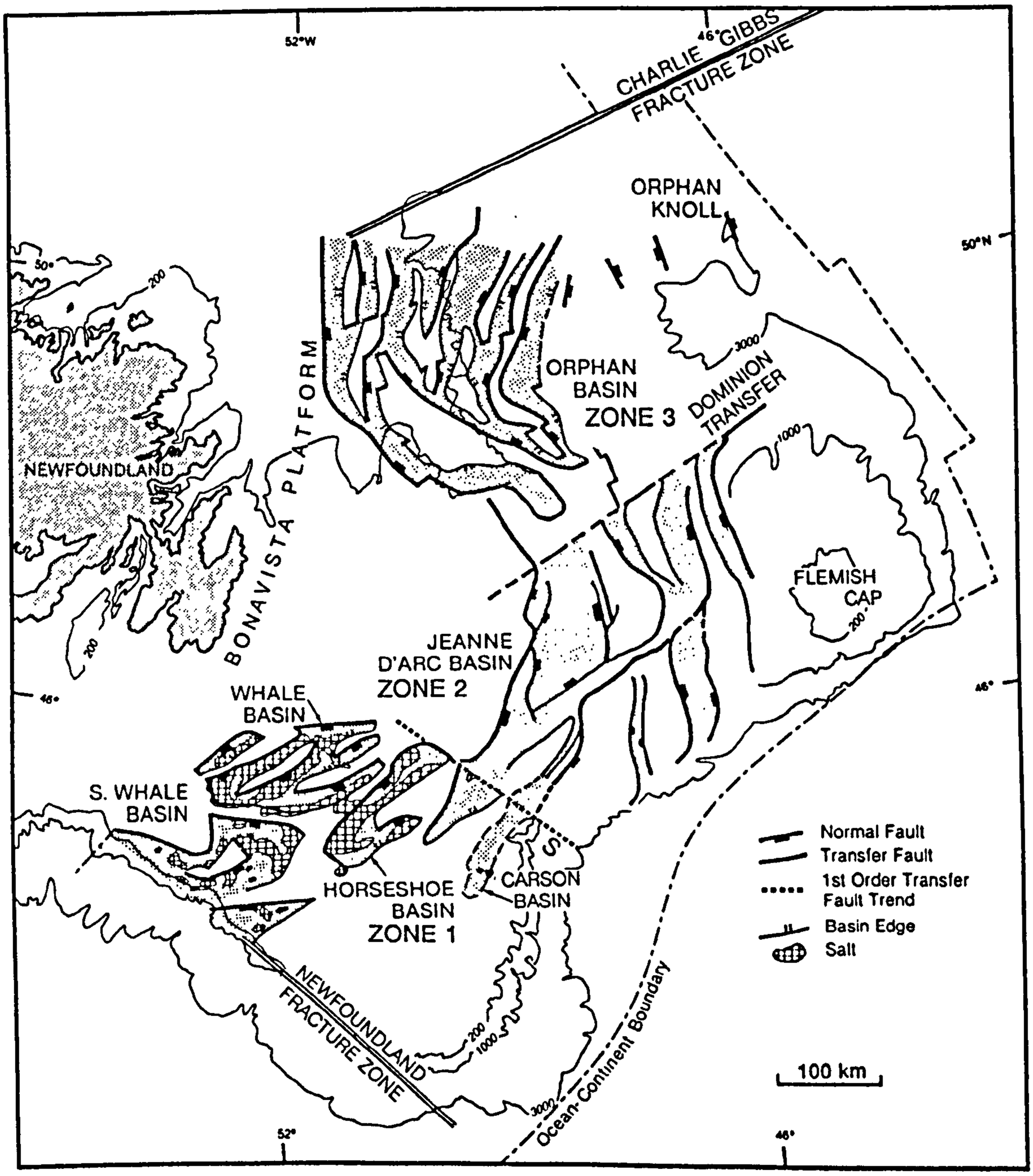


**Figure 5.3** The Grand Banks study area, from Figure 5.2a, enlarged to show the main structural elements and the sub-division into three tectonic zones - 1, 2 and 3.

Banks, which, from south to north are the Whale, Horseshoe, Carson, Jeanne d'Arc, Flemish Pass (Gabriel) and Orphan basins. These basins are separated by the Morgiana High, Vesta Horst, Central, Eastern and Beothuk ridges, and bounded to the west by Bonavista Platform. Prominent basement highs occur in the north, Orphan Knoll, and northeast, Flemish Cap. Four major transform faults cross the Grand Banks and subdivide it into three distinct tectonic zones (Tankard & Welsink 1987). They are a requirement of sequential breakup in the N. Atlantic and accommodate the variation in strain between tectonic zones. Two of the transfer zones trend NW-SE across the southern end of Grand Banks (Figure 5.3). The Newfoundland Fracture zone developed in the middle to upper Jurassic, as the spreading ridge formed by an early breakup migrated along the southern margin of the Grand Banks (Klitgord & Schouten, 1986). The second, unnamed, transfer zone is clearly defined on Figure 5.4 - the gravity anomaly map of Welsink et al. (1989) - and crosses the northern margin of the Horseshoe Basin and the southern end of the Jeanne d'Arc basin. The boundary between zones 2 and 3 is the NE-SW trending Dominion Fault (Figure 5.3), as defined by Enachescu (1987), parallel to the Voyager Fault Zone (Fucke & Daly, 1988). These were normal faults during the first rift phase and subsequently reactivated as transforms prior to the breakup in Zone 3 (Fucke & Daly, 1988). The northwestern boundary of Zone 3 is formed by the Charlie Gibbs Fracture Zone (Figure 5.3, Tankard & Welsink, 1989).

In addition to the three tectonic zones which lie within the 3000 m isobath, it is thought that the tectonics of the area South of the Newfoundland Fracture Zone are linked to the evolution of the Grand Banks. However, a detailed description of the breakup megasequence boundary for this area is beyond the scope of this thesis.

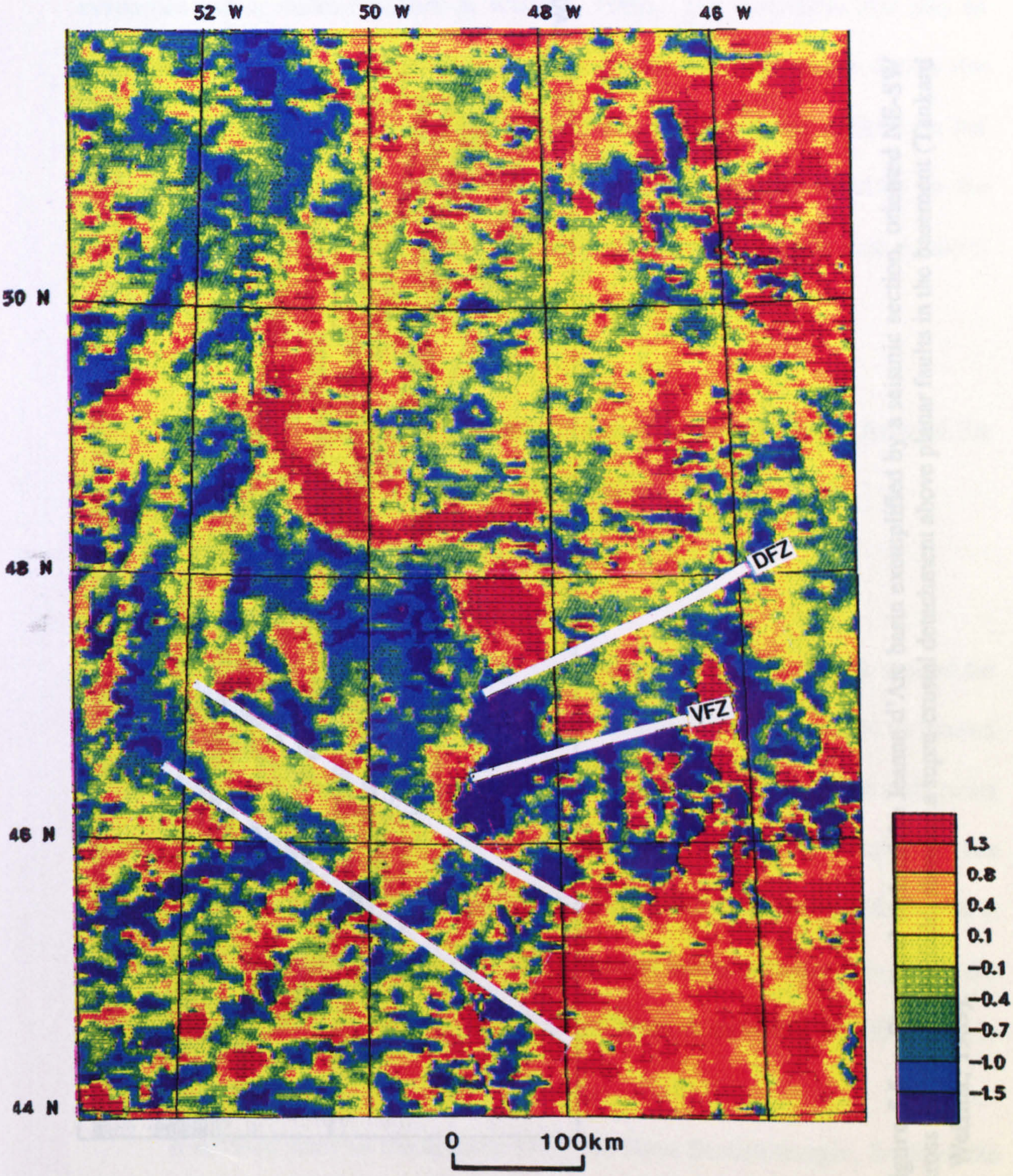


**Figure 5.4** First derivative Bougier gravity anomaly map from Welsink et al. (1989) showing the preferred orientation of the Voyager (VFZ) and Dominion (DFZ) transfer faults.

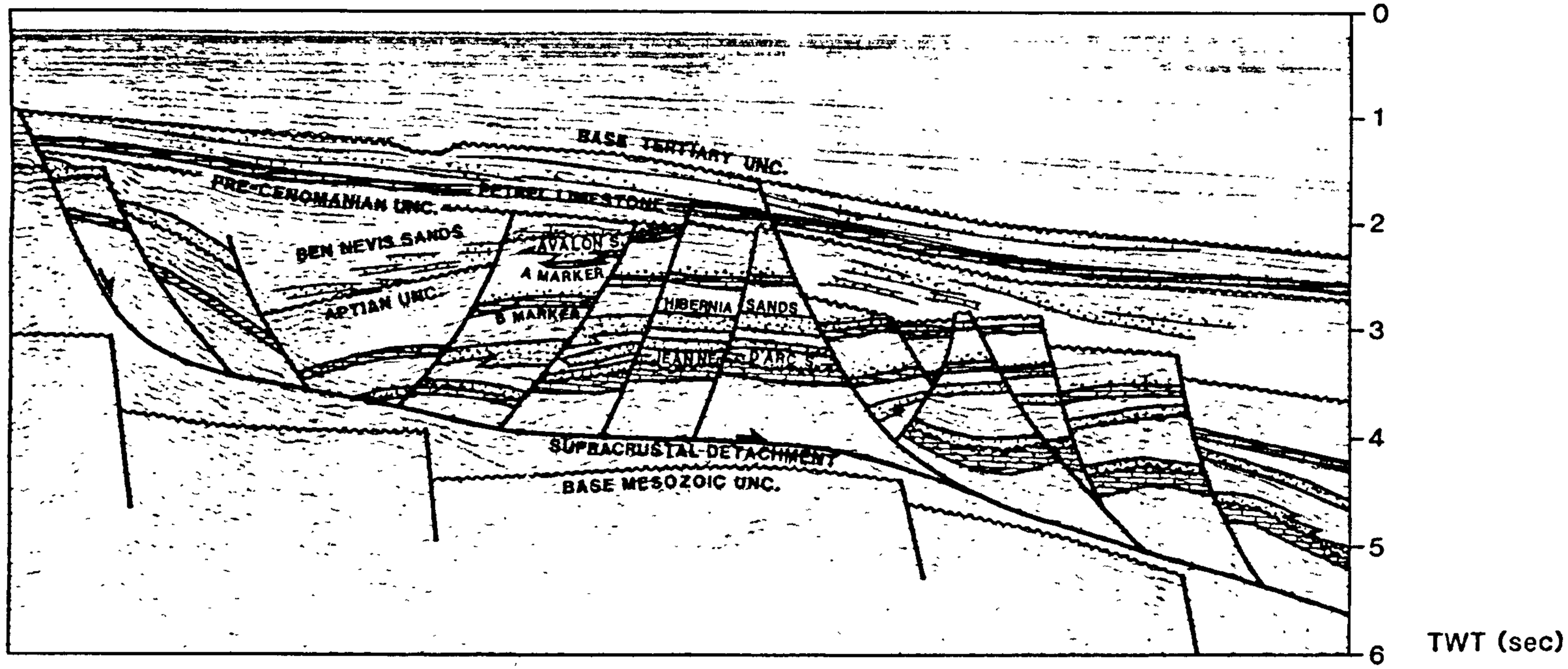


**Figure 5.5** Structural style of the Jeanne d'Arc basin exemplified by a seismic section, oriented NE-SW across the Hibernia oilfield, showing a supra-crustal detachment above planar faults in the basement (Tankard & Welsink, 1989).

The predominant structural style of basins on the Grand Banks is one of grabens and half-grabens, controlled by major planar faults (Figure 5.5), in which the upper part of the sedimentary infill is bounded by listric faults which detach into evaporites and/or shales (Tankard & Welsink, 1989). Salt kinematics also play an important part in the later development of the basins especially where diapirs rise preferentially up fault planes and from fault crests. Hydrocarbon exploration has been concentrated in the Jeanne d'Arc basin where a rollover structure in the hangingwall of the Murre and Nautilus faults has produced a trap in Late Jurassic/ Early Cretaceous clastics of the Hibernia field (Figure 5.5).

## 5.2 Location of the C.O.B. and the Timing of Breakup Events Around the Grand Banks and on the Conjugate Margins.

### Grand Banks.

Considerable debate still exists on the exact position of the C.O.B. around the Grand Banks, especially at the southern margin. Ideally the C.O.B. should be located using gravity, magnetic and deep seismic data, the latter giving the least ambiguous results. Deep seismic data (Figure 5.6a), described in detail in Chapter 6, has enabled objective conclusions to be made in this study and facilitated a critical review of the tectono-stratigraphy. Although there are some minor differences in detail, the present interpretations agree well with those of Keen & deVoogd (1988) shown in Figure 5.6b.

A detailed study of the breakup along the Nova Scotian margin, South of the Grand Banks, is beyond the scope of this thesis. The age of breakup is disputed and

a)

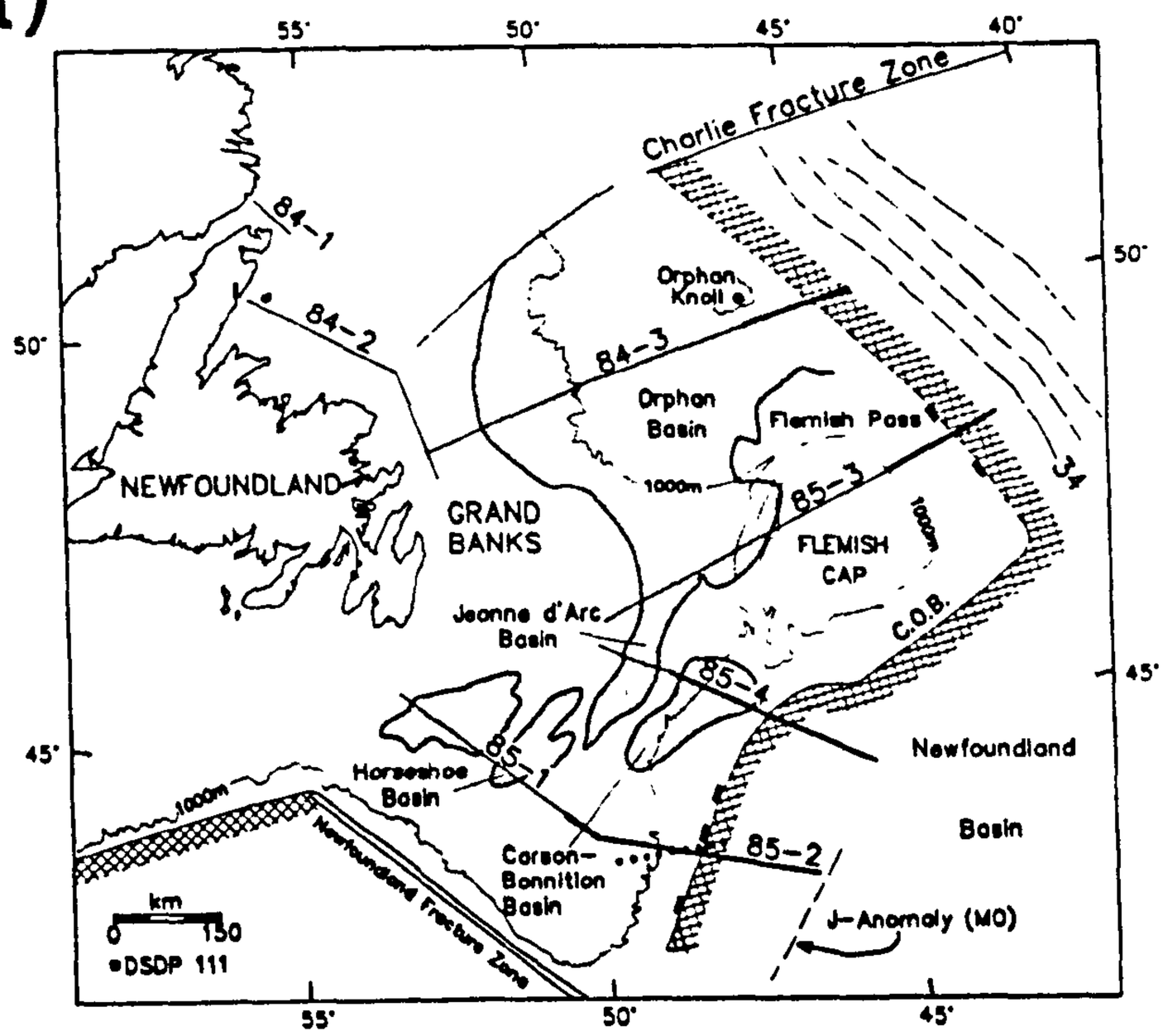


b)

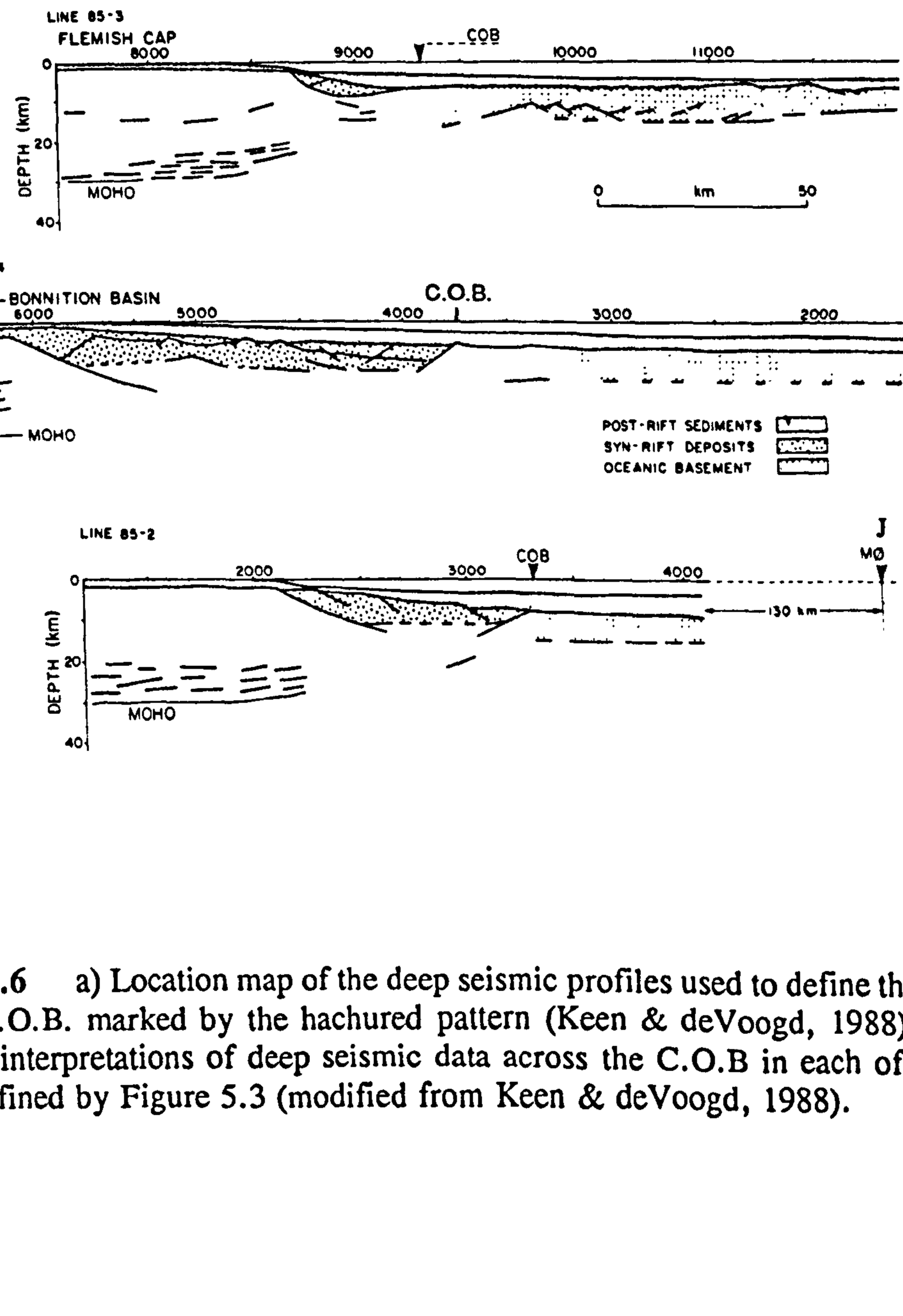


**Figure 5.6** a) Location map of the deep seismic profiles used to define the position of the C.O.B. marked by the hachured pattern (Keen & deVoogd, 1988). b) Line drawing interpretations of deep seismic data across the C.O.B in each of the three zones defined by Figure 5.3 (modified from Keen & deVoogd, 1988).

depends on the post-breakup sea floor spreading rate, prior to a ridge-jump associated with the Blake Spur Magnetic Anomaly (B.S.M.A - 170 Ma). If it assumed that the seafloor spreading rate was constant before and after the ridge-jump (1.91 cm/yr) then the breakup took place at 175 Ma, but if, prior to the ridge jump, a much slower rate is assumed, then the onset of seafloor spreading may lie in the age range 185-188 Ma (Klitgord and Schouten, 1986). Onshore volcanic intrusions, which may be related to the opening (e.g. Pallisade Sills and the Bay of Fundy Basalt), yield both of these ages (Jansa and Pe-Piper, 1988) but the older of the two is considered by Sutter (1985) to be more accurate.

**Zone 1**

The interpretation of the Lithoprobe deep seismic profile 85-2 across the southern Grand Banks has now shown that the C.O.B. in Zone 1 lies 160 km west of the J-Anomaly ridge (Keen & DeVoogd, 1988) (Figure 5.6). It can be defined as the point where the Lithoprobe data shows thinned continental crust wedging out on top of the magmatic oceanic basement. Following Tucholke & Ludwig (1982) and Mauffret et al. (1989), it is preferred to assign the central part of the J-Anomaly ridge to magnetic Anomaly M2 (Figure 5.7) rather than M0 (Keen & deVoogd, 1988). By assuming that the seafloor spreading rate (1.71 cm/yr) was constant either side of magnetic Anomaly M0, it has been calculated that the 160 km of oceanic crust between the J-Anomaly ridge and the C.O.B. represents 9 Ma of seafloor spreading (Mauffret et al., 1989). The age of the breakup adjacent to the southern Grand Banks margin therefore becomes 131 Ma.

Tucholke et al. (1989), who have interpreted a multichannel seismic survey

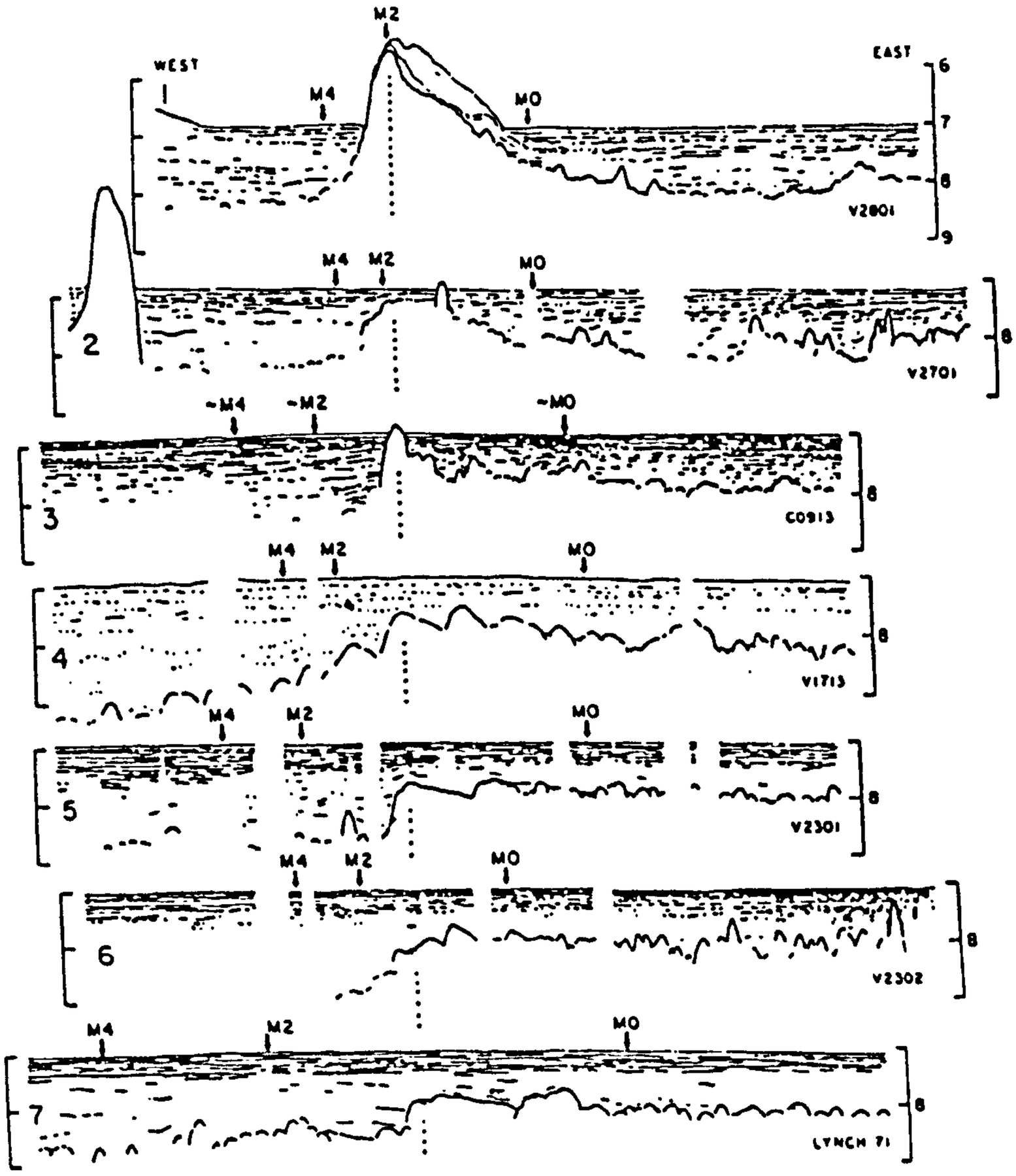


**Figure 5.7** The J-anomaly ridge and associated magnetic lineations (Tucholke & Ludwig, 1982).

across the Newfoundland Basin between the J-Anomaly ridge and the hinge zone, dispute Keen & deVoogd's location of the C.O.B.. However, their profiles (Figure 5.8) although clearly faulted, appear to more closely resemble oceanic basement, e.g. the eastern end of Lithoprobe line 85-2 (Keen, 1992 pers. com.). It is therefore argued here that the C.O.B. is not coincident with the J-Anomaly ridge.

**Zone 2.**

The J-Anomaly ridge on Figure 5.6a is not defined East of Flemish Cap and it is assumed to converge with the C.O.B. just South of the boundary with Zone 2. This is clear on the conjugate margin (see below) and implies that the breakup between Flemish Cap and Galicia Bank took place at, or just after, Anomaly M0 (118 Ma). Breakup then continued round into the Bay of Biscay. Because of the northward propagation of seafloor spreading between Grand Banks & Iberia, reconstructions to M0 should show overlap between Flemish Cap and Galicia Bank (e.g. Srivastava & Tapscott, 1986; Srivastava & Verhoef, 1991).

**Zone 3.**

In Zone 3 the breakup occurred within the Cretaceous Quiet Zone and the onset of seafloor spreading is most often given as "pre- Anomaly 34 (Pre- Santonian 85 Ma). A more precise date for the breakup has now been obtained as a result of the accurate location of the C.O.B. on the deep seismic profile, Lithoprobe 85-3, which crosses the northeastern margin of Grand Banks (Figure 5.6). It is 110 km away from Anomaly 34 and, assuming a constant seafloor spreading rate of 5.5 mm/yr, the age of breakup is placed in the middle Albian (105 Ma) (Srivastava & Tapscott, 1986).

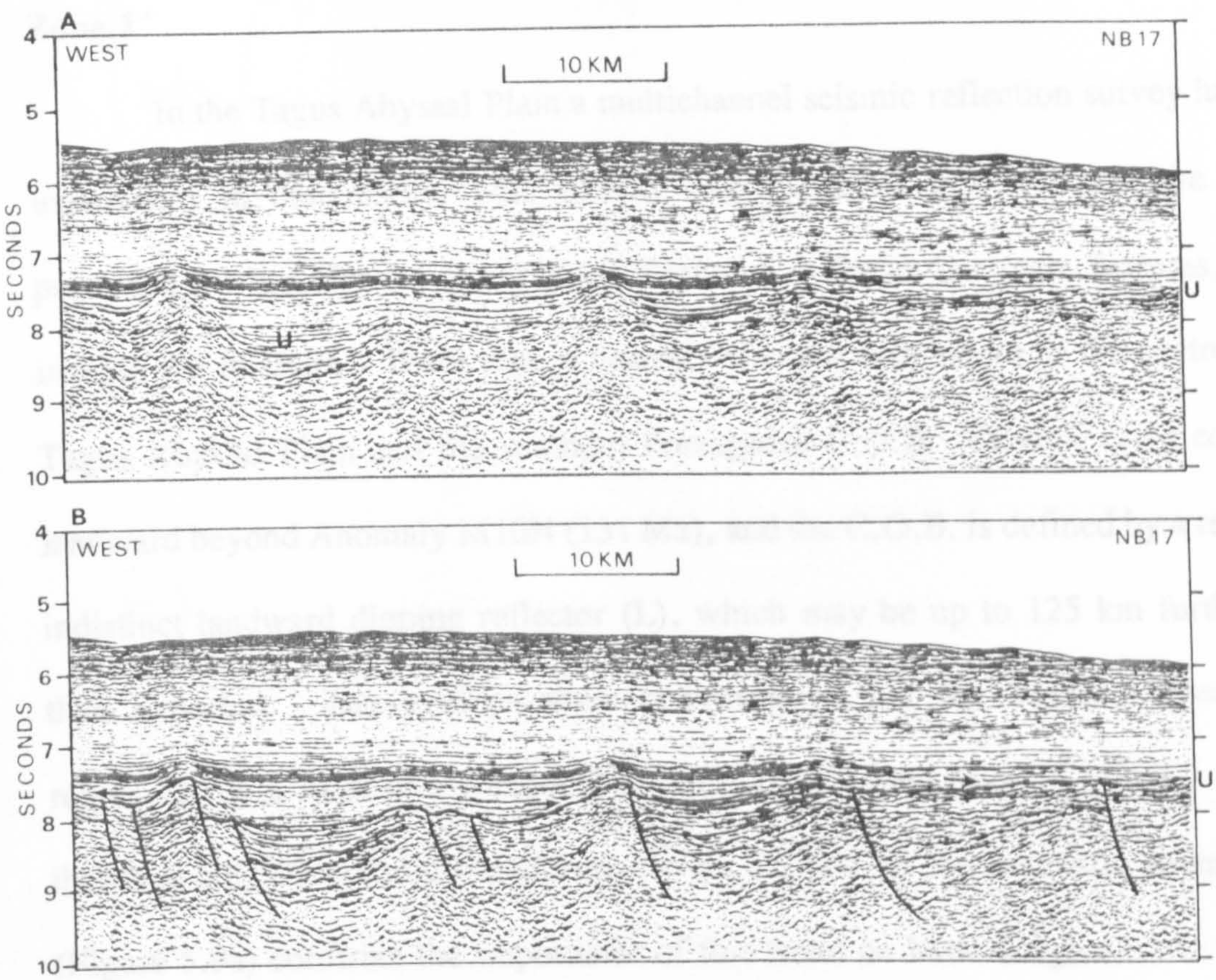


**Figure 5.8** a) Un-interpreted, and b) interpreted seismic profile showing faulted oceanic crust West of the J-anomaly ridge, adjacent to southern Grand Banks zone 1 (seismics taken from Tucholke et al. 1989).

Conjugate Margins.

In order to check that breakup and the subsequent sea-floor spreading follows a simple progression in all zones around the Grand Banks, the conjugate margins have been studied. The southern Portuguese, Galicia Bank and Goban Spur conjugate margins, located on Figure 5.2b, can be defined as conjugate zones 1′, 2′ and 3′ respectively.

**Zone 1′**

In the Tagus Abyssal Plain a multichannel seismic reflection survey has been undertaken in conjunction with gravity and magnetic profiles, and the results presented by Mauffret et al. (1989). Figure 5.9 shows the main features, which include the Madeira - Torre rise, a central "rift-like" alignment in the centre of the Tagus Abyssal Plain and the southern Portuguese C.O.B. Oceanic crust continues landward beyond Anomaly M10N (131 Ma), and the C.O.B. is defined by a relatively indistinct landward dipping reflector (L), which may be up to 125 km further East than expected. The profiles show convincingly that the Tagus Abyssal Plain represents both sides of a spreading segment that existed prior to M10N. The fact that two NE-SW oceanic transforms can be defined on the magnetic anomaly map (Figure 5.9a) confirms the importance of this trend on both margins.

It is implied that at the Valanginian-Hauterivian boundary the spreading ridge moved back to the Grand Banks margin, in response to a major plate motion reorganisation, coincident with Anomaly M10N. The NW-SE plate motion direction and spreading ridge configuration, directly after the ridge-jump, is shown in Figure 5.10b. This event is of regional significance and can be recognised in both the North and South Atlantic (Klitgord & Schouten, 1986).

a)

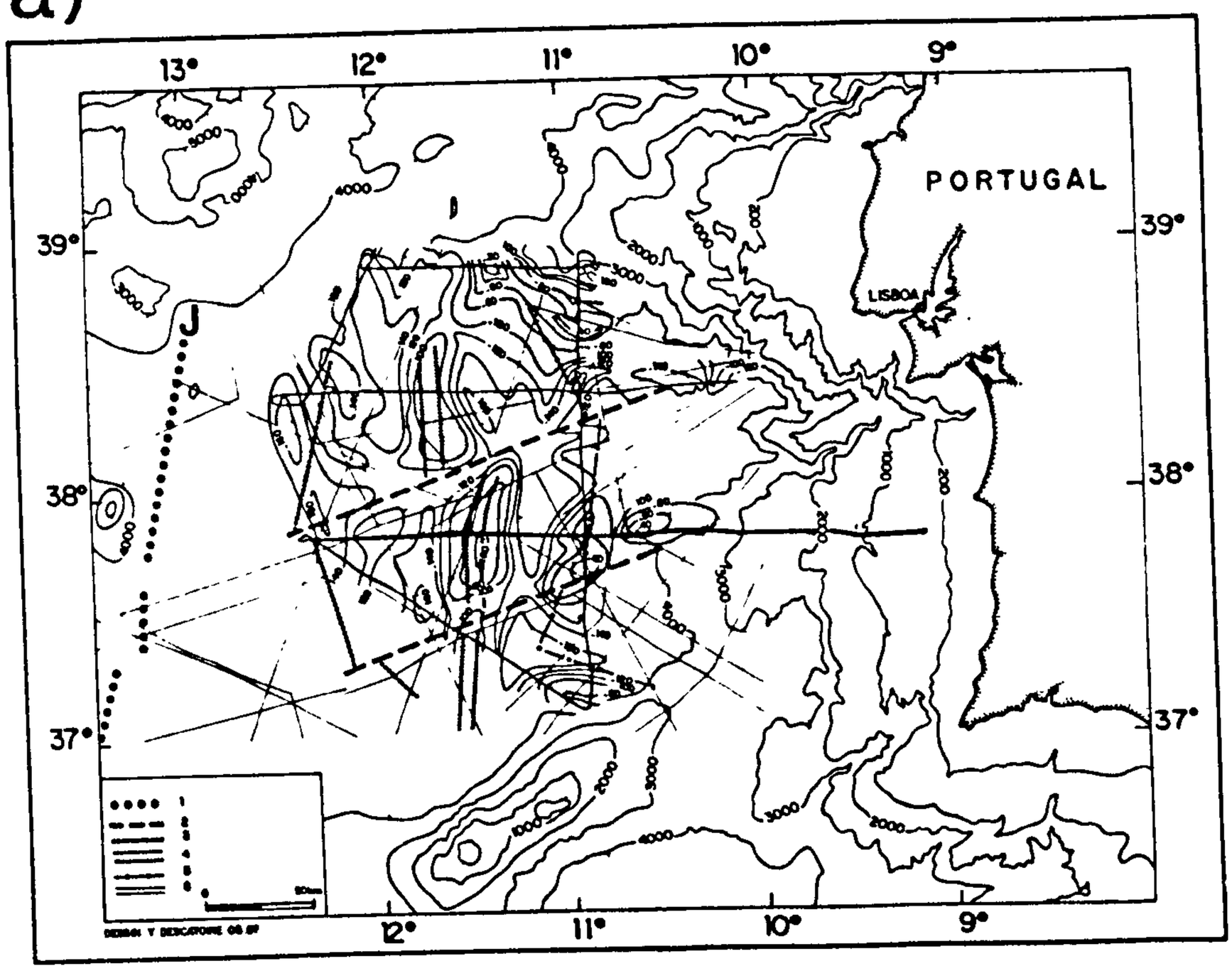


b)

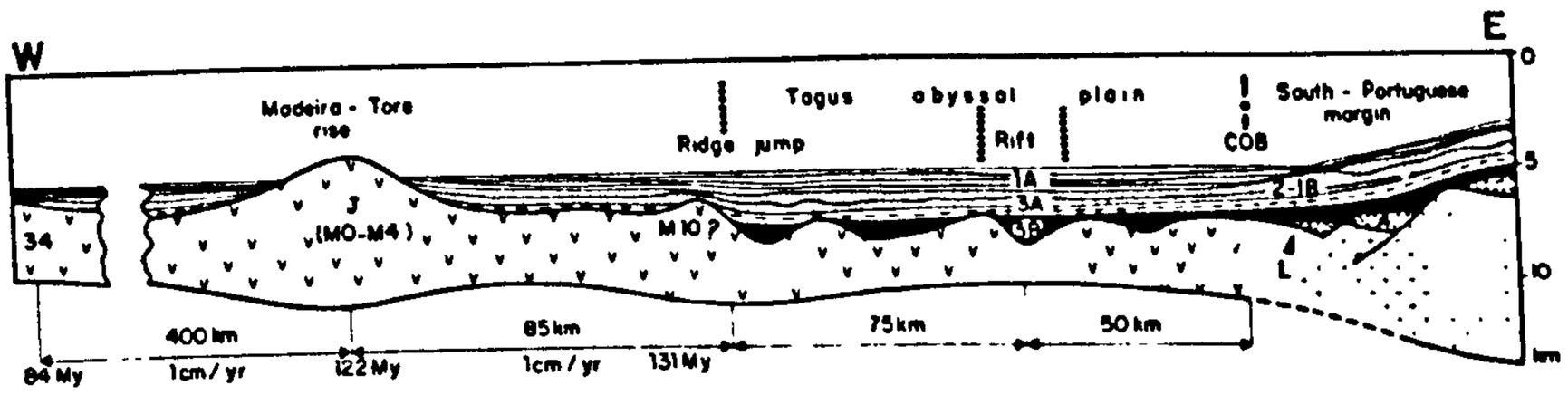


**Figure 5.9** a) Magnetic anomaly map of the Tagus Abyssal Plain (Mauffret et al. 1989). Note the NE-SW orientation of the two fractures zones. b) Schematic profile across the Tagus Abyssal Plain showing the south Portuguese C.O.B., the central abandoned spreading centre and the extrapolated position of Anomaly M10N (after Mauffret et al., 1989)

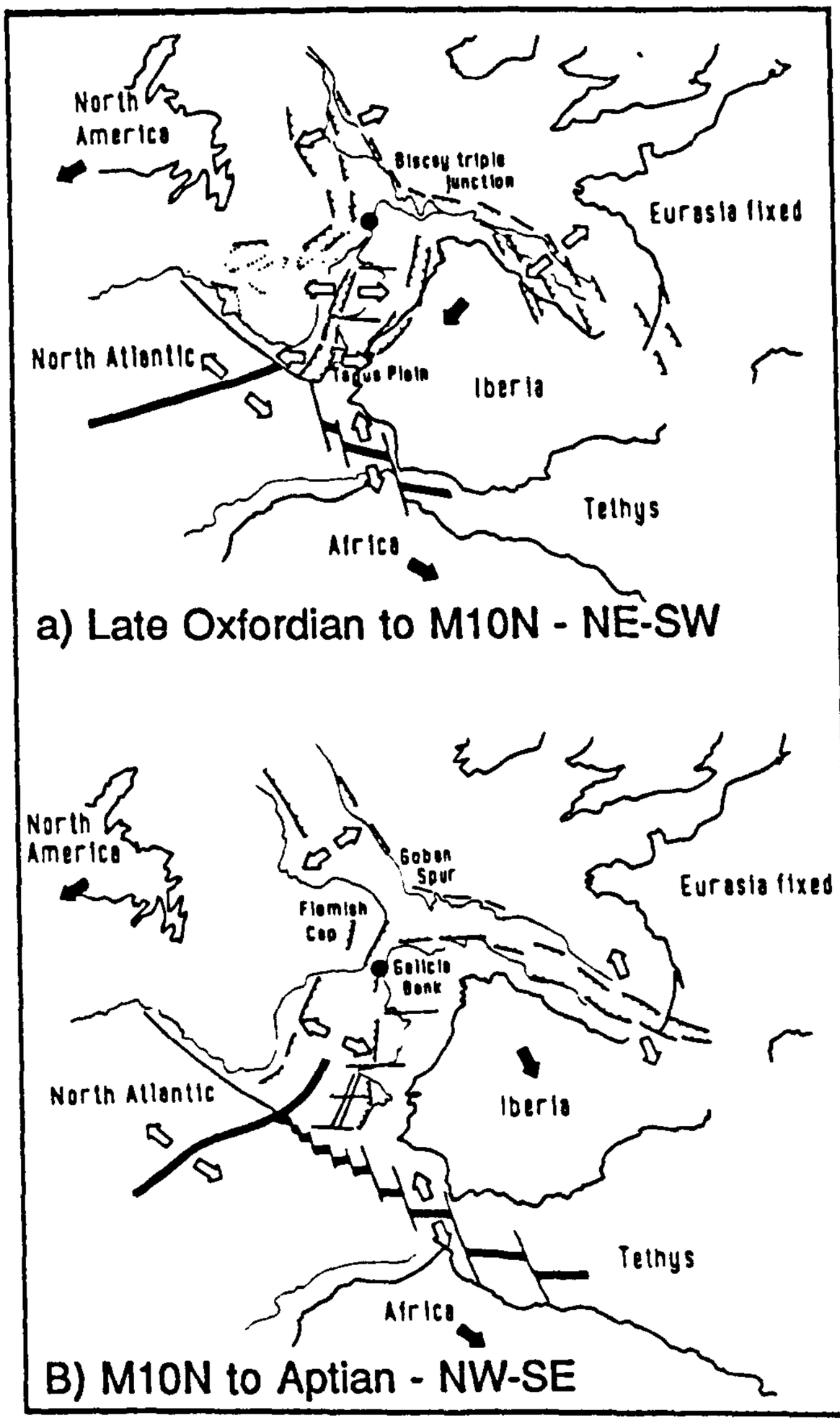


**Figure 5.10** Plate motion reorganisation with a ridge jump at anomaly M10N (131 Ma). NE-SW rifting, from the late Oxfordian onwards culminating at the base Valanginian breakup in the Tagus Abyssal Plain (A), reverts to NW-SE rifting until the base Aptian breakup (B). Modified from Mauffret et al. (1989).

The age of the true breakup in Zone 1´ cannot be defined accurately as result of this seismic survey alone. The results are consistent both with a breakup at 151 Ma (Anomaly M21) with seafloor spreading ceasing at 142 Ma (Mauffret et al. 1989), and also a breakup at 140 Ma with continuous seafloor spreading prior to the ridge jump.

The latter (i.e. basal Valanginian breakup) is preferred, for the reasons listed below:-

i) Syn-sedimentary faulting remained active in the Lusitanian Basin throughout the Tithonian (Wilson et al., 1989).

ii) NW-SE oriented dykes (perpendicular to the extension direction) have been dated at 140 Ma (Willis, 1988).

iii) The late Berriasian-base Valanginian sequence boundary in the Lusitanian Basin (Figure 5.11) meets the first three criteria for the recognition of a breakup megasequence boundary (Wilson, 1992 pers. com.).

iv) A late Berriasian - base Valanginian breakup would closely follow a change in the Atlantic spreading rate at Anomaly M16 (Klitgord & Schouten, 1986)

**Zone 2´**

The recent O.D.P. Leg 103 has defined the structural evolution of the Galicia Bank margin (Figure 5.2b) and deduced the geometrical relationship between the C.O.B., a peridotite ridge and the J-anomaly (Boillot et al., 1989). Figure 5.12a shows that the J-Anomaly (M0 - Base Aptian) cannot be recognised further north than 41.3° N, equivalent to the convergence of the J-anomaly with Flemish Cap in Zone 2. However, the peridotite ridge is directly in line with the J-anomaly and the most likely genesis is as a magmatic underplating wedge formed in the very late

# Zone 1´

# Lusitanian Basin Stratigraphy

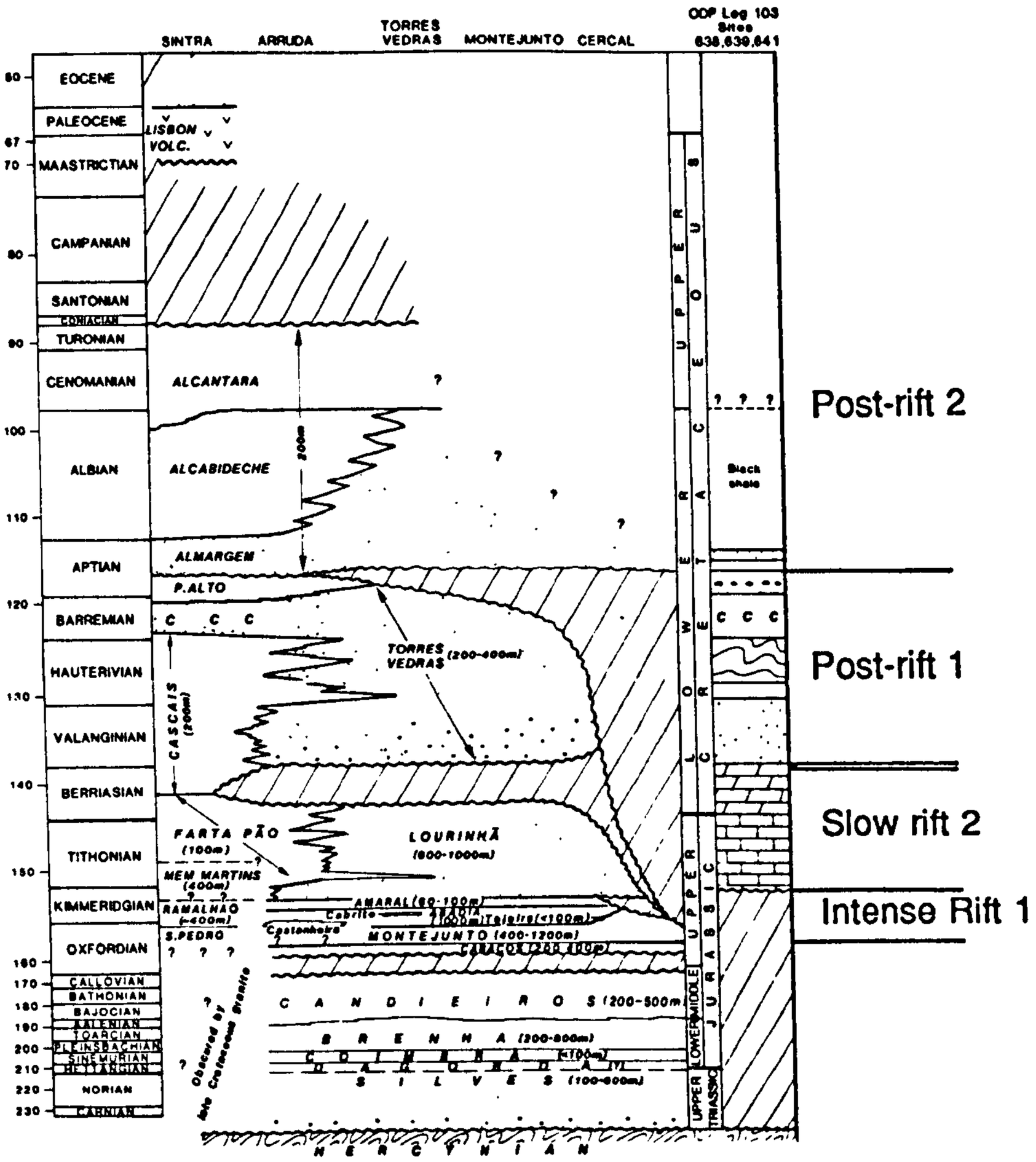


Breakup Megasequence Boundary

**Figure 5.11** Stratigraphy of the Lusitanian Basin (Zone 1^) showing the intense rift phase in the late Oxfordian to mid-Kimmeridgian and the late Berriasian/base Valanginian breakup megasequence boundary. Modified from Wilson et al. (1989).

a)

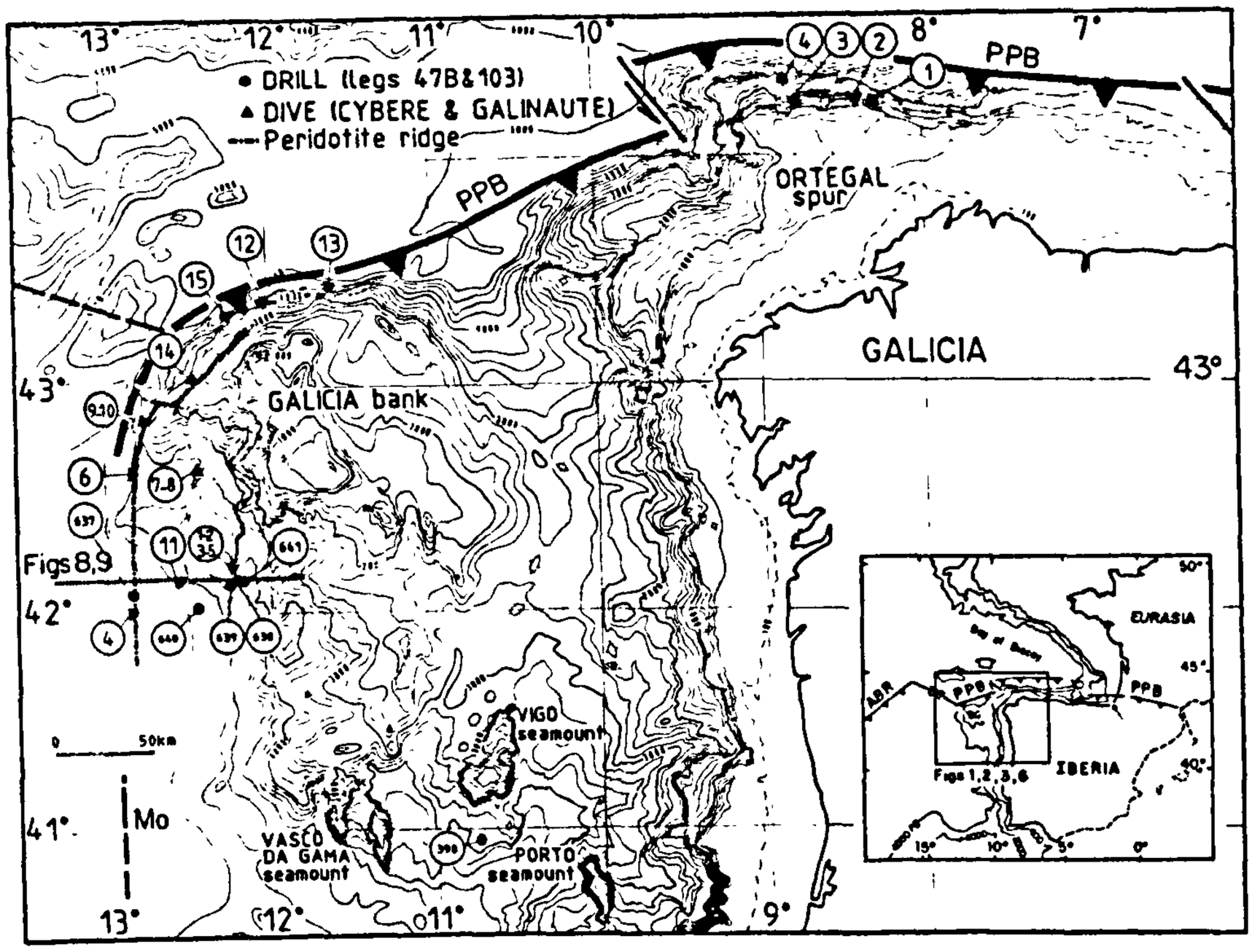


b)

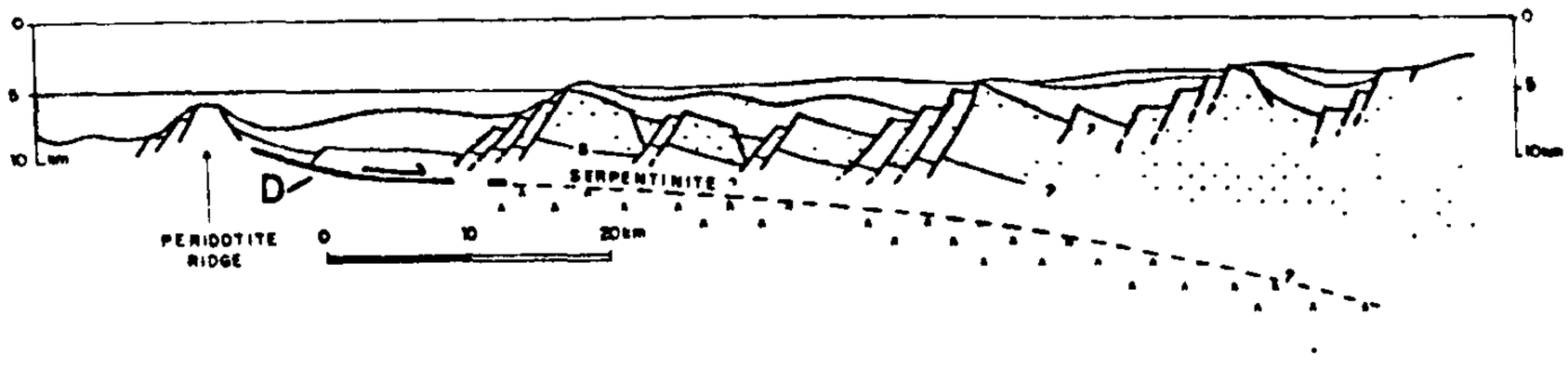


**Figure 5.12** a) Galicia Bank (Zone 2′) showing the contiguity of the J-anomaly (marked Mo) with the peridotite ridge and the location of profile A - A′ across the C.O.B. b) Line drawing interpretation of profile A - A′ with steep, approximately planar faults, dipping uniformly towards the C.O.B. The serpentinised magmatic wedge may be unroofed along a detachment D (modified from Boillot et al., 1989).

stages of rifting, when potential temperatures were elevated prior to M0 (see section 5.5), but which stayed above the blocking temperature and did not therefore acquire an anomalous magnetic signature. The subsequent unroofing of the peridotite ridge prior to organised seafloor spreading, in the early Aptian, may have involved a detachment between the magmatic wedge and the thinned continental crust as shown on Figure 5.12b

**Zone 3´**

On the Goban Spur (Figure 5.2b), tholeitic basalts, of middle Albian age, overly the syn-rift sediments (Masson et al., 1985). Figure 5.13a shows two magnetic model profiles across the Goban Spur (Scrutton, 1985) and the position of the C.O.B., as shown in Figure 5.13b, is also confirmed by gravity and seismic profiles (Masson et al., 1985). The C.O.B. is 115 km from Anomaly 34 and the bio-stratigraphic age of the breakup megasequence boundary is accurately dated at 106 Ma (Masson et al., 1985; Hailwood et al., 1980). A slow initial seafloor spreading rate of 5.5 cm/yr can be deduced. Data from the conjugate margin, in Zone 3´, is therefore almost identical to the northern Grand Banks, indicative of a high degree of symmetry between the two margins.

## 5.3 Grand Banks Tectono-stratigraphy.

Figure 5.14 summarises the tectono-stratigraphic framework of the Grand Banks, with a column for each tectonic zone, incorporating the B.P. revised sequence stratigraphy of Fucke & Daly (1988), from the Jeanne d'Arc basin. This scheme agrees in detail with the author's interpretation of seismic sections from that area (see

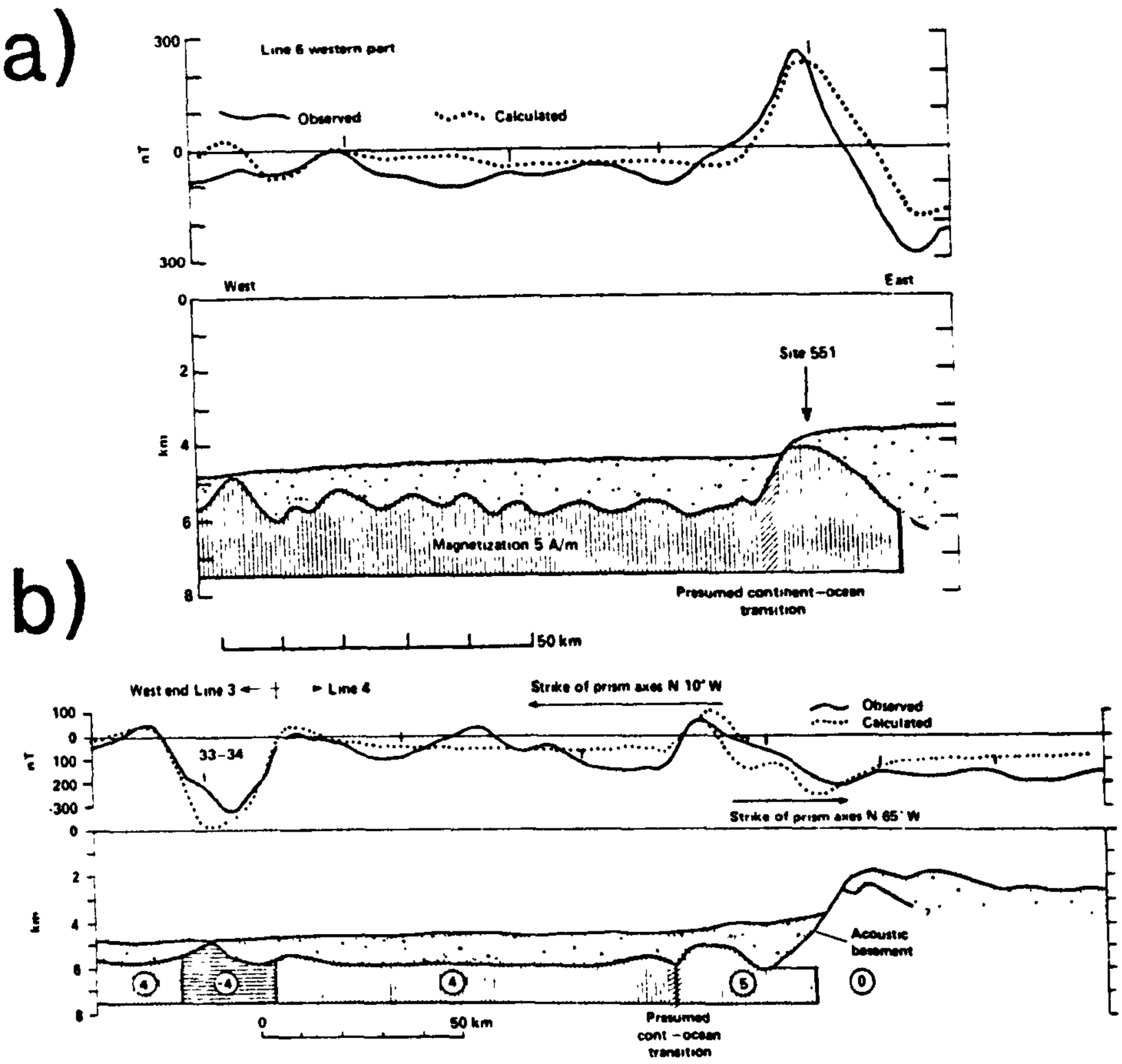


**Figure 5.13** a) Two magnetic model profiles across the Goban Spur C.O.B. (Zone 3′) from Scrutton (1981). Note the continuation of magnetized material beneath the cover west of the C.O.B. which is most likely to result from magmatic underplating. b) Location of the C.O.B. (dotted line) in relation to magnetic Anomaly 34 (Scrutton, 1981).

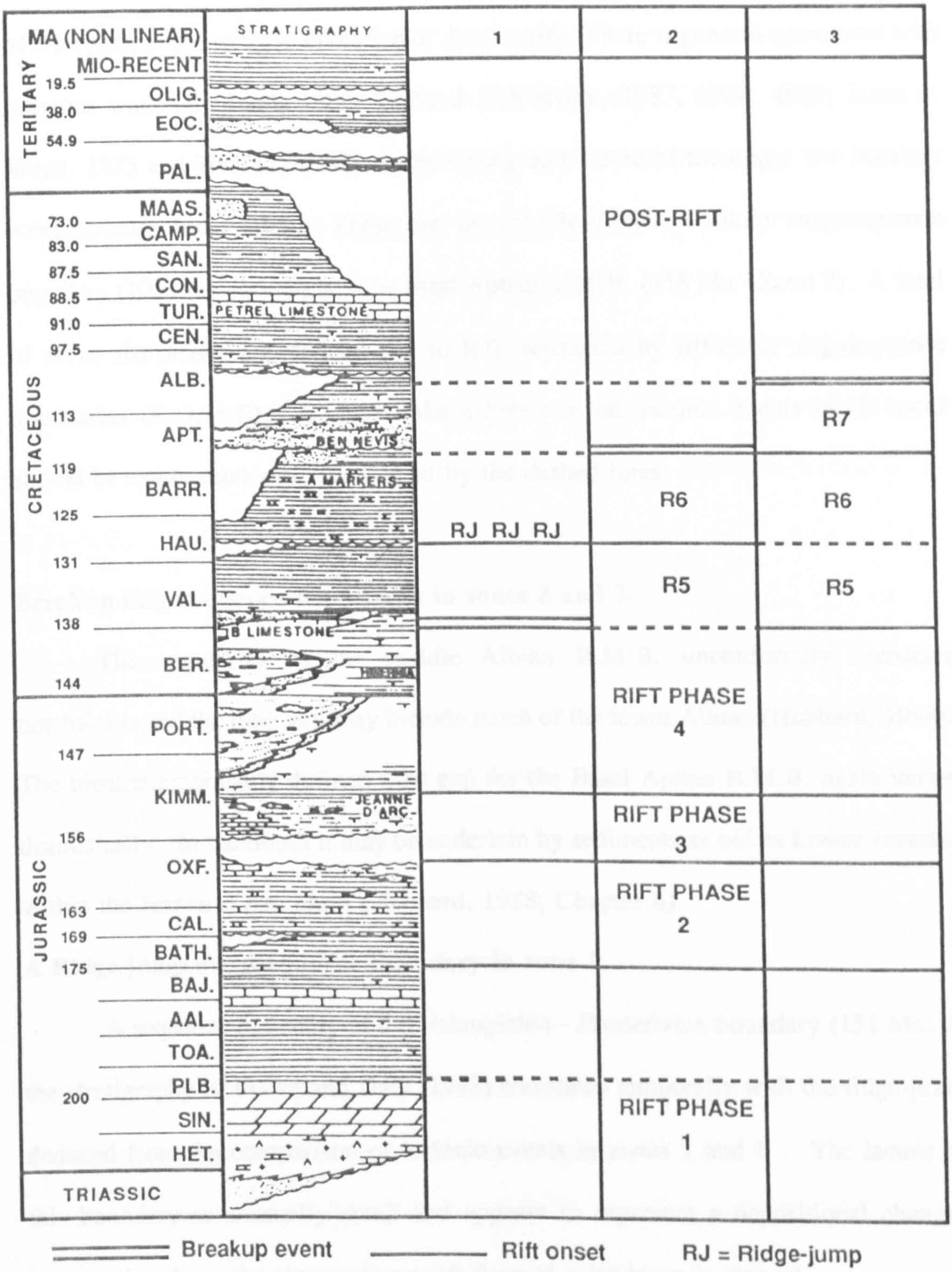


**Figure 5.14** The new tectono-stratigraphy for the Grand Banks with a column for each of the three zones defined in the text and Figure 5.3. A total of seven rift-phases are defined, of which the first four affect all three zones and the seventh is only defined in northern Grand Banks (Zone 3).

Chapter 6) and the well data used to tie them. As a result of its central location the Jeanne d'Arc basin is representative of the Grand Banks as a whole and records all of the events in the tectonic evolution of the margin. There is general agreement with previous work (Hubbard, 1988; Tankard & Welsink, 1987, 1988, 1989; Jansa & Wade, 1975 and Sinclair, 1988) on the timing and nature of the upper two breakup megasequence boundaries. These are the middle Albian breakup megasequence boundary (105 Ma -Zone 3) and the basal Aptian B.M.B. (118 Ma - Zone 2). A total of seven rift phases are defined (R1 to R7), separated by rift-onset megasequence boundaries (R.O.M.B). A close linkage between the tectonic events in all zones should be emphasised - as represented by the dashed lines.

**Breakup megasequence boundaries in zones 2 and 3.**

The angularity of the middle Albian B.M.B. unconformity increases northwards and the time gap may include much of the lower Albian (Hubbard, 1988). The biostratigraphically defined time gap for the Basal Aptian B.M.B. again varies dramatically. In the South it may be underlain by sediments as old as Lower Jurassic within the Jeanne d'Arc basin (Hubbard, 1988; Chapter 6).

**A Ridge-jump megasequence boundary in zone 1.**

A sequence boundary at the Valanginian - Hauterivian boundary (131 Ma) in the stratigraphy of Fucke and Daly (1988) correlates temporally with the ridge-jump deduced from the comparison of tectonic events in zones 1 and 1´. The lacuna at this boundary is unusually small and appears to represent a depositional change, interrupting the early phase of post-rift thermal subsidence in Zone 1.

**The breakup megasequence boundary in zone 1.**

Sinclair (1988) puts forward a convincing argument that the late Berriasian - early Valanginian boundary (Sinclair, 1988; Hubbard, 1988) is the true breakup megasequence boundary for Zone 1 (and also, less likely, Zone 2 as well). This boundary meets the first three criteria for the recognition of a breakup megasequence boundary (see section 1.2.2) with numerous faults terminating below a widespread unit - the B-marker limestone.

The base Valanginian R.O.M.B., for northern Grand Banks, is coincident with the breakup megasequence boundary for Zone 1. According to Hubbard (1988) the basal Valanginian boundary "marks the onset of large-scale fault-driven subsidence" in Zone 3.

**The intra-Kimmeridgian R.O.M.B. (All zones).**

After the intra-Kimmeridgian R.O.M.B. at 154 Ma, (Figures 5.11 & 5.14), the rate of subsidence decreased dramatically in both the Lusitanian Basin (Wilson et al., 1989) and the Jeanne d'Arc basin (Hubbard, 1988). This was a direct result of the decrease in Atlantic spreading rate at magnetic Anomaly M21 (from 1.9 to 1.0 cm/yr) (Klitgord & Schouten, 1986).

**The late Oxfordian R.O.M.B. (All zones).**

The late Oxfordian event is interpreted as the onset of the most intense period of rifting on the Grand Banks. This event correlates directly with the onset of more than 2 km of sediment loaded tectonic subsidence in the Lusitanian Basin, where the direction of extension is clearly defined as NE-SW (Wilson et al., 1989). This orientation is parallel to the fracture zones in the Tagus Abyssal Plain (Figure 5.10a) and its northern boundary - the Nazare Fault - a continuation of the Meguma - Avalon

terrane boundary (Welsink et al., 1989).

**The intra-Bathonian R.O.M.B. (All zones).**

This event, at 170 Ma, marks the onset of renewed rifting and the activation of new transform zones on a NW-SE trend and is coincident with a ridge-jump South of the Grand Banks. The new trend transects Caledonide structures - e.g. the Meguma - Avalon terrane boundary (Keen & Hyndman, 1979). Figure 5.15 shows that this lineament, reactivated as the Collector - Nazare Fault, controlled Triassic basin geometry as the northern bounding fault of a strike-slip duplex during Rift 1 (Welsink et al. 1989).

**The Lower Jurassic megasequence boundary.**

In the older section of the tectono-stratigraphy there is an important sequence boundary within the Pleinsbachian (195 Ma, Hubbard, 1988). This boundary appears to be related to breakup south of the Grand Banks and implies that the older of the two possible dates, given for this event in section 5.2, is the more likely.

## 5.4 Tectonic Control on Sedimentation and Palaeo-bathymetry

Table 5.1, on the following page, summarises the predominant facies within the sequences in the Jeanne d'Arc basin, youngest first, and gives an estimate of the palaeo-bathymetry (positive down water depths) for each one (Elliot, 1990 Pers. Com.). During the second rift phase the quiescent lower Jurassic shale deposition was replaced by differential subsidence with a northward tilt. A carbonate bank developed in the south, indicating that the rift was not too intense.

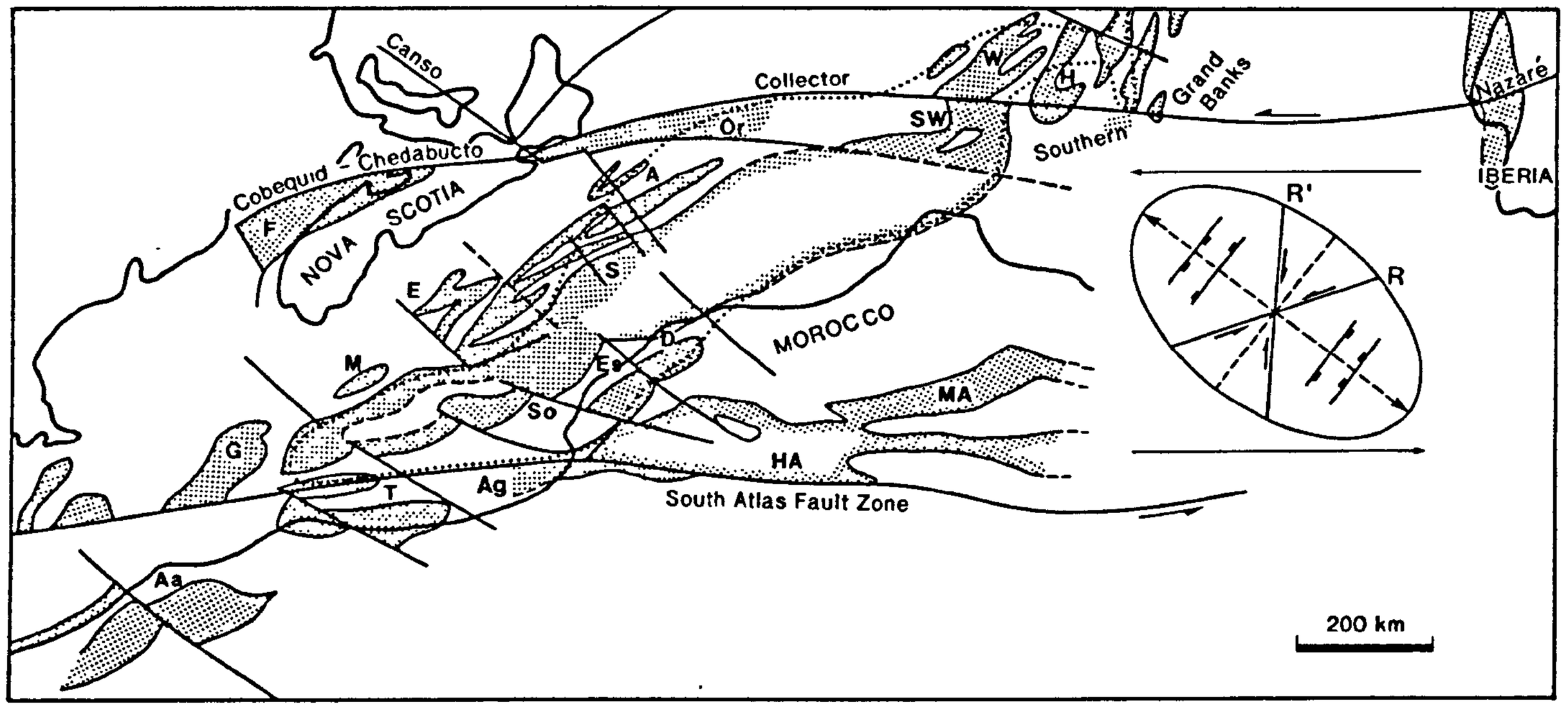


**Figure 5.15** Sinistral strike-slip duplex controlling basin geometry on southern Grand Banks, the Nova Scotian and the North African margins. The predominantly NE-SW trend of basins parallel large-scale "joints" on the Riedel Shear Pattern and the Orpheus and Bay of Fundy basins strongly resemble strike-slip "wedge basins" (Welsink et al., 1989). The northern boundary of the duplex - the Collector - Nazare fault may have controlled the early breakup in Tagus Abyssal Plain.

| Sequence | Facies | Palaeo-bathymetry |
|---|---|---|
| "Post rift" | Mixed limestone and shale | Variable |
| R7 | Shallow marine - mature sands. | 50 to 100 m |
| R6 | Fine sands and shale with limestone markers | 200 m+ |
| R5 | Limestones, fine sands and shale | 300 m+ |
| R4 | Mature delta sands | 200 to 300 m |
| R3 | Alluvial conglomerates (south)<br>Fan delta sands and muds (north) | 0 to -50 m<br>100 to 150 m |
| R2 | Carbonate bank (south)<br>Nearshore sandstones (north) | 10 to 20 m<br>50 to 100 m |
| | Shale with limestone | 200 m |
| R1 | Red beds and evaporites | 0 to -150 m |

Table 5.1

Intense uplift and erosion south of the Jeanne d'Arc basin, with a deep water component in the north comprises the response to the onset of the third, very intense, rift phase. Sediment supply failed to keep pace with rapid basin subsidence and the Jeanne d'Arc sandstone is overlain by a deep water sequences.

## 5.5 Elevation of Potential Temperatures and the Onset of Hotspot Activity

The onset of hotspot activity, within the 2000 km range of influence (White & McKenzie, 1989), causing an elevation of mantle potential temperatures, may have tectono-stratigraphic consequences on the Grand Banks. The thickening of oceanic crust on the J-Anomaly Ridge from Anomaly M4 onwards (Figure 5.7, Tucholke & Ludwig, 1982) could correspond to an Upper Hauterivian (127 Ma) uplift event, shown as an unconformity on Figure 5.14, amalgamated with the basal Aptian

B.M.B. Elevated potential temperatures are also required, just prior to Anomaly M0, to explain the origin of the thick peridotite ridge (Figure 5.13b) adjacent to Galicia Bank (Boillot et al. 1989), the magmatic underplating wedges imaged on the deep seismic lines shown in Figure 5.6b (Keen & DeVoogd, 1988 & section 6.2) and the extrusion of melt along the Newfoundland Fracture Zone (Grant, 1979).

Unfortunately, the precise locations of particular hotspots during the relevant time period are not known. The hotspot tracks of Morgan (1983) are inaccurate in this region because the plate reconstruction on which they are based assumes breakup at (80 Ma) along the entire Grand Banks margin. However, it seems likely that both the Madeira and Canary hotspots migrated across the Grand Banks between 130 and 100 Ma. Furthermore, hotspot activity would explain the origin of the Newfoundland Seamounts (Figure 5.16) which have been dated (giving an $^{40}Ar/^{39}Ar$ age of 97.7 ± 1.5 Ma) and have the usual alkaline geochemistry associated with plumes (Sullivan & Keen, 1979).

## 5.6 Discussion - the Ridge-jump Megasequence Boundary.

In section 5.3 the sequence stratigraphic response to a ridge jump in the adjacent ocean basin has been recognised on a passive margin for the first time. Intuitively it seems unlikely that a ridge jump back to the original position of the C.O.B. is a common event and so ridge jump megasequence boundaries of this magnitude are likely to be rare. However, the discovery emphasises that the initial stages of sea floor spreading are normally complex and the number of tectonically induced unconformities is likely to be large.

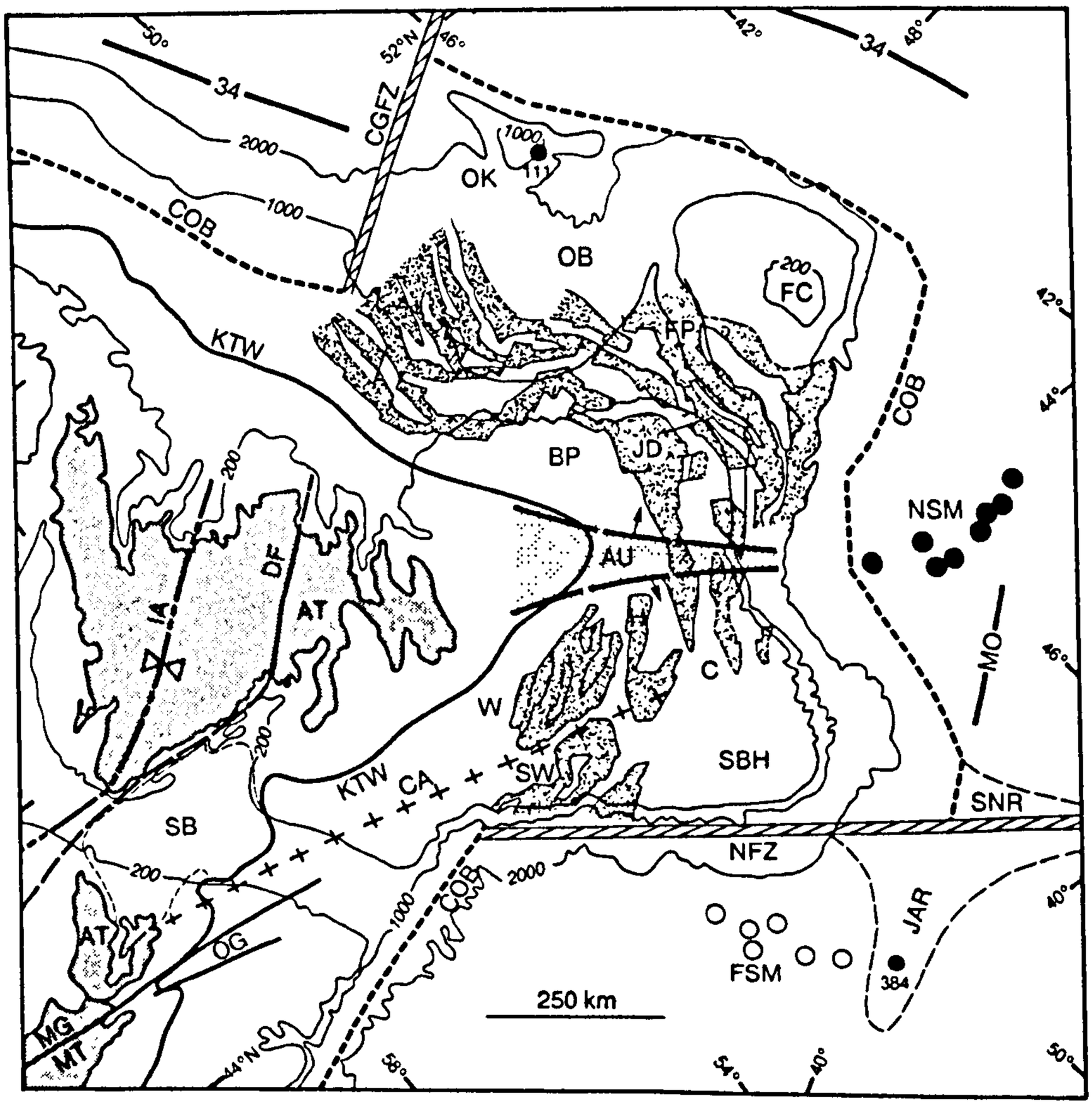


**Figure 5.16** Location of the Newfoundland Seamounts in the abyssal plain East of the Grand Banks. AU - Avalon Uplift; BP - Bonavista Platform; C - Carson Basin; CA - Collector Anomaly; COB - Continent Ocean Boundary; FC - Flemish Cap; JD - Jeanne d'Arc Basin; NFZ - Newfoundland Fracture Zone; NSM - Newfoundland Seamounts; M0 - J-Anomaly. Note that the Newfoundland Seamounts are directly in line both with the Collector Anomaly and with the most intense uplift across south-central Grand Banks - the "Avalon Uplift". Modified from Balkwill & Legall (1989)

# CHAPTER 6

# THE MORPHOLOGY OF BREAKUP MEGASEQUENCE BOUNDARIES BASED ON SEISMIC SECTIONS ACROSS THE GRAND BANKS.

## 6.1 Introduction.

Figure 6.1 shows a location map of the two deep seismic lines studied in this thesis. In Chapter 5 it was shown that deep seismic data, across the Grand Banks, constrains the location of the C.O.B., but in addition they provide regional profiles across which the variation in morphology of the breakup megasequence boundaries can be studied. Industrial seismic data from the Soquip survey (1983) is used to describe the details of the breakup megasequence boundary morphologies in the Jeanne d'Arc Basin. Well data was used to tie the deep seismic data directly (e.g. Gabriel well on line 85-3) and via ties to Soquip survey (see section 6.3 and Figure 6.8). The eastern extensions of some of the lines were interpreted across the Gabriel / Flemish Pass basin, but are not presented in this thesis because of the lack of adequate well control. Note that all figures in this chapter use the following codes to refer to the three breakup megasequence boundaries:-

**ALB** = Middle Albian, **APT** = Base Aptian, **VAL** = Base Valanginian.

## 6.2 General Description of the Deep Seismic Profiles.

### Lithoprobe Line 85-3.

Line drawing interpretations of the original time section (T.W.T.T.) are shown

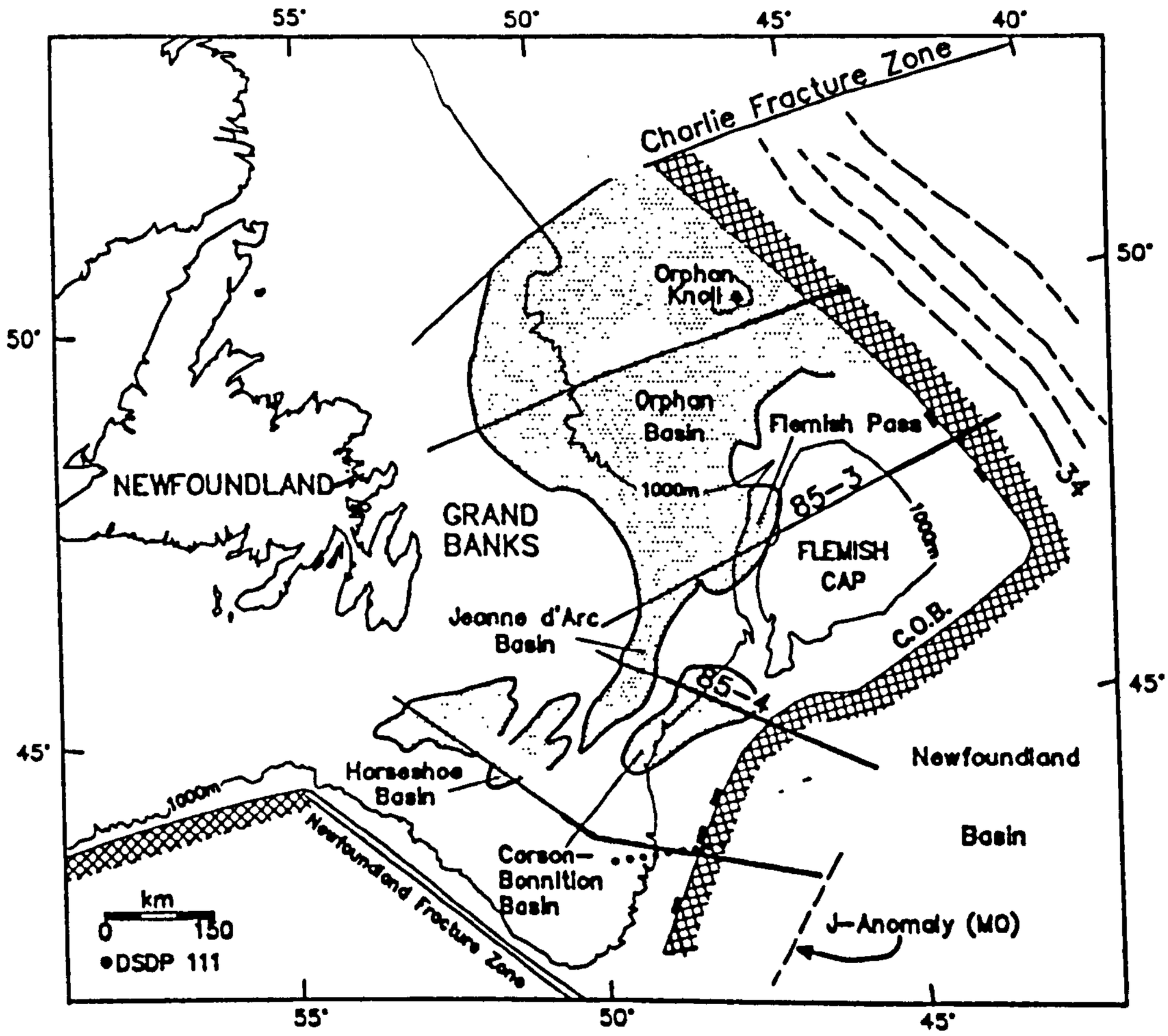


**Figure 6.1** Location map for the Lithoprobe deep seismic lines 84-3 and 85-4 (Keen & deVoogd (1988). The continent ocean boundary is marked in the hachured pattern.

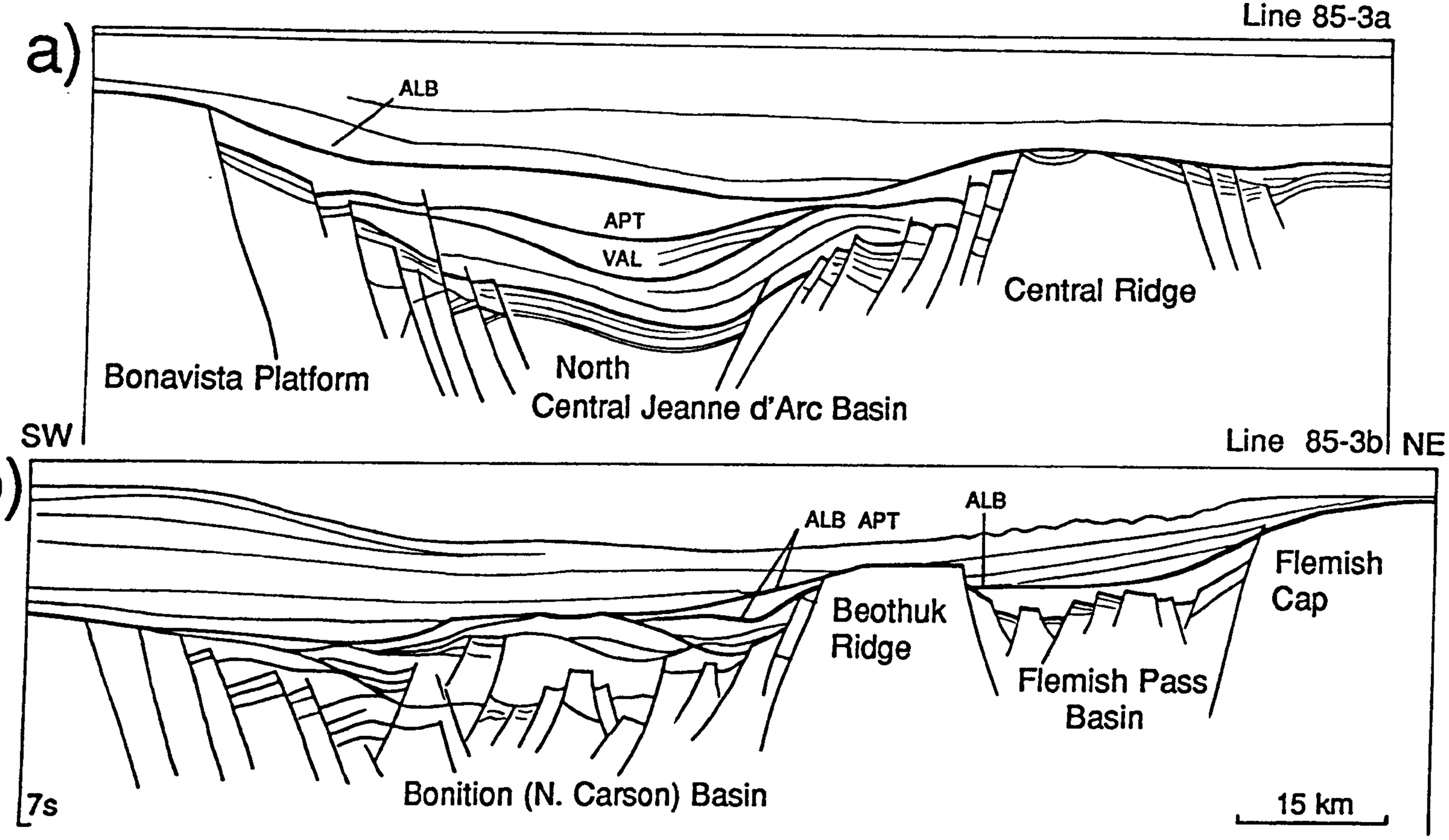


**Figure 6.2** Line drawing interpretations of Lithoprobe line 85-3. a) Transect of the northern part of Jeanne d'Arc Basin, flanked by the Bonavista Platform and Central Ridge, showing the classic "steers-head" geometry and reflector terminations on structural highs. Vertical scale to 7 secs T.W.T.T. b) Transect of the northern part of the Carson - Bonition basin, Beothuk Ridge, Flemish Pass Basin and Flemish Cap. Vertical scale - as for a).

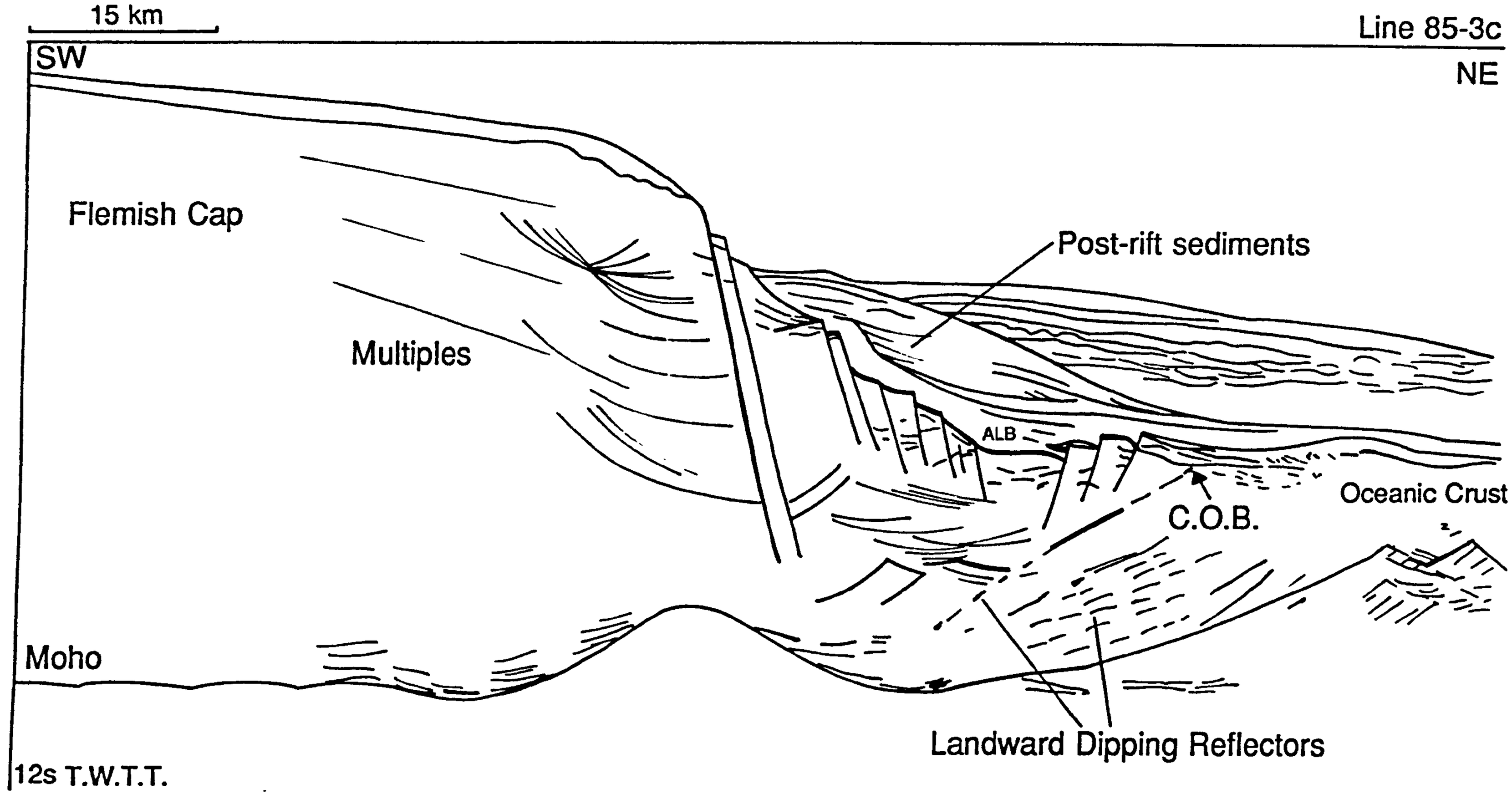


**Figure 6.3** Line drawing interpretation of the northern portion of Lithoprobe line 85-3, transecting the C.O.B., showing the landward dipping reflector above the wedge-shaped zone of magmatic underplating and faulted continental crust, in a relatively narrow zone, South of the C.O.B. Vertical scale to 12 secs T.W.T.T.

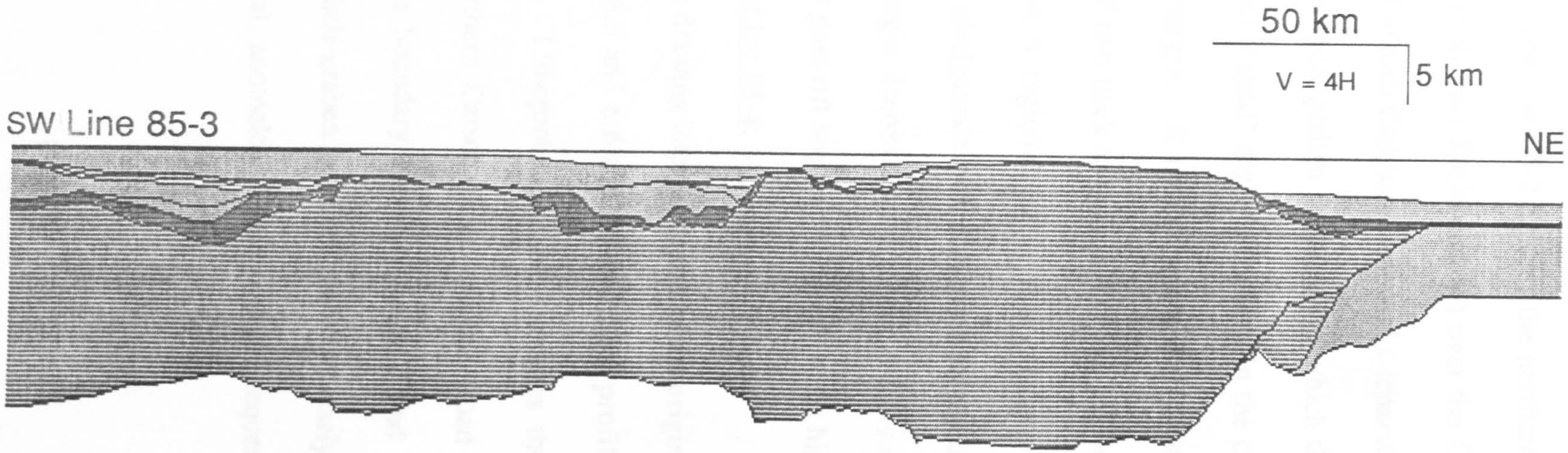


**Figure 6.4** Digitized and depth converted complete profile of Lithoprobe Line 85-3 (V = 4H).

in Figures 6.2 and 6.3 and the complete depth converted profile is shown in Figure 6.4. Lithoprobe line 85-3 crosses the northern part of the Jeanne d'arc Basin, The Gabriel/Flemish Pass Basin and out over the C.O.B.. The Central Ridge, Beothuk Ridge and Flemish Cap basement highs separate the basins. The Jeanne d'arc basin has a symmetrical graben geometry in which the breakup megasequence boundaries have a "bowl-shaped" sag morphology in the centre but are faulted and truncated at the basin margin. It is significant that Beothuk ridge, formed by uplift in the footwalls of two back-to-back faults has sedimentary wedges on its SW side which may indicate a regional tilt in that direction. All three breakup megasequence boundaries amalgamate over Central Ridge and Flemish Cap. Northeast of Flemish Cap the margin deepens rapidly over three steeply dipping normal faults and both syn-rift and post-rift sequences appear to be highly condensed.

Lithoprobe Line 85-4.

Line drawing interpretations of the original time section (T.W.T.T.) are shown in Figures 6.5 and 6.6 and the complete profile is shown in Figure 6.7 after depth conversion. Lithoprobe line 85-4 crosses the southern Jeanne d'Arc Basin, the shallow northern Carson Basin and the broad extensional zone out to the C.O.B., close to the boundary between zones 2 and 1. The Jeanne d'arc basin has an archetypal half-graben geometry, with an early Jurassic syn-rift fill, but is overlain by horizontal, anomalously thin post-rift sequences

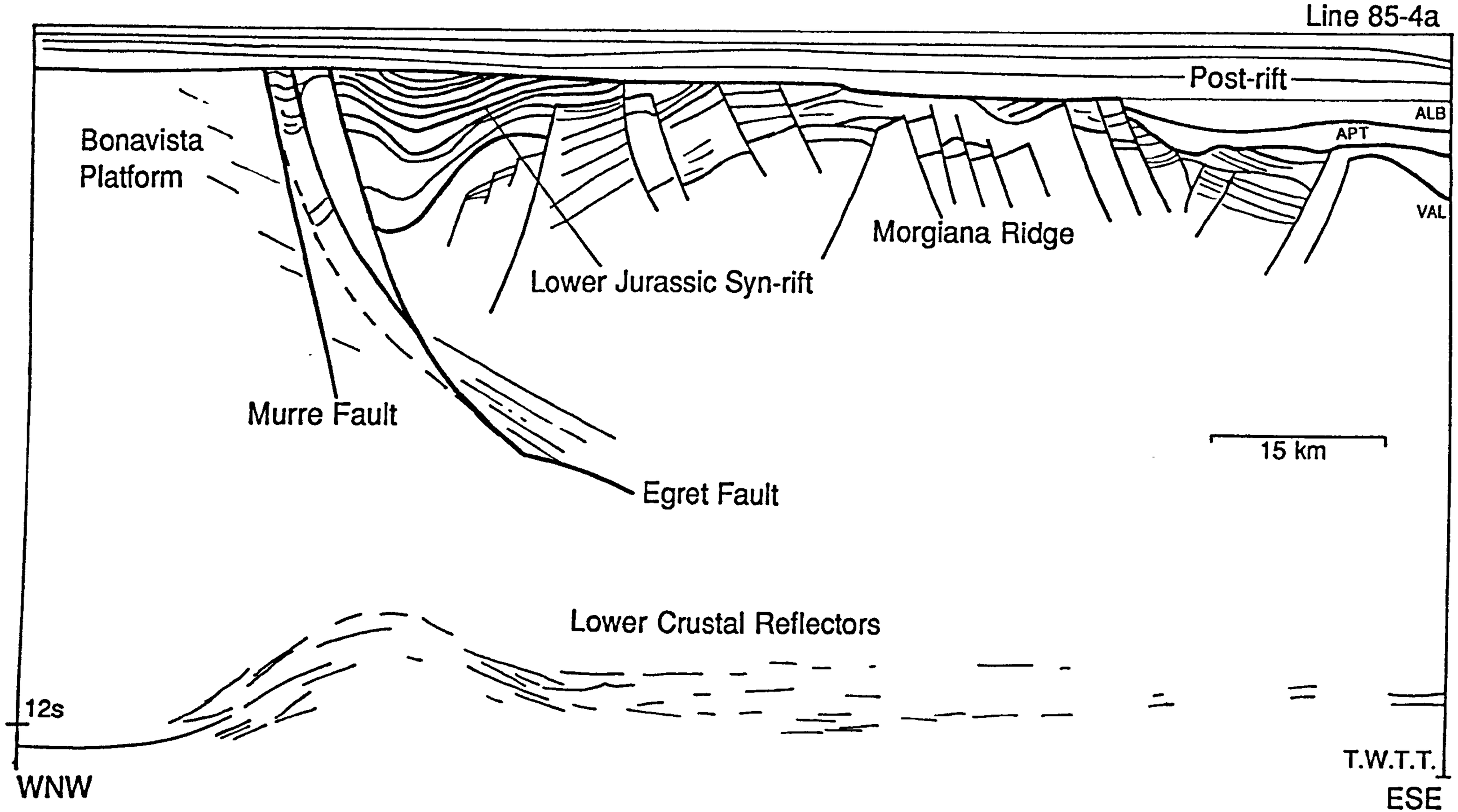


**Figure 6.5** Line drawing interpretation of the western portion of Lithoprobe line 85-4 including the seismically defined Moho. Note the clearly defined truncation of reflectors at the almost flat amalgamated breakup megasequence boundary and the very thin post-rift sequence. Vertical scale to 12 secs T.W.T.T.

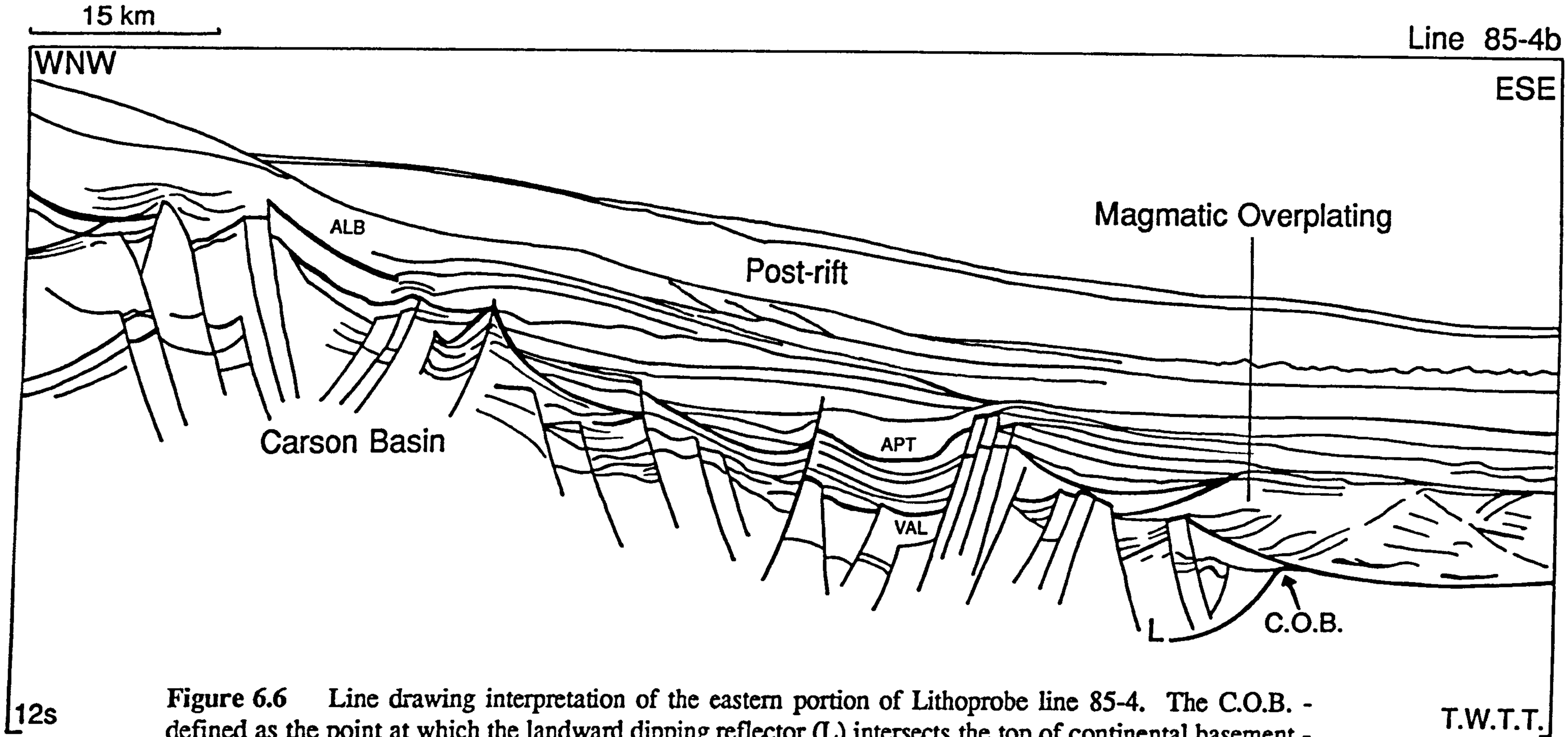


**Figure 6.6** Line drawing interpretation of the eastern portion of Lithoprobe line 85-4. The C.O.B. - defined as the point at which the landward dipping reflector (L) intersects the top of continental basement - appears to be overlain by a "downlapping" unit which continues eastward into oceanic crust. This is interpreted as "magmatic overplating" - basalts extruded onto highly attenuated crust soon after breakup. Vertical scale to 12 secs T.W.T.T.

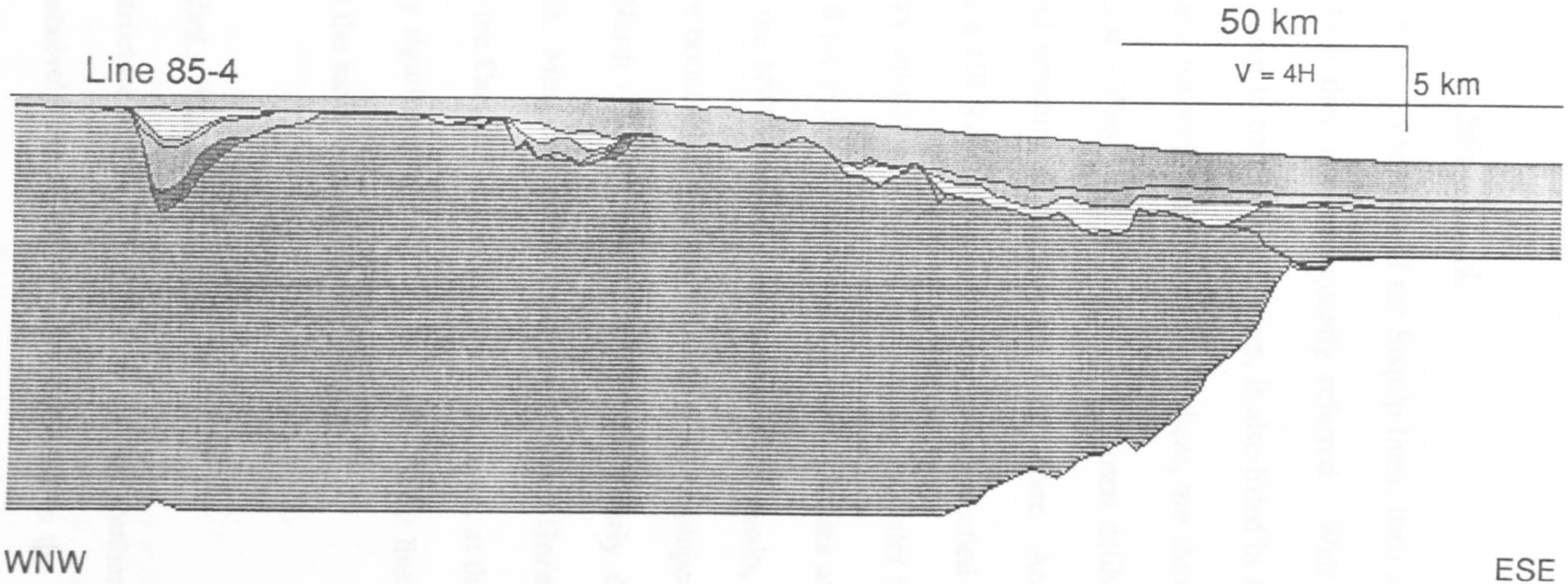


**Figure 6.7** Digitized and depth converted complete profile of Lithoprobe Line 85-4. (V = 4H)

## 6.3 General Description of the Soquip Survey Lines - Jeanne d'Arc Basin.

### 6.3.1 Design of the Seismic Grid.

Appendix C gives a list of the Soquip lines, their orientation, length and the number to which they are subsequently referred. Well data, including synthetic seismograms, used to tie the Soquip lines, is also listed in Appendix C. The location of the lines, and the wells used to calibrate them, are shown in Figure 6.8.

The East - West lines 2 and 3 were chosen deliberately, to investigate the orientation and structure of the Voyager Fault Zone. According to Fucke & Daly (1988) this is a NE-SW trending structure which exerted a fundamental control on basin geometry initially as a normal fault which was later reactivated as a transform. Lines 7 and 8 are much shorter than the other profiles and were included because they crossed the NW Terrace of the Jeanne d'Arc basin, where it was known that megasequence boundaries were particularly well developed.

The North - South lines 12 to 16 also clearly define the location of the Voyager Fault. Most lines terminate on the Voyager Horst block but lines 14 and 16 continue into the Carson Basin to the South. Line 11, at the western side of the grid, is particularly significant since it ties the East - West lines on the NW Terrace and runs close to the basin bounding Murre Fault.

### 6.3.2 The East - West Lines.

The structure of line 1 (Figure 6.9a), at the southern end of the Jeanne d'Arc Basin, is a relatively simple half-graben, bounded to the west by the Murre Fault. The syn-rift deposits are up-domed by salt moving up the fault, but the top of this

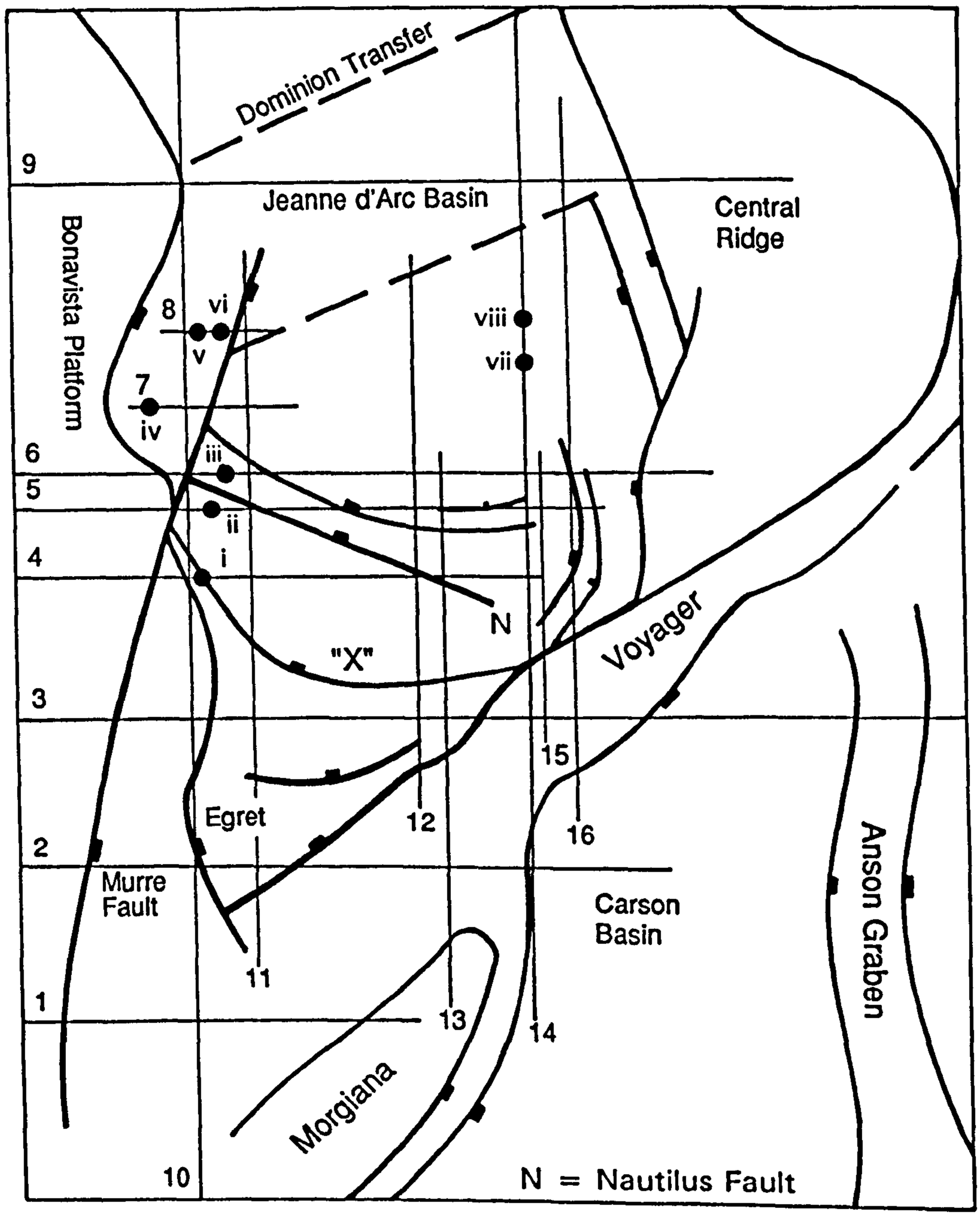


i) - Hibernia G55

ii) - Hibernia B08

iii) - Nautilus C92

iv) - Mercury K76

v) - Flying Foam W.

vi) - Flying Foam I13

vii) - Adolphus D50

viii) - Adolphus 2K41

**Figure 6.8** Location map for the Soquip Survey seismic lines and wells used to study the detailed morphology of breakup megasequence boundaries in the Jeanne d'Arc Basin.

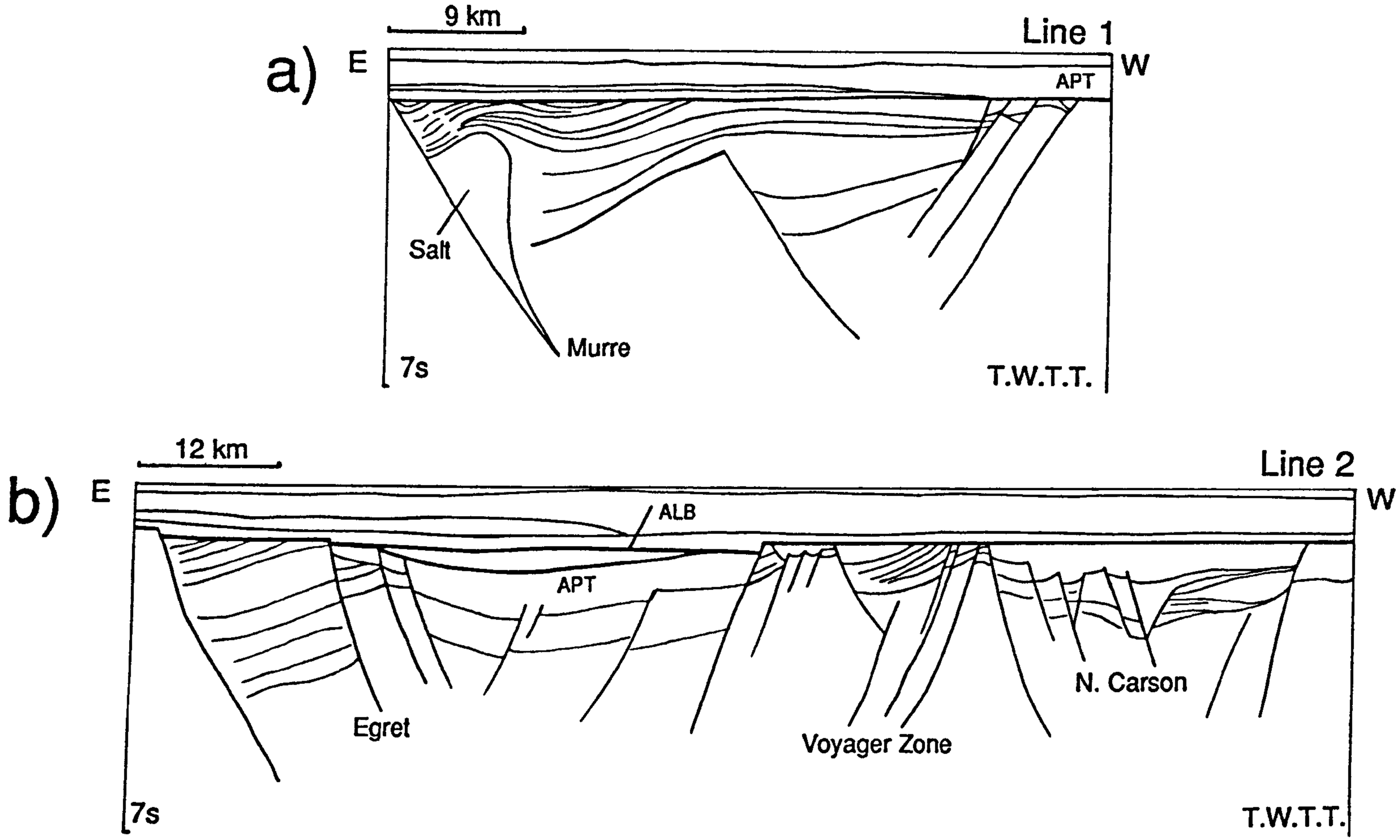


**Figure 6.9** Line drawing interpretations. a) Line 1 and b) Line 2. Vertical scale to 7 secs T.W.T.T.

structure is truncated by the basal Aptian B.M.B. Erosional truncation extends across the entire profile (45 km) such that the basal Aptian B.M.B. (amalgamated with the basal Valanginian and ridge-jump megasequence boundaries) is almost completely flat. **Line 2** (Figure 6.9b) shows a symmetrical graben and an extra fault (Egret Fault), forming a terrace at the western margin. The basal Aptian B.M.B. resembles the flat lying erosional unconformity of line 1 over this western terrace (and extending 10 km into the basin). B.M.B.s in the centre of the basin have a broadly conformable "sag-like" morphology. The Jeanne d'Arc Basin is separated from the shallow northern part of the Carson Basin by a broad high (24 km wide), bounded to the east by the Voyager Fault and to the west by two back-to-back faults, and shows well defined erosional truncation.

Further North, on **line 3** (Figure 6.10a), erosional truncation is harder to define on the western terrace because the basal Aptian B.M.B. is cut by several faults, but appears to be present. At the eastern margin the Voyager horst has narrowed to 12 km and erosional truncation continues across the Anson Graben and Vesta Horst.

**Lines 4** and **5** (Figures 6.10b and 6.11a) have a very similar structure and cross the Hibernia oilfield in the hangingwall of the Murre Fault and the footwall of the NW-SE trending Nautilus Fault. Like line 3, most of the erosional truncation on the western terrace is obscured by faulting. The prominent reflectors of the late Jurassic sequences, cut by dense faults, are well defined northeast of the Nautilus Fault.

The western margin of **line 6** (Figure 6.11b) is a broad fault zone (22 km wide) across which the basin gradually deepens and then steps down across the

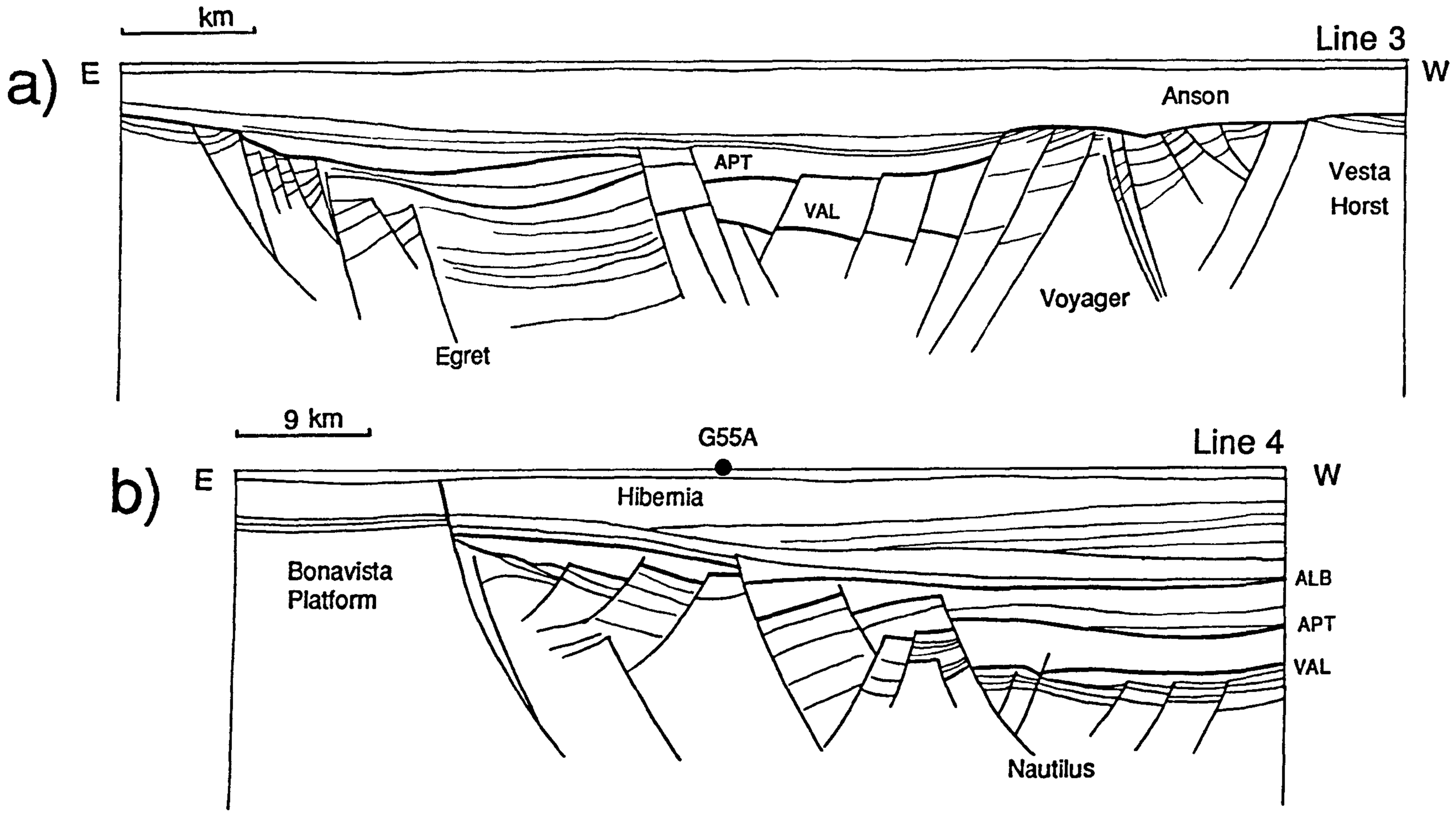


**Figure 6.10** Line drawing interpretations. a) Line 3 and b) Line 4. Vertical scale to 7 secs T.W.T.T.

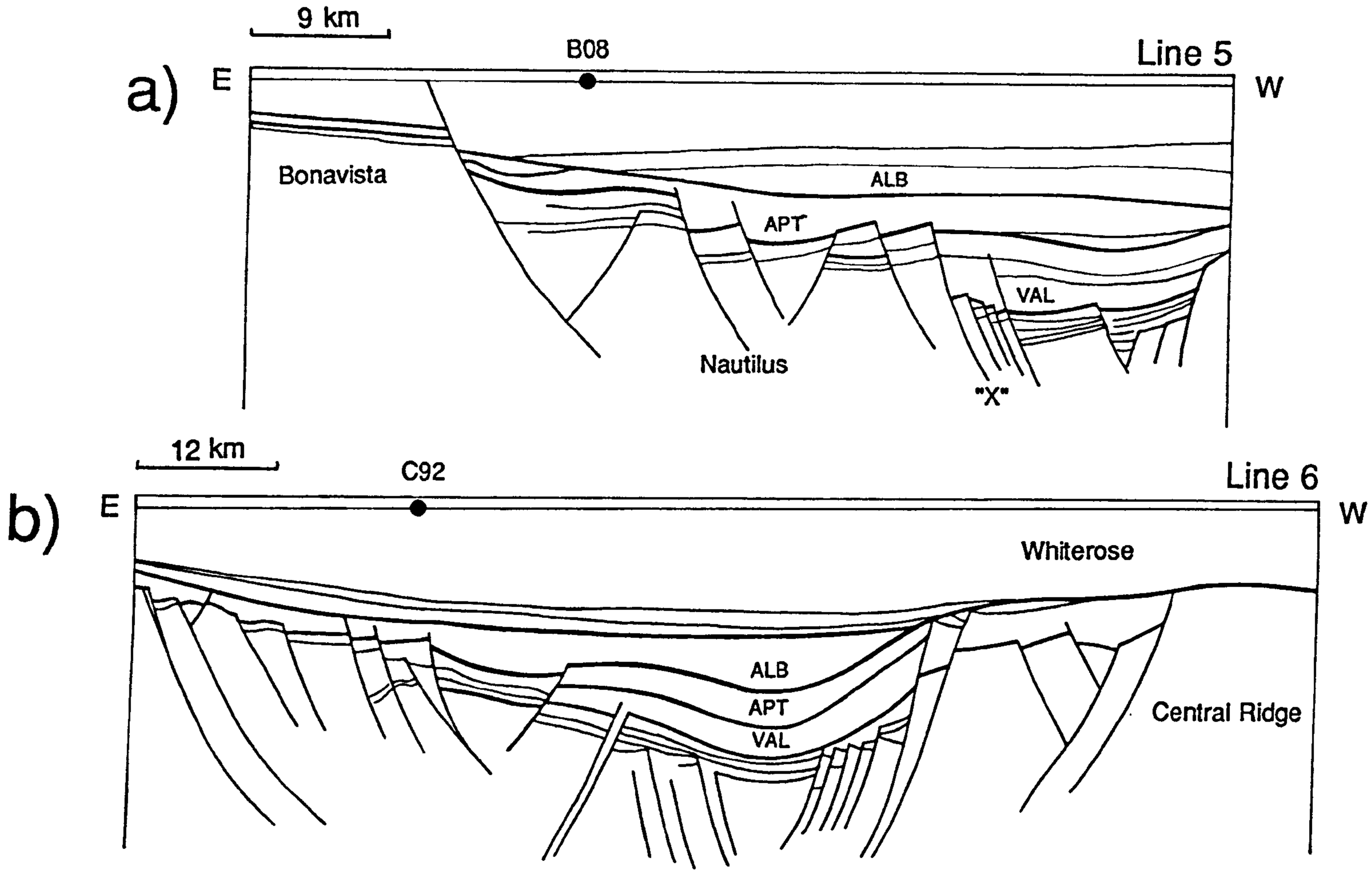


**Figure 6.11** Line drawing interpretations. a) Lines 5 and b) Line 6. Vertical scale to 7 secs T.W.T.T.

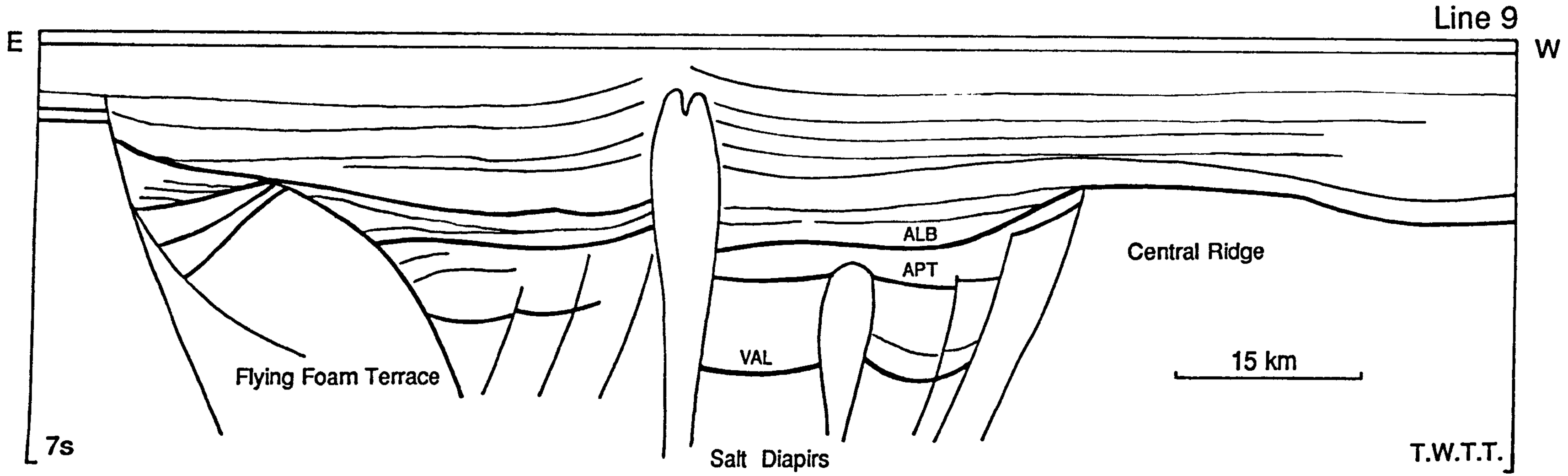


**Figure 6.12** Line drawing interpretation of Line 9. Vertical scale to 7 secs T.W.T.T.

curvilinear detachment fault north of the Nautilus Fault. The centre of the basin has a characteristic "bowl-shaped" morphology within which all three of the megasequence boundaries are unfaulted. Syn-rift "wedges" above numerous fault blocks are particularly well defined below the base Valanginian B.M.B (B-Marker Limestone). The basin is bounded to the east by the Central Ridge across which erosional truncation is well defined.

On line 9 (Figure 6.12) the western bounding fault switches to the Mercury Fault (12 km west of the Murre Fault) and the most striking feature is the rotated sequences in the hangingwall of a listric detachment on Flying Foam Terrace.

Details of the structure of Flying Foam Terrace are shown on lines 7 and 8 (Figure 6.13). It should be emphasised that this deformation is controlled by two phases of salt movement, rather than deep, basement involved faults.

### 6.3.3 The North - South Lines.

**Line 10** (Figure 6.14a) crosses the western margin of the Jeanne d'arc basin and therefore transects the terrace regions described above. Erosional truncation is evident over the southernmost 25 km of the line, across Morgiana High and the basin South of the Voyager Fault. Salt diapirism obscures the footwall geometry of the Egret fault which line 10 crosses obliquely. Further north, line 10 crosses the intensely faulted margin of the Bonavista Platform, close to the bend into the Mercury Fault, and then Flying Foam Terrace where the northward plunging basement is clearly imaged. The northern end of line 10 crosses back into the deeply subsided northern end of the Jeanne d'arc basin, overlain by an extremely thick post-rift sequence.

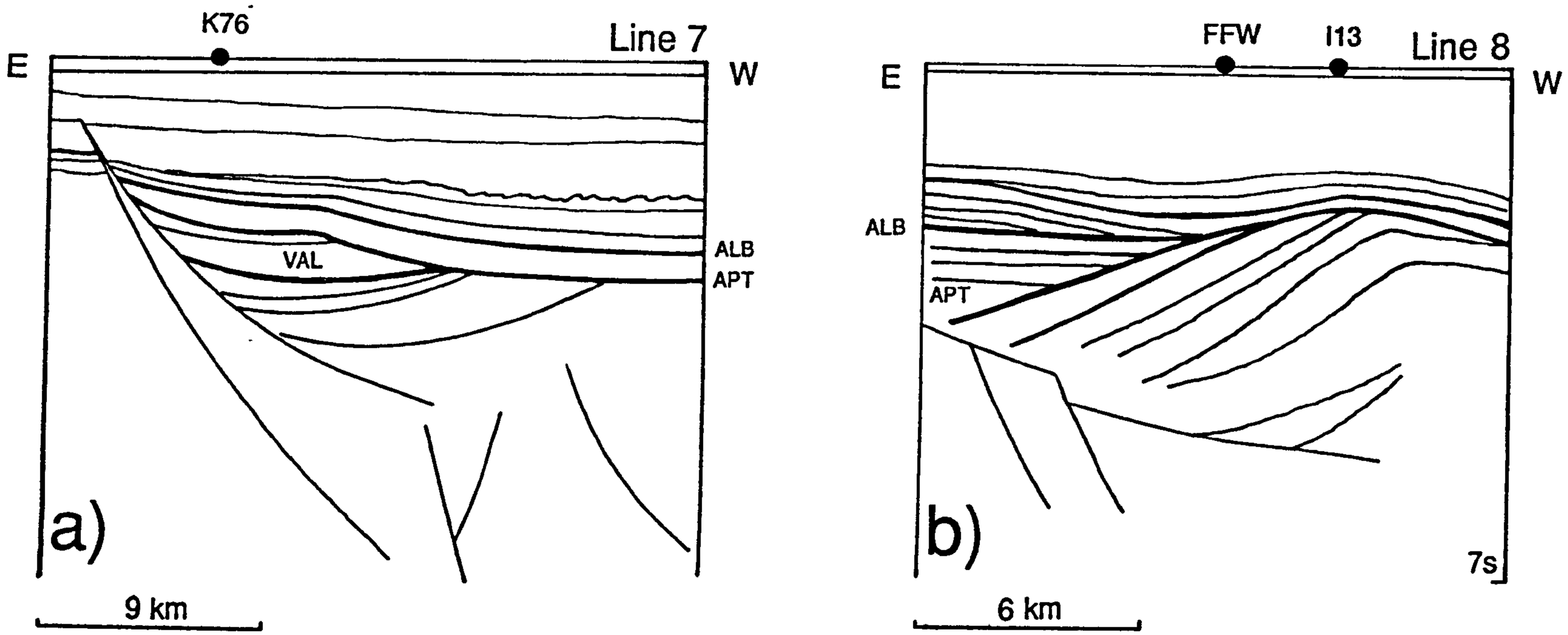


**Figure 6.13** Line drawing interpretations. a) Lines 7 and b) Line 8. Vertical scale to 7 secs T.W.T.T.

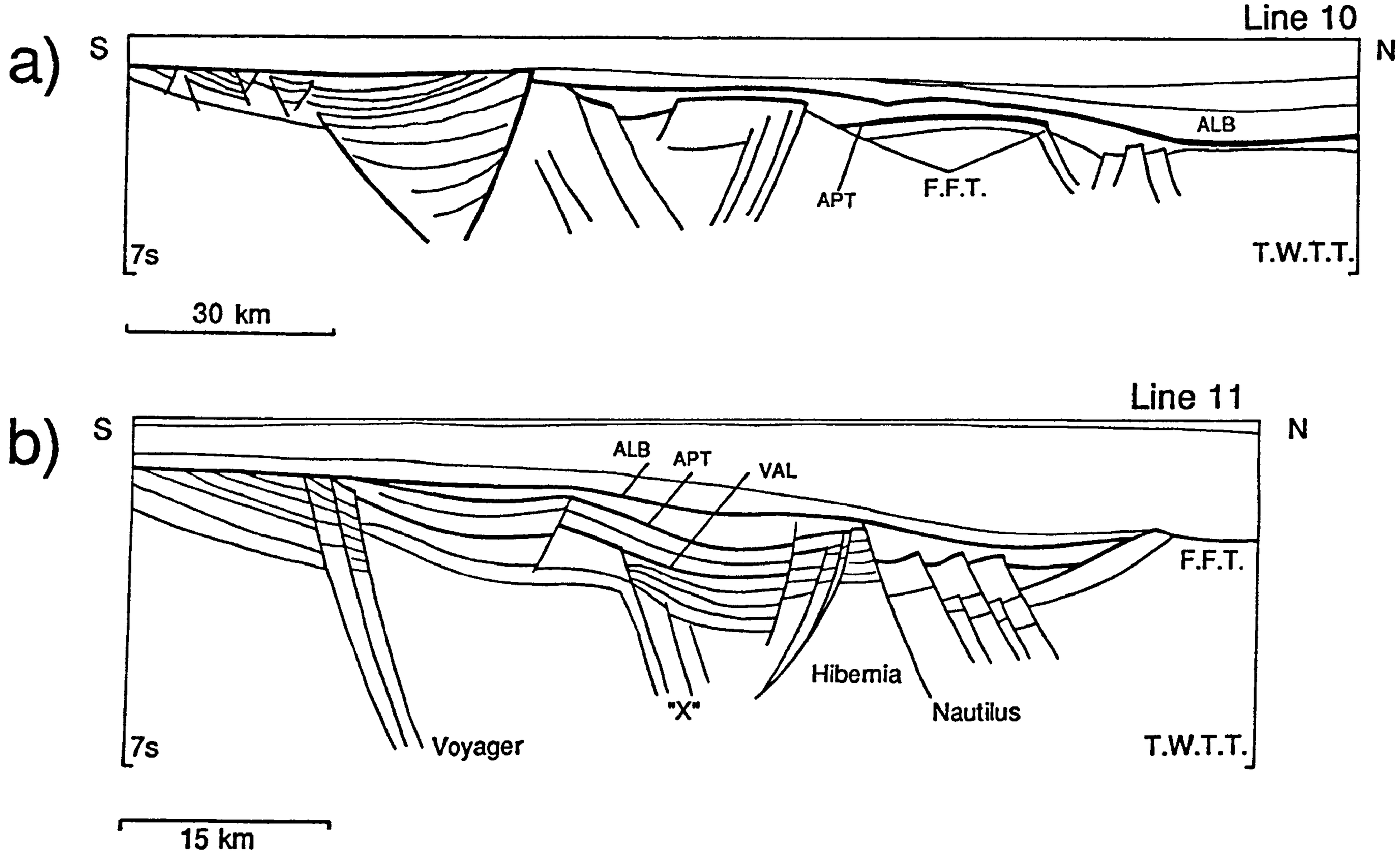


**Figure 6.14** Line drawing interpretations. a) Line 10 and b) Line 11. Vertical scale to 7 secs T.W.T.T.

Amalgamation of B.M.B.s and erosional truncation (over 18 km) is clearly defined on **line 11** South of the Voyager Fault (Figure 6.14b). North of the "X" fault all three B.M.B.s have the characteristic "bowl - shaped" sag geometry and are unfaulted. The base Aptian B.M.B. is conspicuously flat over the eastern equivalent of the Hibernia structure - an intra-basin horst bounded to the North by the Nautilus Fault - and may have been subaerial at breakup. In the north, line 11 crosses the eastern edge of Flying Foam Terrace, almost parallel to the Murre fault.

The structure of **line 12** south of the Nautilus Fault (Figure 6.15a) is very similar line 11. North of Nautilus, however, a minor antithetic fault forms a "keystone wedge" in the hangingwall rollover.

The southern end of **line 13** crosses the widest part of the Voyager High where it combines with the Morgiana high to produce a 45 km basement high over which all three B.M.B's are amalgamated (Figure 6.15b). North of the Voyager Fault the basin plunges gently northwards but deepens dramatically over the Nautilus Fault. Deep in the hangingwall of this fault the basal Valanginian B.M.B is clearly imaged, underlain by syn-rift wedges of the Jeanne d'Arc and Hibernia sequences.

The structure of the Voyager Fault Zone is most clearly defined on **line 14** (Figure 6.16a). A 15 km wide horst block is bounded by back-to-back faults, separating the Carson and Jeanne d'arc basins, over which the breakup megasequence boundaries amalgamate. Two large salt diapirs disturb the deepest part of the northern Jeanne d'Arc basin North of the Nautilus wells.

The shorter North-South **line 15** (Figure 6.16b) terminates southwards at the Voyager Fault Zone and therefore does not continue into the Carson Basin. The Nautilus fault cannot be defined on line 15.

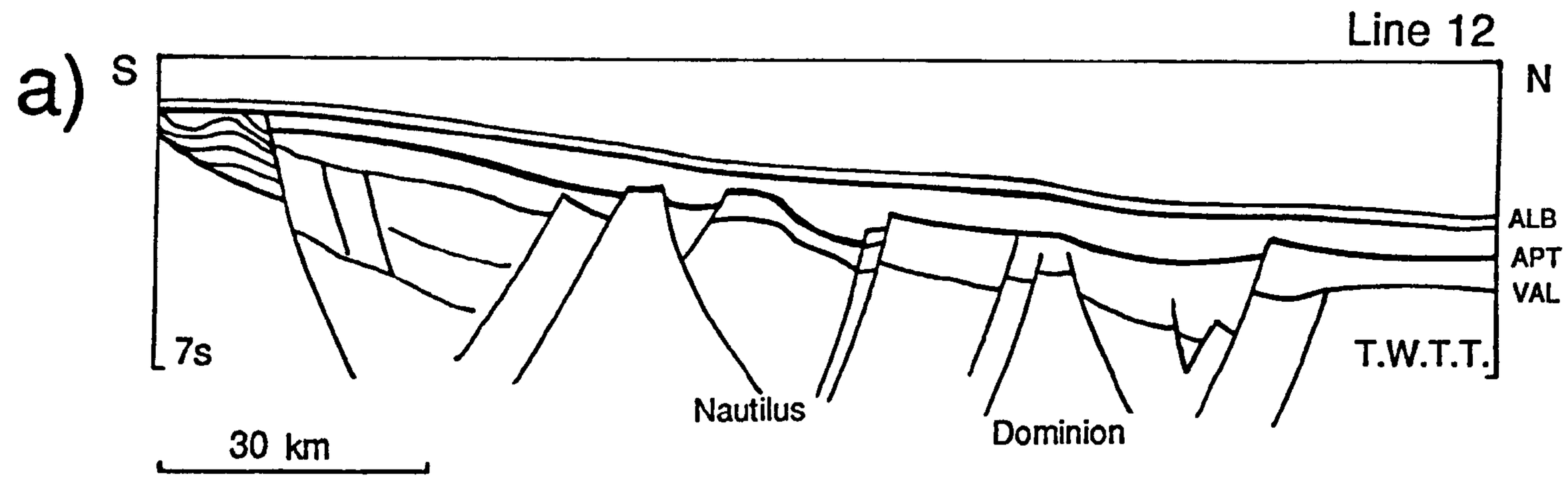


**Figure 6.15** Line drawing interpretations. a) Line 12 and b) Line 13. Vertical scale to 7 secs T.W.T.T.

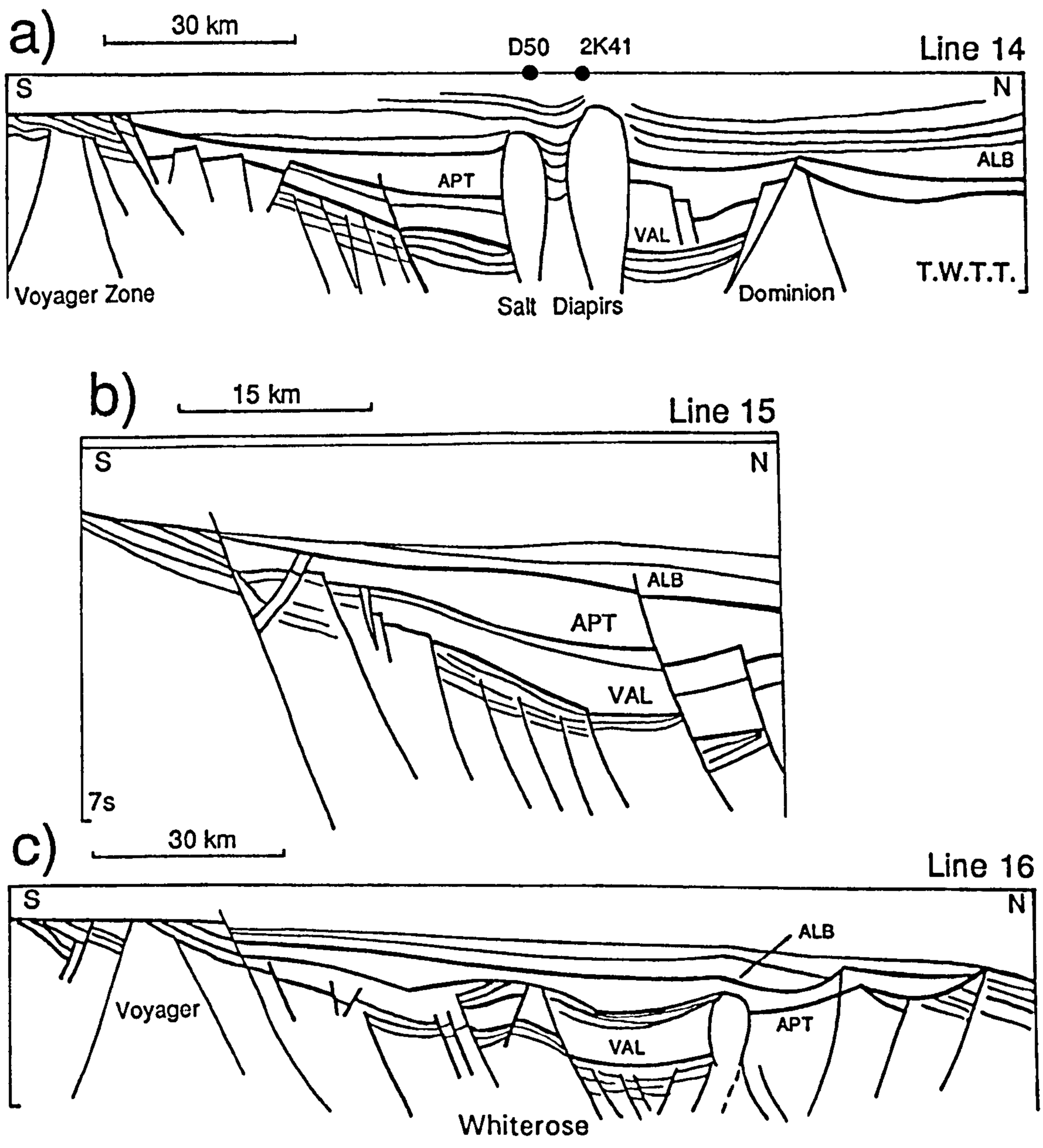


**Figure 6.16** Line drawing interpretations. a) Line 14, b) Line 15 and c) Line 16 Vertical scale to 7 secs T.W.T.T.

Figure (6.16c) shows that the Voyager Fault Zone horst has narrowed to only 10 km between the Jeanne d'Arc basin bounding fault and the Anson Graben on line 16. The basin deepens northwards but then rises onto an intra-basin high (Whiterose) associated with erosional truncation of the overlying sedimentary cover. A single salt diapir, near the northern margin of the basin, is on a NW-SE trend which may be associated with the Dominion transfer (Enachescu, 1987). Line 16 transects the normal faults bounding the Central Ridge very obliquely and they are therefore poorly imaged. All B.M.B.'s are amalgamated over the central ridge.

### 6.3.4 Fault Terminations.

The bar charts in Figures 6.17 to 6.20 are simple graphical plots of the frequency of fault terminations at various horizons on the Soquip survey. The lighter shaded columns refer to terminations of the Murre fault within the post-rift section indicating, as expected, that the basin bounding fault was active the longest. Across the rest of the basin, fault terminations are recognised *only* at B.M.B.s. No spatial distribution pattern emerges for the middle Albian (ALB) and base Aptian (APT) B.M.B's. In general there are fewer base Valanginian (VAL) terminations. An increase in frequency of terminations at this level towards the North is in part real, since they are absent south of the Voyager Fault, and partly due to sampling bias because the base Valanginian is better imaged North of the Nautilus Fault.

## 6.4 Seismic Survey Overview.

Figure 6.21 shows the Jeanne d'Arc basin and the location of seismically defined erosional truncation - shaded in a hachured pattern. All three breakup

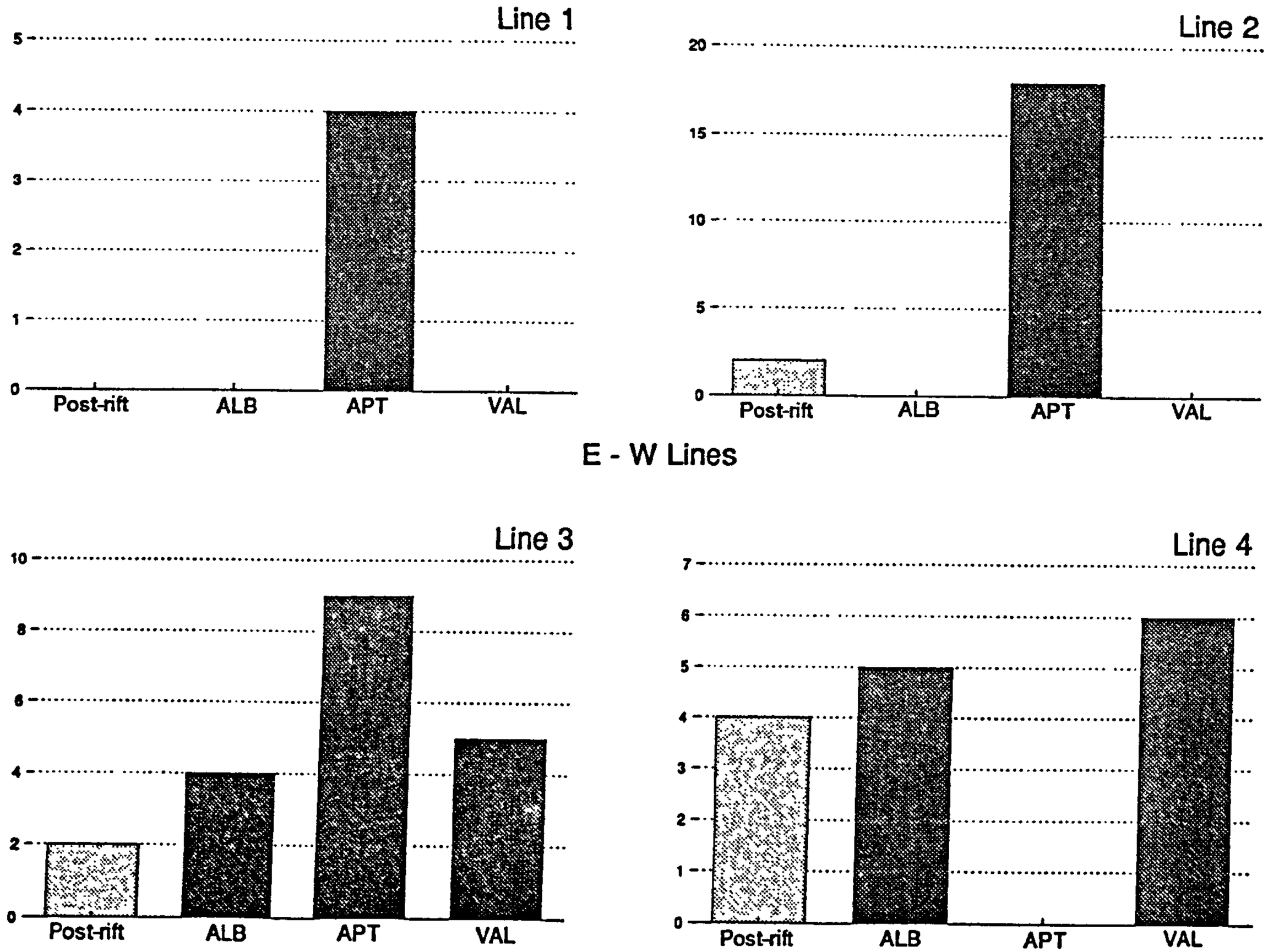


**Figure 6.17** Bar charts for lines East - West lines 1, 2, 3 and 4, showing the frequency of fault terminations at various seismic horizons. Fault terminations within the post-rift megasequence are shaded a lighter colour. Terminations at B.M.B.s have the normal code - see section 6.1.

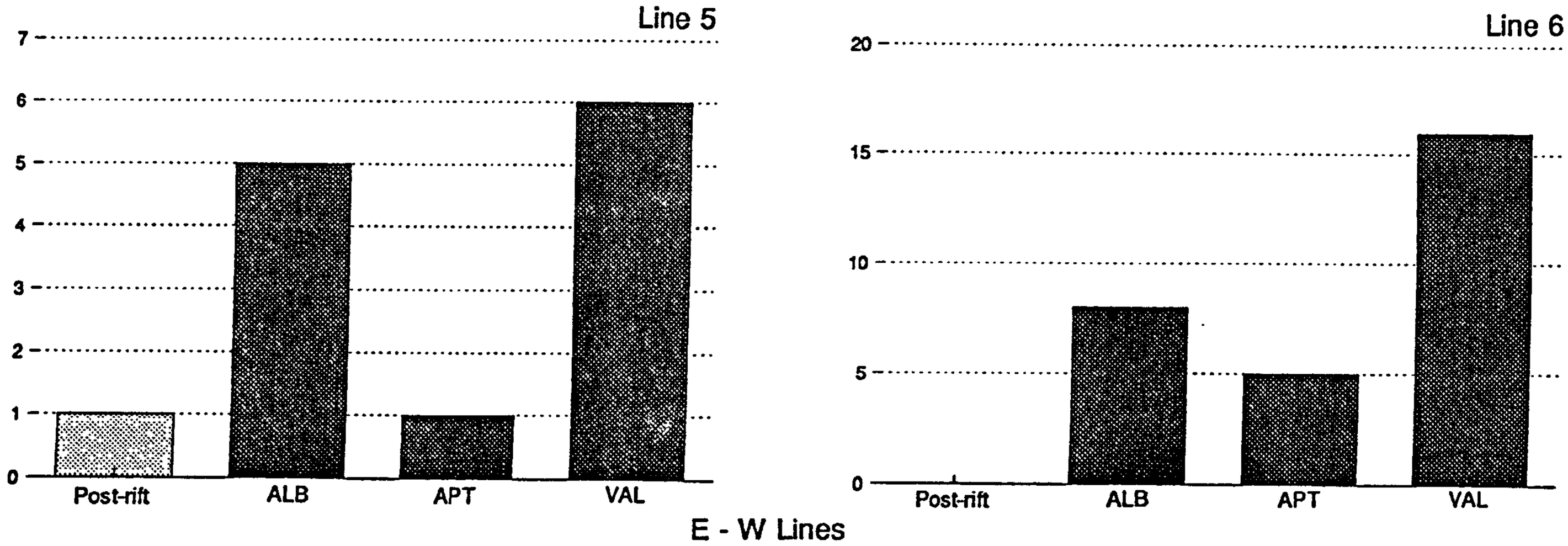


**Figure 6.18** Fault termination bar charts for East - West lines 5 and 6.

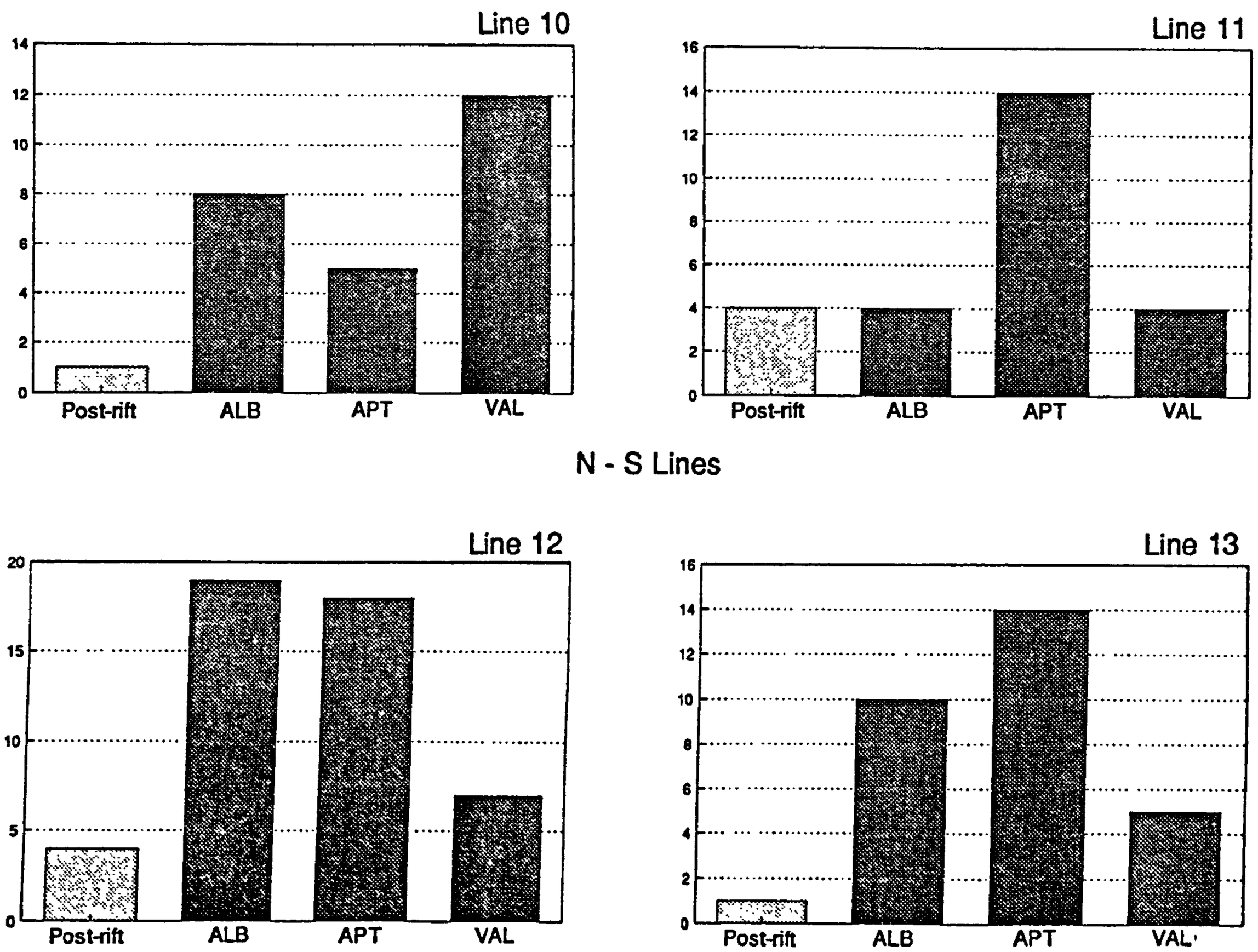


**Figure 6.19** Fault termination bar charts for North - South lines 10, 11, 12 and 13.

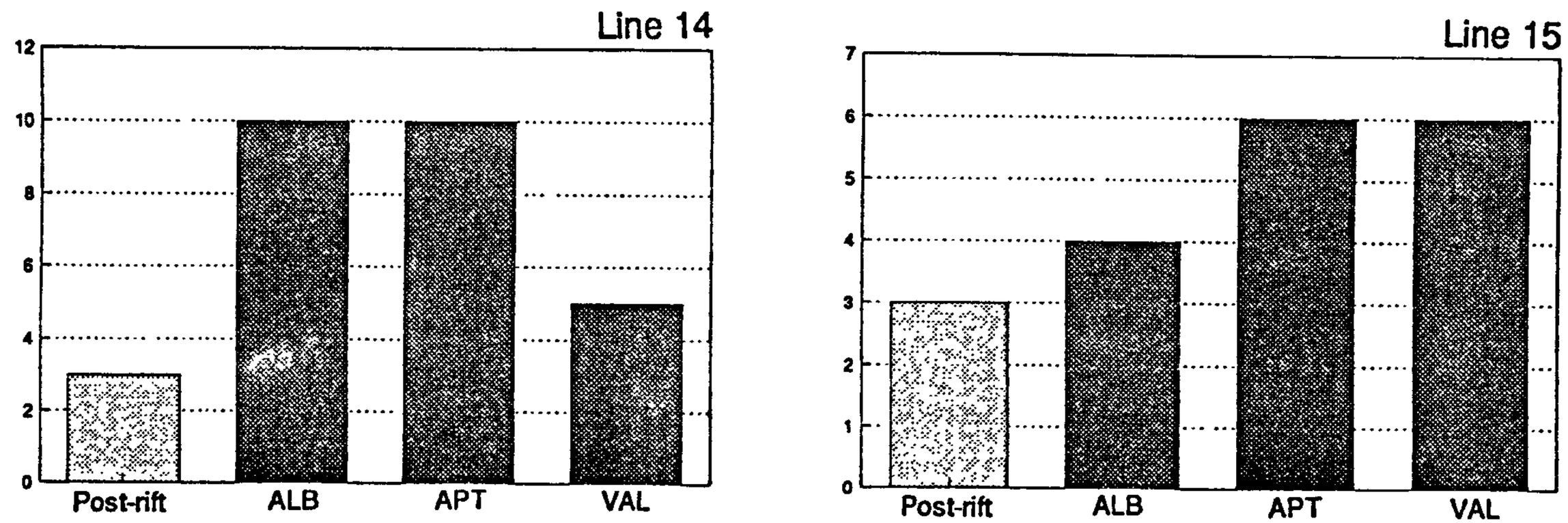


**Figure 6.20** Fault termination bar charts for North - South lines 14, 15, and 16.

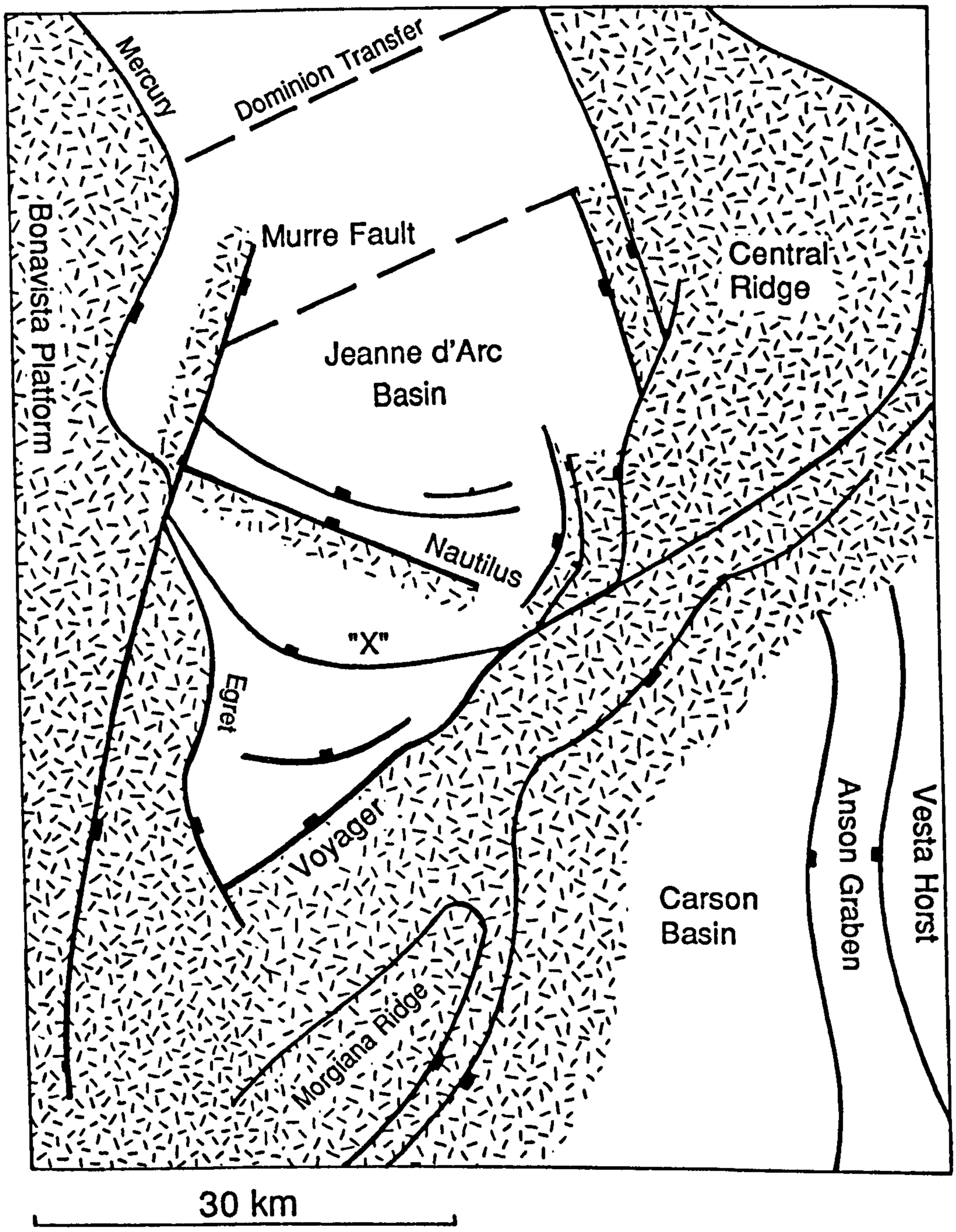


**Figure 6.21** Location of erosional truncation defined by the deep seismic and Soquip surveys. The formal definition of the Jeanne d'Arc Basin includes the area South of the Egret and Voyager Faults, over which erosional truncation is particularly well defined. Other areas include the eastern marginal terrace, adjacent to Central Ridge and the footwalls of the Murre and Nautilus Faults.

megasequence boundaries are amalgamated over the areas of erosional truncation but expand into the deeper part of the basin and to the North. The diagram clearly shows that erosional truncation continues over terraces on both the West and East margins of the Jeanne d'arc Basin -specifically in the footwall of the Egret Fault and adjacent to the Central Ridge. Erosional truncation is particularly strong over the horst bounded to the North by the Voyager Fault and to the South by the Carson Basin. Back-to-back faults appear to have produced significant footwall uplift, as predicted by the flexural cantilever model. Other areas of erosional truncation include the footwall of the intra-basinal Nautilus Fault and the crest of the sediments rotated by the detachment on Flying Foam Terrace.

## 6.5 The Systematic Variation in Breakup Megasequence Boundary Morphology Defined by Seismic Stratigraphic Analysis.

### 6.5.1 Introduction.

Taking the two data sets together, there appears to be a systematic variation in breakup megasequence boundary morphology. This can be explained as the product of regional breakup uplift (Figure 6.22b) superimposed on the syn-rift morphology (Figure 6.22a). Three zones, A, B and C, are defined, parallel to the margin in each of the three tectonic zones (1, 2 & 3) of the Grand Banks (Figure 6.22c). The section shown in Figure 6.22 can be thought of as a composite of deep seismic line 85-3 (zone A) and line 85-4 (zones B & C). Readers should refer back to Figures 6.1 and 5.3 for a plan view.

**ZONE A.**

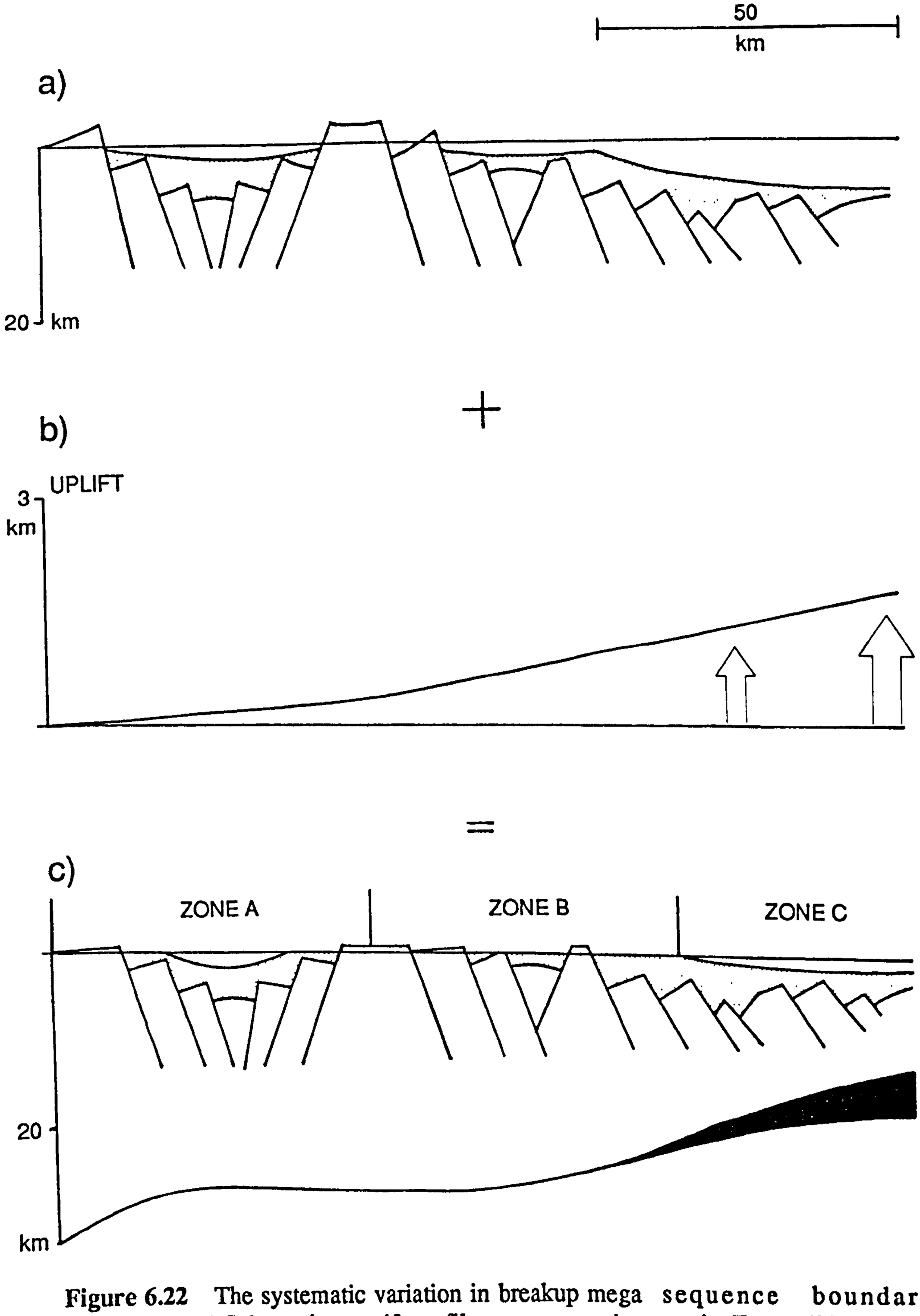


**Figure 6.22** The systematic variation in breakup mega sequence boundary morphology. a) Schematic syn-rift profile across a passive margin. Footwall blocks are above sea level at the western margin and on the central high. Palaeo-bathymetry increases towards the centre of the western basin and towards the eastern end of the profile. b) Regional breakup uplift increases towards the eastern end of the profile due to the combined effects of thermal expansion of the lithosphere and magmatic underplating. c) Profile a) after the addition of regional breakup uplift and the flexural isostatic effects of erosion.

This zone characterises the internal basins (e.g. Jeanne d'Arc) in a distal position relative to the C.O.B. Subaerial erosion is relatively common on the flanks and side terraces of these basins, usually associated with the footwall uplift adjacent to major extensional faults. In some cases the angular unconformity extends further into the basin, indicative of a sub-regional component of uplift. By contrast, breakup in the deeper parts of the basin is marked by a change in deposition within a conformable succession.

**ZONE B.**

In this middle zone there is evidence not only of more widespread erosion but also of a greater intensity of erosion. Good examples of the erosional truncation of reflectors are relatively common and they extend across central parts of the basins.

**ZONE C.**

As the C.O.B. is approached, the resolution tends to decrease as multiples and diffractions become more common. However, it would appear that erosional truncation disappears in zone C. The breakup megasequence boundary deepens dramatically and eventually amalgamates with the landward dipping reflector as defined by Keen & deVoogd (1988). It is concluded that the breakup megasequence boundary in this outer zone is depositional, and that it was below sea level at the onset of seafloor spreading.

### 6.5.2 Detailed Examples of the Breakup Megasequence Boundary Morphology from Zones A & B.

Seismic sections E1 to E5 have been chosen to best illustrate the variation in breakup megasequence boundary morphology and are located on Figure 6.23. The margins and centre of the Jeanne d'Arc basin in zone A are compared and contrasted, together with an example from zone B. The colour scheme, used to define megasequence boundaries on the interpreted sections, is given below.

| Megasequence | Colour |
|---|---|
| Middle Albian B.M.B | Light Blue |
| Base Aptian B.M.B | Red |
| Hauterivian Ridge Jump | Orange |
| Base Valanginian Lmst | Light Green |
| Base Jurassic | Dark Brown |

**Breakup megasequence boundaries at the centre of Zone A.**

Figure 6.24 (modified from Sinclair, 1988) shows the basal Aptian breakup megasequence boundary and the basal Valanginian B-marker limestone horizon in the central part of the Jeanne D'Arc Basin. Four faults terminate in, or just above, the B- marker limestone which explains its definition by Sinclair (1988) as a breakup megasequence boundary. Reflectors are approximately parallel above and, to a lesser extent, below the base Valanginian boundary. The basal Aptian sequence passively onlaps the breakup megasequence boundary close to the fault but becomes conformable further up the hangingwall. It is concluded that the boundary is a depositional break.

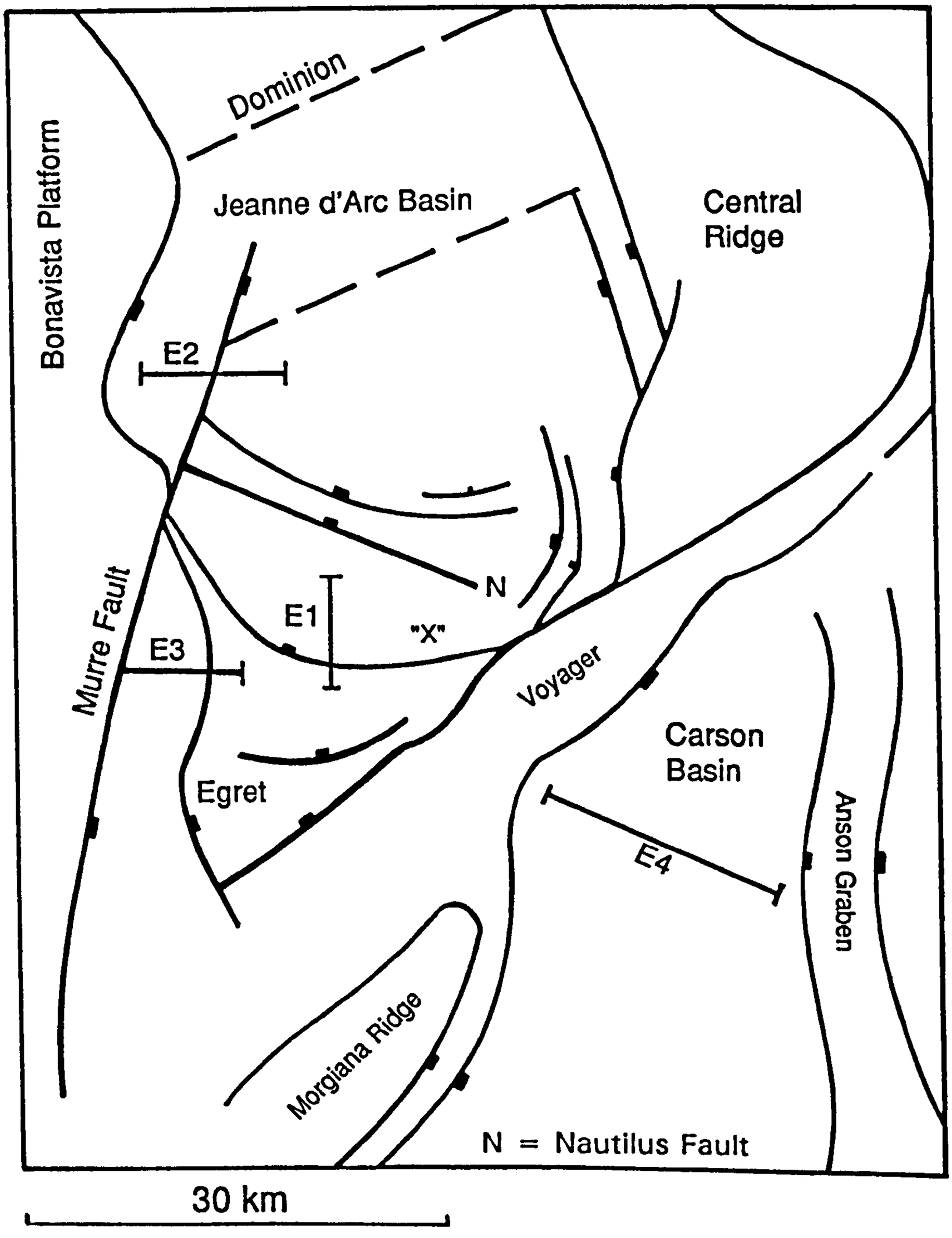


**Figure 6.23** Location map of the seismic sections used to describe the breakup megasequence boundary morphology in two of the three zones defined in section 6.5.1.

**Breakup megasequence boundaries at the margins of zone A.**

Figures 6.25 and 6.26 (Enachescu, 1987) show the amalgamation of breakup megasequence boundaries, at the western margin of the Jeanne D'Arc basin. Figure 6.25, from the Flying Foam Terrace, shows erosional truncation at the level of the basal Aptian breakup megasequence boundary. It has a hummocky topography, consistent with subaerial exposure, localised at the crest of a rotated block of detached sediments. The parallel reflectors of the post-rift Aptian-Albian sequence are interpreted as a passive infill derived by erosion from the crest.

Figure 6.26 (Enachescu, 1987) shows the amalgamated Aptian and middle Albian breakup megasequence boundaries forming an erosional unconformity at the southwest margin of the Jeanne d'Arc Basin, truncating earlier Jurassic sequences. Rather than being confined to the footwall of a major fault, the erosional truncation extends across the entire terrace, implying that regional uplift affected the area.

**Breakup megasequence boundaries from the centre of zone B.**

Figure 6.27 shows a good example of erosional truncation at the level of the basal Aptian megasequence boundary. Up to half a second of the underlying sequence has been removed by erosion forming a "bowl-shaped" depression with undulating edges. The scale of the feature is consistent with either a sub-marine or subaerial canyon, but the latter is favoured because of the proximity of the section to areas of erosion so widespread that they can only be realistically formed by subaerial truncation. There is also a lack of hummocky character to the canyon infill that one would expect from a submarine environment.

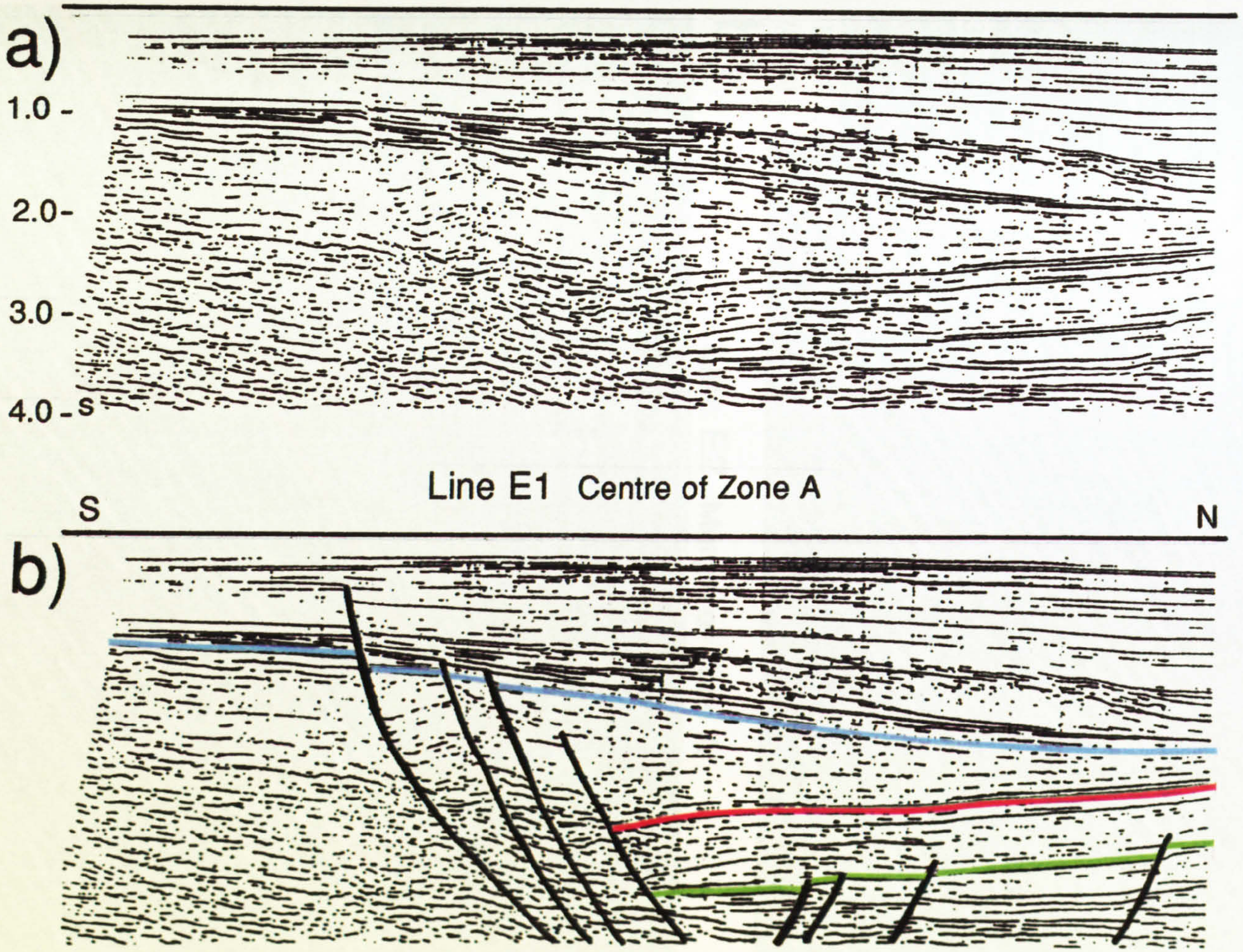


**Figure 6.24** Seismic example Line E1 from the centre of zone A. a) Un-interpreted b) Colour line interpretation, showing numerous fault terminations at the base Valanginian B.M.B. and a smooth base Aptian B.M.B. with sub-parallel reflectors above and below. N.B. See text for key to horizons. (From Sinclair, 1988).

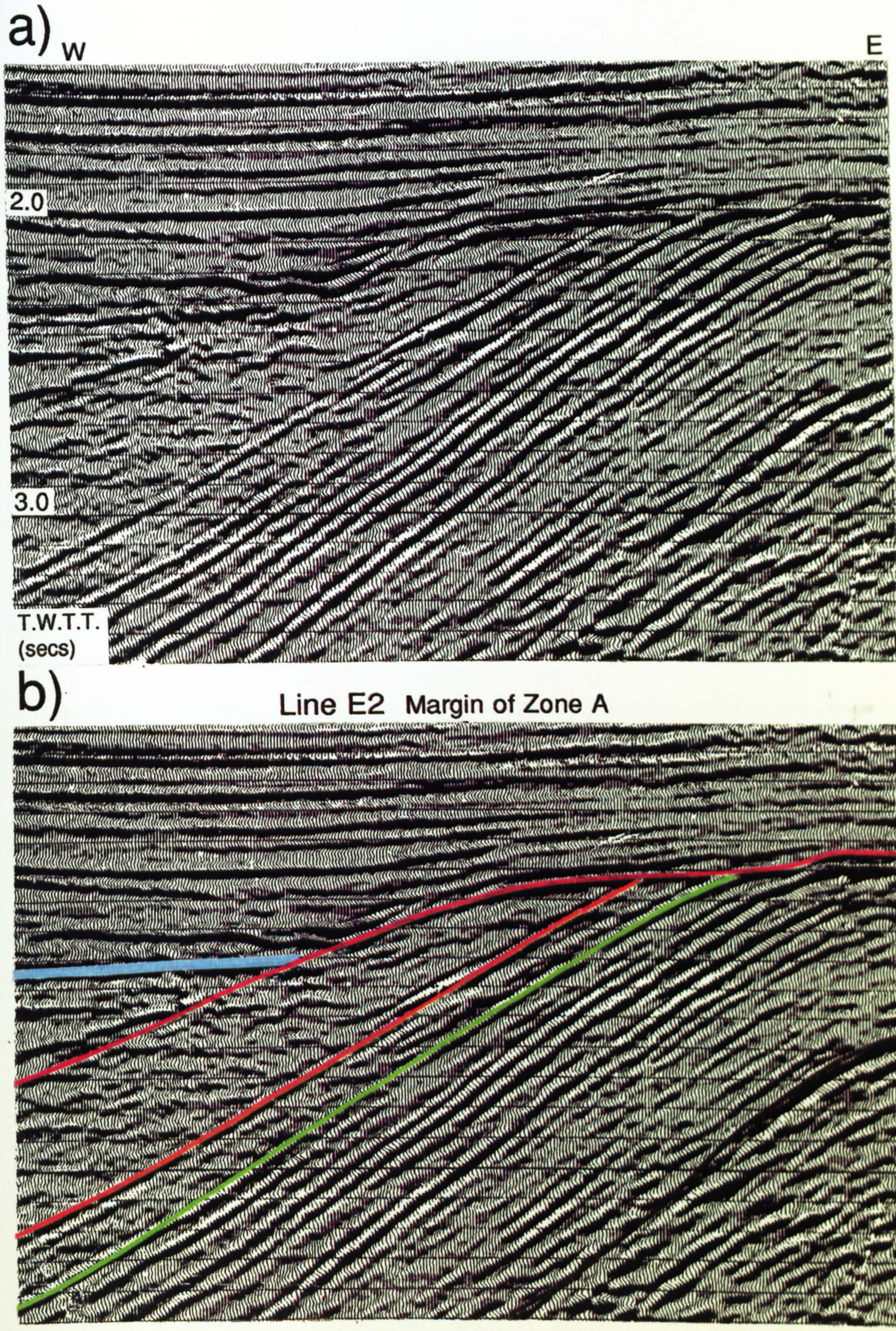


**Figure 6.25** Seismic example Line E2 from the margin of zone A. a) Un-interpreted and b) Colour line interpretation, showing erosional truncation at the crest of the rotated detachment block on the Flying Foam Terrace at the NW margin of Jeanne d'Arc basin.

a)

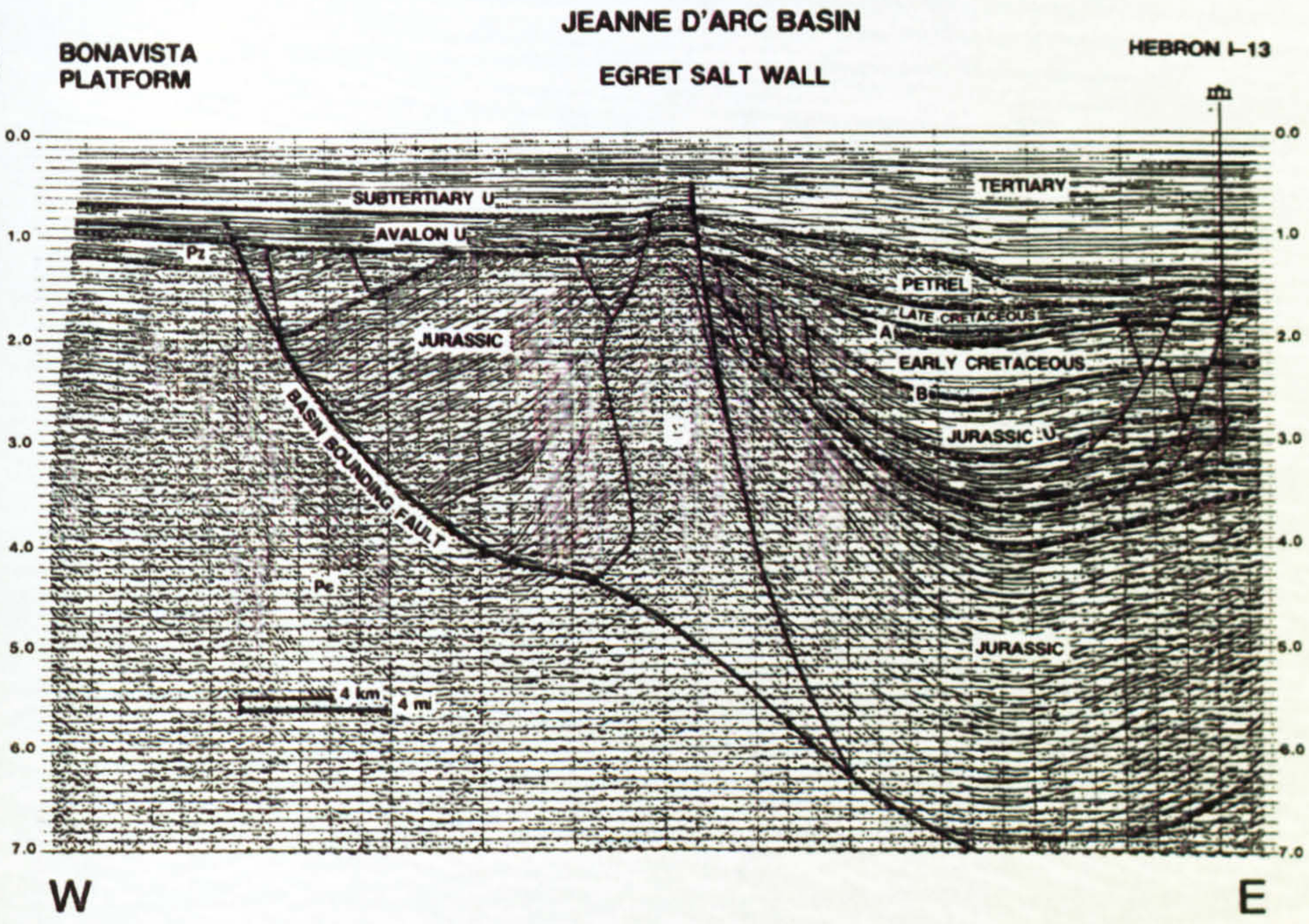


Line E3 Margin of Zone A

b)

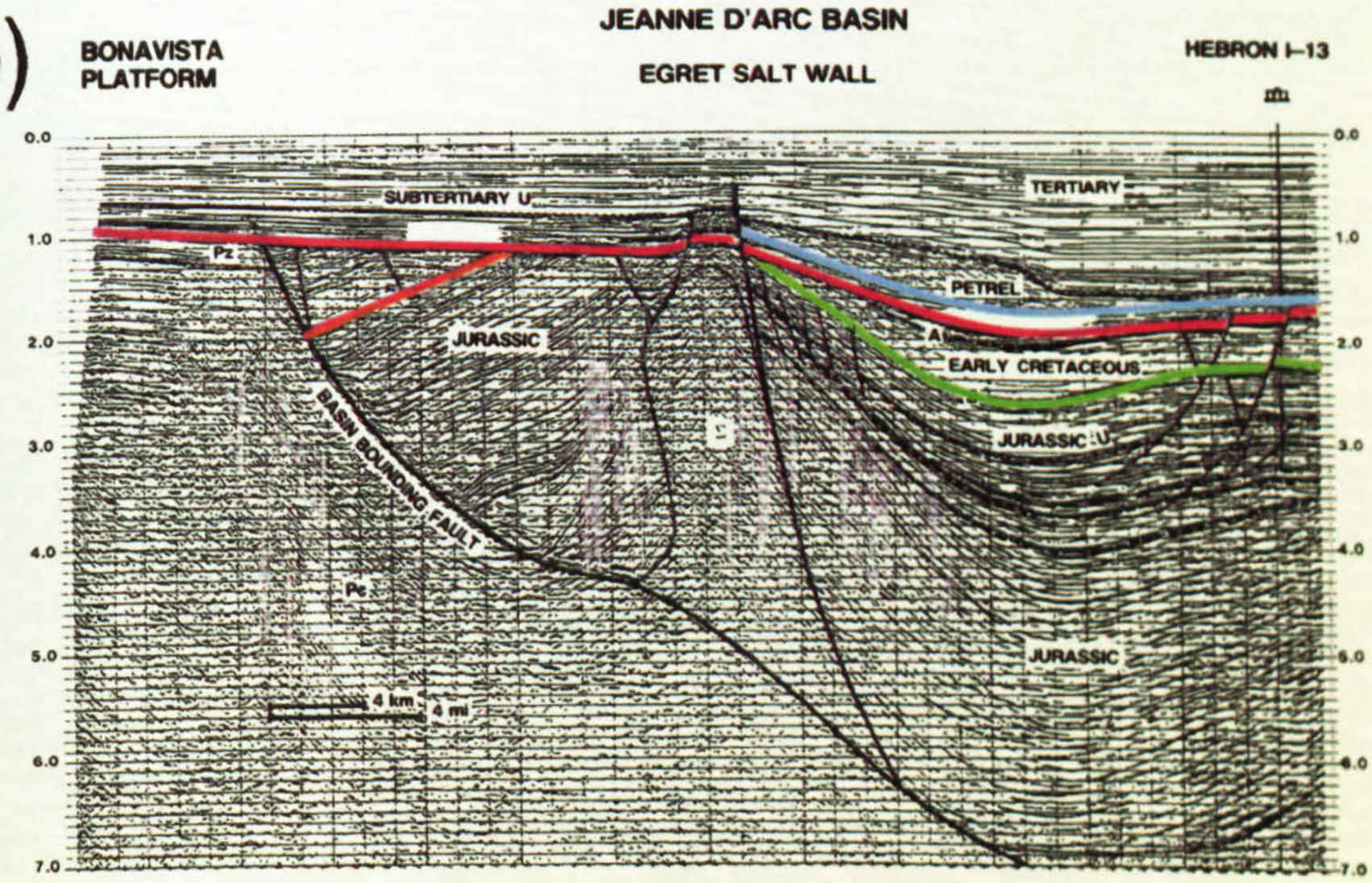


**Figure 6.26** Seismic example Line E3 from the margin of zone A. a) Without colour b) with colour, showing erosional truncation continuing over the western margin of the Jeanne d'Arc Basin in the footwall of the Egret Fault. (From Enachescu, 1987).

a) WNW ESE

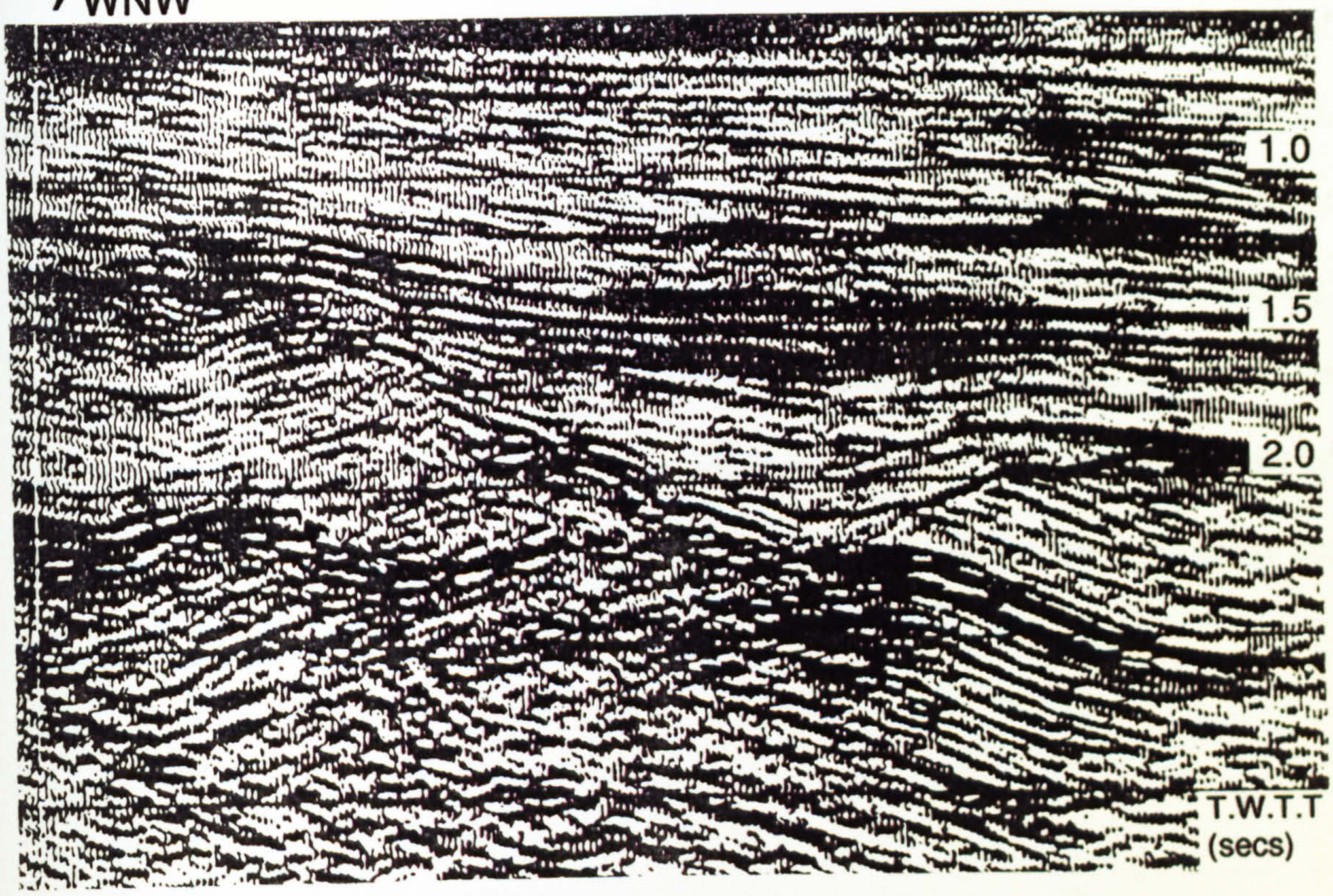


b) Line E4 Centre of Zone B

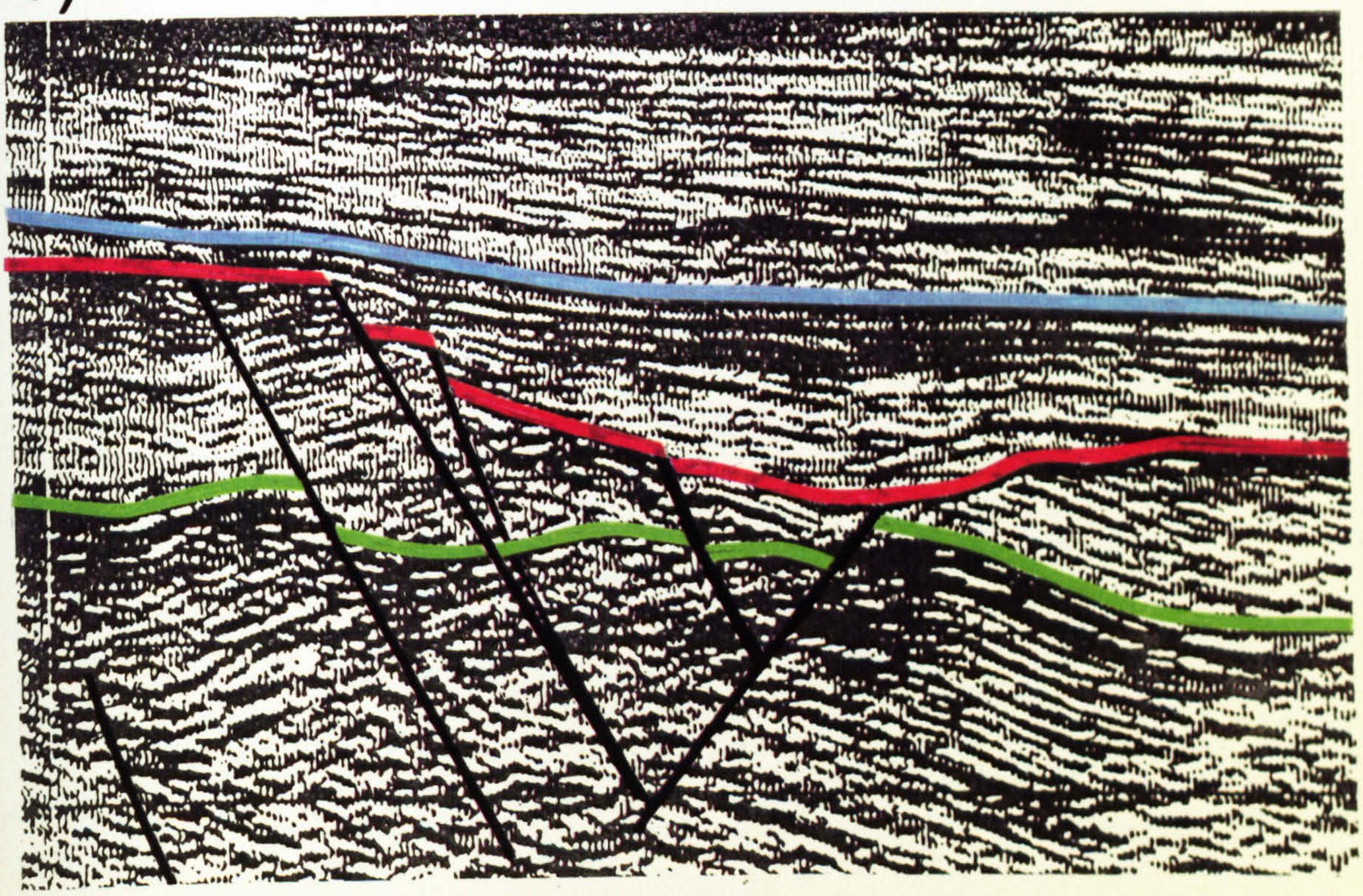

**Figure 6.27** Seismic example Line E4 from the centre of zone B. a) Un-interpreted and b) Colour line interpretation, showing a "bowl-shaped" depression with well defined erosional truncation at the edges implying that up to half a second of syn-rift sediments have been removed.

## 6.6 Discussion.

Although the seismic evidence is sufficient on its own to define the nature of the breakup megasequence boundary in the first two zones (A & B), a third zone (C), close to the C.O.B. can only be postulated tentatively. Further investigation is therefore necessary. Flexural backstripping, with post-rift reverse thermal modelling, has been used to provide additional information about zone C and to check the conclusions drawn from the seismic megasequence analysis. The results, presented in the following chapter, provide a quantitative value for the amount of uplift and erosion in all three zones.

# CHAPTER 7

# MODELLING PHILOSOPHY AND THE RESULTS OF THE APPLICATION TO THE GRAND BANKS

## 7.1 Introduction.

In the previous two chapters the breakup megasequence boundary has been described in terms of its timing and the spatial distribution of subaerial uplift and erosion. However, the fundamental objective of this thesis is to quantify the magnitude of the uplift and erosion using computer modelling techniques. A model profile at the time of breakup can be derived in two ways:-

i) By using a flexural cantilever forward model for the syn-rift phase.

ii) By reverse modelling the post-rift phase, including the sequential backstripping of post-rift sequences and "re-winding" the thermal subsidence.

The great advantage of the second technique lies in the fact that the starting point is the present-day profile (i.e. directly observable) rather than a subjective initial condition or model template. Two assumptions are made, such that, with the exception of post-rift sedimentation, the system remains essentially closed. It is assumed that neither tectonic events or major erosional episodes interrupt the thermal subsidence of the basin, and that sedimentary sequences are added gradually throughout the post-rift phase.

## 7.2 Methodology of Reverse Post-rift Modelling - Flexural backstripping, decompaction and Thermal Uplift.

Reverse post-rift modelling entails three distinct processes: The sequential stripping away of post-rift layers and calculation of the flexural isostatic response to this unloading, the decompaction of the underlying sediments and reverse thermal modelling to replace the heat conducted away during the post-rift phase. The flexural isostatic response to basin unloading is calculated in the Wavenumber Domain, as described in Chapter 2, and need not be elaborated here.

### 7.2.1 Decompaction.

The equations governing the decompaction of sediments during backstripping have been derived by Sclater & Christie (1980) using well data from the North Sea basin. Their derivation can be subdivided into four distinct sections.

The empirical relationship between the porosity of a rock and the depth of burial is obtained first. By using a mathematical relationship between sonic log velocity and porosity, Sclater & Christie (1980) were able to convert the velocity-depth plots of Schlumberger (1974) to porosity-depth plots which show an exponential decrease of porosity with depth (Figure 7.1). This can be expressed mathematically as:-

$$\phi = \phi_0 e^{-cz} \qquad (7.1)$$

where $\Phi_0$ is the initial porosity (at the surface), $z$ is the depth of burial and $c$ is the porosity decay constant (or compaction length). Each curve is slightly different for a given lithology - shale, sandstone shaley sand and chalk. Figure 7.2a shows that the relevant values of $\Phi_0$ and $c$, for each lithology, can be obtained from the linear

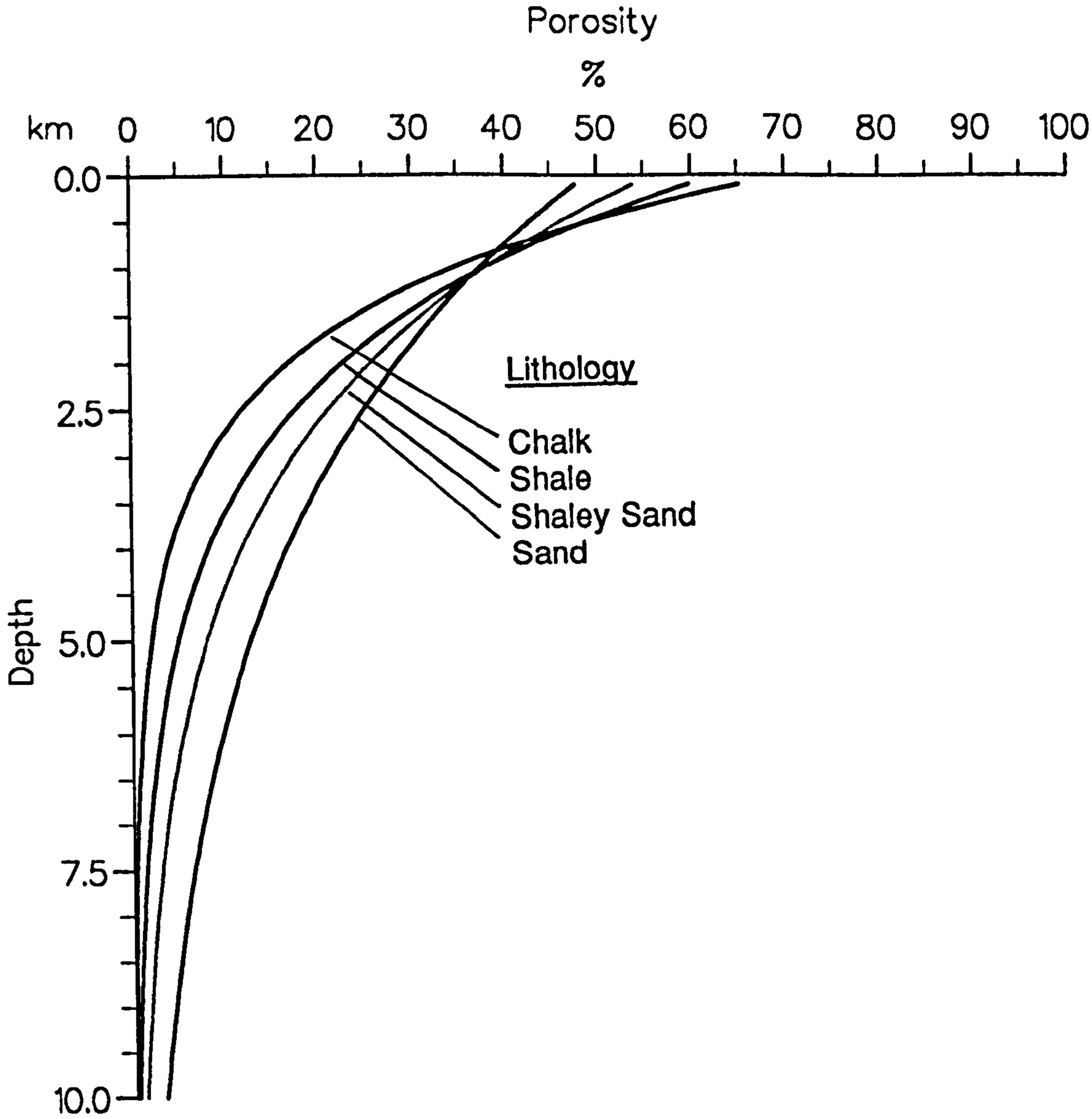


**Figure 7.1** The exponential decay of porosity with burial depth for four different lithologies (modified from Newall, 1991).

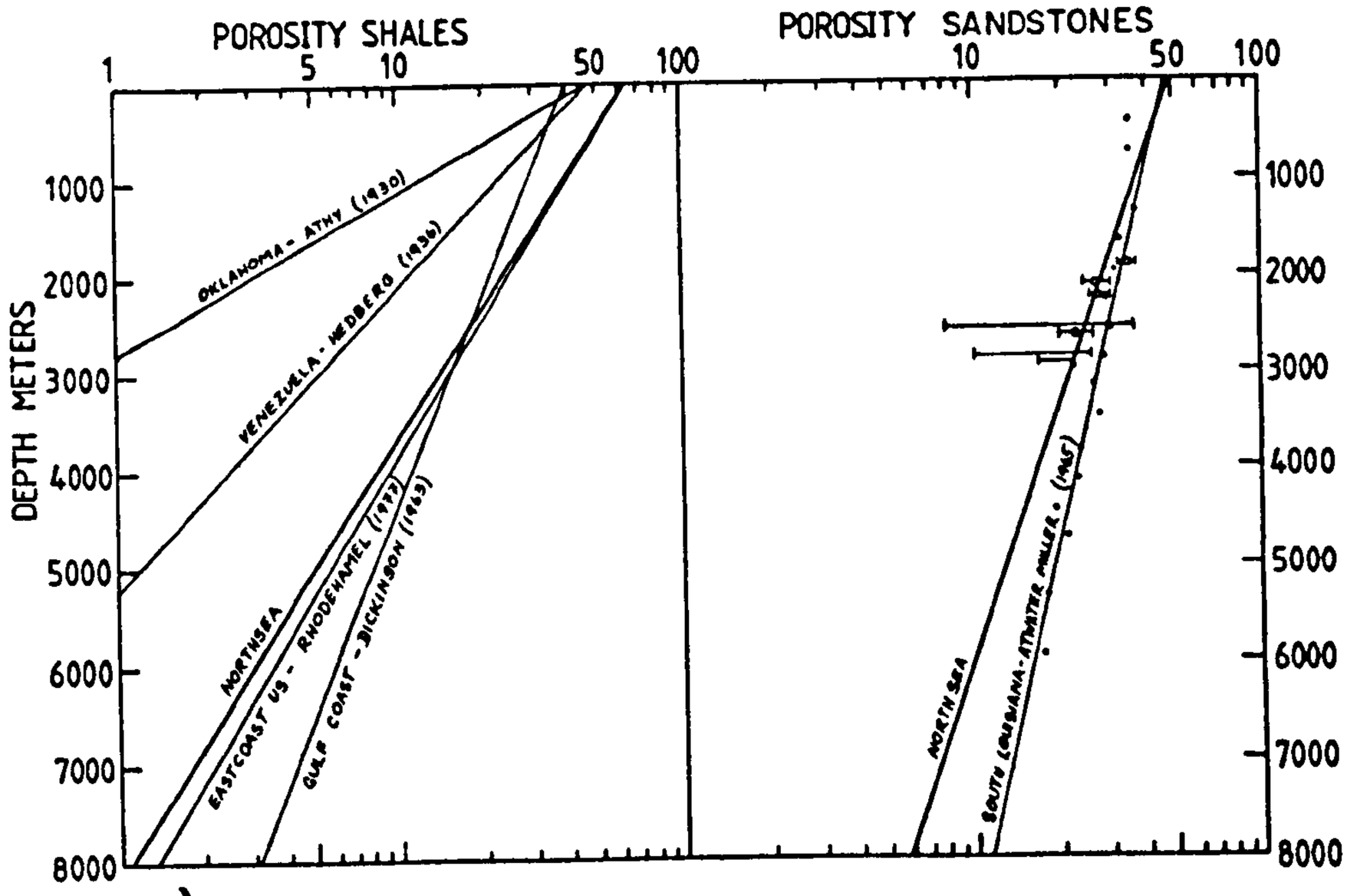


a)

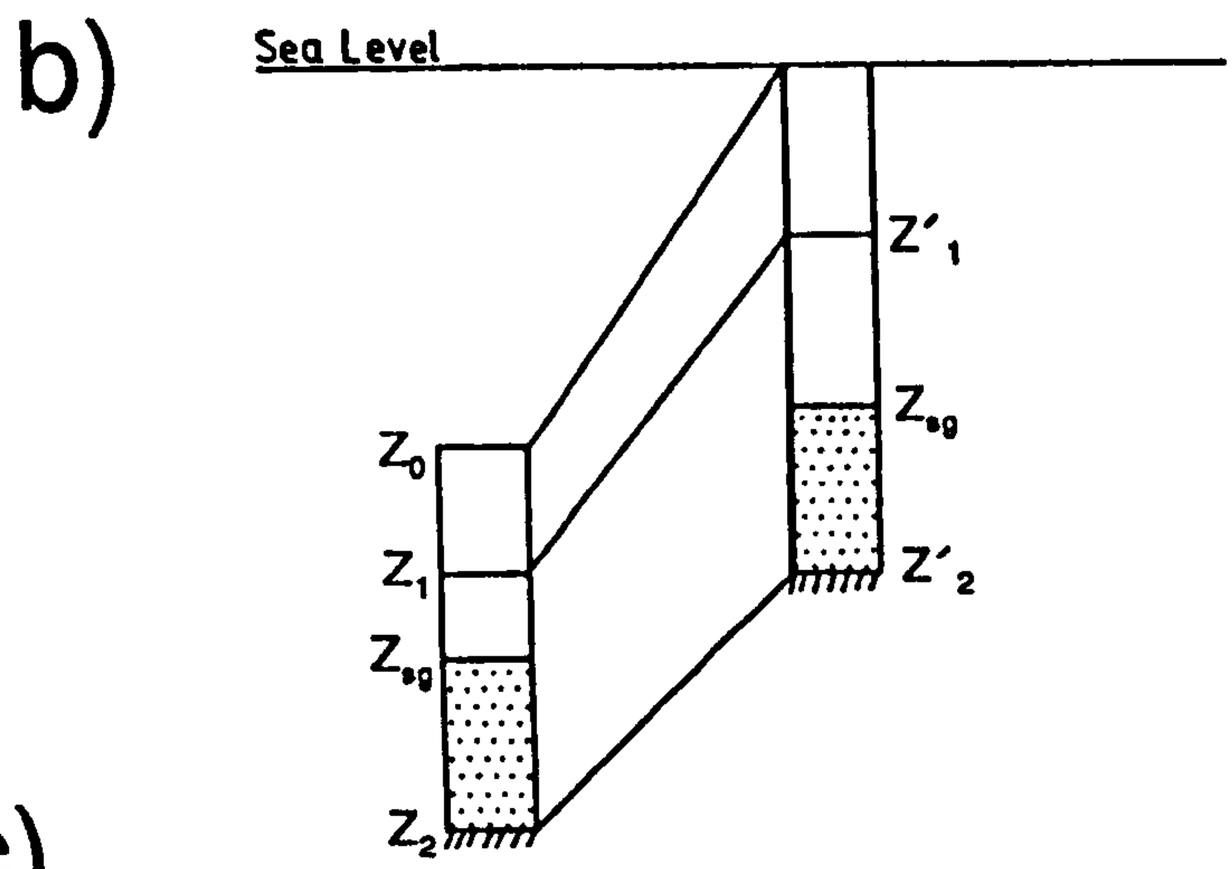


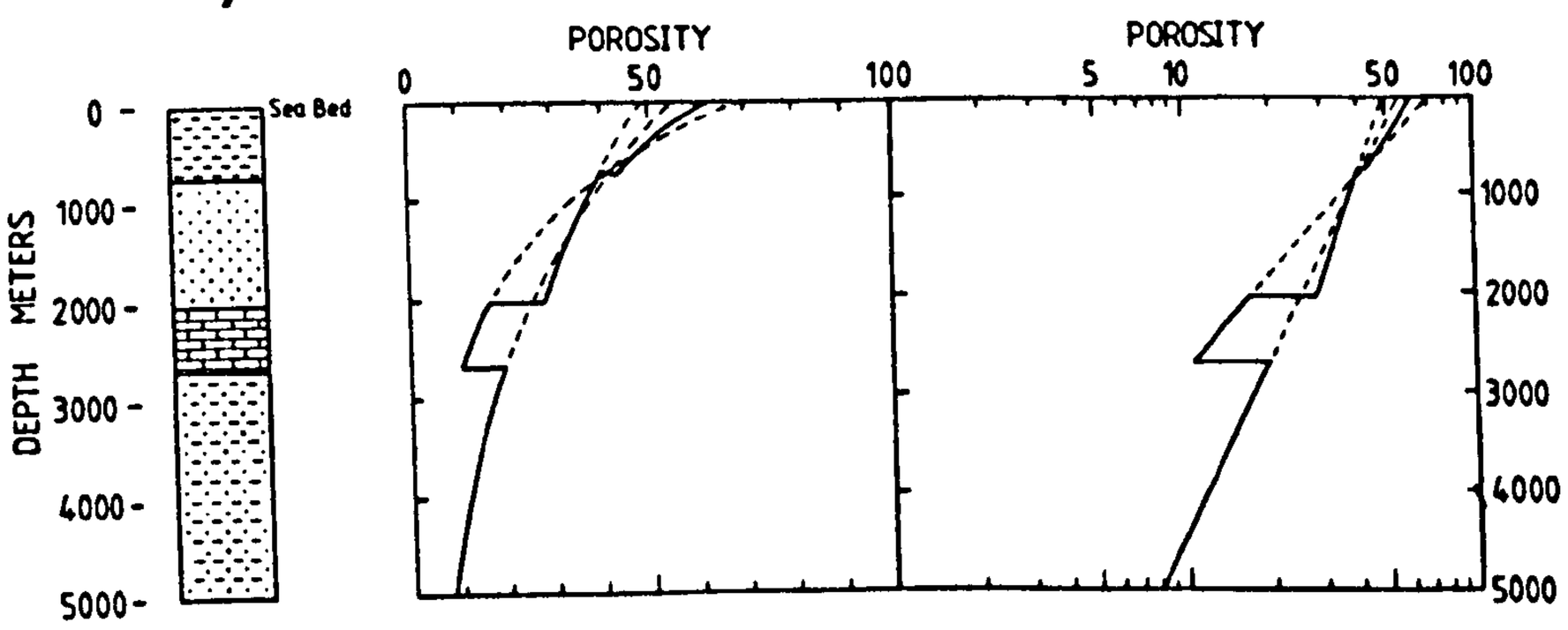


**Figure 7.2** a) The linear relationship between log porosity and depth for 5 shale sequences and two sands. b) Decompaction, by separating the sediment grains and water in a column and expanding the water column. c) The porosity of each layer in the sedimentary column after decompaction is calculated by moving up the relevant porosity-depth curve. (From Sclater & Christie, 1980).

log porosity versus depth plot (Sclater & Christie, 1980). It should be noted that the global data set for the porosity of shale, as described by Sclater & Christie (1980), shows a considerable scatter (Figure 7.2a) which has been attributed to variation in silt content (Schlumberger, 1974). Therefore, wherever possible, locally derived decompaction parameters should be used, based on the sonic log characteristics of a particular lithology. The porosity-depth relationships for mixed lithologies such as "shaley sand" are obtained by interpolating a line on the log-porosity / depth graph, mid-way between the lines for each component (Sclater & Christie, 1980).

The volumes of the two constituents of the rock - matrix and pore-filling water - are separated (Figure 7.2b). The total volume of a column of rock is equal to the volume of the sediment grains, $V_{sg}$, plus the volume of the pore filling water $V_w$ i.e.

$$V_{(w+sg)}=V_{sg}+V_w \tag{7.2}$$

$V_w$, for a column of unit section, is obtained by integrating Equation 7.1 between the lower and upper boundaries.

$$V_w=\int_{z_1}^{z_2}\phi_0 e^{-cz}dz \tag{7.3}$$

$$=\frac{\phi_0}{c}\left[e^{-cz_1}-e^{-cz_2}\right] \tag{7.4}$$

Rearranging Equation 7.2, again for a column of unit cross-sectional area, and substituting $V_w$ from Equation 7.4 gives the height of matrix component:-

$$z_{sg}=z_2-z_1-\frac{\phi_0}{c}\left[e^{-cz_1}-e^{-cz_2}\right] \tag{7.5}$$

The expansion of the pore-filling component, in response to the removal of the

overburden, is calculated next. The total height of the column is assumed to expand during decompaction by absorbing water, while the matrix component remains constant. The magnitude of this expansion is calculated by moving to new upper a lower depth limits - $z'_1$ and $z'_2$ (Figure 7.3b), such that the integral solution of Equation 7.3 becomes:-

$$z'_w = \frac{\phi_0}{c}\left[e^{-cz'_1} - e^{-cz'_2}\right] \tag{7.6}$$

Figure 7.3c shows the situation for a multi-porosity, layer-cake sequence. Decompaction is equivalent to moving to shallower depths along the dashed line extrapolations of the porosity-depth curve for each layer.

Lastly, the new total thicknesses of the underlying sequences is obtained by recombining the expanded water column with the matrix:-

$$z'_{(w+sg)} = z_{sg} + z'_w \tag{7.7}$$

which, by substitution from Equations 7.4 and 7.5, becomes:-

$$z'_2 - z'_1 = z_2 - z_1 - \frac{\phi_0}{c}\left[e^{-cz_1} - e^{-cz_2}\right] + \frac{\phi_0}{c}\left[e^{-cz'_1} - e^{-cz'_2}\right] \tag{7.8}$$

The sequential (top down) solution of Equation 7.8 uses a Newton - Raphson method of numerical approximation iteratively.

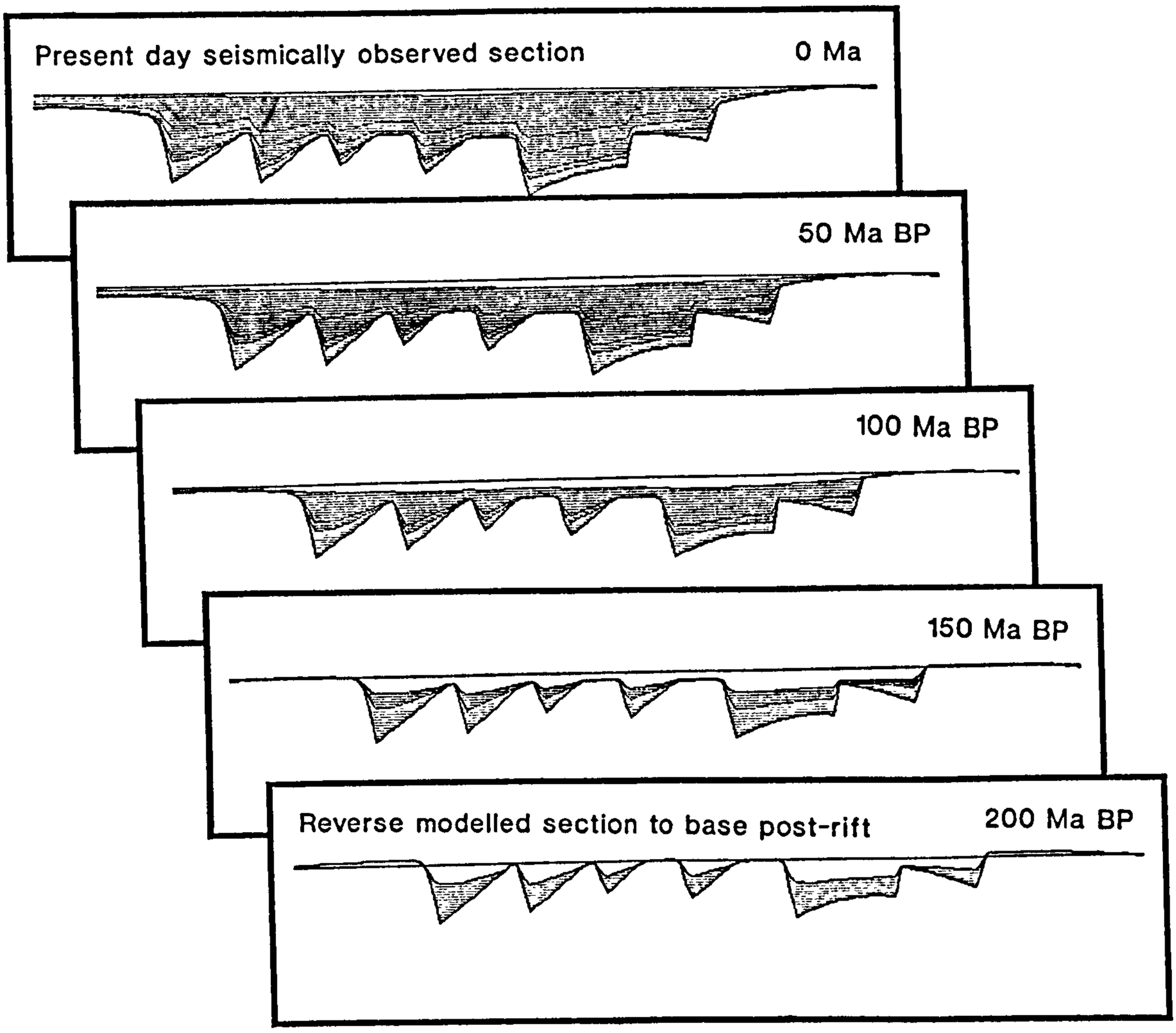


**Figure 7.3** Sequential backstripping of four post-rift sequences and reverse thermal modelling back to the end of the rift phase at 200 Ma. Note that the rift flanks are elevated above sea level and the footwalls of the two central faults appear to have been truncated at sea level.

The decompaction parameters used in the application to the Grand Banks are taken directly from Sclater & Christie (1980):-

| Lithology | Initial Porosity Φ | Decompaction Length C |
|---|---|---|
| Shale | 63 | 0.51 |
| Sandstone | 49 | 0.27 |
| Carbonate | 70 | 0.71 |
| Shaley Sandstone | 56 | 0.39 |

Table 7.1

## 7.2.2 Flexural Backstripping and the effective elastic thickness parameter Te.

Figure 7.3 shows the sequential flexural backstripping and reverse post-rift modelling of a schematic profile back to a rift event at 200 Ma B.P. As each of the four post-rift layers are removed, the profile is unloaded, flexurally isostatically restored and the underlying layers are decompacted or "fluffed out". It can be seen that the thickness of the syn-rift (shaded lighter on Figure 7.3) increases as the backstripping proceeds. Reverse thermal modelling has been included - the details of which are dealt with in the next section.

Perhaps the most important contrast with previous backstripping models is the assumption of flexural rather than Airy isostatic compensation. Figure 7.3 clearly shows that the slope of the flanks towards the centre of the basin has been reversed and the intra-basin footwall highs appear to have been truncated (by erosion) at sea level. Flanking uplift is even more prominent in Figure 7.4b, backstripped with a Te

of 5.4 km, where it accentuated by thermal uplift. When Te is lowered to 0.5 km (approaching the Airy case) the flanking uplift disappears and palaeo-bathymetry of the basin is greatly reduced (Figure 7.4c).

### 7.2.3 Reverse Thermal Subsidence Modelling

By reversing the process described in section 2.8.1, heat can be returned to the profile such that the thermal uplift at the onset of the post-rift phase can be calculated. A simple approach is to assume that the elevated geothermal gradient end of the rift phase is controlled by a constant Beta factor across the profile. The thermal uplift added to the reverse model shown in Figure 7.5b is calculated by assuming a constant Beta factor of 1.7. Without reverse thermal modelling (Figure 7.5c) the basin is too deep and flanking uplift is under-estimated.

In the following chapters it will be shown that more accurate reverse modelling is achieved by estimating the end-rift Beta profile using an initial forward model.

## 7.3 Coupled Reverse Post-rift and Forward Syn-rift Modelling.

Although reverse post-rift and forward syn-rift modelling can be applied separately, a more powerful approach combines the two techniques by comparing the model results at the end-rift / onset of the post-rift stage. The link between the two models is the stretching factor profile used to define the thermal structure at the onset of the post-rift subsidence phase, which can be predicted by the forward syn-rift flexural cantilever model. Figure 7.6 shows the four main stages of the integrated

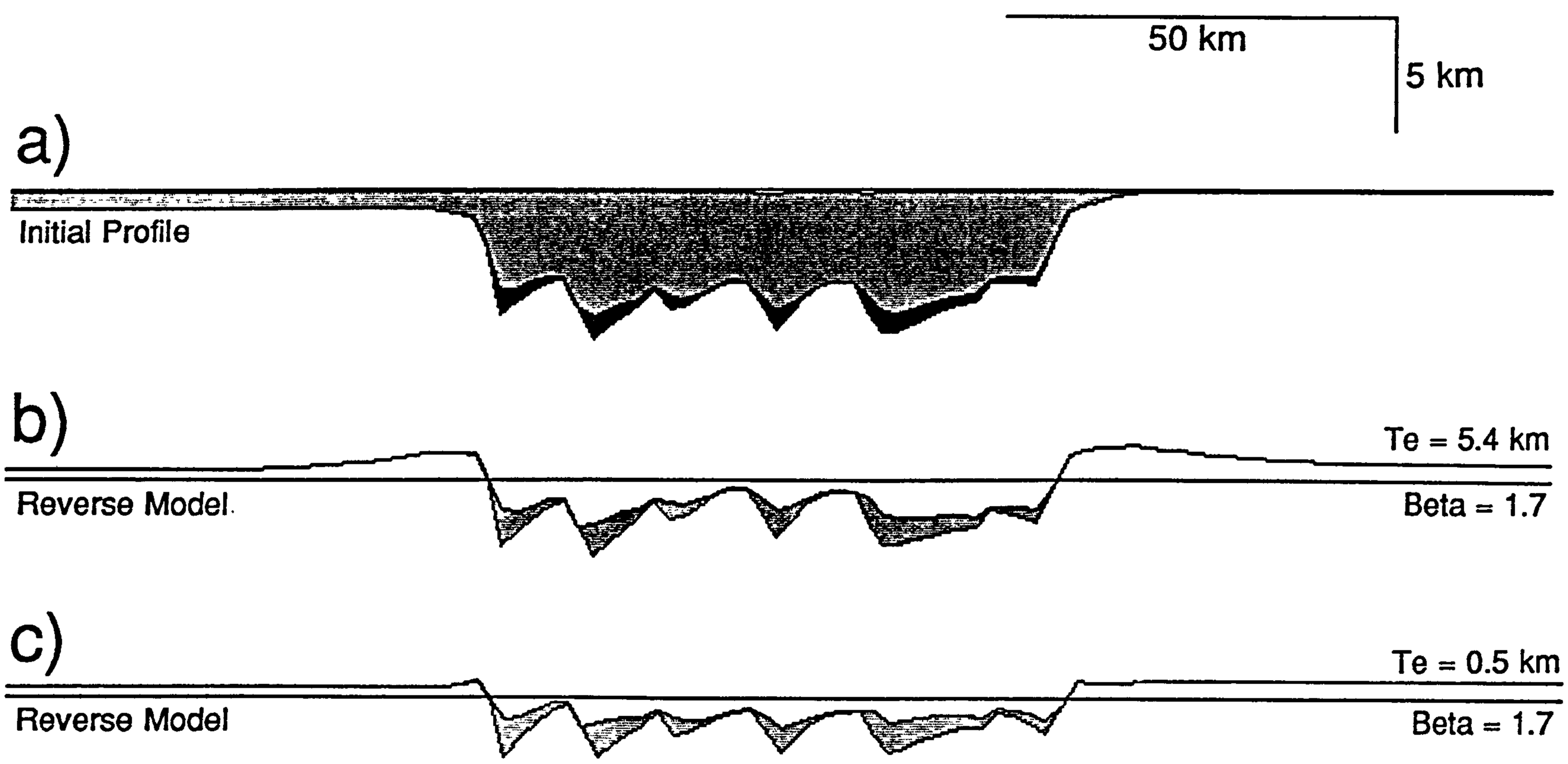


**Figure 7.4** The effect of varying Te on reverse post-rift modelling results. a) Initial profile. b) Reverse model result with Te = 5.4 km, producing rift-shoulder uplift and deep bathymetry in the basin. c) Te = 0.5 km - approximating to Airy backstripping, produces a profile with small differences in elevation. Constant Beta = 1.7 for b) and c).

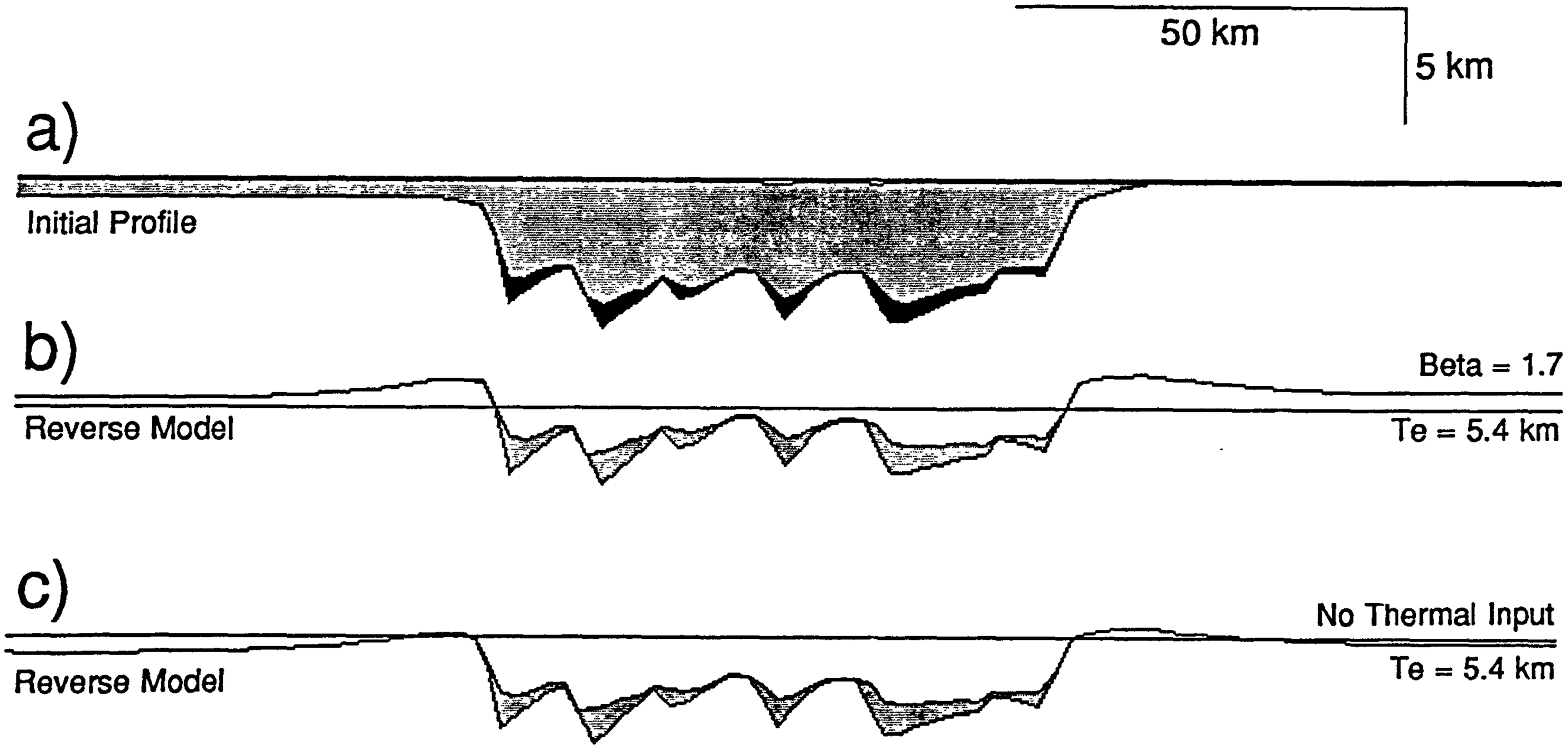


**Figure 7.5** The effect of thermal input on reverse post-rift modelling results. a) Initial profile b) With thermal uplift for a constant stretching factor - Beta = 1.7. c) Without thermal uplift. Te = 5.4 km for b) and c).

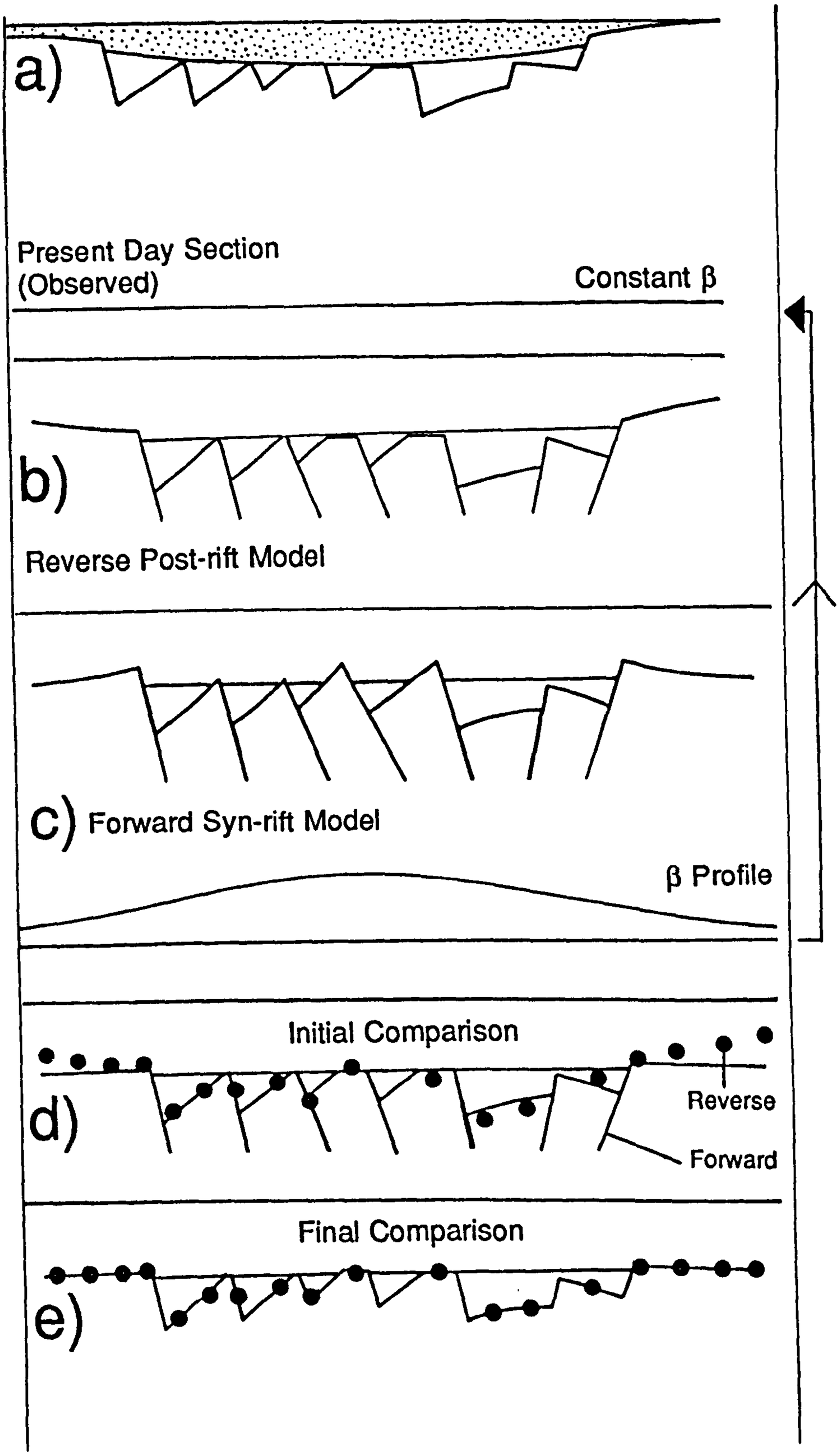


**Figure 7.6** Modelling methodology used in this thesis. a) Present day section (post-rift sediments are shaded). b) Reverse post-rift model using a constant Beta factor. c) The forward syn-rift model. d) Comparison of b and c (dots - reverse, solid - forward). e) Final comparison of updated forward model with the revised reverse model, which uses the Beta profile in c.

modelling sequence:-

1) Reverse post-rift modelling with a constant Beta factor (Figure 7.6a & b). Syn-rift palaeo-bathymetric constraints are important at this stage and erosional truncation is also used to define areas that were at, or above, sea level at breakup.

2) Forward modelling a "first-pass" end-rift stratigraphy (Figure 7.6c) and comparing the results (after erosion) to the reverse model derived in the first step. Figure 7.6d shows that a common discrepancy arises at the margins of the profile where the degree of stretching has been over-estimated by the constant Beta factor in step 1. Too much heat is input by the reverse thermal model and the elevation of the profile is too high compared to the forward model.

3) The third step - importing the more realistic Beta factor from the "first-pass" flexural cantilever model and reverse modelling for a second time - as marked by an arrow in Figure 7.6.

4) The final model is obtained by "fine-tuning" the flexural cantilever model until a best fit is obtained with the end-rift stratigraphy predicted by the reverse model from step 3 (Figure 7.6e).

## 7.4 Application of combined reverse post-rift and forward syn-rift modelling to the Grand Banks.

### 7.4.1 Introduction.

Figure 7.7 shows the location of the two deep seismic lines, across the Grand Banks, included in this study. The objective of this section is to quantify the magnitude of breakup uplift and erosion and to test the conclusions of the qualitative

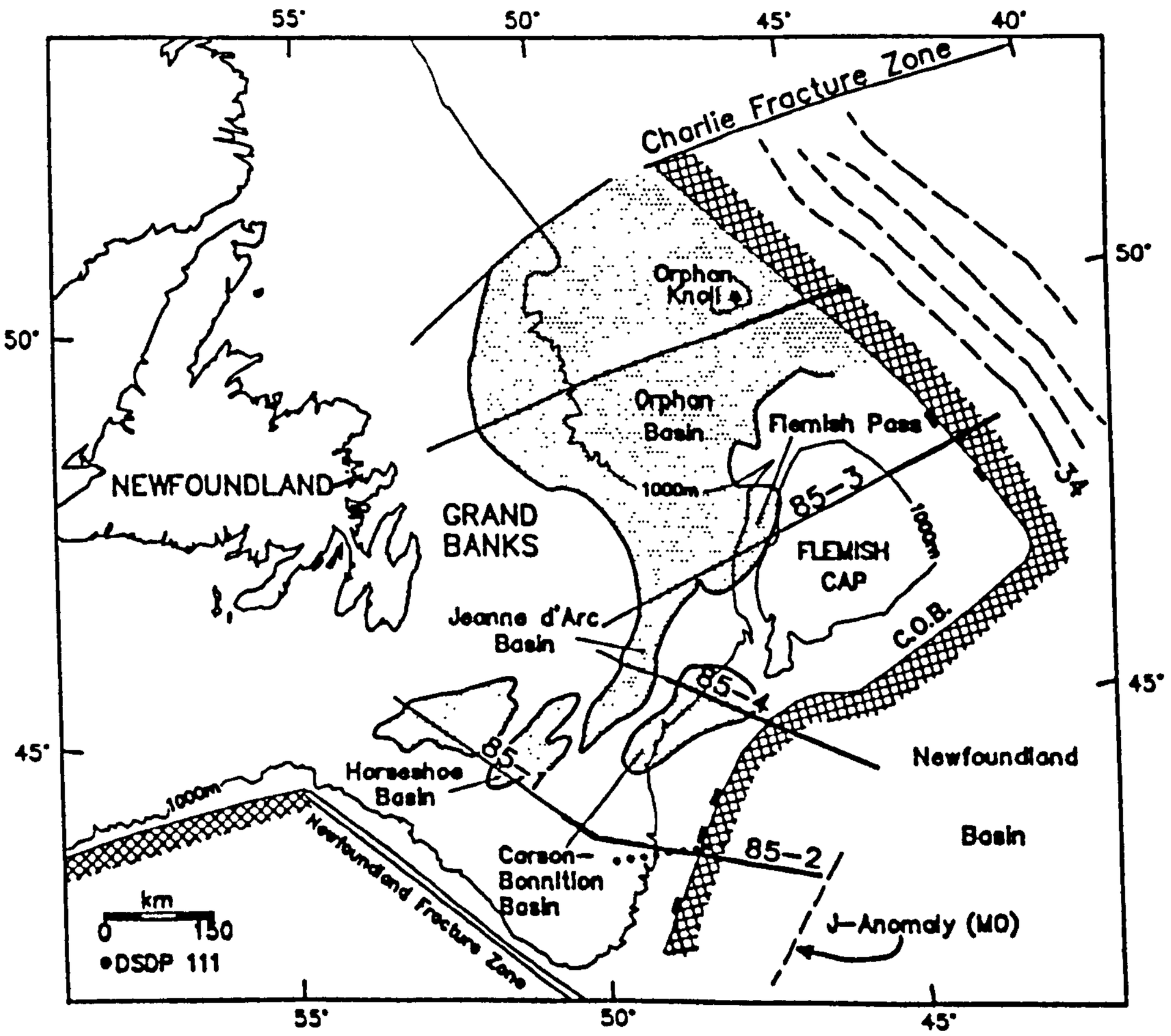


**Figure 7.7** Location map for the Grand Banks deep seismic profiles modelled in Chapter 7.

study outlined in the previous chapter. Reverse post-rift and initial forward syn-rift modelling, undertaken for this thesis, utilises two computer software packages, developed by Professor N.J. Kusznir at the University of Liverpool. These are "Backstrip", which incorporates all of the calculations outlined in section 7.2, and "Stretch", which is an interactive computer program of the flexural cantilever model. "Backstrip" takes account of the flexural isostatic rebound created by removing post-rift layers, decompaction of the underlying layers, reverse thermal subsidence modelling and the extra water loading due to the filling of a larger pore volume.

Before the technique of combined reverse post-rift and forward syn-rift modelling is applied to deep seismic sections, they are first depth-converted using the velocity structures described below.

### 7.4.2 Velocity Analysis and depth conversion of the Deep Seismic Data from the Grand Banks.

The stacking velocity boxes at the top of the seismic sections were sampled at regular intervals, representative of the velocity structure as a whole. As expected, there was a good correlation between changes in interval velocity and picked seismic horizons. At the middle Albian breakup megasequence boundary there is a large increase in seismic velocity which can be interpreted as a lithological change from shale to (syn-rift) sandstone. At the lower, base Aptian B.M.B. the increase in seismic velocity is more variable.

It was found that the number of velocity intervals in the Tertiary post-rift section were sufficient to calculate the linear depth dependency such that seismic velocity can be given by an equation in the form :-

$$V = A + B.z$$

where z is depth and A and B are constants. For deeper layers this was not possible and constant interval velocities were used for depth conversion. Tables 7.2 and 7.3 list the velocities used for Lines 85-4 and 85-3 respectively.

| Layer | Sequences | Velocity ($ms^{-1}$) |
|---|---|---|
| 1 | Tertiary and Upper Cretaceous Post-rift | V = 1586 + 0.39.z |
| 2 | R7 | 3100 |
| 3 | R6 | 4300 |
| 4 | R5 | 4550 |
| 5 | R4 | 5575 |
| 6 | R3 | 6125 |

Table 7.2

| Layer | Sequence | Velocity ($ms^{-1}$) |
|---|---|---|
| 1 | Tertiary Post-rift | V = 1718 + 0.486.z |
| 2 | Upper Cretaceous Post-rift | 3114.3 |
| 3 | R7 | 3666.7 |
| 4 | R6 | 3920.0 |
| 5 | R5 | 4400.0 |
| 6 | R4 | 4440.0 |

Table 7.3

## 7.5 Modelling Results for Lithoprobe Profile 85-3.

Figures 7.8 shows the original profile Lithoprobe Line 85-3, after depth conversion, the individual tectonic elements of which have been described in detail in Chapter 6. The section is backstripped by removing the thick Tertiary clastic wedge and the thin Upper Cretaceous post-rift sediments and the underlying syn-rift sequences decompacted. A rift age of 105 Ma is used for the reverse thermal modelling and the results are therefore pertinent to the generation of the middle Albian breakup megasequence boundary in Zone 3 (northern Grand Banks - see Chapter 5).

### 7.5.1 Reverse Post-Rift Thermal Modelling Using a Seismically Defined Crustal Stretching Beta Factor.

Although the methodology of reverse post-rift modelling, outlined in the previous sections, started with a constant Beta factor to define the thermal input, a more accurate starting point is possible on the Grand Banks. A crustal stretching Beta profile can be calculated by simply taking the ratio between thinned and un-thinned continental crust, defined by the seismically imaged Moho. (The Beta factor for the oceanic part of the profile is taken to be infinity). When this crustal stretching Beta factor is utilised, in the reverse post-rift model, the resulting section is shown in Figure 7.9. The most remarkable feature is that, with the exception of the 50 km closest to the C.O.B. and Flemish Pass Basin, the profile is at, or just above, sea level across its entire length. The tops of Flemish Cap and Beothuk Ridge are almost perfectly flat. Bad picking in the Gabriel Basin has resulted in the backstripping of

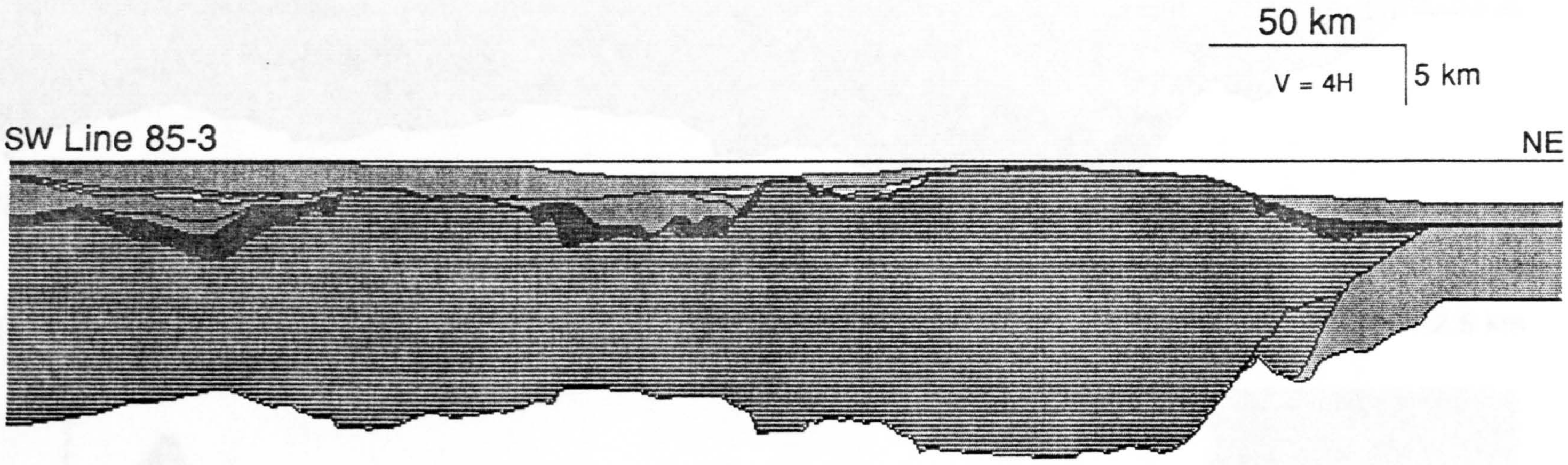


**Figure 7.8** Original section of Lithoprobe Line 85-3 after depth conversion.

an extra sequence and thus the palaeo-bathymetry predicted by the reverse modelling is incorrect. (The basin is in fact full of fluvial clastics deposited at, or close to, sea level - Roberts, 1993 pers. com.)

### 7.5.2 Variation in Te for Reverse Post-Rift Modelling.

The reverse post-rift model, shown in Figure 7.9 is controlled by a post-rift effective elastic thickness of 12.5 km. This value is much larger than the Te used for the forward models (3.5 to 4 km) and the effect of lowering Te has therefore been investigated (Figure 7.10). It is found that smaller values of Te produce unacceptable geometries where the syn-rift sediments form a "dome" above sea level.

### 7.5.3 Coupled Reverse Post-rift and Forward Syn-rift Modelling for Line 85-3

All of the reverse post-rift models described so far share one serious flaw. As discussed in section 5.4, the centre of the Jeanne d'Arc Basin should have a significant water depth at the onset of the post-rift phase. Palaeo-bathymetry in the modelled basins of Line 85-3 has been under-estimated because of the Beta factor used to calculate the reverse thermal subsidence. The crustal stretching Beta factor represents the cumulative effect of the entire rifting history but the reverse thermal model should be controlled only by the latest rift event prior to breakup. Figure 7.11 shows that an initial forward model can be used to determine the pure-shear geometry at the end of the rift-phase and thus more accurately predict the Beta factor. It should be emphasised that, at this stage, no attempt is made to accurately model the geometry of the margin close to the C.O.B.

Figure 7.12 shows the results of reverse modelling Line 85-3 with a combined

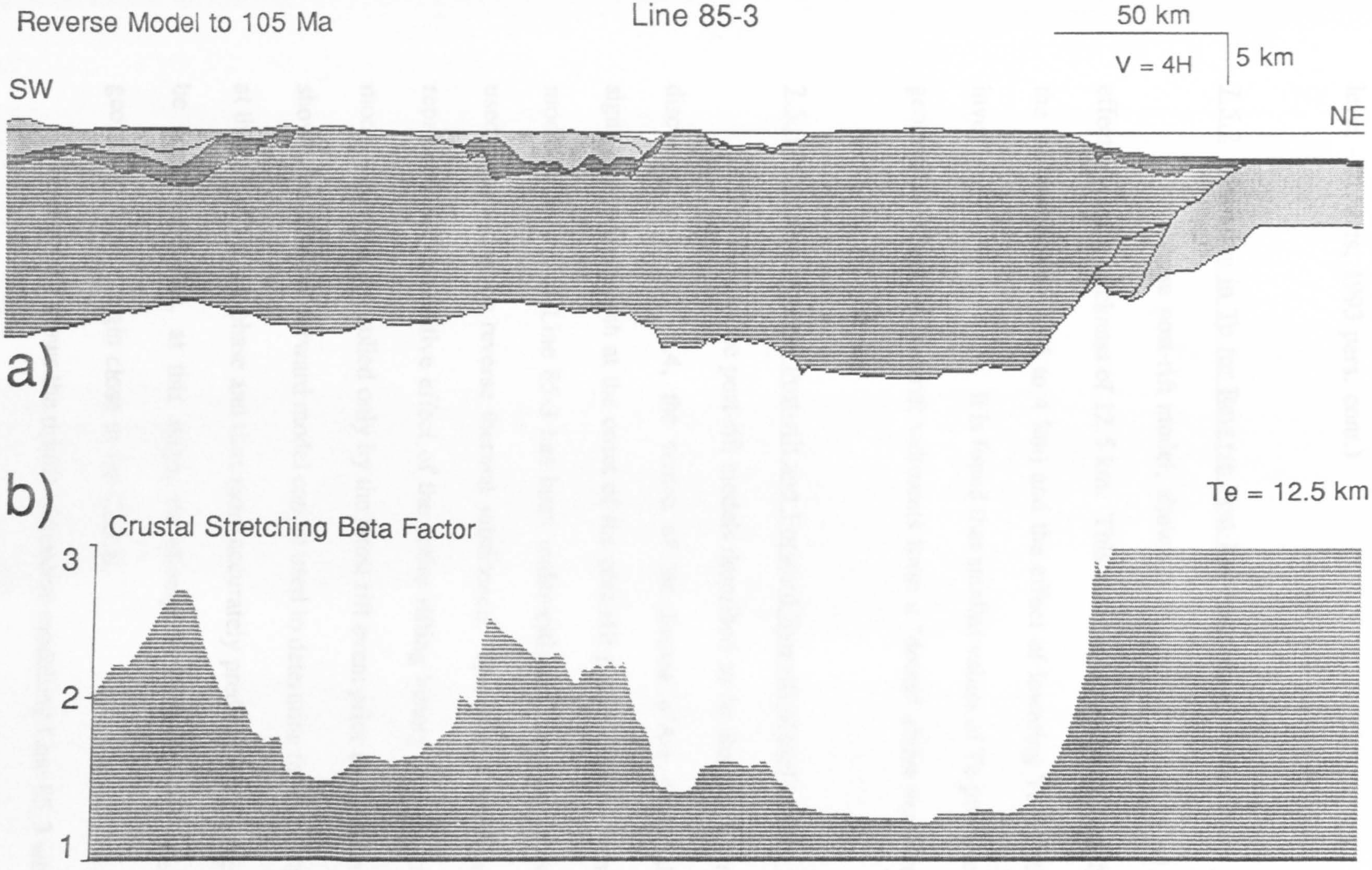


**Figure 7.9** a) Reverse post-rift model of 85-3 using the crustal stretching Beta factor (b) derived from the seismically defined Moho. Te = 12.5 km.

an extra sequence and thus the palaeo-bathymetry predicted by the reverse modelling is incorrect. (The basin is in fact full of fluvial clastics deposited at, or close to, sea level - Roberts, 1993 pers. com.)

### 7.5.2 Variation in Te for Reverse Post-Rift Modelling.

The reverse post-rift model, shown in Figure 7.9 is controlled by a post-rift effective elastic thickness of 12.5 km. This value is much larger than the Te used for the forward models (3.5 to 4 km) and the effect of lowering Te has therefore been investigated (Figure 7.10). It is found that smaller values of Te produce unacceptable geometries where the syn-rift sediments form a "dome" above sea level.

### 7.5.3 Coupled Reverse Post-rift and Forward Syn-rift Modelling for Line 85-3

All of the reverse post-rift models described so far share one serious flaw. As discussed in section 5.4, the centre of the Jeanne d'Arc Basin should have a significant water depth at the onset of the post-rift phase. Palaeo-bathymetry in the modelled basins of Line 85-3 has been under-estimated because of the Beta factor used to calculate the reverse thermal subsidence. The crustal stretching Beta factor represents the cumulative effect of the entire rifting history but the reverse thermal model should be controlled only by the latest rift event prior to breakup. Figure 7.11 shows that an initial forward model can be used to determine the pure-shear geometry at the end of the rift-phase and thus more accurately predict the Beta factor. It should be emphasised that, at this stage, no attempt is made to accurately model the geometry of the margin close to the C.O.B.

Figure 7.12 shows the results of reverse modelling Line 85-3 with a combined

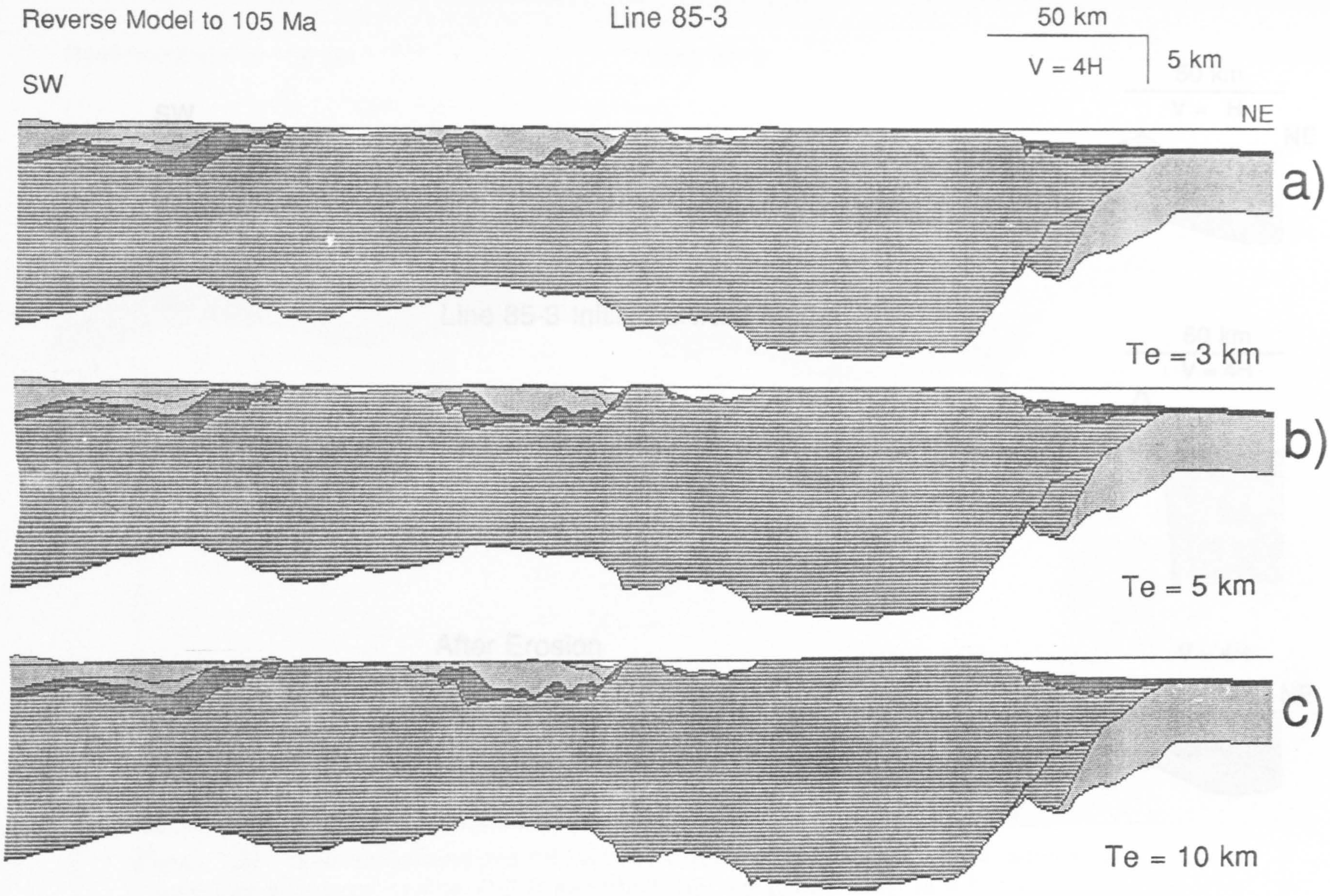


**Figure 7.10** The effect of elastic thickness on the reverse model results for line 85-3:- a) Te = 3 km. b) Te = 5 km. c) Te = 10 km.

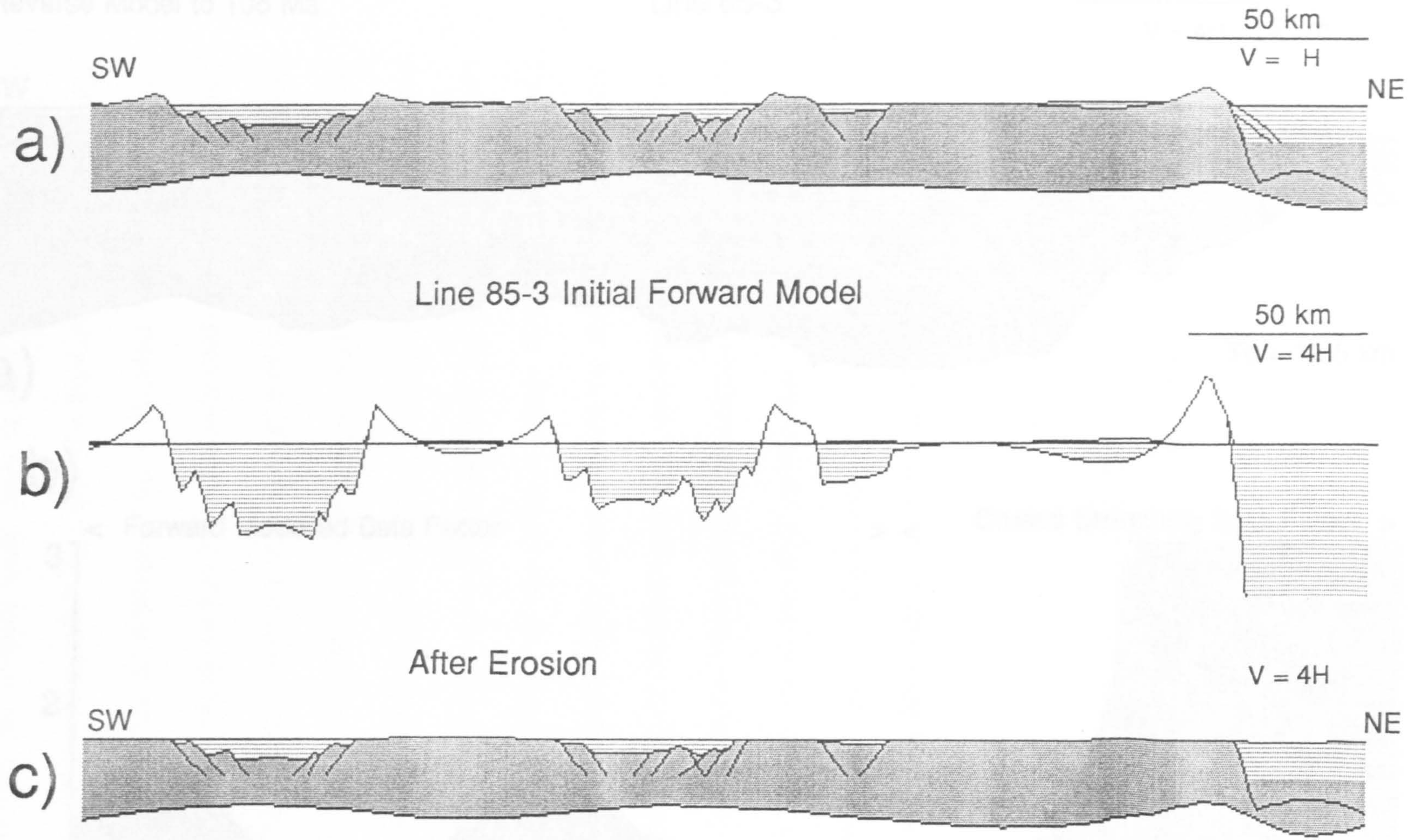


**Figure 7.11** a) Initial forward flexural cantilever model, used to generate the Beta profile for the landward portion of Line 85-3. V = H. b) As for a) but plotted at V = 4H. c) The initial forward model after erosion (V = H). Te = 5 km

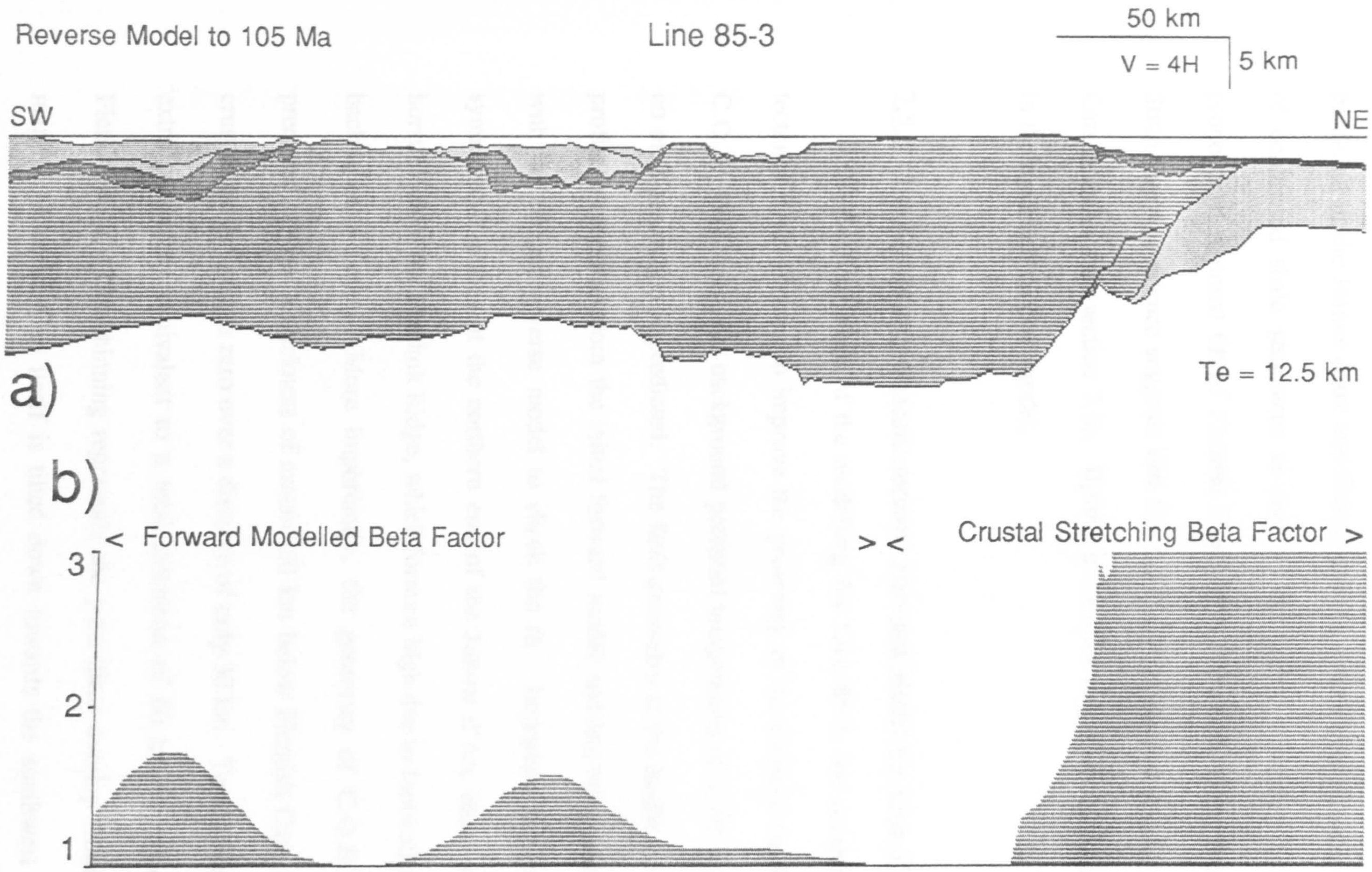


**Figure 7.12** a) Revised reverse post-rift model for Line 85-3 using a combination of modelled Beta profile, crustal stretching factor near the C.O.B. and infinity beneath oceanic crust. Te = 12.5 km.

Beta profile - modelled over the landward portion but taken from the crustal stretching values towards the C.O.B. Palaeo-bathymetry of up to 1.2 km is now predicted in the Jeanne d'arc and Carson Basins, which corroborates the deposition of condensed shale sequences as seen in the wells. Another difference is the pronounced regional tilt of Flemish Cap to the southwest, away from the C.O.B. Stratigraphic evidence suggests that this tilt is also evident at the NE margin of the Carson Basin (see section 7.8). Uplift on Beothuk ridge is slightly underestimated in the modified reverse model.

### 7.5.4 The Combined Magmatic-tectonic Forward Model for Line 85-3.

In the final stage of the modelling for Line 85-3, the combined magmatic-tectonic model is used to improve the geometry of the forward model close to the C.O.B. With a normal background potential temperature of 1280 °C (Figure 7.13) no melt generation is predicted. The fault geometry at the landward portion of the profile is modified from the initial forward model and has been compared directly with the revised reverse model to check the fit. Important features include the symmetrical graben at the northern end of the Jeanne d'Arc basin and the narrow horst block of the Beothuk Ridge, which forms a high due to footwall uplift from two back-to-back faults. More importantly, the geometry of C.O.B. is accurately predicted. From a thickness of around 30 km below Flemish Cap, the continental crust thins abruptly to zero over a distance of only 30 km. To achieve this thinning, extra pure-shear equivalent to a total extension of 60 km is added northeast of Flemish Cap. This thinning represents the pure-shear overlap from the conjugate margin. Flemish Cap itself is tilted down towards the southwest (matching the

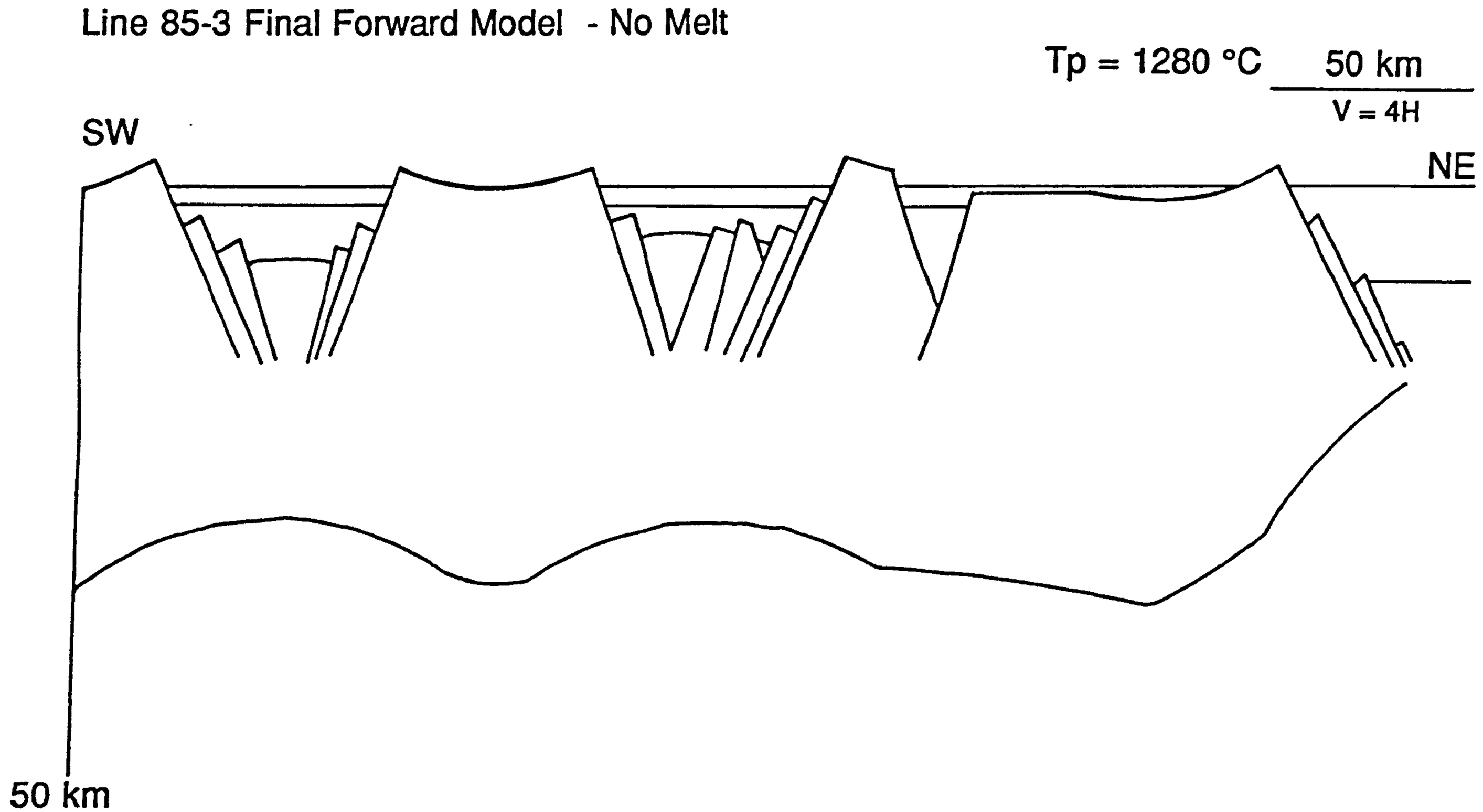


**Figure 7.13** The combined magmatic-tectonic forward model applied to Line 85-3. Tp = 1280 °C and no melt is produced. Palaeo-bathymetry varies across the profile, from 2 km at the SW end to 8 km near the C.O.B.

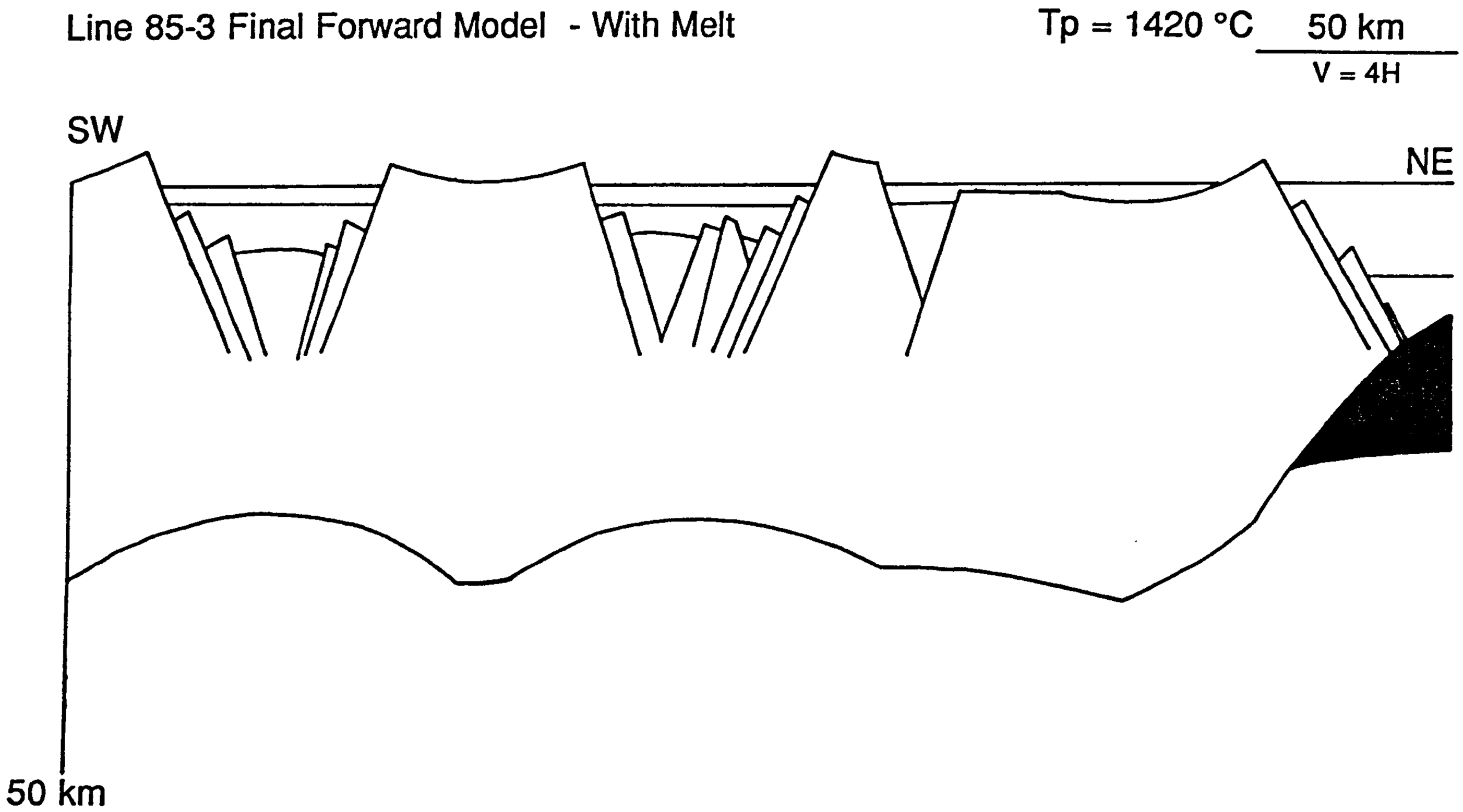


**Figure 7.14** The combined magmatic-tectonic forward model applied to Line 85-3. Potential temperature is elevated - Tp = 1420 °C - producing a magmatic underplating wedge up to 8 km thick. Palaeo-bathymetry varies as before.

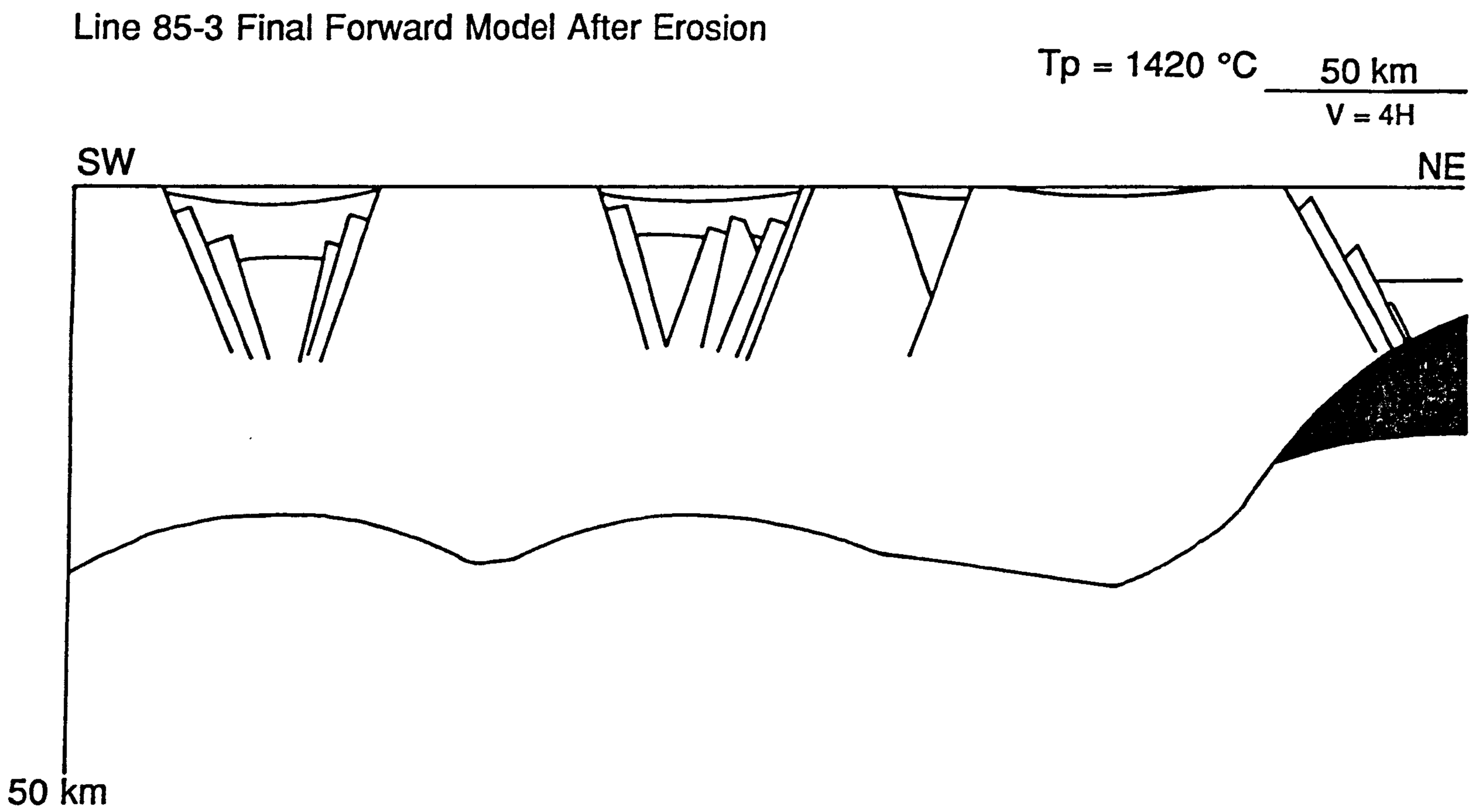


**Figure 7.15** The combined magmatic-tectonic forward model applied to Line 85-3. Tp = 1420 °C, palaeo-bathymetry varies as before. The flexural isostatic consequences of erosion to sea level are included.

reverse modelling results) away from footwall uplift of 2.5 km. By contrast to the initial forward model, palaeo-bathymetry varies across the combined magmatic-tectonic model for Line 85-3. The systematic increase in water depth towards the C.O.B. is designed to reproduce the effect of sediment starvation in the deeper parts of the section.

Elevating the mantle potential temperature to 1420 °C has the effect of producing a magmatic underplating wedge up to 8 km thick, extending 35 km back from the C.O.B. (Figure 7.14). Uplift due to hot, low density melt replacing mantle significantly increases the uplift and southwesterly tilt of Flemish Cap. The same profile, after the flexural isostatic effects of erosion have been calculated, is shown in Figure 7.15. Significant palaeo-bathymetry is maintained and the predicted end-rift geometry implies that synclinal depressions are due to marginal uplift in addition to post-rift compaction.

## 7.6 Modelling Results for Lithoprobe Profile 85-4.

Figures 7.16 shows the original profile Lithoprobe Line 85-4 after depth conversion. As with Line 85-3, the details of the tectonic elements have been described in detail in Chapter 6. Although the results of the reverse post-rift modelling of line 85-4 are pertinent to formation of the Base Aptian B.M.B., a rift age of 131 Ma has been used for the reverse thermal modelling. This represents the last thermal uplift event to affect the margin, caused by the ridge-jump back to the Grand Banks margin, rather than a breakup event itself. It is an appropriate figure to use because line 85-4 crosses zones 1 and 2 on the Grand Banks.

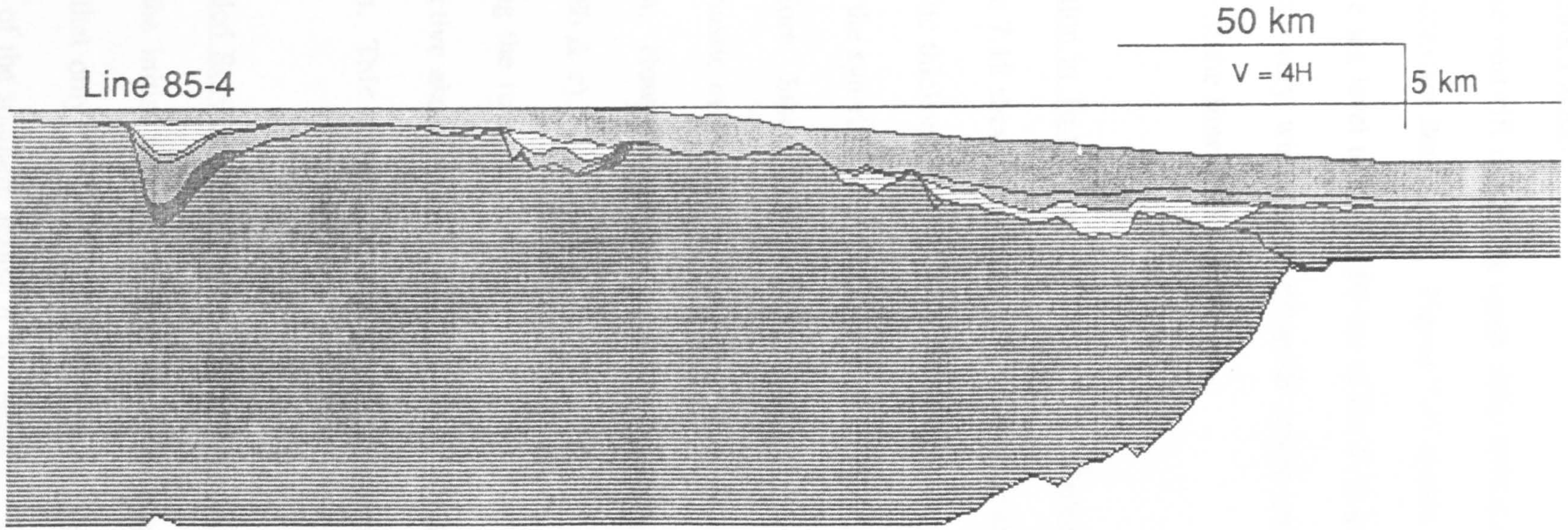


**Figure 7.16** Original section of Lithoprobe Line 85-4 after depth conversion.

### 7.6.1 Reverse Post-Rift Thermal Modelling using a Seismically Defined Crustal Stretching Factor.

Reverse post-rift modelling again starts with a crustal stretching Beta profile, rather than a constant Beta factor. Figure 7.17 shows a post-rift onset profile which is at, or above sea level to within 60 km of the C.O.B. and remarkably flat. This is consistent with very widespread subaerial uplift and erosion over much of this southern area at the time of breakup.

### 7.6.2 Variation in Te for Reverse Post-Rift Modelling

Figure 7.18 shows the results of reverse modelling line 85-4 with a variety of effective elastic thicknesses (Te), from 3 km up to 10 km. At low values of Te, the "doming" of the syn-rift sediments above sea level is even more pronounced on Line 85-4 than before. Since the syn-rift fill on line 85-4 is relatively old -lower Jurassic sands and Triassic evaporites - part of the "doming" can be accounted for by over-decompaction. However, the "doming" effects disappear when the Te is increased (Figures 7.18b & c).

Taking the reverse modelling results for both lines together, it is suggested that the effective elastic thickness of a passive margin increases relatively quickly after breakup. This is largely due to the relaxation of the syn-rift thermal gradient

### 7.6.3 Coupled Reverse Post-rift and Forward Syn-rift Modelling for Line 85-4

For the initial forward model, shown in Figure 7.19, it should again be emphasised that only the landward portion is designed to be accurate. The total model depth of the southern Jeanne d'Arc Basin is identical to the models described

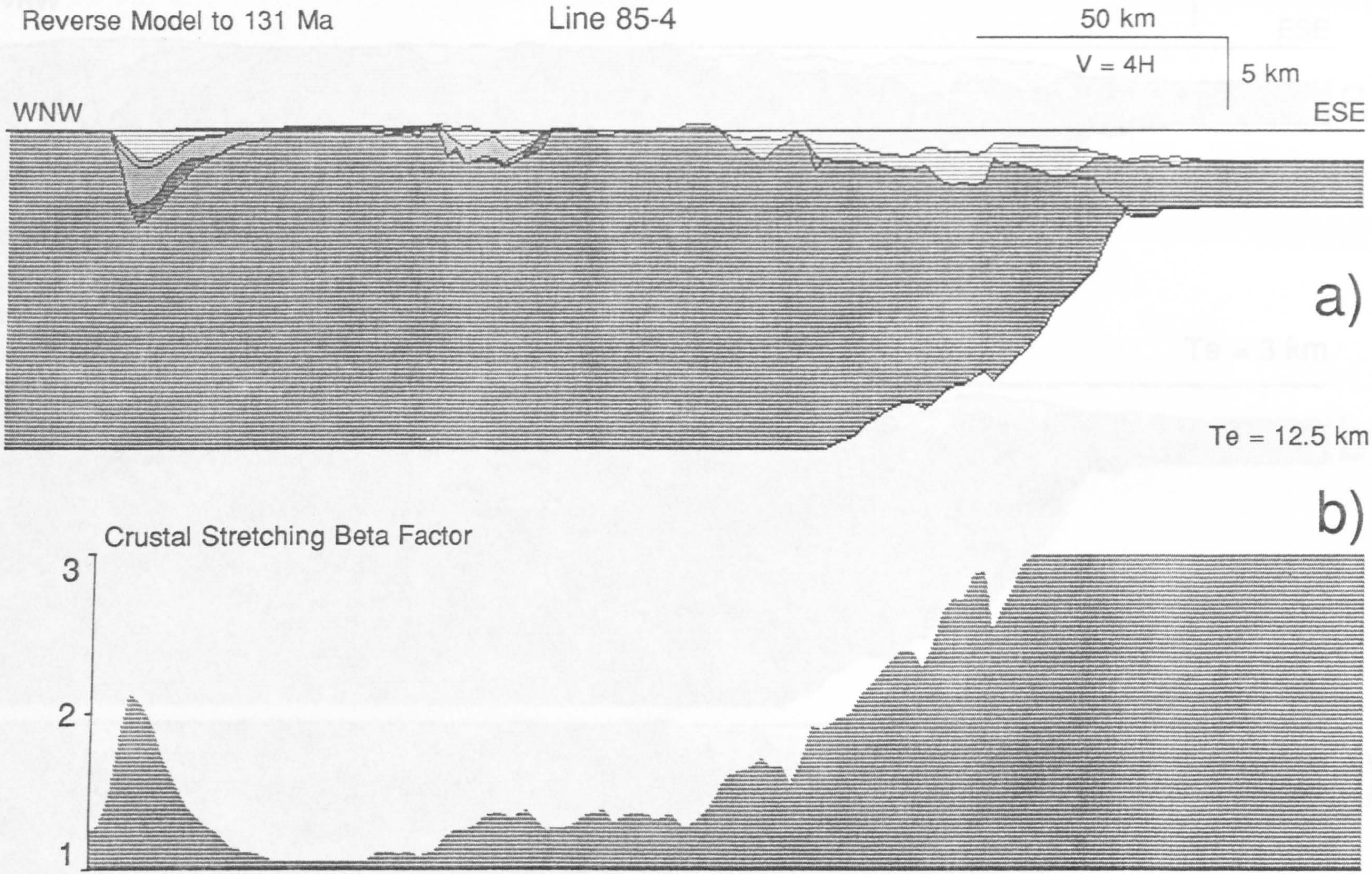


**Figure 7.17** a) Reverse post-rift model of 85-4 using the crustal stretching Beta factor (b) derived from the seismically defined Moho. Te = 12.5 km.

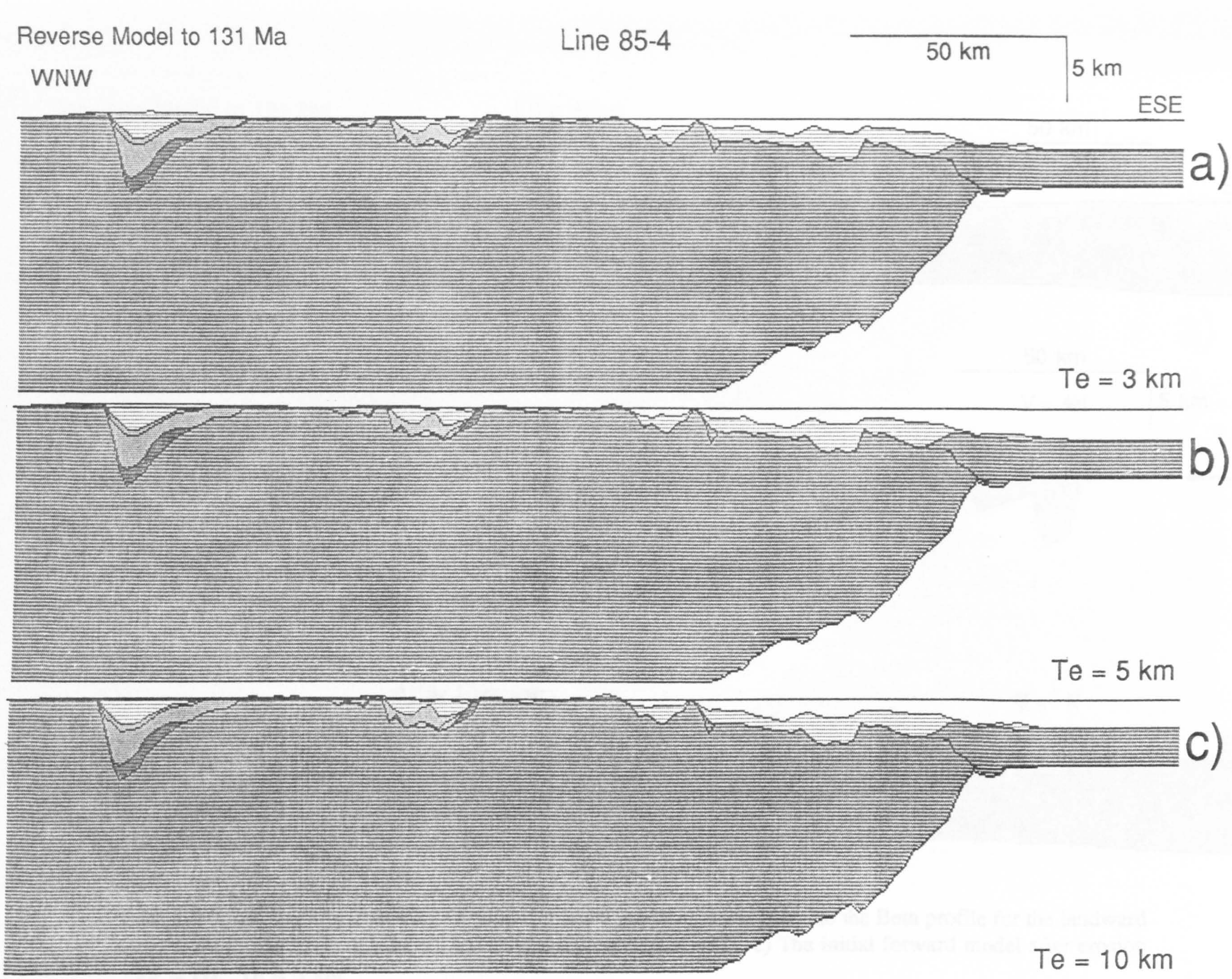


**Figure 7.18** The effect of elastic thickness on the reverse model results for line 85-4:- a) Te = 3 km. b) Te = 5 km. c) Te = 10 km.

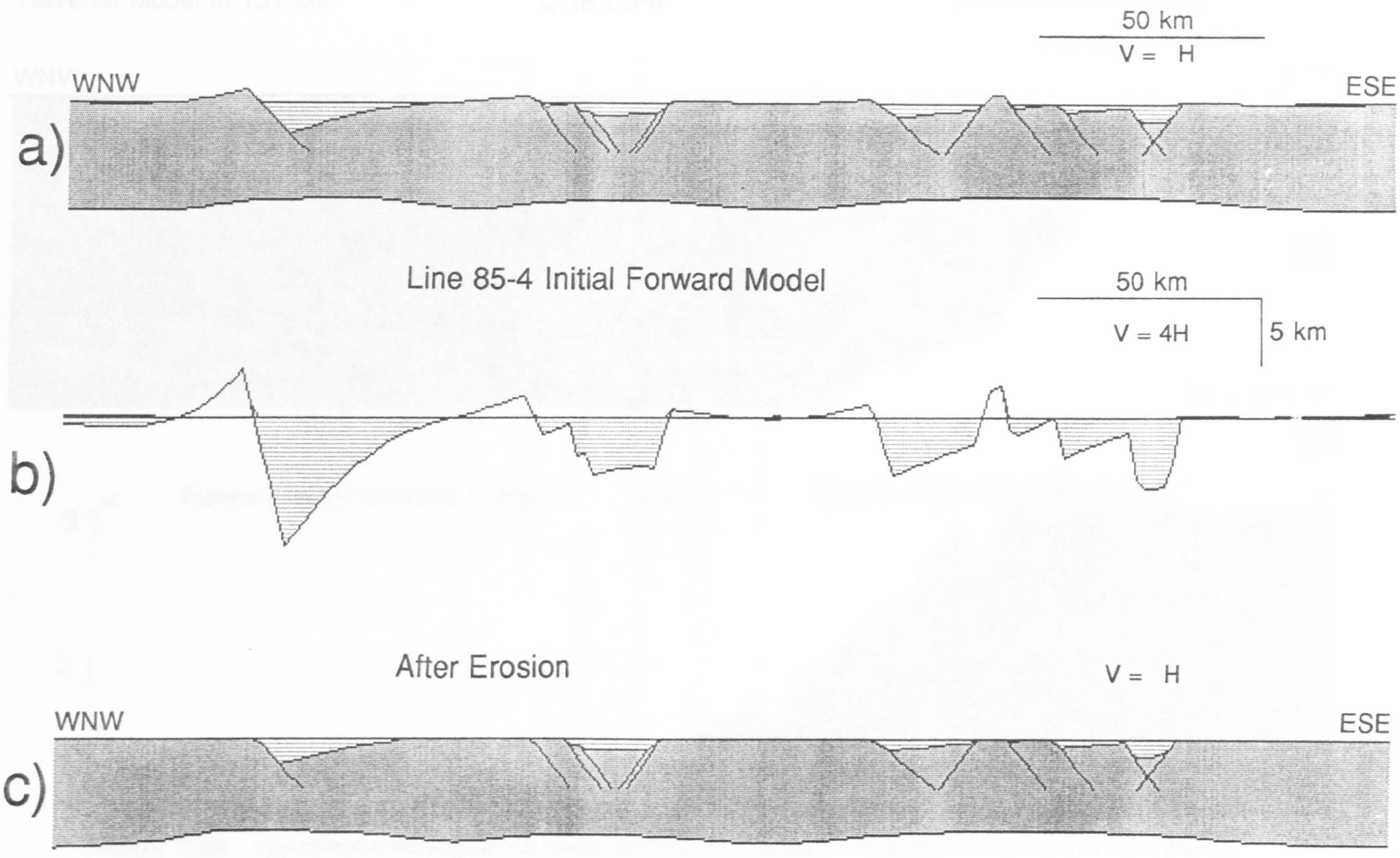


**Figure 7.19** a) Initial forward flexural cantilever model, used to generate the Beta profile for the landward portion of Line 85-4. V = H. b) As for a) but plotted at V = 4H. c) The initial forward model after erosion (V = H). Te = 5 km.

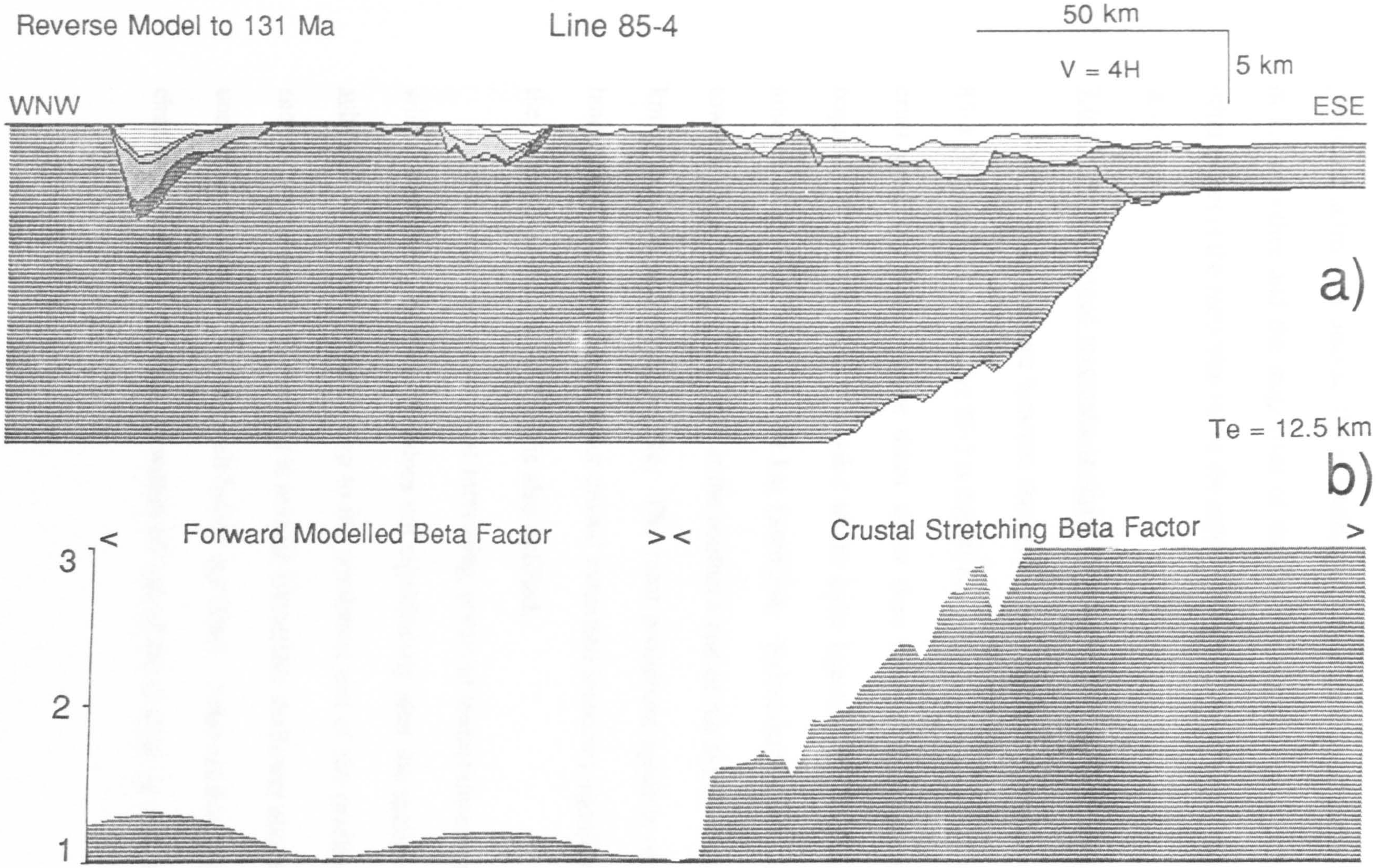


**Figure 7.20** a) Revised reverse post-rift model for Line 85-4 using a combination of modelled Beta profile, crustal stretching factor near the C.O.B. and infinity beneath oceanic crust. Te = 12.5 km.

in Chapter 2. An important contrast to Line 85-3 is evident when the combined Beta factor is used in the revised reverse model (Figure 7.20). No palaeo-bathymetry is predicted across the Jeanne d'Arc basin, even though the modelled Beta profile is much smoother and the magnitude of the reverse thermal uplift is less. The only other effect is the reduction in the elevation of the Morgiana high, East of the Carson Basin.

### 7.6.4 The combined magmatic-tectonic forward model for Line 85-4

The main contrast between the combined magmatic-tectonic model for Line 85-4 (Figure 7.21) and Line 85-3 is the 90 km wide zone over which the continental crust gradually thins - three times wider than before. Extra-pure shear is still required to thin the crust to a point where dyke injection would take over, but the amount is equivalent to only 40 km extension. Palaeo-bathymetry again increases towards the C.O.B. - from zero at the southern end of the Jeanne d'Arc basin to 2.5 km at the ESE end of the profile. The most prominent uplift is concentrated just landward of the point where upper crustal extension increases significantly, although the footwall of the Murre Fault is also uplifted.

It is important to note that increasing potential temperature beneath a margin with the geometry of Line 85-4 does not significantly alter the spatial distribution of subaerial uplift from Flemish Cap to the southwest end of the profile. Figure 7.22 shows that the depth-to-basement is several kilometres shallower above the magmatic underplating wedge - but still well below sea level. After erosion (Figure 7.23) the characteristically flat profile, to within 60 km of the C.O.B. is well matched.

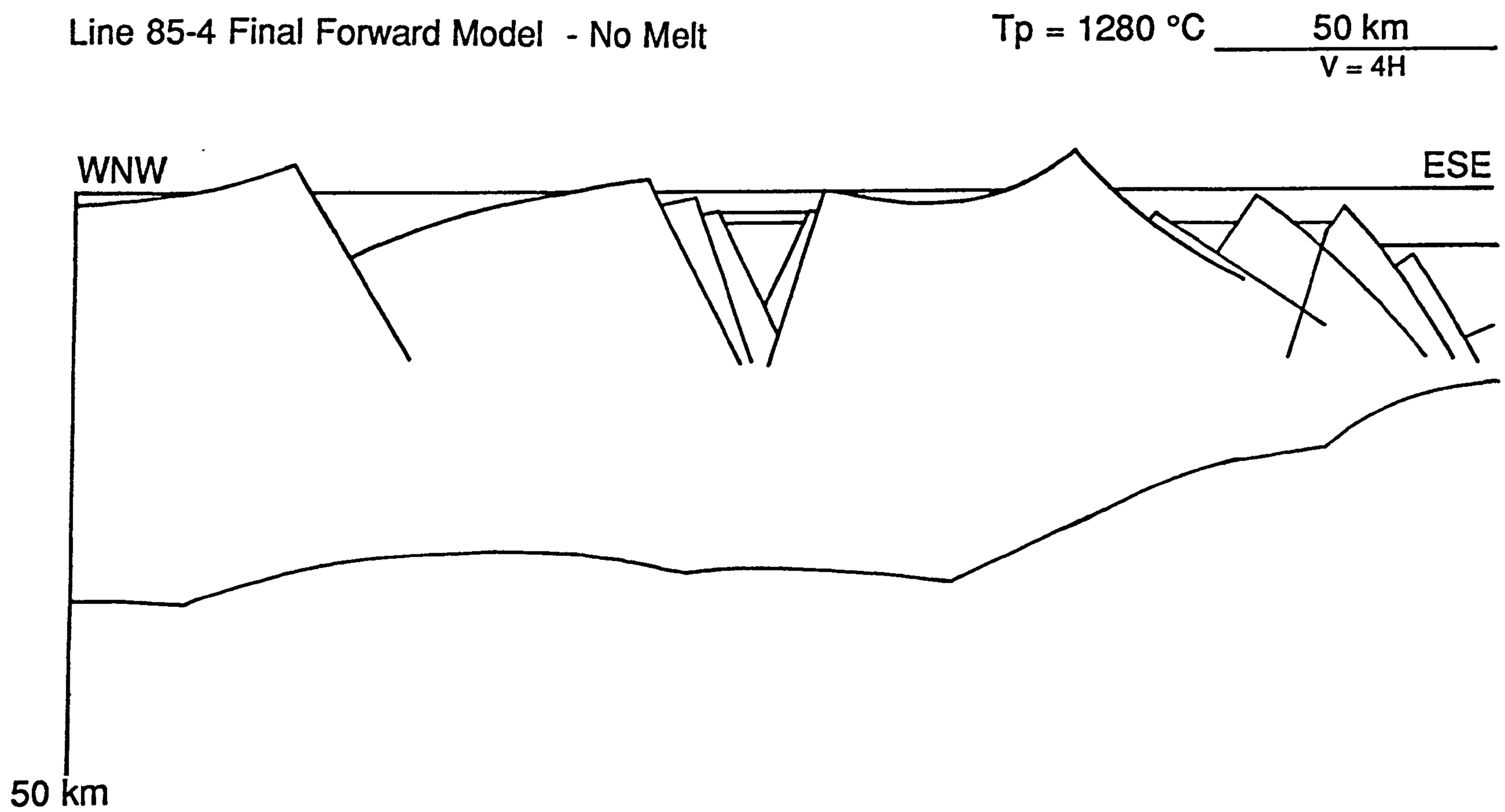


**Figure 7.21** The combined magmatic-tectonic forward model applied to Line 85-4. Tp = 1280 °C and no melt is produced. Palaeo-bathymetry varies across the profile, from 2 km at the SW end to 8 km near the C.O.B.

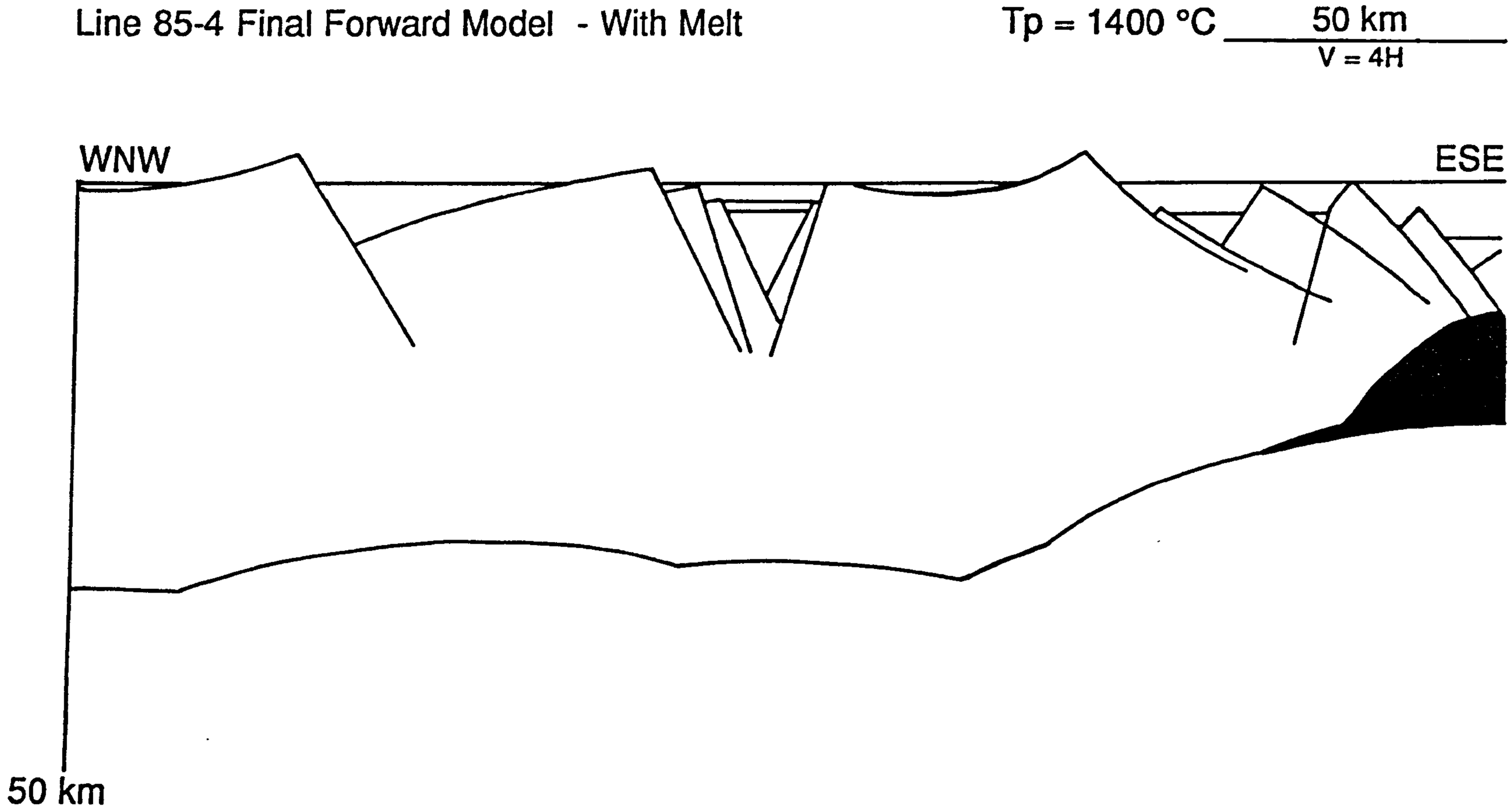


**Figure 7.22** The combined magmatic-tectonic forward model applied to Line 85-4. Potential temperature is elevated - Tp = 1420 °C - producing a magmatic underplating wedge up to 8 km thick. Palaeo-bathymetry varies as before.

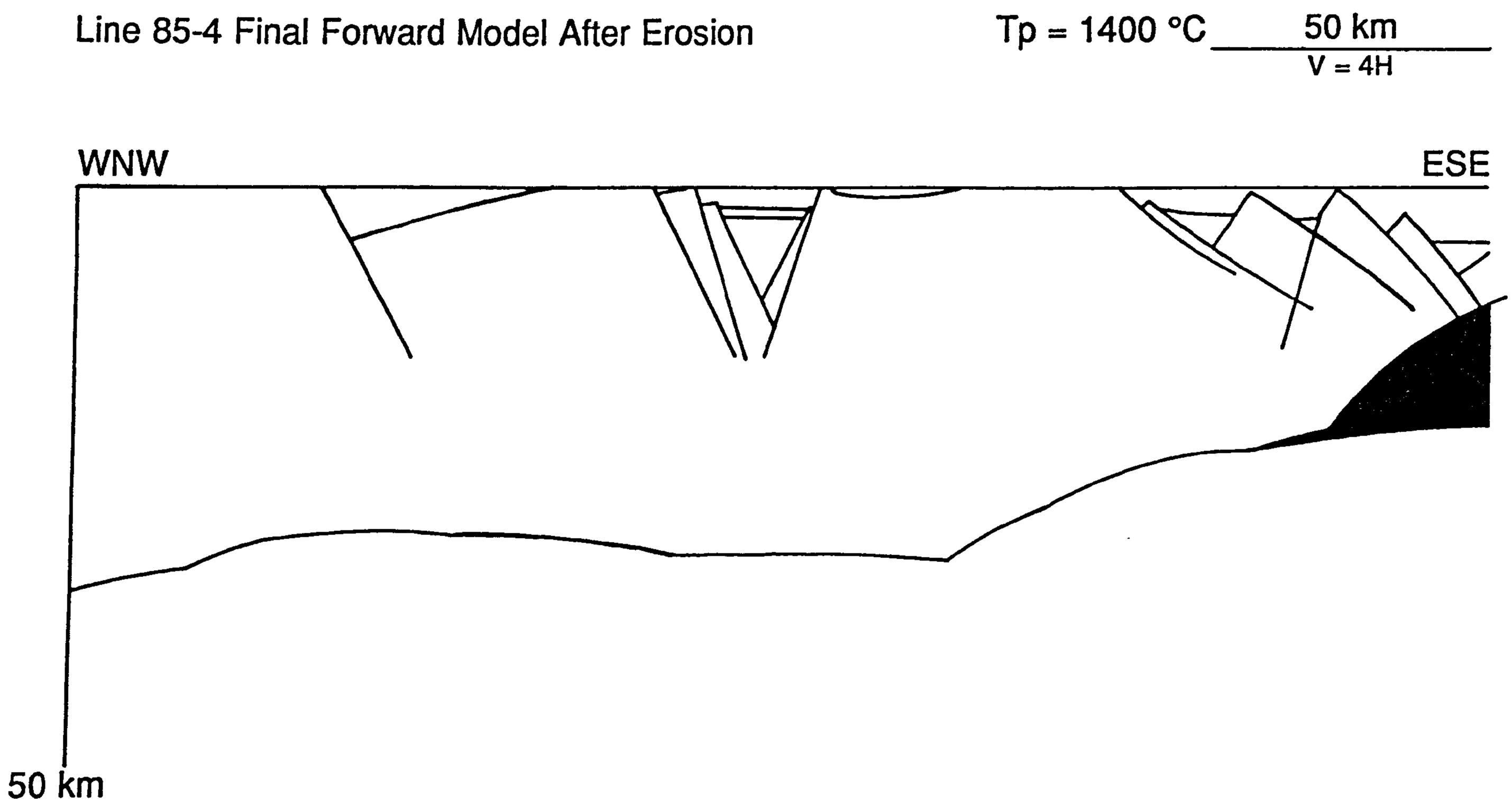


**Figure 7.23** The combined magmatic-tectonic forward model applied to Line 85-4. Tp = 1420 °C, palaeo-bathymetry varies as before. The flexural isostatic consequences of erosion to sea level are included.

## 7.7 Systematic Variation in Megasequence Boundary Morphology.

The final forward model for Line 85-3, which includes magmatic underplating, conforms to the threefold division of the passive margin, as described in Chapter 6 and shown in Figure 7.24. The northern part of the Jeanne d'Arc Basin corresponds to Zone A with the Central Ridge and Carson Basin in Zone B. In the combined magmatic - tectonic model for Line 85-4, the broad extensional zone, out towards the C.O.B., is the archetypal geometry for Zone C. By contrast, Zone C on Line 85-3 is much narrower, but the principle that the breakup megasequence boundary is in relatively deep water still holds. Subaerial uplift in Zone A is variable and largely controlled by the extensional geometry of the landward part of the passive margin. Line 85-3 has two 2.5 km high rift flanks whereas Line 85-4 has only one flank (coincidentally also 2.5 km high) but is eroded across the entire width of Zone A because the basin is full at breakup. Zone B can be thought of as an intermediate zone, where geometry contributes to the overall amount of uplift but regional effects play an important part. This is one of the most important contrast between the two lines. In Zone B on Line 85-3, the NW end of Flemish Cap is uplifted by underplating at the C.O.B. Once the horst becomes emergent flexural erosion takes over and augments the net anti-clockwise rotation of the block. On Line 85-4 the basement high in Zone B is too far from the C.O.B. to be affected by underplating and geometry plays a more important causative role for uplift and erosion either side of the Carson Basin.

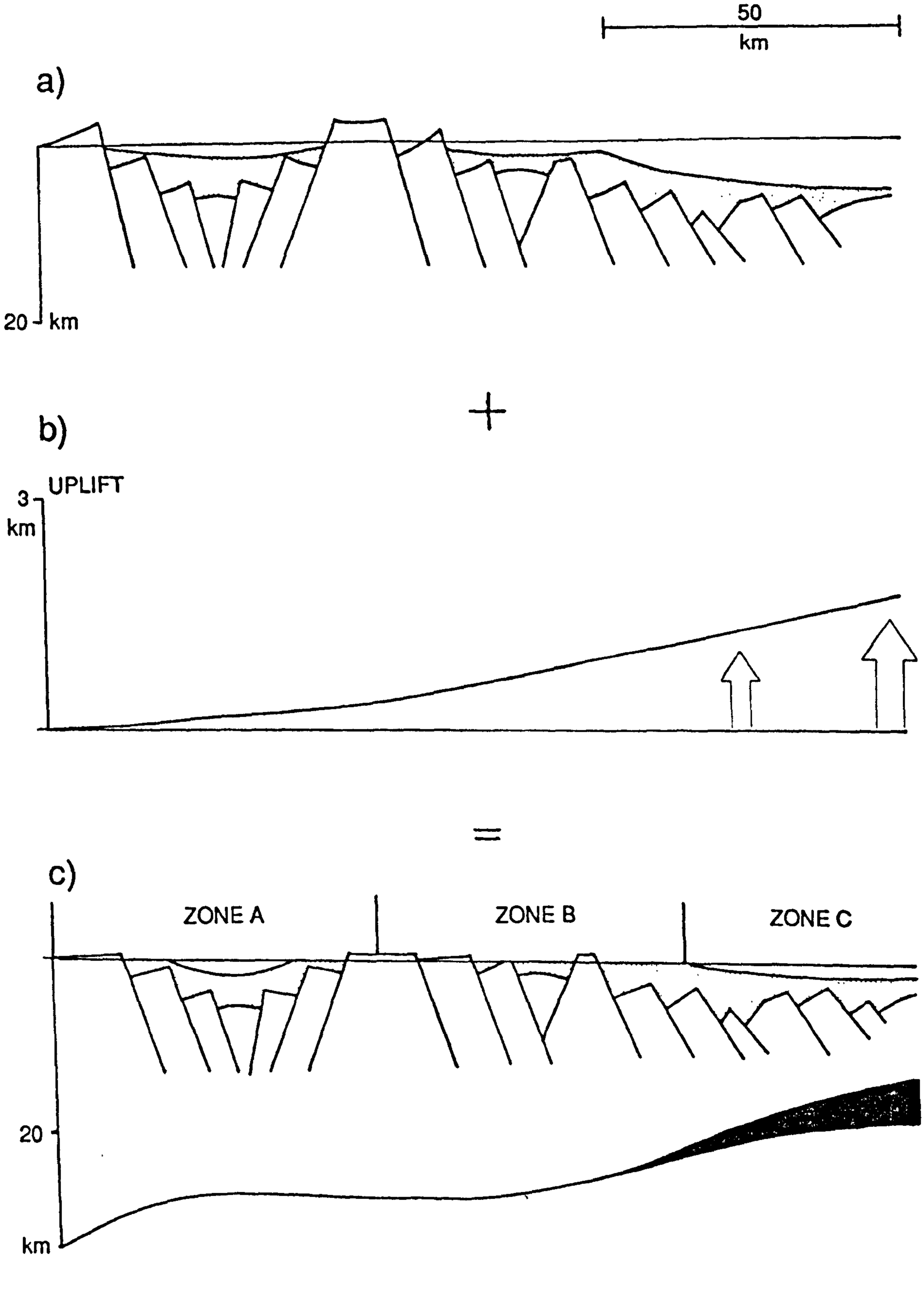


**Figure 7.24** The systematic variation in breakup megasequence boundary morphology.

## 7.8 Stratigraphic implications of the modelling results.

Figure 7.25a shows a present day section across Beothuk Ridge - a prominent horst-block on Lithoprobe Line 85-3 (see Figure 7.8). A preliminary study might conclude that there are two syn-rift wedges in the SE footwall of the ridge. However the Middle Albian breakup megasequence boundary divides these two wedges and the upper sequence is removed by reverse post-rift modelling (Figure 7.25b). As noted in section 7.5.3, the uplift on the ridge is underestimated by the reverse post-rift model and the true situation at the end of the rift phase is given by the forward model (Figure 7.25c). Before erosion (dashed lines on Figure 7.25c) the height of the top of Beothuk Ridge varies between 3.0 and 2.5 km above sea level - tilting down towards the northeast. Despite this geometry, sediment is nevertheless transported to the footwall on the opposite side of the ridge, into the southwest syn-rift wedge. The most likely controlling factor on sediment transport direction is the *regional* tilt of the passive margin, with uplift in the northeast caused by magmatic underplating. Sediment continued to be shed onto the southwest footwall in the post-rift phase, implying that Beothuk Ridge remained above sea level for some time after breakup. In this case the upper wedge shape is the depositional geometry rather than the effect of active extensional tectonics.

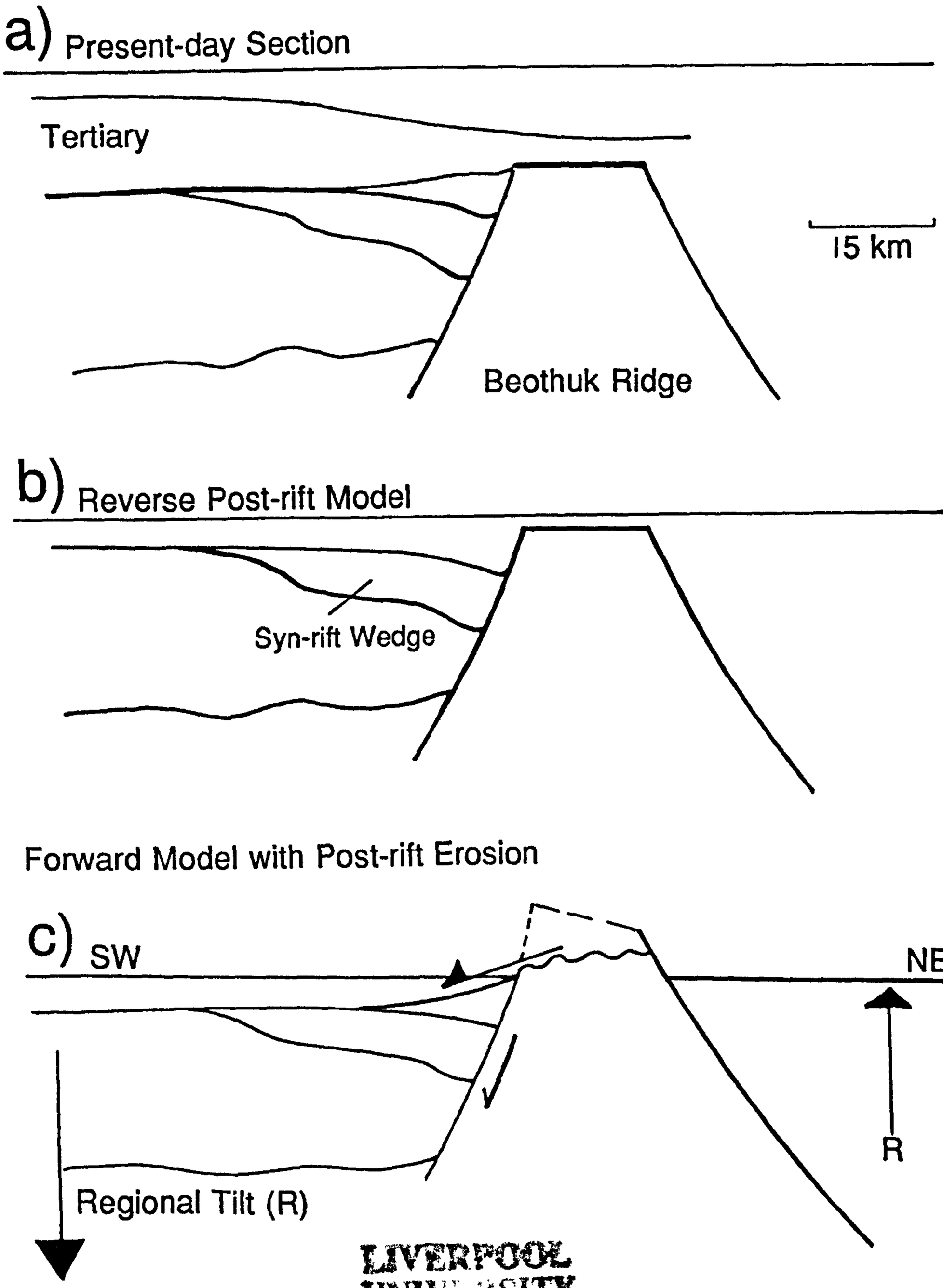




**Figure 7.25** The stratigraphic implications of the modelling results - Beothuk Ridge and the Carson Basin, Lithoprobe Line 85-3. a) Present-day section. b) Reverse post-rift model. c) Forward model with post-rift erosion showing the effect of regional tilt on sediment transport direction.